AD-A216 881

Laboratory
for the
Processing and Evaluation of Inorganic Matrix Composites

contract No. N00014-85-K-0645

James A. Cornie, Principal Investigator

Annual Technical Report
June, 1989

Materials Processing Center
Massachusetts Institute of Technology
77 Mass. Ave. Rm 8-401
Cambridge, MA 02139

Laboratory
for the
Processing and Evaluation of Inorganic Matrix Composites

contract No. N00014-85-K-0645

James A. Cornie, Principal Investigator

Annual Technical Report
June, 1989

Materials Processing Center
Massachusetts Institute of Technology
77 Mass. Ave. Rm 8-401
Cambridge, MA 02139

CONTENTS

Summary of Results

1. Introduction

The research program at MIT on the fundamentals of processing of inorganic matrix composites focuses on developing a basic understanding of solidification processing of metal matrix composites and the behavior and modification of interfaces. This understanding is applied to the development of processes for the manufacture of evaluation specimens which are used, in turn, to determine the microstructure/ processing/ materials properties relationships. Technical areas discussed in this report as follows:

2. Kinetics of Infiltration

The metal matrix processing work has both fundamental and practical aspects. The fundamental work has been directed toward developing analytical models for the infiltration of fibrous preforms by molten metals and alloys. This group has, in previous work on this program, developed an analytical model that accurately describes the infiltration of well characterized preforms (Saffil™ in this case) and gives physical and analytical insight into the kinetics of infiltration. The predictions of the model are compared to experimental results in Figure 1.

The infiltration of fibrous preforms by an alloy is a much more complicated case. Severe macrosegregation effects were noted when fibrous preforms at a temperature below the liquidus were pressure infiltrated. Since it is desirable to minimize the preform temperature in order to avoid severe degradation between the molten metal and the fiber reinforcement and to refine the the composite microstructure, it was necessary to develop models of the infiltration of alloys into fibrous preforms. This was done using the basic similarity solution approach of the earlier model; Professor Mortensen and V. Michaud were able to use the Boltzmann transformation of location and time into a single variable which transformed the governing partial differential equations into ordinary differential equations. The predictions of this model are shown in Figure 2 and compared to experiment in Figure 3 with Al 4.5%Cu serving again as a model alloy.

Earlier work in the IST/SDIO-ONR Consortium on Advanced Materials, especially that of S-Y Oh, has shown that wetting of a ceramic surface by a liquid metal is a time dependent process and that an incubation time is generally observed with sessile drop and capillary rise experiments. In pressure infiltration experiments as well as in production process, this lack of wettability manifests its self as a threshold pressure that must be overcome before infiltration can take place. During active infiltration experiments or manufacturing operations, it is the instantaneous infiltration that is important to understand and model. Using the liquid position probe developed during the dissertation of Larry Masur and the basic analytical model for infiltration, we have developed a technique to determine the dynamic wettability. The basic equations and graphic approach are given in Figure 4. This technique has been used to measure the dynamic wettability of Saffil™ alumina preforms. To measure the wettability of conductive or semiconductive fibers or particulates, other methods for the measurement of the liquid metal position had to be devised. In one set of experiments on the measurement of dynamic wettability of carbon preforms, one of our students, J. Sommer, measures the overall resistance change of the preform as it is being infiltrated and to derive the instantaneous liquid

1

metal position. T. Fletcher is measuring the dynamic wettability of SiC particulate preforms with Al and Zn alloys. She uses a capacitance device to determine the position of the moving infiltration front. All three methods are shown in Figure 5. These data will be used to develop physical insight into the infiltration process and to investigate surface and mold environmental influences on the infiltration process and the subsequent quality of composites. This effort gives insight into such processes as the Lanxide "Pressureless Infiltration Casting Process" which utilizes Al-Mg alloys at high temperatures with a mold environment of a flowing nitrogen gas doped with hydrogen, and the Katzmann air stable coating for Gr/Mg composite fabrication by vacuum infiltration.

3.   **Pressure Infiltration Casting Technology**

While developing the experimental techniques for measuring the kinetics of infiltration, we had actually developed a low cost, high quality approach toward the manufacture of infiltrated metal matrix composites. A prototype casting machine now in operation in our laboratory is shown in Figure 6. The most significant features of this machine are the use of low cost tooling, its ability to independently control and vary the important casting parameters, namely, melt temperature, preform temperature, applied pressure, pressurization rate, preform environment (atmosphere), and solidification time. We are now using this machine to determine the structure/property/processing relationships for carbon fiber reinforced Al and Mg alloys. Preliminary results on the effect of processing parameters on the work of fracture of P-55 reinforced unalloyed Mg is shown in Figure 7. These data show that the work of fracture is proportional to the amount of fiber/matrix interfacial area and that for the case of graphite/Mg, the interfacial reactions are not deleterious.

The pressure infiltration approaches developed in this group have resulted in the formation of the PCAST Equipment Co. of Pittsburgh, PA. Their concept of the infiltration process is given in Figure 8. They plan to develop a prototype foundry and to license and sell turn-key operations to their clients.

4.   **Semi-Solid Slurry Processing**

H-K. Moon is investigating the rheology of semi-solid slurries of Al-7%Si with SiC particulates and is evaluating issues affecting the particulate distribution and hence the strength and toughness of cast particulate reinforced composites. Eric Klier developed a process for the infiltration of packed beds of particulates with Mg and later Al alloys. These infiltrated bodies were then considered to be "Master Composites" which were later diluted and shear dispersed to the desired alloy composition and volume fraction. This process, shown in Figure 9 results in high quality dispersed castings with no residual gas porosity. This technology has been licensed to the Norton Company for commercialization.

The second phase of this process, shear dilution, has been incorporated into a continuous casting machine in our laboratory. This device, shown in Figure 10, subjects the redispersed master composite and dilluent alloy to high shear rates just prior to continuous solidification in a controlled temperature gradient. Initial results (Figure 11) on material supplied by Dow Chemical show that B_4C clusters are effectively redispersed to a very uniform distribution. The current research is now directed toward the shear dispersion of Mg/SiC master composites and continuous casting. We intend to examine such mechanical properties as tensile strength,

2

ductility and work of fracture. Our plans include thixoforging of the billet stock produced by our continuous casting machine and the evaluation of the rheology of high rate semi-solid thixoforging processes.

5.   **Engineering the Interface in Inorganic Matrix Composites**
Our work has concentrated on the development of experimental methods for the measurement of the work of fracture and the cohesive strength of interface, the deposition of model interfaces, and the characterization of those interfaces in pressure cast Al matrix composites. The technique for measurement of work of fracture of the interface is shown in Figure 12. The method developed by H. Landis in his dissertation consists of loading the interface by applying a residual stress that is induced by certain processing conditions for the PACVD (Plasma Assisted Chemical Vapor Deposition) deposition of amorphous SiC. The mechanical properties of the residually stressed coating are first calibrated on a Si crystal wafer as shown in Figure 12-a. The stored energy of the coating is a function of the coating thickness. At a critical thickness, the coating delaminates and the work of fracture is deduced through a simple calculation shown in Figure 12-b and c. When calibrated coatings are applied to a fiber to the critical thickness as shown in Figure 12-d, the work of fracture is measured on the engineering material of interest. The PACVD amorphous SiC films can then be used to apply a delamination force to any interface by simply overcoating an unknown thin coating with the thicker strained coating. Similar calculation approaches will then be used to determine the work of fracture of any interface. At this point, we have the basic tools to commence our engineering of the interface.
Professor Argon and V. Gupta have devised a laser spallation experiment for measuring the cohesive strength of interfaces. Both of these techniques are being used to guide our selection and synthesis of interfaces for inorganic matrix composites.

6.   **Synthesis of BN and B$_4$C from Pre-Ceramic Polymer Chemistry**
Professor D. Seyferth and Dr. W. Reese have had much success in synthesising BN and B$_4$C from a decaborane precursor. The former material, BN, is of particular interest because it has a 100% yield of boron in the form of BN and can be produced in either its hexagonal crystalline form or as amorphous BN depending upon the pyrolysis temperature (in an ammonia atmosphere). The pre-ceramic polymer can be diluted in solvents and used to coat fibers with as little as 0.1μm thick layers of BN after subsequent pyrolyzing. We intend to use this material in our interface program as a fiber coating. BN is almost totally inert in contact with molten Al. Its expected low cohesive strength and work of fracture at the fiber interface makes it a good candidate for interface control. Seyferth and Reese have succeeded in spinning fibers from the pre-ceramic polymer. This is a very attractive technology. However, it has one drawback. Decaborane is only available from government storage. While these sources are sufficient for research purposes, production facilities now in moth-balls would have to be reactivated. It may be desireable to search for alternative, lower cost approaches to BN and B$_4$C.
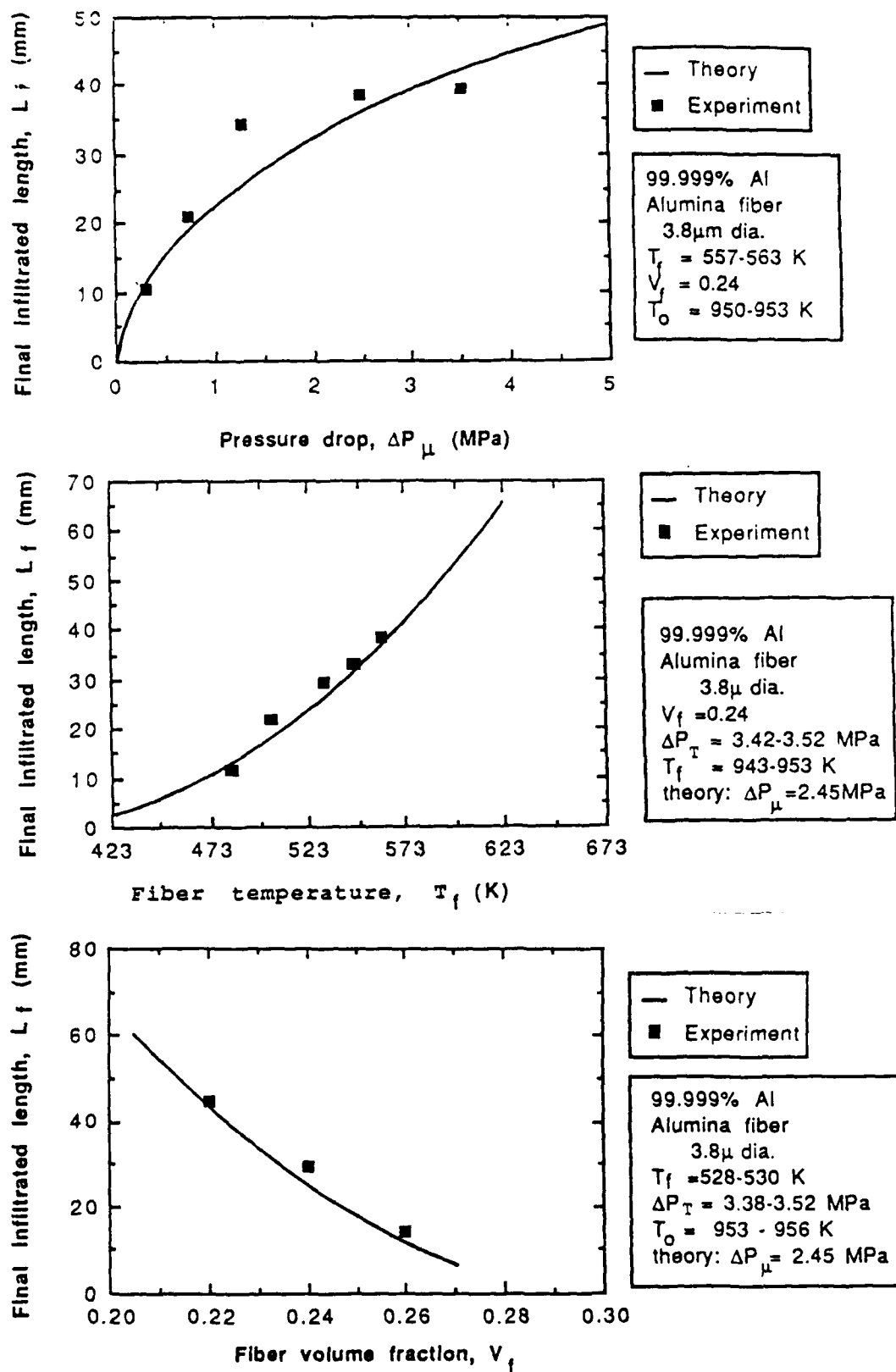
Figure 1: Comparison of experimental results with predictions of model for infiltration of a ceramic preform with a pure metal

part 1: Final infiltrated length vs pressure drop, fiber temperature, and fiber volume fraction

Figure 1: Comparison of experimental results with precictions of model for infiltration of a ceramic preform with a pure metal

part 2: lenth of infiltration/√time vs fiber temperature and initial metal temperature

Fig.2 : Profiles of temperature, fraction solid and average composition versus the dimensionless length $\chi = x/L$, for two cases.
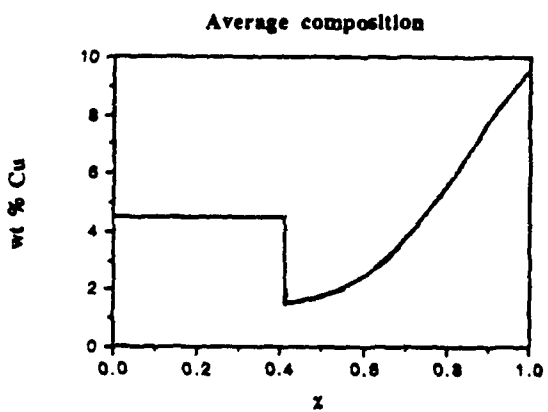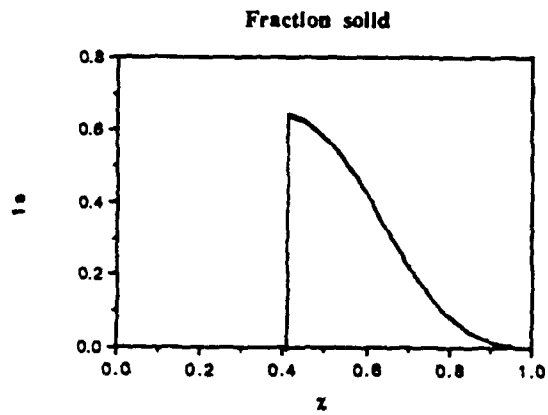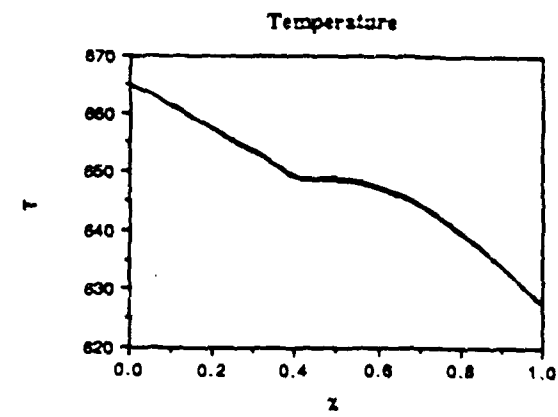
Conditions :
$T_f = 298\ °C$, $T_0 = 665°C$
$Vf = 23.5\%$, $L/\sqrt{t} = 0.005\ m/\sqrt{s}$
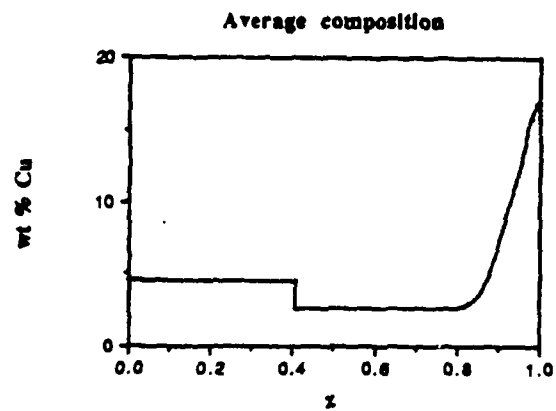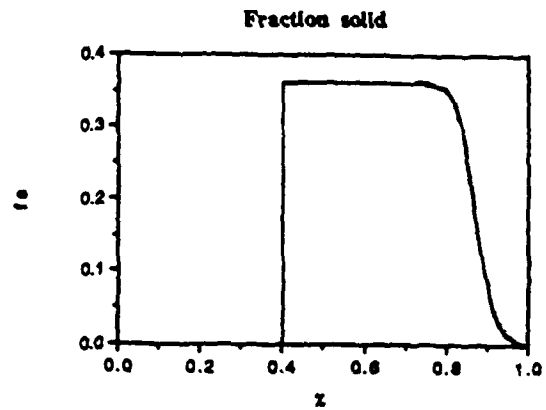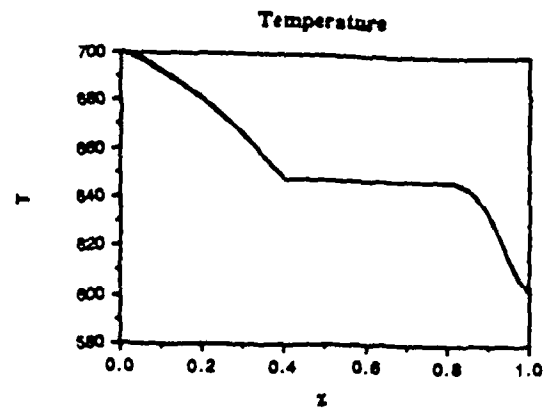
Conditions :
$T_f = 400\ °C$, $T_0 = 700°C$
$Vf = 24\%$, $L/\sqrt{t} = 0.015\ m/\sqrt{s}$
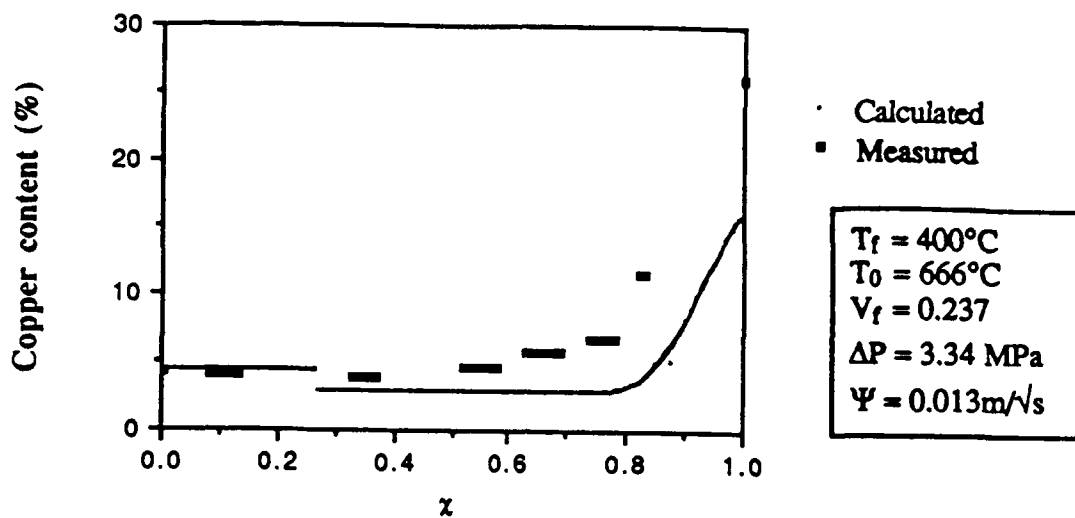
Fig.3 : Comparison between theoretical work and preliminary experiments : average composition profile along the sample length. The experimental data were obtained as follows : a composite sample is cut into slices at various locations along the sample length, perpendicular to the sample axis. Each slice is immersed in Aqua Regia, to dissolve the matrix. The composition of the solutions, after filtration to eliminate the fibers, is determined by atomic absorption.

$$\Delta P_\mu = \Delta P_t - \Delta P_\gamma$$

Integration of Darcy's Law, assuming constant applied pressure:

$$\frac{L^2}{t} = \frac{2K}{\mu\,(1-V_f)}\,(\,\Delta P_t - \Delta P_\gamma\,)$$

Rearranging:

$$\frac{L^2}{t} = \frac{\mu\,(1-V_f)}{2K}\,(\,\Delta P_t - \Delta P_\gamma\,)$$

$$\Delta P_\gamma = (\,\sigma_{FL} - \sigma_{FA}\,)\,S_f$$

$$\Delta P_\gamma = -\,\sigma_{LA}\cos(\theta)\,S_f$$
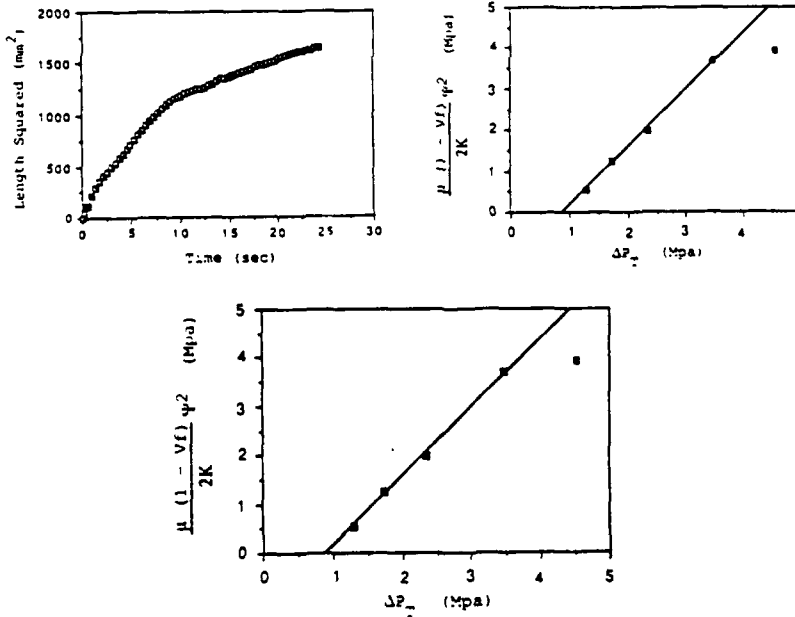
Figure 4- Equations and graphical methods for the measurement of infiltration kinetics and dynamic wettability of ceramic preforms with a molten metal.
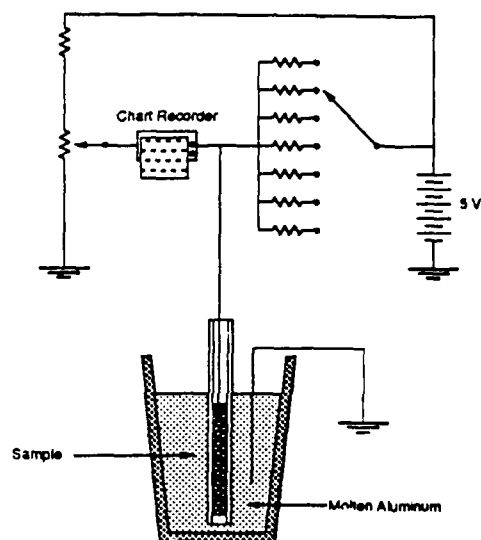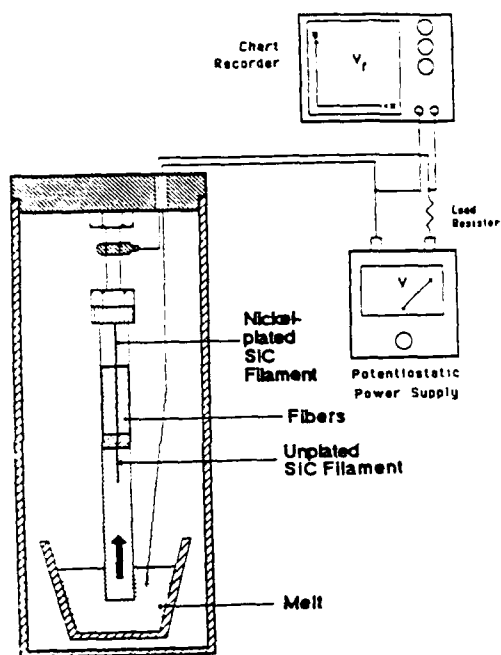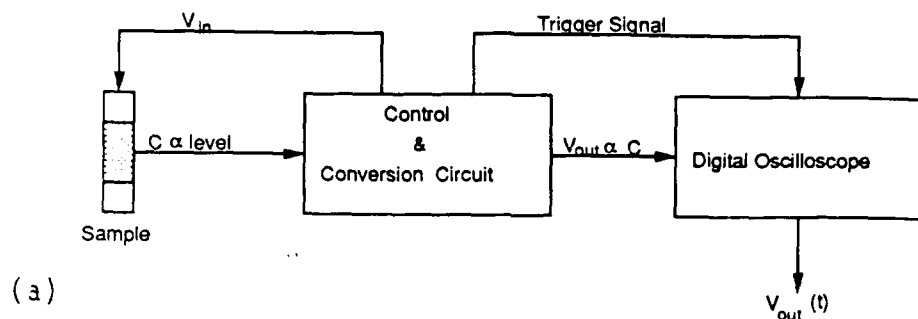
Figure 5: Liquid metal position sensor techniques for kinetics of infiltration and dynamic wettability experiments

a) capacitance method
b) fiber resistance shunt method
c) preform resitance shunt method
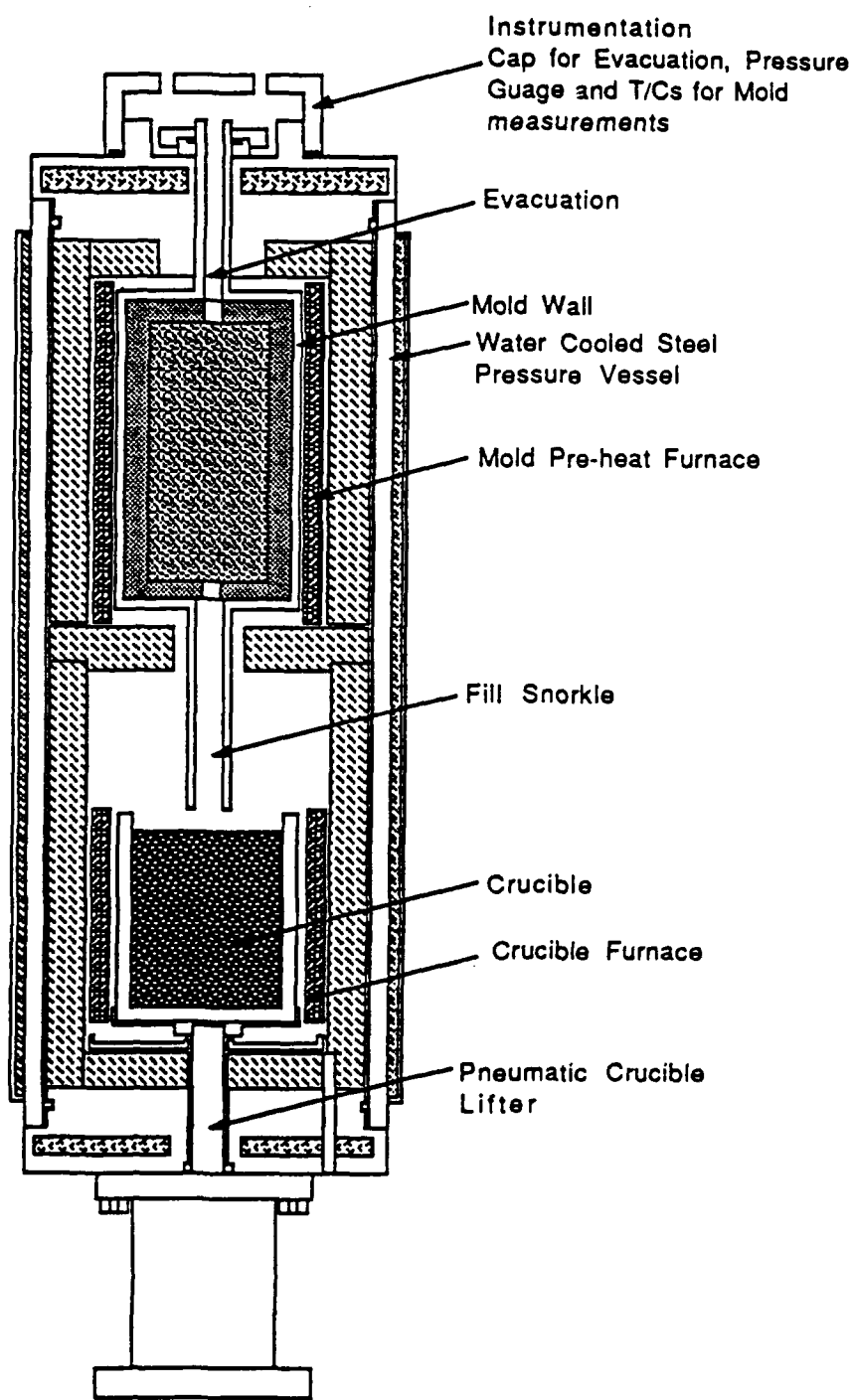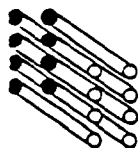
Figure 6- Schematic of the M.I.T. Pressure Infiltration Machine.

Work of Fracture as a Function of Preform Temperature
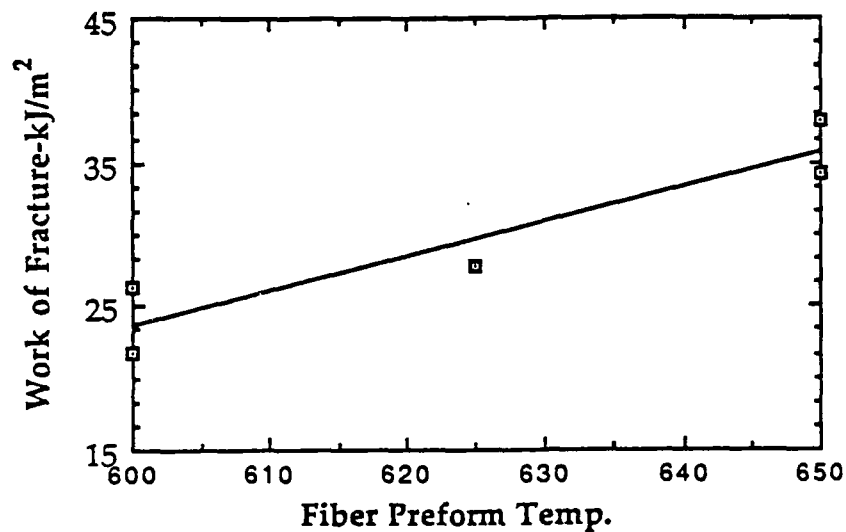
Work of Fracture Vs. Vol. Fraction Fibers
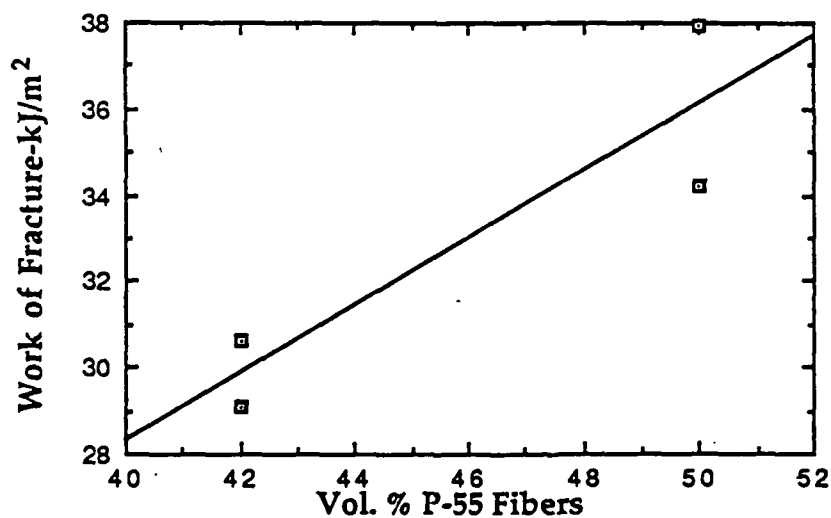
Figure 7- Variation of work of fracture of P-55/Mg composites as a function of processing parameters.

1. Preform Load

quick release heads
vacuum tube
pressure vessel
preform
mold furnace
solidification control
melt furnace
fill tube
matrix material
lift mechanism

2. Vessel Load

thin wall mold
mold clamped with gasket

3. Melt and Evacuation

Mold, preform and melt are evacuated through the mold.
vacuum

4. Vacuum Isolation

vacuum
vacuum isolated in mold
melt is raised to contact feed tube

5. Fill

vacuum
gas pressure pushes mold together
start pressurization

6. Mold Seal

vacuum
solidification plug forms at the entrance to the vacuum tube

7. Pressurization

vacuum
preform is infiltrated
shrinkage fed by pressurized melt
controlled pressurization

8. Solidification

vacuum
directional solidification initiated
high pressure maintained

9. Unload

Figure 8- Conceptional Schematic of Pressure Infiltration Casting (PIC)
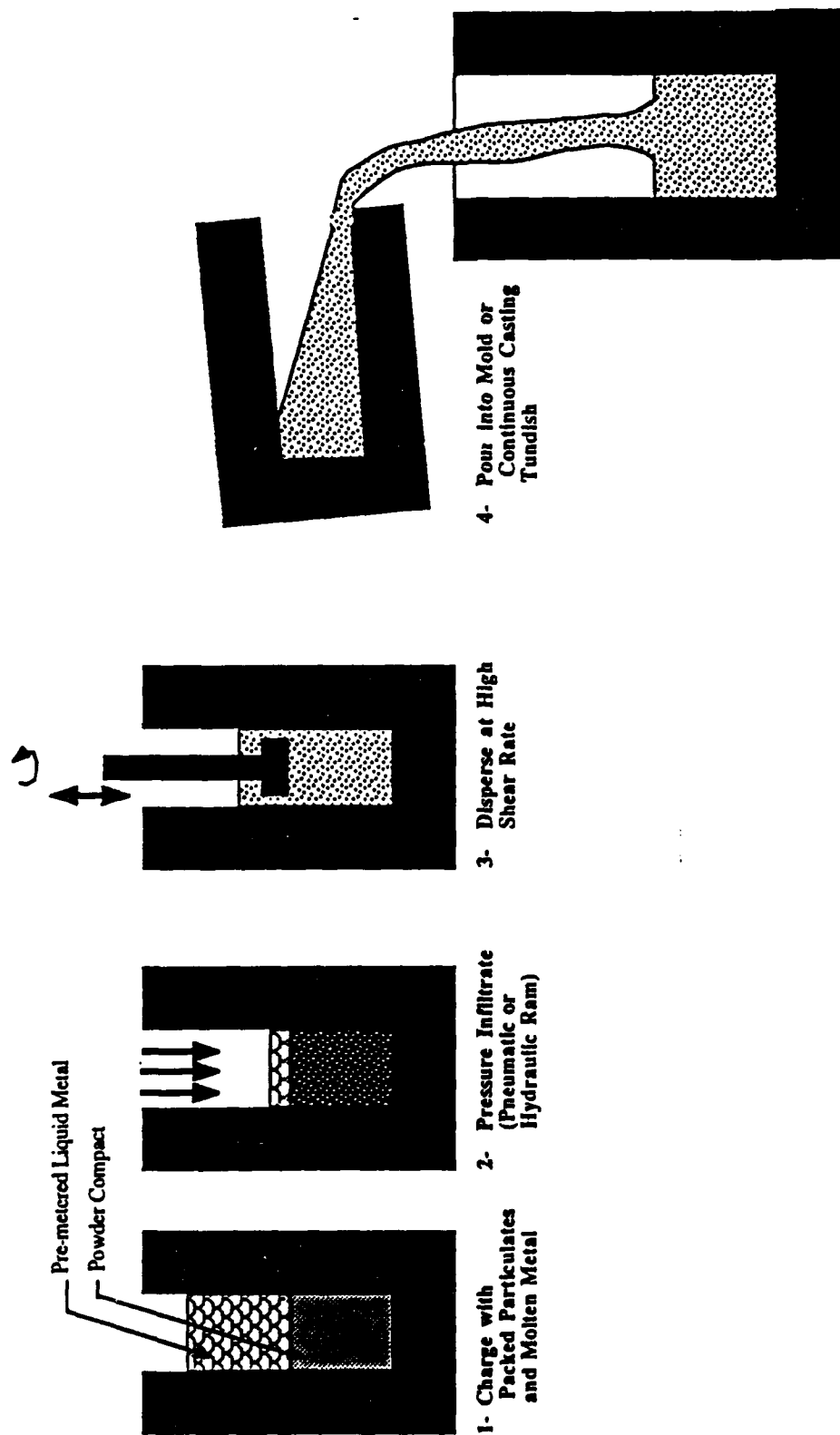
Figure 9 - The production of Porosity-Free PRM Composites by a Pressure Infiltration/Shear-Dispersion Process
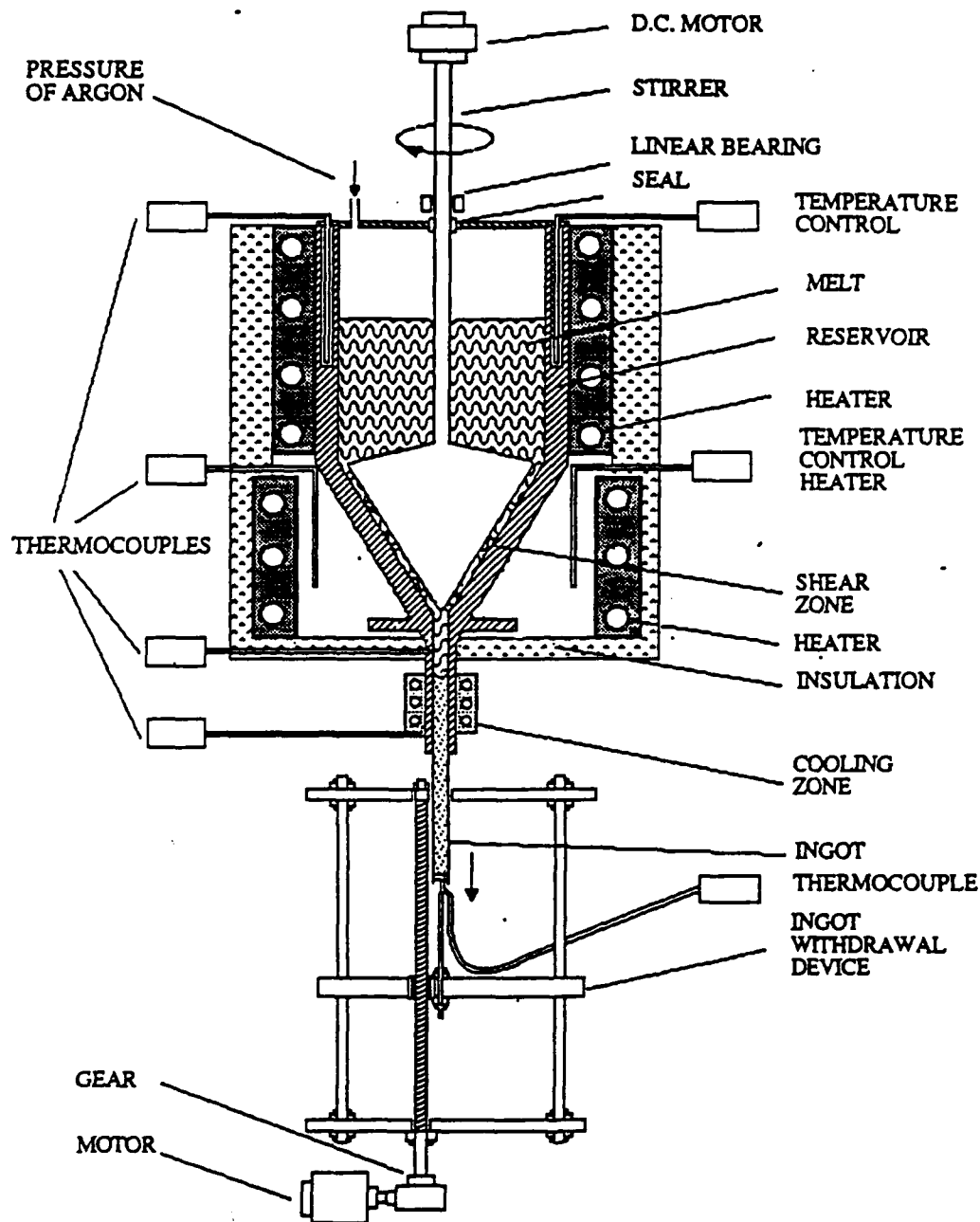
Figure 10 -   Experimental apparatus for continuous casting of particulate composites
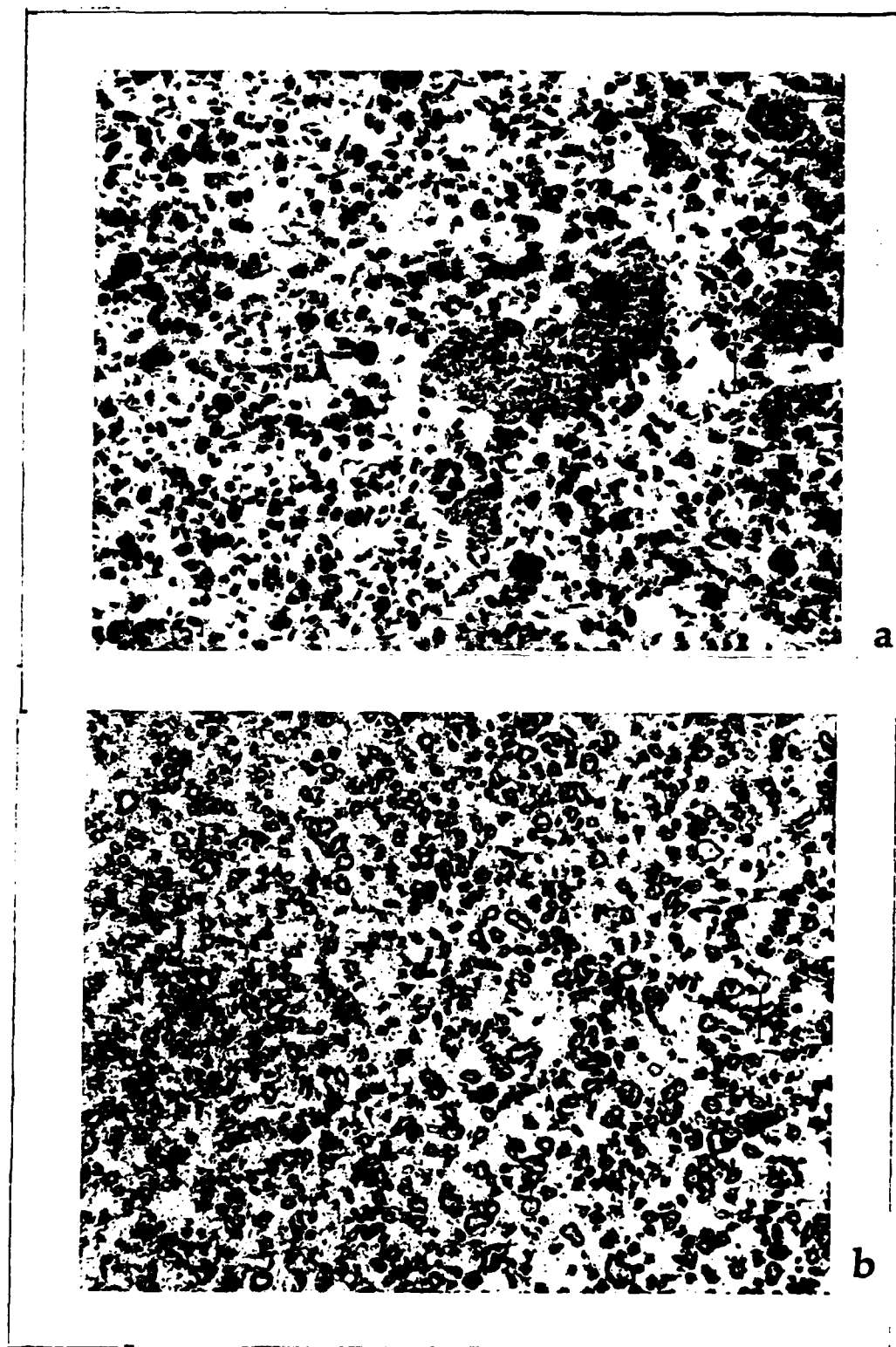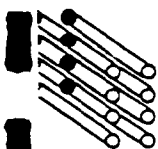
Figure 11- Microsturcture of 10 v/o B$_4$C/Mg AZ91C alloy
(a) as recieved   (b) after shear/casting
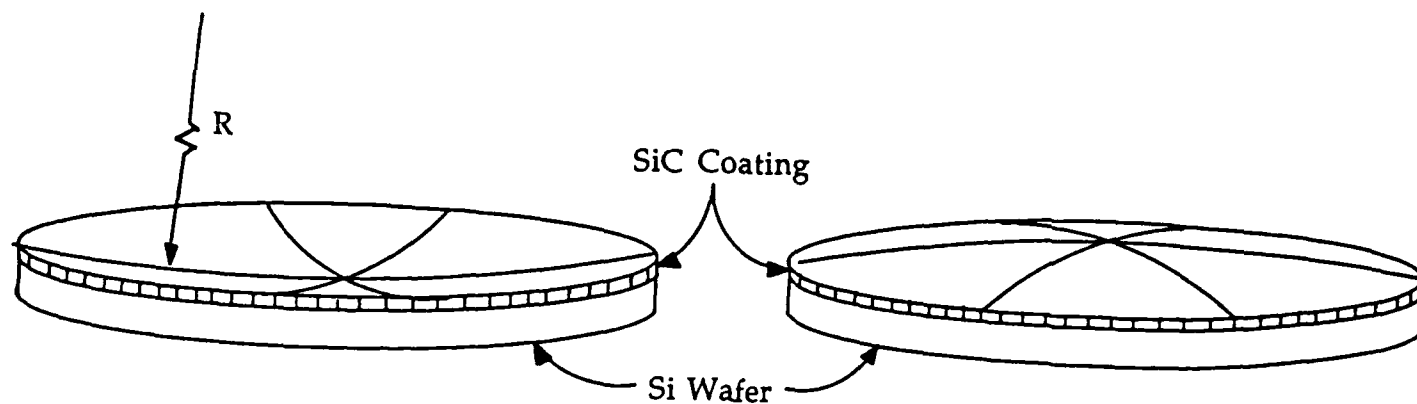
Coating in Tension — Coating in Compression
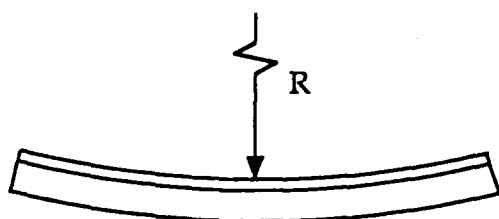
$$\sigma_c = \frac{\varepsilon_c E_m}{(1 - \nu_c)}$$
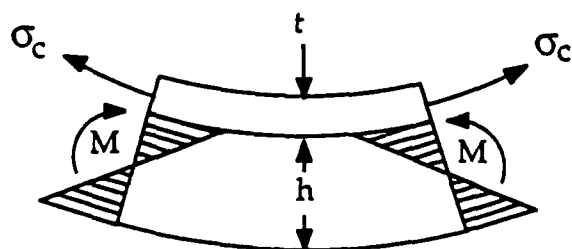
$$\sigma_c = \frac{1}{R} \frac{E_s h^2}{6(1 - \nu_s) t}$$

Figure 12-
(a)   Residual stresses in SiC coating on silicon substrates.
(b)   For coatings in biaxial tension, strain is determined from free-standing
         delamination strips of coating. R is measured with a profilometer.

SiC Coating

Silicon Substrate

Delamination
Crack

$\ln v$

$\ln t_{TN}$ $\ln t_s$

Delamination Driving
Force
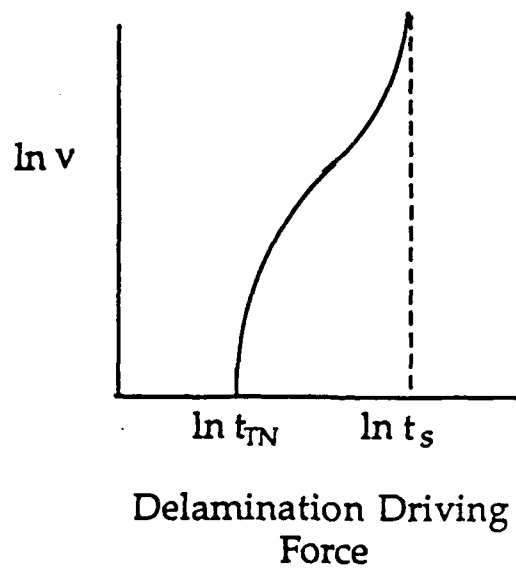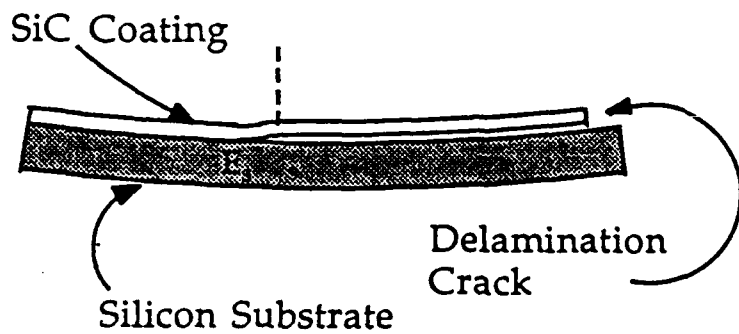
$$U = \frac{\varepsilon_m^2\, E\, t_s}{(1-\nu)} \left[1 + 3\left(\frac{E}{E_t}\right)\left(\frac{1-\nu}{1-\nu_s}\right)\left(\frac{t_s}{h}\right) \right] =$$

negligible

$$U = G_c = \frac{\varepsilon_m^2\, E\, t_s}{(1-\nu)}$$

$$\frac{K_I^2\,(1-\nu^2)}{E} = G_c = \frac{\varepsilon_m^2\, E}{(1-\nu)}\, t_s$$

Figure 12- c- Intrinsic Interface toughness between SiC coating and silicon substrate.
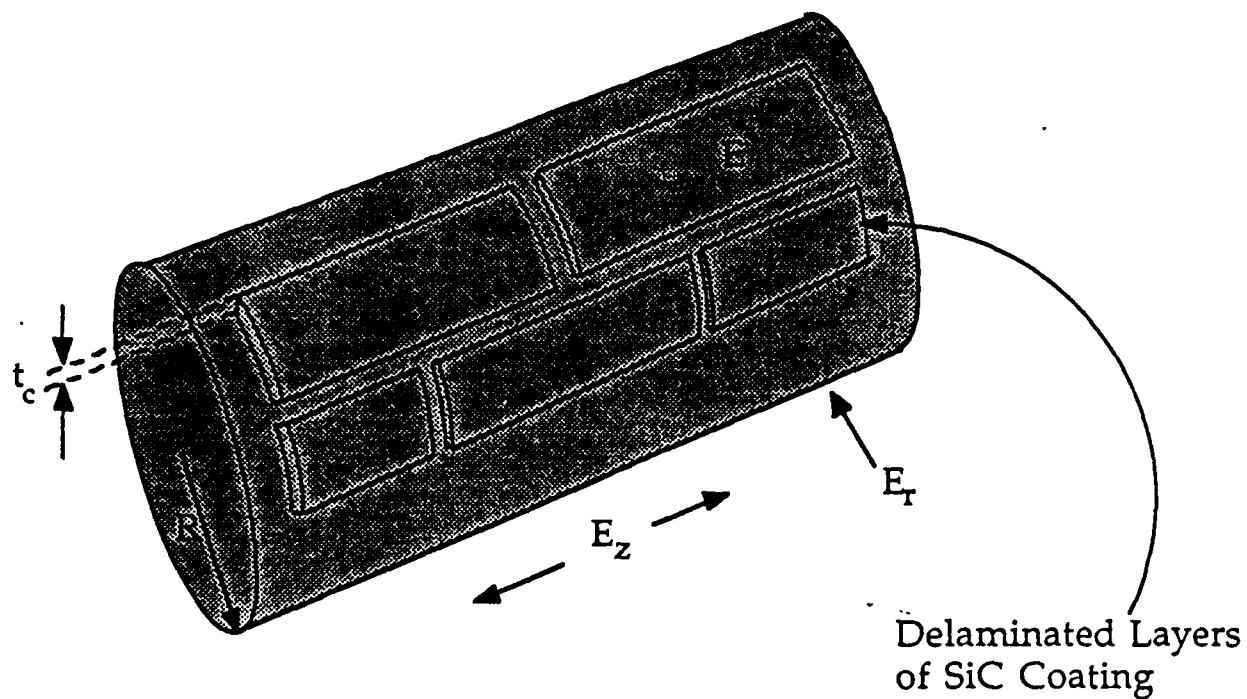
$$G_c = \frac{\varepsilon_m^2 \, E \, t_c}{2 \, H^2} \, F$$

$$F = 2(1-\nu) + \left[(3-5\nu)\frac{E}{E_r} + 6(1-\nu)\frac{E}{E_z}\right]\frac{t}{R}$$

$$H = (1-\nu) + \left[(1-2\nu)\frac{E}{E_r} + 2(1-\nu)\frac{E}{E_z}\right]\frac{t}{R}$$

Figure 12- d- Interface toughness between P-55 carbon fibers and SiC coating.

LABORATORY for the PROCESSING AND EVALUATION OF INORGANIC MATRIX COMPOSITES

PARTICIPANTS

Faculty and Professional Research Staff

Prof. A.S. Argon	Dept. of Mechanical Engineering
Dr. J.T. Blucher	Materials Processing Center
Prof. Y-M. Chiang	Dept. of Materials Science and Engineering
Prof. J.P. Clark	Dept. of Materials Science and Engineering
Dr. J.A. Cornie	Materials Processing Center
Prof. M.C. Flemings	Dept. of Materials Science and Engineering
Dr. J.S. Haggerty	Materials Processing Center
Prof. R.M. Latanision	Dept. of Materials Science and Engineering and Director of Materials Processing Center
A.M. Lightfoot	Dept. of Materials Science and Engineering
Dr. J. Megusar	Materials Processing Center
Prof. A. Mortensen	Dept. of Materials Science and Engineering
Prof. D.M. Parks	Dept. of Mechanical Engineering
Prof. R.M. Pelloux	Dept. of Materials Science and Engineering
Dr. Z. Raczynski	Materials Processing Center
Prof. K.C. Russell	Dept. of Materials Science and Engineering
Prof. D. Seyferth	Dept. of Chemistry
Prof. J. Szekely	Dept. of Materials Science and Engineering

Consultants

Prof. T. Kattamis	University of Connecticut
Mr. J. Schoutens	MMCIAC, Santa Barbara

Post Doctorates

O. Ilegbusi	Dept. of Materials Science and Engineering
W. Rees	Dept. of Chemistry

Visiting Professors and Scientists

Feng, Shaoren	Nei Mongolia Research Institute
A. Grenni	Montedison
Prof. G. D. Zhang	Shanghai Jiao Tong University
T. Yamamoto	Ube
P. Metenier	Renault Research Lab
Prof. H. Goldenstein	University De Sao Paulo, Brazil

LABORATORY for the PROCESSING AND EVALUATION OF INORGANIC MATRIX COMPOSITES

PARTICIPANTS (Continued)

Research Assistants (Graduate Students)

R. Andrews**		Dept. of Materials Science and Engineering
B. Chambers**	(SM-5/87)	Dept. of Materials Science and Engineering
J. Collins		Dept. of Materials Science and Engineering
C. Correa	(SM-5/87)	Dept. of Civil Engineering
D. Dunand**		Dept. of Materials Science and Engineering
A. Figuereda**		Dept. of Materials Science and Engineering
T. Fitzgerald**		Dept. of Materials Science and Engineering
T. Fletcher**		Dept. of Materials Science and Engineering
N. Frier**		Dept. of Materials Science and Engineering
C. Fujiwara	(SM-6/86)	Dept. of Materials Science and Engineering
D. Grande	(ScD-2/87)	Dept. of Materials Science and Engineering
M. Gungor	(ScD-9/86)	Dept. of Materials Science and Engineering
V.J. Gupta**	(SM-5/87)	Dept. of Civil Engineering
L. Hihara**		Dept. of Materials Science and Engineering
J. Issacs**		Dept. of Materials Science and Engineering
E. Klier	(SM-5/88)	Dept. of Materials Science and Engineering
H. Kaufman**		Dept. of Materials Science and Engineering
H. Landis	(ScD-2/88)	Dept. of Materials Science and Engineering
Q. Li	(SM-9/88)	Dept. of Materials Science and Engineering
L. Masur	(PhD-2/88)	Dept. of Materials Science and Engineering
R. Messner**		Dept. of Materials Science and Engineering
V. Michaud**		Dept. of Materials Science and Engineering
H-K. Moon**		Dept. of Materials Science and Engineering
L.H. Ng**		Dept. of Materials Science and Engineering
S-Y. Oh	(ScD-9/87)	Dept. of Materials Science and Engineering
P. Roudier*		Dept. of Materials Science and Engineering
N. Saluja**		Dept. of Materials Science and Engineering
B.W. Sheldon**		Dept. of Materials Science and Engineering
I.P. Smyth**		Dept. of Materials Science and Engineering
J. Sommer**		Dept. of Materials Science and Engineering
S. Yang**		Dept. of Materials Science and Engineering
E. Zwicz	(SM-5/86,Sc.D-5/88)	Dept. of Mechanical Engineering

* Working toward S.M. dissertation
** Working toward doctorate dissertation

LABORATORY for the PROCESSING AND EVALUATION OF INORGANIC MATRIX COMPOSITES

Degrees Awarded

B. Chambers	S.M. - May, 1987, M.I.T. Dept. of Materials Science and Engineering
C. Correa	S.M. - May, 1987, M.I.T. Dept. of Civil Engineering
C. Fujiwara	S.M. -June, 1986, M.I.T. Dept. of Materials Science and Engineering
D. Grande	Ph.D. - February, 1987, M.I.T. Dept. of Materials Science and Engineering
M. Gungor	Sc.D. -September, 1986, M.I.T. Dept. of Materials Science and Engineering
V.J. Gupta	S.M. - May, 1987, M.I.T. Dept. of Civil Engineering
E. Klier	S.M. -May, 1988, M.I.T. Dept. of Materials Science and Engineering
H. Landis	Ph.D. - February, 1988, M.I.T. Dept. of Materials Science and Engineering
Q. Li	S.M. -September, 1988, M.I.T. Dept. of Materials Science and Engineering
L. Masur	Ph.D. -February, 1988, M.I.T. Dept. of Materials Science and Engineering
Oh, S-Y.	Ph.D. - September, 1987, M.I.T. Dept. of Materials Science and Engineering
E. Zwycz	S.M. -May, 1986, M.I.T. Sc.D. -May, 1988, M.I.T. Dept. of Mechanical Engineering
L. Hihara	Sc.D. -May, 1989, M.I.T. Dept. of Materials Science and Engineering

8816-006

KINETICS OF FIBER PREFORM INFILTRATION

Andreas Mortensen, Veronique J. Michaud, James A. Cornie, Merton C. Flemings
Massachusetts Institute of Technology
Cambridge, Massachusetts, USA

Larry Masur
American Superconductor Corp.
Cambridge, Massachusetts, USA

ABSTRACT

The various fluid flow and heat transfer mechanisms governing the infiltration of fibrous preforms by a liquid metal are presented in a description of the process and its governing laws based on recent experimental and theoretical work at M.I.T. The influence of adjustable parameters of the process such as preform or metal temperature, applied pressure as well as external cooling from the mold is discussed. Conclusions are drawn from this work for optimization of the infiltration process for metal matrix composites, with particular focus on infiltration of fibers initially at a temperature below that at which solid metal forms.

THE LIQUID METAL INFILTRATION process for fabricating fiber reinforced metals consists of the injection and subsequent solidification of liquid metal into the interstitial spaces within a collection of ceramic fibers. This process is at present well established, and an increasing number of fibrous composite materials are being produced on both a commercial scale and in laboratories via one or another form of infiltration: squeeze casting, pressure casting, die casting, gravity casting, etc [1]. Fundamental principles governing the kinetics of infiltration and the microstructural evolution of the composite are therefore of considerable practical interest. Recent progress on the physics of the process is presented in what follows [1 - 4]. The present paper will address the topic in somewhat condensed form, to propose a more synthetic view of the process and in particular to outline practical consequences of recent work on the subject.

DESCRIPTION OF THE PROCESS AND GOVERNING EQUATIONS.

Consider the infiltration of a composite such as the simplified selectively reinforced part described in Figure 1. Molten metal is poured at temperature T_m into a cavity of initial temperature T_c which contains a preform of the fibers, preheated to a temperature T_f. The metal infiltrates the preform

under a positive pressure differential ΔP_μ between that in the metal at the entrance of the preform P_0 and the pressure at the infiltration front. This latter pressure is equal to the pressure in the gaseous atmosphere in the non-infiltrated portion of the preform, P_a, diminished by the pressure drop at the infiltration front ΔP_γ:

$$\Delta P_\mu + \Delta P_\gamma = P_0 - P_a.$$

Several equations have been proposed for calculating the capillary pressure drop at the infiltration front ΔP_γ. The authors have recently proposed an expression for this pressure drop [5], on the basis of a simple analysis of the energy required for reversible infiltration of a porous body:

$$\Delta P_\gamma = (\sigma_{FL} - \sigma_{FA})S_f \qquad (1)$$

$$= -\sigma_{LA} \cos(\theta) S_f \qquad \text{(provided } \theta \text{ exists)}$$

where σ_{FL} is the fiber/liquid metal interfacial energy, σ_{FA} is the fiber surface energy, σ_{LA} is the surface tension of the metal, θ is the contact angle of the metal on the reinforcement and S_f is the specific surface area (i.e. the fiber surface area per unit volume of metal matrix) of the region of the preform that is being infiltrated at time t. In the limiting case of $\theta = 0$, this expression is identical to that derived by Carman in 1941 for capillary rise in sands using a force balance at the infiltration front [6]. For the case of a fibrous preform consisting of fibers of uniform radius r_f, S_f is given by:

$$S_f = \frac{2 V_f}{r_f (1 - V_f)} \qquad (2)$$

Fluid flow within the preform will be governed by Darcy's law, provided the relevant Reynold's number

$$R_e = \frac{2 r_f \rho_m V_0}{\mu V_f} \qquad (3)$$

is less than about one [7]. This will generally be the case in the

7
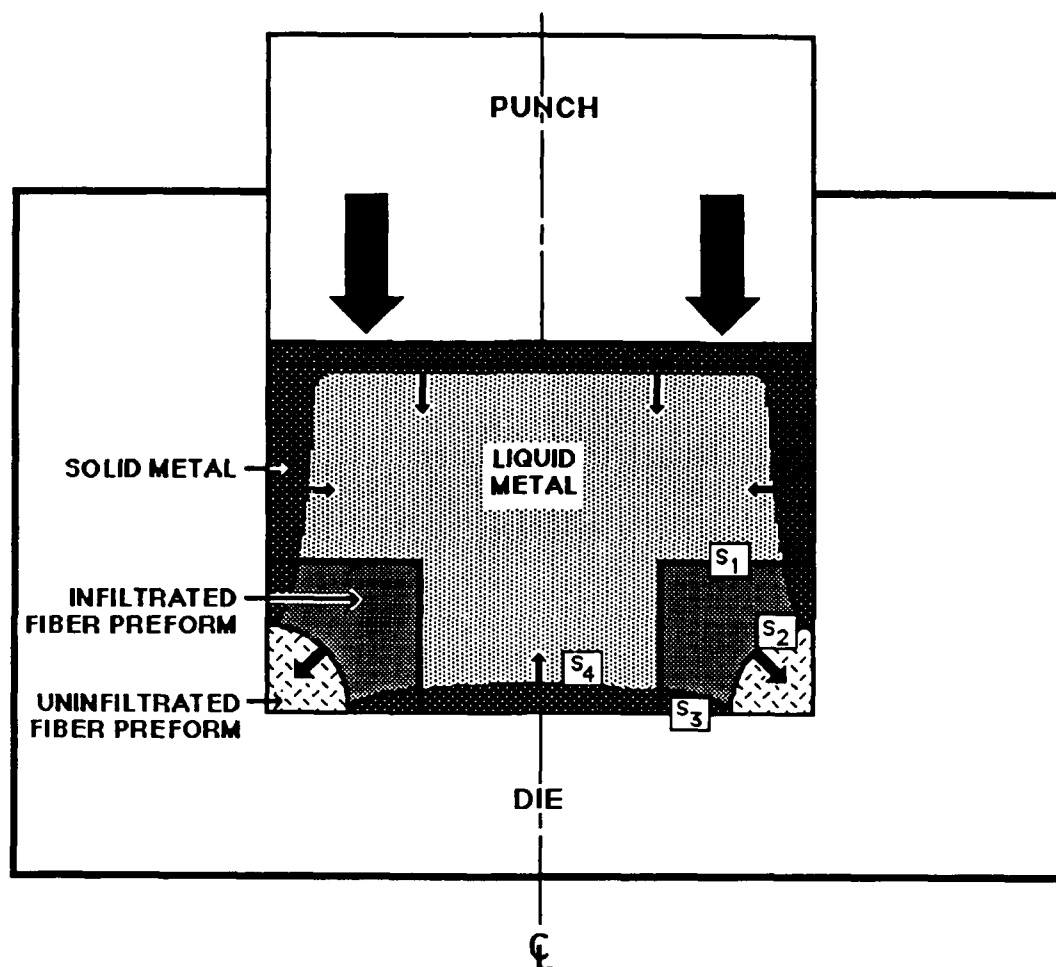
Figure 1 - Generalized three-dimensional problem of infiltration of a fibrous preform. In this case, the part is a simplified version of a selectively reinforced piston manufactured by squeeze casting. S1 denotes the preform entrance, S2 the infiltration front, S3 the mold-casting interface and S4 the solidification front. Both S3 and S4 are moving boundaries.

infiltration of metal marix composites due to the fine scale of the reinforcement. Flow of the fluid can then be analysed on the scale of an elementary volume element dV that is small on the scale of the casting, but comprises at least several fibers so that fluid velocity and pressure can be averaged over this volume element. Fluid flow is then measured by the "superficial" velocity or "seepage" velocity v_o, a vector of direction given by the average flow direction of the liquid and of magnitude equal to the volume of liquid flowing per unit time through a unit surface cut into the porous medium perpendicular to the average flow direction. Darcy's law then correlates the pressure gradient in the liquid and the superficial velocity:

$$v_o = -\frac{K}{\mu}[\text{grad}(P) - \rho_m g] \qquad (4)$$

where

v_o = superficial velocity of liquid metal

μ = viscosity of liquid metal

K = (symmetric) permeability tensor of the preform.

P = pressure in the metal

ρ_m = density of the metal

g = gravity field vector.

If we assume that both the liquid matrix and the preform are incompressible, the continuity equation is:

$$\text{div}(v_o) = 0 \qquad (5)$$

The pressure drop ΔP_μ is then the integral of the pressure gradient from the preform entrance to the infiltration front, and increases with increasing flow velocity of the metal, increasing viscosity of the metal and decreasing permeability of the preform. The energy required for the infiltration process is then the sum of two terms, corresponding respectively to the volume of metal displaced multiplied by the sum of the two terms $(\Delta P_\mu + \Delta P_\gamma)$ of the total driving pressure gradient. The

8

former term measures an irreversible energy expenditure due to viscous losses in the flowing metal while the second term measures the minimum energetic requirement of the process (positive or negative according to wettability of the preform), due to capillarity.

Heat and solute transport can also be analyzed on the scale of the same volume element dV if heat transfer is rapid enough within that element to equalize temperature and if diffusion is rapid enough to homogenize the liquid composition within dV. One can then characterize the element with a single temperature T and a single liquid solute composition, given by the concentration C_{iL} in solute i of the liquid. The heat transfer equation is then:

$$\rho_c C_c \frac{\partial T}{\partial t} + \rho_m C_m V_o \cdot grad(T) = div(\, k_c\, gradT\,)$$
$$+ (1-V_f)\, \rho_m L \frac{\partial g_s}{\partial t} \qquad (6)$$

where:

$\rho_c C_c$ = volumetric heat capacity of composite, $= \rho_f C_f V_f + \rho_m C_m (1-V_f)$,

$\rho_f C_f$ = volumetric heat capacity of fibers,

$\rho_m C_m$ = volumetric heat capacity of metal,

V_f = volume fraction fibers in the composite,

k_c = thermal conductivity tensor in the composite,

T = temperature,

g_s = fraction solid,

L = latent heat of solidification of the metal.

Solute conservation dictates:

$$\frac{\partial((1-V_f)\overline{C_i})}{\partial t} = - div(\, C_{iL}\, V_o) \qquad (7)$$

where

C_{iL} = concentration of solute i in liquid metal phase

$\overline{C_i}$ = average concentration of solute i in total metal phase for each solute element, if density differences between liquid and solid metal phases are neglected. Depending on the solidification mechanism, an additional relationship correlates the average concentration with the liquid metal composition and fraction solid metal g_s:

$$\overline{C_i} = f(C_{jL}, g_s) \qquad (8)$$

while the composition of the liquid and the temperature in dV are linked by the phase diagram if equilibrium is assumed at the solid/liquid metal interface:

$$C_{iL} = g(T) \qquad (9).$$

In the case of a binary alloy, there will be eight unknowns: V_{ox}, V_{oy}, V_{oz}, P, T, C_L, g_s, and C at each point of the preform and one parameter, time. Equations (4) to (9) yield eight relations between these unknowns. The problem is therefore defined by specification of the boundary conditions, and of a relation giving the value of the permeability(ies) at each point of the infiltrated preform as a function of the nature

of the fibers including their volume fraction, and the volume fraction solid metal present g_s. Calculation of K can be based on the Blake-Kozeny approximation or on appropriate relationships derived for the particular preform in question [1,3,8]. Of particular interest is the role played by the fraction solid metal g_s present in the composite during infiltration, because the permeability will depend largely upon the solidification morphology of that solid metal phase.

There is at least one moving boundary in this problem, the infiltration front S_2 in Figure 1. There will in general be a second moving boundary, delineating the region of fully solid metal, S_4 in Figure 1, which is formed by concomitant solidification of the whole casting due to external cooling at the mold wall. The anisotropic and inhomogeneous nature of many fiber preforms may further complicate the problem. The permeability of preforms consisting of parallel fibers is greater by a factor of about two along the fiber axis compared to along an axis transverse to the fibers [8]. Flow of the metal will therefore be much more rapid parallel to the fibers. Furthermore, the distribution of the fibers is never regular, and there will be regions of high volume fraction fiber, and therefore opposing higher resistance to penetration by the liquid metal, due to increased capillary forces in these regions (equations (1) and (2)) and due to a much lower permeability in these regions. The infiltration front will then be very irregular, as metal will first penetrate the preform along wider channels, and later complete infiltration of the preform into regions of higher local V_f either by transverse flow from the larger channels or longitudinally as in Fukunaga and Goda's experiments [9].

The presence in this problem of moving boundaries, the anisotropy of the permeability tensor and the presence of inhomogeneous packing in most fiber preforms complicate immensely its solution for the most general case. The approach in research has therefore been to utilize model systems which facilitate analysis and data acquisition. This approach allows to (i) determine fundamental physical phenomena underlying the problem, in particular validation or definition of equations presented above, and (ii) suggest possible approximations facilitating treatment in cases of practical interest. Recent results along these lines from research at MIT is presented in the following section. A complete presentation of experimental procedures and results and of their theoretical analysis will be given elsewhere [1-4].

UNIDIRECTIONAL PLANE FRONT INFILTRATION.

a - EXPERIMENTAL PROCEDURE. The matrix metal, aluminum or an aluminum-base alloy, is unidirectionally infiltrated into preforms of Saffil™ alumina fibers with a pressure caster, using pressurized gas to force molten metal into an evacuated die. Figure 2 is a sketch of the device. It consists of two main components: the pressure vessel, containing the melt furnace and crucible, and the cap, attached to which are the control valves and the die. There are also feedthroughs for thermocouples, power leads, and a pressure transducer. The die is attached to the center of the cap and can be evacuated.

To operate the device the cap is placed on the pressure vessel, immersing the bottom of the die in the molten metal. The vessel is then pressurized with nitrogen, forcing the metal up through the die and into the fibers. Gas feed-through lines feature a large diameter, allowing full pressurization in less than 1.2 seconds. The metal and the fibers do not come in
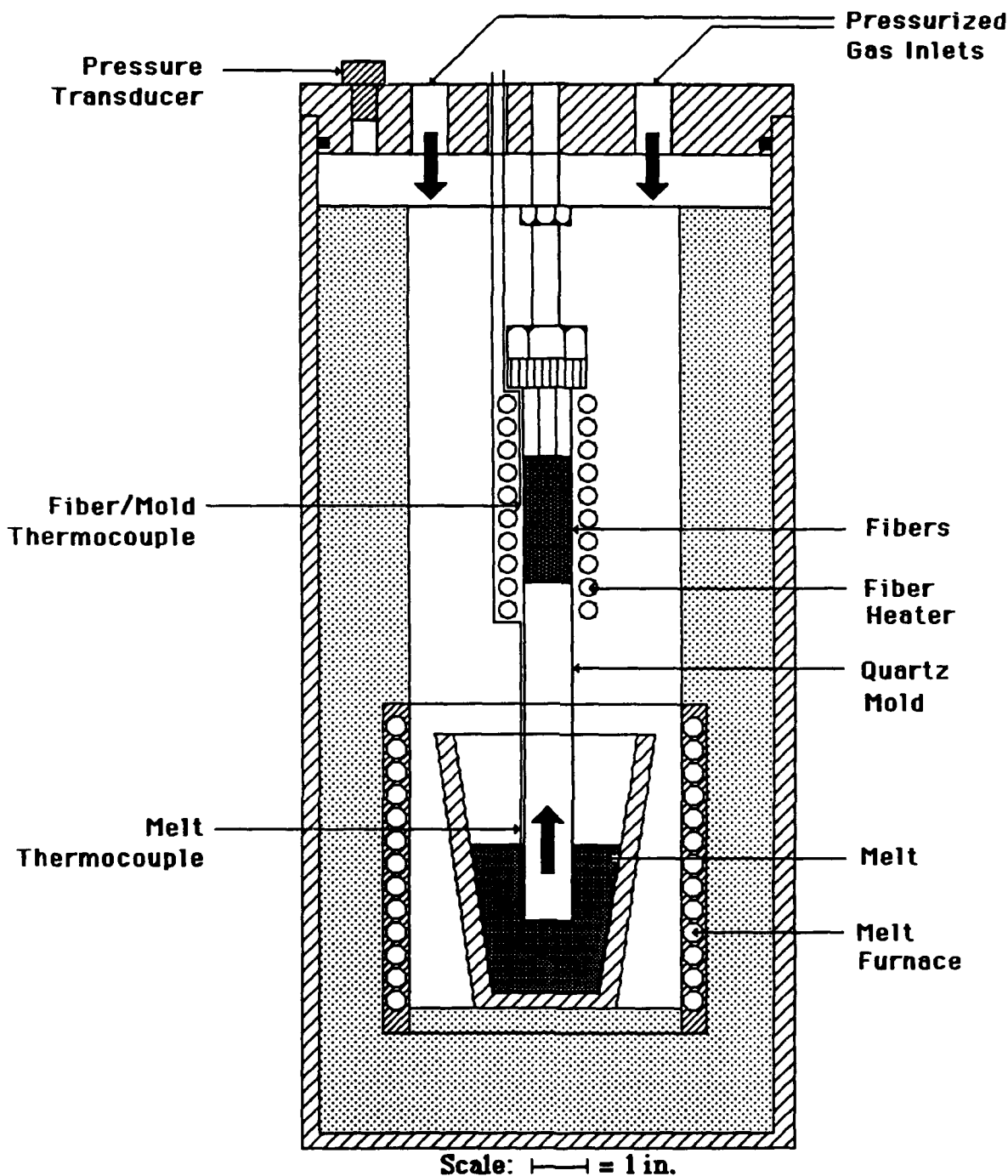
Figure 2 - Schematic drawing of pressure casting apparatus for unidirectional infiltration of fiber preforms by molten aluminum.

contact until infiltration begins, which enables accurate and independent control of the fiber and metal temperatures. In addition, because of the design of the device, the die need only sustain the compressive stresses imposed by the pressurized gas: heavy-walled metal dies common to other pressure casters are replaced with a quartz tube.

A technique was developed to measure the position of the molten metal front as it moves through the fiber preform during infiltration. This is achieved by inserting a SiC filament between the preform and the quartz tube mold. A potential is applied between the filament and the metal crucible, with the molten metal acting as a switch to close the circuit. A chart recorder then measures the potential drop across the SiC filament over time. As the metal infiltrates the preform, the potential measured across the filament decreases due to the decrease in effective electrical length of the SiC filament.
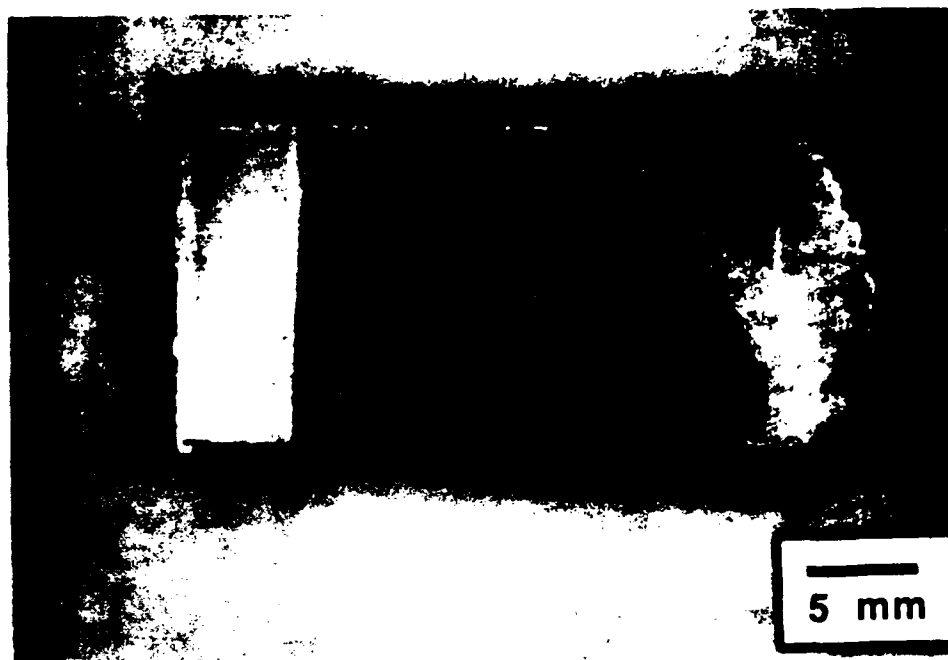
Figure 3 - Sample of unidirectionally infiltrated Saffil™ alumina reinforced aluminum produced in apparatus schematically described in Fig. 2. Infiltration was from left to right. Note the relatively plane infiltration front.

Monitoring the potential drop during infiltration then allows a calculation of the position of the metal front and its velocity over time.

The experimental procedure yields a dynamic measure of infiltration kinetics during infiltration under constant applied pressure, and produces a sample of composite (Figure 3), which can be investigated using conventional metallography and chemical analysis. The relatively planar and well defined infiltration front observed with these preforms and the unidirectionality of the infiltration path simplify considerably analysis of the infiltration process, and the equations given above can be tested against experimental data.

b - CASE OF A PURE METAL. In the case of a pure metal, liquid and solid metal can only coexist at the melting point of the metal T_M if equilibrium is assumed at the solid/liquid interface. Therefore, the problem is much simplified, since there can be no heat transport where solid metal is present, and therefore g_s cannot vary continuously in the composite. Furthermore, with a pure metal, the composition is no longer an issue, and equations 7 to 9 are irrelevant.

If the initial fiber temperature is above the metal melting point, no solid metal will form, save for solidification due to cooling at the mold walls. The problem is then one of uncoupled fluid flow in that the infiltration kinetics can be derived first independently, to yield, for unidirectional infiltration, the position of the metal front as a function of time:

$$L^2 = \int_0^t \frac{2\,K\,\Delta P_\mu(t)}{\mu\,(1-V_f)}\,dt \qquad (10)$$

$$= \frac{2\,K\,\Delta P_\mu}{\mu\,(1-V_f)}\,t \quad \text{if the applied pressure is constant}$$

If the initial fiber temperature is below the melting point of the metal, some solid metal will form at the infiltration front to heat the fibers up to the metal melting point by release of latent heat. In the case of a pure metal, this solid metal must solidify as a sheath surrounding the fibers since solidification is limited by heat transfer to the cold fibers. This assumption is substantiated by measured infiltration kinetics, predicted as above, but with a changed value of permeability in the region close to the infiltration front, which can be predicted by increasing the effective fiber diameter and volume fraction to account for a volume fraction solid g_s in the metal phase. g_s is given by a thermal equilibration at the infiltration front:

$$g_s = \frac{\rho_f c_f V_f (T_M - T_f)}{\rho_f L (1-V_f)} \qquad (11)$$

Formation of this solid metal phase will substantially influence the kinetics of infiltration when the fibers are initially below the melting point of the metal. Low T_f will be deleterious from the point of view of infiltration kinetics, but

11

may result in vastly improved composite properties due to reduced chemical reactions between the fibers and the metal [10]. Experiments with high purity aluminum have demonstrated the validity of these assumptions, and the physics of infiltration by a pure metal are presently fairly well understood [2,3,9].

c - CASE OF AN ALLOY. In the case of an alloy, the problem is more complex with cold fibers than in the case of a pure metal because: (i) solid and liquid metal can coexist over a range of temperatures, making heat transfer posible within the region of partly solid metal, (ii) the morphology of the solidifying metal is no longer that of a sheath surrounding the fibers because solidification is now controlled by solute diffusion and (iii) mass transfer must also be accounted for.

Even with a slightly impure matrix, the infiltration kinetics can be noticeably reduced when the fibers are initially at a temperature below the melting point of the metal [2,11]. This effect is interpreted as arising due to a different morphology of solid formed in contact with cold fibers.

Experiments have been reported elsewhere wherein it was shown that macrosegregation results in the composite after infiltration with Al-4.5wt%Cu of a preform initially at a temperature below the liquidus of the metal [12]. A theoretical analysis of the problem, to be presented in a forthcoming publication [4], allows to predict the concentration profile in the composite. The problem is solved for unidirectional infiltration with constant applied pressure P_o, based on the equations given above, and the resulting concentration profile is given in Figure 4. It is seen that variations in concentration and in fraction solid are predicted in the composite during infiltration, which agree qualitatively with data reported in reference [12].

d - EFFECT OF EXTERNAL COOLING. As mentioned above, the effect of concomitant solidification is to complicate significantly the problem. For example, macrosegregation observed in a composite with an alloyed matrix will be a result of the dual contributions of solidification due to the fibers, treated analytically as reported above, and of solidification from the mold walls interacting with fluid flow in the preform during infiltration, Figure 5. Both will redistribute solute in the composite, and the macrosegregation profiles reported earlier are a result of both processes.

It was shown following the experimental procedure described above that solidification due to external cooling also influences fluid flow in the case of a pure metal [2]. With a constant applied pressure, the total infiltrated length of composite is solely determined by external cooling. Also, feeding of solidification shrinkage will depend on external cooling from the mold walls. The importance of mold temperature and external cooling must not, therefore, be underestimated in interpreting occurences of incomplete infiltration of a preform (other causes may exist, however, such as incomplete venting of gases initially in the preform).

CONCLUSIONS

From a practical point of view, the following can be concluded from results presented above and from previous work on the infiltration of metal matrix composites:
1 - The infiltration of a fibrous preform is a moving boundary problem, the solution of which is therefore generally not trivial. The basic equations governing the process and given above have been substantiated by experimental work on unidirectional infiltration of Saffil™ alumina preforms by aluminum and aluminum alloys. These equations must,
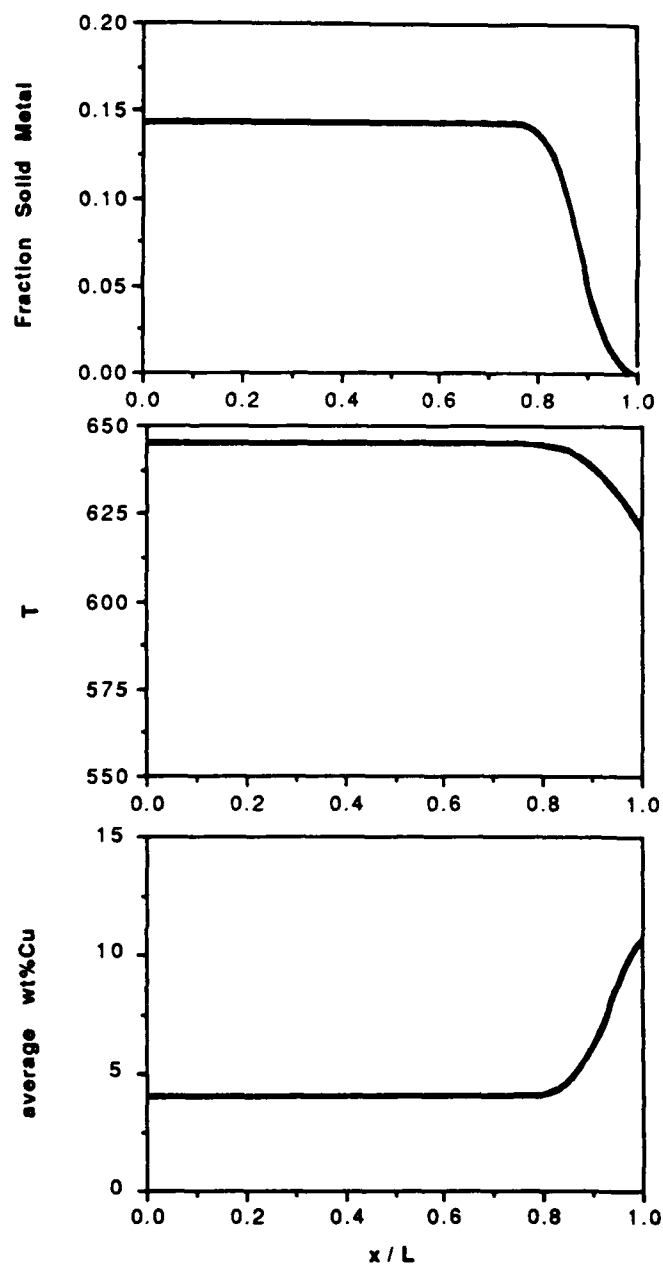
Figure 4 - Calculated fraction solid metal, temperature and average metal composition for Al-4.5 wt%Cu infiltrating a preform of 24 Vol.% Saffil™ fibers initially at 550°C with no metal superheat. No external cooling, $L/\sqrt{t}$ = 0.018 m/√s, where L is the total infiltrated length, x is distance along the infiltrated composite with x≈0 at the preform entrance and t is time.
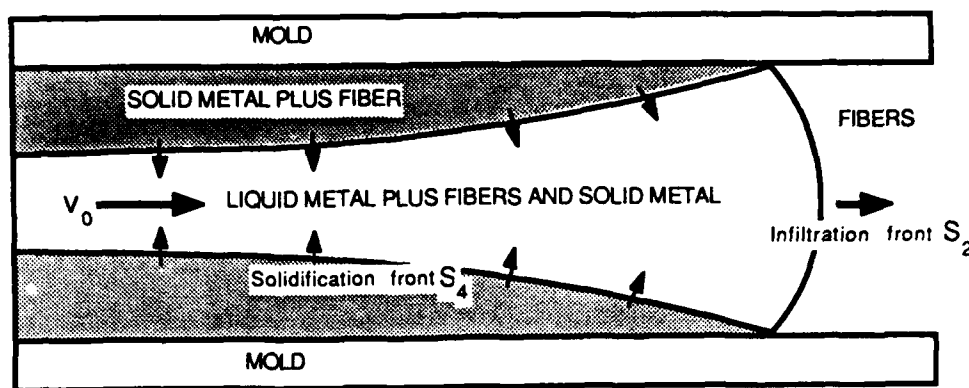
Figure 5: Schematic drawing of solidification due to external heat losses during unidirectional infiltration.

however, be modified to take into account additional effects such as preform compressibility, heat released by chemical reactions between fibers and metal, etc.

2 - Infiltration of fibers initially at a temperature below the liquidus or the melting point of the metal is possible and results in the formation of solid metal between the fibers at the infiltration front. Infiltration kinetics are then determined to a large extent by the amount and morphology of this solid metal.

3 - The grain size of the matrix and the extent of fiber/matrix interfacial reaction can therefore be largely influenced by controlling the initial preform temperature. A low initial fiber preform temperature will result in a fine-grained matrix and reduced interfacial reactions between fibers and metal. Additionally, in the case of an alloy matrix, macrosegregation will then be observed within the composite.

4 - External cooling from the mold wall results in solidification of the matrix during infiltration. In the case of unidirectional infiltration under constant applied pressure, flow of the metal ceases due to choking by fully solid metal formed by solidification from the mold walls at the preform entrance.

ACKNOWLEDGEMENTS.

REFERENCES

1.   A.Mortensen, L.J. Masur, J.A. Cornie and M.C. Flemings, "Infiltration of Fiber Preforms by a Pure Metal Part I: Theory", unpublished work, MIT, 1988.

2.   L.J. Masur, A. Mortensen, J.A. Cornie and M.C. Flemings, "Infiltration of Fiber Preforms by a Pure Metal Part II: Experiment", unpublished work, MIT, 1988.

3.   L.J. Masur, "Infiltration of Fibrous Preforms by a Pure Metal", Ph.D. Thesis, Department of Materials Science and Engineering, MIT, February 1988.

4.   A. Mortensen, V. Michaud, J.A. Cornie and M.C. Flemings, "Infiltration of Fiber Preforms by Al-4.5wt%Cu Part I: Theory", unpublished work, MIT, 1988.

5.   A.Mortensen and J.A.Cornie, Metallurgical Trans. 18A (1987), pp.1160-1163.

6.   P.C.Carman, Soil Science 52 (1941) pp.1-14.

7.   S. Ergun: Chem. Eng. Prog. 48 (1952) pp.89-94.

8.   G.W.Jackson and D.F.James: Can. J.of Chem. Eng. 64 (1986) pp.364-374.

9.   H. Fukunaga and K. Goda: Bull. of Japan. Soc. of Mech. Eng. 27 (1984) pp.1245-1250.

10.   H. Fukunaga and K. Goda: J. of Japan Inst. of Metals 49 (1985) pp.78-83.

11.   L.J. Masur, A. Mortensen, J.A. Cornie and M.C. Flemings, Proceedings of the Sixth International Conference on Composite Materials ICCM 6, F.L.Matthews, N.C.R.Buskell, J.M.Hodgkinson and J.Morton Eds., London, Elsevier, 1987, pp.2.320-2.329.

12.   Experimental work by L.J.Masur, cited by J.A.Cornie, A.Mortensen and M.C.Flemings, Proceedings of the Sixth International Conference on Composite Materials ICCM 6, F.L.Matthews, N.C.R.Buskell, J.M.Hodgkinson and J.Morton Eds., London, Elsevier, 1987, pp.2.297-2.319.

Infiltration of Fibrous Preforms by a Pure Metal: Part I. Theory

A. MORTENSEN, L.J. MASUR, J.A. CORNIE, and M.C. FLEMINGS

General expressions are derived to describe fluid flow and heat transfer during infiltration of fibrous preforms by a pure metal. Analytical solutions to the problem are given for the case of unidirectional infiltration into a uniform preform of aligned fibers under constant applied pressure. Calculations are carried out for infiltration kinetics (including total infiltrated length) and temperature distribution, using as an example alumina fiber/aluminum composites. Limiting cases leads to very simple expressions. Initial fiber temperatures both above and below the metal melting point are considered. In the case of fibers at a temperature significantly below the metal melting point, it is concluded that the factor most strongly influencing infiltration is the solidification of metal in the interfiber region. In the calculations, it is assumed that this solidification is in the form of a uniform solid metal sheath around the fibers. Metal superheat, when present, serves to progressively remelt the solidified sheath from the upstream end of the preform. Fiber volume fraction and initial temperature are predicted to have a major effect on infiltration kinetics, while metal superheat exerts a relatively minor influence. When no external heat extraction is present and a constant pressure is applied to the metal, flow through the preform continues indefinitely. For the case of external heat extraction, flow ceases when sufficient solidification occurs to block flow.

I. INTRODUCTION

THE liquid metal infiltration process for fabricating fiber-reinforced metals consists of the injection and subsequent solidification of liquid metal within the interstitial spaces of a fiber preform. Fluid flow aspects of the infiltration process can be treated readily following the extensive literature on flow of fluids through porous media, an important topic in soil science and chemical engineering. The problem of interest here has additional heat flow and solidification aspects, since the fibers are often held at a temperature significantly below the melting point of the matrix to minimize chemical reactions. In an adiabatic infiltration problem, heat will be exchanged between the metal and the fibers. In a nonadiabatic problem, heat flow will additionally take place between the composite and its surroundings, as is usually the case in casting processes. These heat transfer phenomena are of importance, because they influence both infiltration kinetics and the resulting metal microstructure in the composite.

Because of its considerable engineering relevance to metal matrix composite fabrication, the infiltration process has already been studied by several authors, from both theoretical and experimental standpoints. Nagata and Matsuda[1,2] have investigated the infiltration of particles ranging in size from 37 to 3400 μm. They propose the existence of a critical preheat temperature based upon physical constants of the metal and particles, above which the particles must be heated in order for infiltration to occur. Their calculations are based upon an overall thermal balance between the particles and the metal. Hosking and Netz[3] have studied the infiltration of an aluminum alloy into a packed bed of particles ranging in size from 3 to 9 mm. They present a statistically derived expression that is based upon their experimental results.

On the flow of liquid metals through assemblies of fibers, Fukunaga has made experimental measurements and theoretical calculations of the permeability of a fibrous preform, which are summarized in a recent publication.[4] Fukunaga and Goda propose the formation of a layer of solidified metal on the fibers and verify its existence through the use of mechanical tests on leached-out fibers.[5] They then derive a Kozeny-type expression for the infiltration coefficient which agrees with experimental measurements.[6] Fukunaga and Goda also propose a critical infiltration velocity as the mechanism for cessation of flow. Girot et al.[7,8] have performed a numerical analysis of the infiltration of liquid alloys into fibrous preforms. They propose that flow ceases when the metal cools to its liquidus and, therefore, do not account for the release of latent heat of solidification by the metal in their calculations. Clyne et al.[9,10,11] have investigated the critical pressure necessary for melt infiltration and the effect of infiltration pressure on fiber preform deformation. They also explain the evolution of the composite microstructure, including an interpretation of the role of metal superheat.

Recently, Martins et al.[12] have adapted a model by Brittin[13] for infiltration of a straight capillary to the infiltration of a metal matrix composite. This treatment is geometrically simplified but has the advantage of including inertial and end-drag effects that might arise in some instances.

A. MORTENSEN, Assistant Professor, J.A. CORNIE, Principal Research Associate, and M.C. FLEMINGS, Professor and Department Head, are with the Department of Materials Science and Engineering, Massachusetts Institute of Technology, Cambridge, MA 02139. L.J. MASUR, formerly a Graduate Student with the Department of Materials Science and Engineering, Massachusetts Institute of Technology, is Senior Scientist with the American Superconductor Corporation, Cambridge, MA 02139.
Manuscript submitted June 7, 1988.

In the present paper. we present the basic relations for flow of a pure liquid metal into a fibrous preform and provide a solution of the problem for the case of unidirectional infiltration under constant applied pressure. The problem is treated here in a manner that draws upon the analysis of Fukunaga and Goda[4,5,6] but incorporates variations in temperature and fraction solid metal with time and position in the preform, which considerably broadens the scope of the analysis. In Part II of this work, the calculations are compared with experimental measurements of infiltration kinetics and with microstructural observations of the resulting composites. Since experiments were performed on alumina preforms infiltrated by pure aluminum, we use that system here to illustrate the results of our analysis in a real system.

II. THE GENERAL PROBLEM

Consider the infiltration of a fibrous preform by a pure liquid metal. Figure 1 schematically illustrates the process of injection of metal into a preform held within a die with several general physical phenomena that characterize the problem. In the general case, the initial fiber temperature. T_f, the initial mold temperature. T_i, and the initial metal temperature at the die entrance, T_0, are all different from one another. Often, the fibers are initially at a temperature lower than that of the metal. and heat will flow locally from metal to fibers when the two phases come in contact.

When the fiber temperature is below the metal melting point and superheat is not too great, solid metal will form in the interfiber regions as a result of heat flow from the metal to the fibers. A region in the casting thus forms behind the infiltration front where both liquid and solid metal coexist (region 1). Heat exchange can also occur between the mold and the casting. leading to the formation of a region of fully solid metal along the mold wall (region 2). Superheated metal entering the preform will remelt the solid metal in regions 1 and 2, leading to the formation of a zone comprising only liquid metal and fibers (region 3).

Gas initially present in the preform or formed during infiltration is expelled under proper casting conditions ahead of the advancing liquid metal front through the uninfiltrated portion of the preform (region 4) to a vent. This last region of the preform may also be heated by the metal due to conduction through the preform fibers and conduction and convection in the expelled gas phase. A temperature gradient then develops in the preform ahead of the infiltration front.

Surface energy differences act to promote or impede infiltration at the infiltration front. depending on whether the fibers are "wetted" by the metal or not. In general, infiltration of the preform is progressive. because the metal first fills large pores in the preform and later fills the finer spaces left between the fibers. Thus, the infiltration front separating regions 1 and 4 is of finite thickness, containing decreasing amounts of porosity as one crosses the front from the uninfiltrated preform (region 4) into the infiltrated composite (region 1 or 3).

Flow of the liquid metal into the preform dissipates

(a)

(b)
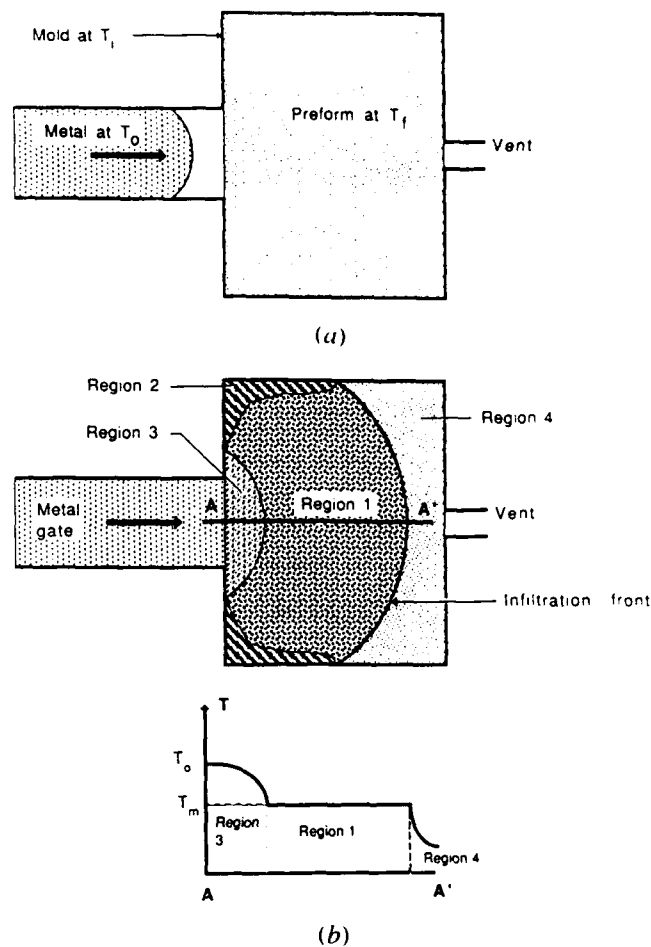
Fig. 1 — Schematic illustration of the injection of metal into a mold containing a preform. under conditions such that solid metal forms at the infiltration front in contact with the fibers and along the mold wall due to external cooling. (a) right before infiltration begins and (b) during infiltration. The fiber preform then contains four regions, shown in the figure: region 1, which is composed of fibers. solid metal. and flowing liquid metal: region 2, in which the metal is fully solid: region 3, in which the metal is fully liquid and flowing: and region 4, the uninfiltrated portion of the preform.

energy (due to viscous friction, kinetic energy losses, etc.) and, therefore, requires a driving force, supplied by gravity or by a pressure differential. The latter can be due to capillary forces when wetting is favorable or to deliberate application of a pressure differential across the advancing liquid within the preform. Modeling of the process thus centers around a treatment of both fluid flow and heat transfer in the infiltrated composite.

We treat the composite as a macroscopic continuum, with the aid of the schematic volume element, ΔV, of Figures 2(a) and (b). respectively, for regions 3 and 1 of the composite. We take this volume element as being large enough to comprise a meaningful local average fraction solid metal and fiber but small enough to be treated as a differential element, as is commonly done in two-phase heat and fluid flow problems. Our approach is explained in the next section, where we state the essential assumptions that define our treatment of the problem.

(a)

(b)
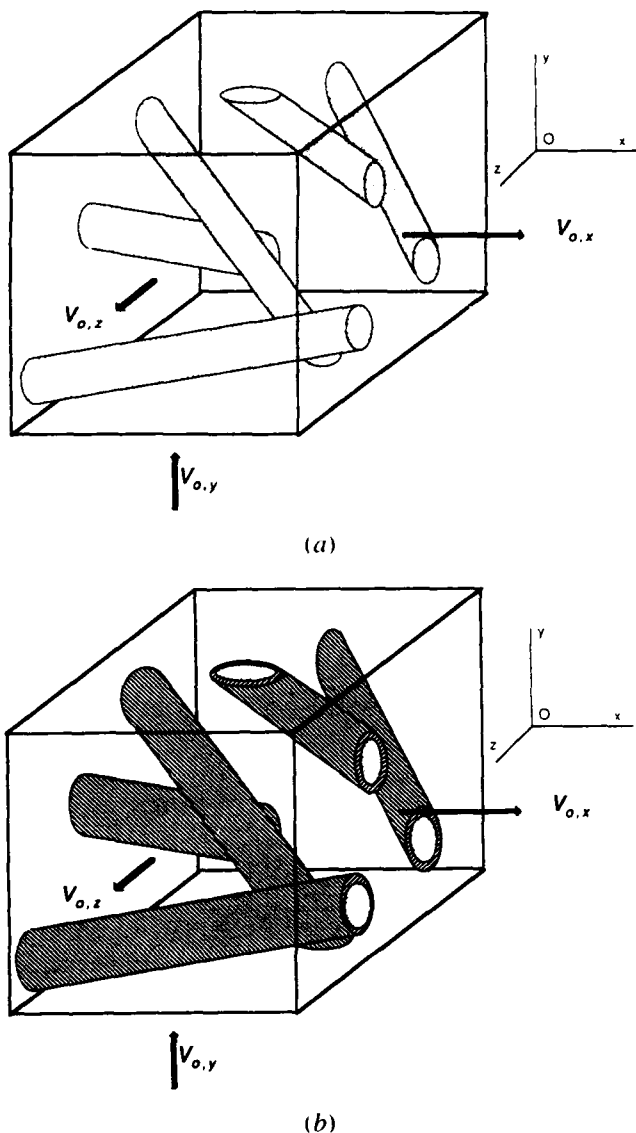
Fig. 2 — Volume element ΔV, small on the scale of the composite but sufficiently large to allow for averaging of superficial velocity, fraction solid metal present, and temperature. (a) within region 3 of Fig. 1, i.e., with no solid metal present and (b) within region 1 of Fig. 1, with solid metal present in the form of a uniform layer coating all fibers.

III. ASSUMPTIONS AND GENERAL EQUATIONS

A. Fluid Flow

Consider a volume element ΔV in any of the regions defined above, small on the scale of the composite but containing several fibers (Figure 2). The fibers occupy a local volume fraction, V_f, the metal a volume fraction, V_m, of which a volume fraction, g_s, is solid. We assume that the metal and the preform are incompressible and ignore density differences between the solid and liquid metal. We use a coordinate system which is fixed with respect to the fiber preform.

We simplify the complex surface force phenomena, which govern details of the infiltration process, by as-

suming that the first imbibition curve of the preform by the metal is a single-step function with the step at pressure $P_g + \Delta P_\gamma$, where P_g is the pressure in the gaseous phase initially present in the preform. The capillary pressure drop at the infiltration front is ΔP_γ, and $\Delta P_\gamma > 0$ corresponds to nonwetting, while $\Delta P_\gamma < 0$ corresponds to wetting of the fibers by the metal. We assume that this pressure drop is independent of the infiltration front velocity. The preform is composed of an uninfiltrated portion (region 4) and a fully dense composite portion (regions 1, 2, and 3), with the two portions separated by a sharp infiltration front. This assumption, termed the "slug-flow" assumption, has been successfully used by other authors (e.g., to model infiltration of glass beads by water and various solvents[14]) and is expected to describe the process adequately when the applied pressure significantly exceeds the capillary pressure needed to infiltrate the majority of the space between the fibers. A consequence of the slug-flow assumption is that $1 - V_f = V_m$ everywhere in the infiltrated composite, comprising regions 1, 2, and 3 in Figure 1(b).

We assume that flow of the fluid through ΔV is within the range of validity of Darcy's law,

$$\mathbf{v_o} = -\frac{\mathbf{K}}{\mu}(\nabla P - \rho_m g) \qquad [1]$$

where μ is viscosity of liquid metal, $\mathbf{K}$ is the (symmetric) permeability tensor of the preform, P is the average pressure in ΔV, ρ_m is the metal density, and g is the acceleration due to gravity. The superficial velocity, $\mathbf{v_o}$, is defined as the average velocity over the entire volume element ΔV. With the assumptions above, the continuity equation is

$$\nabla \mathbf{v_o} = 0 \qquad [2]$$

Equations [1] and [2] are valid in both regions 1 and 3 of the composite. For a given uniform fiber preform of volume fraction V_f, fiber distribution and fiber diameter, the permeability, K, is a function of the local volume fraction and morphology of any solid metal present within ΔV. The viscosity, μ, is a function of temperature. The range of validity of Darcy's law for flow of a metal through a fibrous preform is discussed in Appendix I.

B. Heat Transfer

It is assumed that the size of ΔV is sufficiently small so that the temperature T is uniform within ΔV. Thus, we assume that the time for heat exchange between the fibers and the metal is very short on the scale of the time for infiltration. Furthermore, it is assumed that viscous dissipation of heat within the flowing metal is negligible. The validity of these assumptions is examined in Appendix I.

We assume that the interface between solid and liquid metal is at equilibrium everywhere, and we neglect the effect of curvature on the melting point of the metal, T_m. Thus, for the pure metal matrix, solid and liquid can coexist only at T_m, and the solid metal volume fraction g_s is a step function of position and time. Thus, solidification or remelting of solid metal can only occur at

(moving) interfaces separating region 1 or 2 in the composite from neighboring regions.

The solid metal within region 1 forms as a result of the liquid metal encountering cold fibers. Since solidification of the pure metal is governed by enthalpy removal to the fibers, solid metal in region 1 will be in the form of a uniform sheath coating all fibers within ΔV, as depicted in Figure 2(b).

We also assume that the heat capacity of the gaseous phase is negligible in comparison with that of the metal and fibers. Therefore, whether a gaseous phase is initially present in the preform or not, its contribution to convective heat transfer is negligible.

Consider an element ΔV within region 3 or 1 of the infiltrated composite (Figures 2(a) and (b), respectively). Writing a balance between the heat accumulated in ΔV and that introduced by convection of the metal, as well as conduction through the composite (fibers and metal), into ΔV results in the heat transfer equation

$$\rho_c c_c \frac{\partial T}{\partial t} + \rho_m c_m \mathbf{v_o} \cdot \nabla T = \nabla \cdot (\mathbf{k_c} \nabla T) \qquad [3]$$

where $\mathbf{k_c}$ is the thermal conductivity tensor of the composite, ρ is density, c is heat capacity, and subscripts c, m, and f refer to the composite, the matrix, and the fibers, respectively. Heat capacity of the composite is given by

$$\rho_c c_c = \rho_f c_f V_f + \rho_m c_m V_m \qquad [4]$$

Within region 2 of the composite, there is no fluid flow, and the heat transfer equation simply becomes

$$\rho_c c_c \frac{\partial T}{\partial t} = \nabla \cdot (\mathbf{k_c} \nabla T) \qquad [5]$$

Likewise, within the uninfiltrated preform, the heat transfer equation is

$$\rho_p c_p \frac{\partial T}{\partial t} = \nabla \cdot (\mathbf{k_p} \nabla T) \qquad [6]$$

where $\rho_p c_p$ is the volumetric heat capacity of the preform and $\mathbf{k_p}$ is the thermal conductivity tensor of the preform.

C. Interregion Boundary Equilibria

In addition to the boundary conditions at the periphery of the preform, a solution to the problem must obey mass and energy conservation equations across the moving boundaries separating regions 1 through 4. Each of these surfaces moves at a velocity $v_{i,j}(x,t)$, where the subscripts i and j denote the two regions which the boundary separates, and x and t are the position along the boundary and time, respectively. Depending on the initial temperatures of the metal, mold, and fibers, any or all of the four regions can exist in the preform during infiltration. Therefore, we must concern ourselves with derivation of conservation equations across all pairs of these moving boundaries, except for the case of a boundary between regions 2 and 4, which cannot possibly exist. These are as follows and are derived on the basis of con-

servation of flowing metal and energy across the boundaries:

Boundary 1-2

$$T_1 = T_2 = T_m \qquad [7]$$

$$(\mathbf{k_c} \nabla T_2) \cdot \mathbf{n_{1,2}} = (1 - V_f)(1 - g_s)\Delta H \rho_m v_{1,2} \qquad [8]$$

$$v_{o1} \cdot n_{1,2} = 0 \qquad [9]$$

Boundary 1-3

$$P_1 = P_3 \qquad [10]$$

$$T_1 = T_3 = T_m \qquad [11]$$

$$-(\mathbf{k_c} \nabla T_3) \cdot \mathbf{n_{1,3}} = (1 - V_f)g_s \Delta H \rho_m v_{1,3} \qquad [12]$$

$$(\mathbf{v_{o1}} - \mathbf{v_{o3}}) \cdot \mathbf{n_{1,3}} = 0 \qquad [13]$$

Boundary 1-4

$$P_1 = P_4 = P_g + \Delta P_\gamma \qquad [14]$$

$$T_1 = T_4 = T_m \qquad [15]$$

$$-(\mathbf{k_p} \nabla T_4) \cdot \mathbf{n_{1,4}} = (1 - V_f)g_s \Delta H \rho_m v_{1,4} \qquad [16]$$

$$\mathbf{v_{o1}} = (1 - V_f)\mathbf{v_{1,4}} \qquad [17]$$

Boundary 2-3

$$T_2 = T_3 = T_m \qquad [18]$$

$$\mathbf{k_c}(\nabla T_2 - \nabla T_3) \cdot \mathbf{n_{2,3}} = (1 - V_f)\Delta H \rho_m v_{2,3} \qquad [19]$$

$$\mathbf{v_{o3}} \cdot \mathbf{n_{2,3}} = 0 \qquad [20]$$

Boundary 3-4

$$P_3 = P_4 = P_g + \Delta P_\gamma \qquad [21]$$

$$T_3 = T_4 \qquad [22]$$

$$(\mathbf{k_c} \nabla T_3 - \mathbf{k_p} \nabla T_4) \cdot \mathbf{n_{3,4}} = 0 \qquad [23]$$

$$\mathbf{v_{o1}} = (1 - V_f)\mathbf{v_{3,4}} \qquad [24]$$

where subscript i signifies within region i along the boundary, $\mathbf{n_{i,j}}$ is the normal to the boundary separating regions i and j, oriented from i to j, and $\mathbf{v_{i,j}} = v_{i,j}\mathbf{n_{i,j}}$ is the local boundary velocity. The volume fraction solid metal in the matrix is g_s, and ΔH is the enthalpy of fusion of the metal.

The solution is then specified by boundary conditions along the preform outer surface, as well as the dependence of the permeability and thermal conductivity tensors on local variables, including volume fraction solid metal, g_s. The complete solution comprises the temperature, the superficial velocity, and fraction solid metal in all regions of the composite, and the position of all interregion boundaries, as a function of time.

D. Expressions for Preform Permeability and Composite Thermal Conductivity

A comprehensive summary of existing experimental and theoretical work on the permeability of fibrous preforms has been published recently by Jackson and James.[15] Work to date has concentrated on aligned fiber networks, for flow both parallel and transverse to the fibers, on random two-dimensional (2-D) filter mats, and

on random three-dimensional (3-D) fiber arrays. From their review, it is apparent that

(1) Reliable experimental data exist over a wide range of fiber diameters, from 10 Å to 10 mm. In a plot of nondimensionalized permeability as a function of solid volume fraction, all data fall roughly on a single curve, with a scatter band that is narrower when data for flow parallel to the fibers, perpendicular to the fibers, and through random 3-D mats are separated into sets. In each of these sets, most data fall within a factor of 2 of one another.

(2) Theoretical work has been proposed to model the permeability of each of these media. Most models agree well with the data; thus, it generally makes little difference whether a square or triangular array, for example, is assumed in the model.

(3) The permeability for flow parallel to the fibers is about twice that for flow perpendicular to the fibers. The permeability of most fiber preforms (2-D random and parallel fiber preforms, in particular) is therefore not isotropic, and for a 3-D problem, the average metal flow direction and the pressure gradient are generally not colinear.

(4) The presence of inhomogeneities in the fiber distribution within the preform increases the average permeability significantly.

In the present study, we are concerned with homogeneous fiber preforms with minimum solid volume fractions of 0.20 for 2-D random preforms and 0.50 for parallel fiber preforms. Of the various models proposed, we have chosen to use the following expressions due to their range of validity and relative simplicity. Both assume that the fibers are continuous, with parallel axes located on a square grid. The first of these is

$$K = \frac{0.427 r_{sf}^2}{V_{sf}} \left[1 - \sqrt{\frac{2V_{sf}}{\pi}} \right]^4$$
$$\cdot \left[1 + 0.473 \left(\sqrt{\frac{\pi}{2V_{sf}}} - 1 \right) \right] \qquad [25]$$

for flow parallel to the fiber axes, where r_{sf} is the radius of the solid material and V_{sf} is its volume fraction. Equation [25] is valid for solid volume fractions ranging from 0.5 to $\pi/4$ and is based on the calculations of Drummond and Tahir.[16] The second equation is

$$K = \frac{2\sqrt{2} r_{sf}^2}{9V_{sf}} \left[1 - \sqrt{\frac{4V_{sf}}{\pi}} \right]^{5/2} \qquad [26]$$

for flow perpendicular to the fiber axes. Equation [26] is valid for solid volume fractions ranging from approximately 0.2 to $\pi/4$ and is based on an approximation to the numerical calculations of Sangani and Acrivos.[17] It is accurate to within a factor of 2.

Several authors have proposed calculations for the thermal conductivity of fiber composites.[18–22] For parallel continuous fibers, the thermal conductivity in the direction of the fiber axes is given by the rule of mixtures, regardless of the fiber distribution:

$$k_c = k_f V_f + k_m (1 - V_f) \qquad [27]$$

For heat flow in the direction perpendicular to the axes of parallel continuous fibers lying on a square array, the equation we adopt for the thermal conductivity of the composite is

$$k_c = k_m \frac{(k_f + k_m) + (k_f - k_m)V_f}{(k_f + k_m) - (k_f - k_m)V_f} \qquad [28]$$

This relatively simple equation is given independently in two articles[18,19] and matches closely with the more precise (but more complex) equation of Perrins et al.[20]

For a preform consisting of parallel fibers oriented along the z-axis, Eqs. [25] and [27] give the zz component and Eqs. [26] and [28] give the xx and yy components of K and k_c, respectively, while the xy, xz, and yz components of these tensors are zero.

IV. THE SIMILARITY SOLUTION

The nature of the governing equations allows for considerable simplification under the conditions of unidirectional infiltration and a constant pressure difference.

Suppose that infiltration of a uniform porous preform of constant reinforcement geometry, size, and volume fraction V_f takes place along one direction, $x'Ox$, and is driven by a constant pressure differential, $\Delta P_T = P_o - P_g$, where P_0 is the pressure in the unreinforced metal bath which contacts the preform at $x = 0$ and $t = 0$ (Figure 3). When flow is not horizontal, we neglect the gravitational force field under the assumption that the applied pressure gradient is comparatively high. For the problem to be truly unidirectional, the axis $x'Ox$ must lie along one of the principal directions of the permeability and conduction tensors of the preform (and, hence, the composite), K and k_c, respectively. We assume this is the case and define K and k_c as the permeability and the thermal conductivity along $x'Ox$, respectively. We assume that the fiber volume fraction, V_f, is constant everywhere in the preform. We also assume no heat flux from the mold wall; i.e., the infiltration process is adiabatic, and region 2 in Figure 1 does not form. In the infiltrated composite, Eqs. [1], [2], and [3] now become

$$v_o = -\frac{K}{\mu} \frac{\partial P}{\partial x} \qquad [29]$$

$$\frac{\partial v_o}{\partial x} = 0 \qquad [30]$$

and

$$\rho_c c_c \frac{\partial T}{\partial t} + \rho_m c_m v_o \frac{\partial T}{\partial x} = k_c \frac{\partial^2 T}{\partial x^2} \qquad [31]$$

respectively, if we neglect variations of k_c with temperature.

Then, provided that all initial and boundary conditions can be expressed as functions of $x/\sqrt{t}$, the entire problem can be solved as a function of that variable, multiplied by a convenient constant scalar. We call this the similarity solution by analogy with other moving boundary problems.[23]
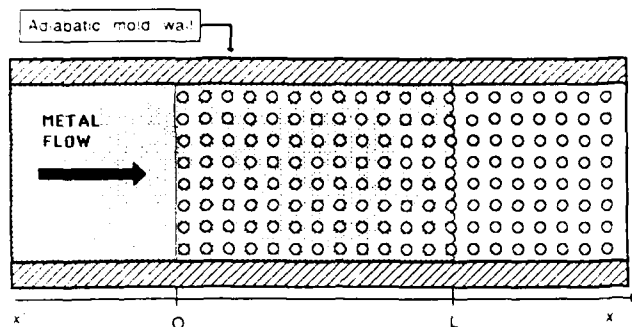
Fig. 3 — Schematic illustration of the case of unidirectional adiabatic infiltration perpendicular to the fiber axis. Fiber size is exaggerated.

We thus define

$$\chi = x/\psi\sqrt{t} \qquad [32]$$

and replace two parameters, x and t, with this single parameter, χ. The solution to the problem is then similar in time, except for a scaling factor $\psi\sqrt{t}$ acting on distance x (hence, its name). We choose the scaling factor such that $\chi = 1$ corresponds to the position of the infiltration front, at $x = L(t)$. Hence,

$$L = \psi\sqrt{t} \qquad [33]$$

The superficial velocity, v_o, must then be constant in the entire infiltrated composite (Eq. [30]) and equal to

$$v_o = (1 - V_f)\frac{\psi}{2\sqrt{t}} \qquad [34]$$

Equations [29] and [31] now become

$$-\frac{(1 - V_f)\mu\psi^2}{2K} = P' \qquad [35]$$

and

$$(\chi - \beta)T' = -\frac{2\alpha_c}{\psi^2}T'' \qquad [36]$$

respectively, where a prime denotes differentiation with respect to χ,

$$\alpha_c = \frac{k_c}{\rho_c c_c} \qquad [36a]$$

is the thermal diffusivity of the composite, and

$$\beta = \frac{(1 - V_f)\rho_m c_m}{\rho_c c_c} \qquad [36b]$$

Specification of the relation $K = K(g_s)$ and conservation equations for heat and metal across boundaries of discontinuity in g_s (i.e., Eqs. [7] through [24] in unidimensional form) define flow and heat transfer within the composite. In the uninfiltrated portion of the preform, region 4, only the heat transfer Eq. [5] is of interest, taking the form

$$\chi T' = -\frac{2\alpha_p}{\psi^2}T'' \qquad [37]$$

where

$$\alpha_p = \frac{k_p}{\rho_p c_p} \qquad [37a]$$

At the preform entrance, $x = 0$, temperature and pressure must be constant for applicability of the similarity solution.

In summary, with the assumptions above and given the initial and boundary conditions of the problem can be expressed in terms of $x/\sqrt{t}$, the problem of unidirectional adiabatic infiltration of a fibrous preform by a pure metal can be solved by the similarity solution, which describes the entire problem in terms of the independent variable, χ. This allows for considerable simplification, because the partial differential equations are now rendered ordinary. In the following sections of this paper, we consider some problems of engineering interest, which can be solved using the similarity solution. We assume in these subsequent sections that the viscosity, μ, of the metal is independent of temperature.

V. UNIDIRECTIONAL ADIABATIC INFILTRATION

A. In the Absence of Solidification

When the initial fiber preform temperature, T_f, is sufficiently high (a statement to be quantified below), no solidification of the matrix occurs, even though T_f may be below T_m, the melting point of the metal. The permeability in the composite then is constant everywhere and given by Eq. [25] or [26] with $r_{sf} = r_f$, the fiber radius, and $V_{sf} = V_f$ for flow parallel or perpendicular to the fibers, respectively.

By integration of Eq. [35] from $\chi = 0$ to $\chi = 1$, ψ is then expressed as

$$\psi = \sqrt{\frac{2K\Delta P_\mu}{\mu(1 - V_f)}} \qquad [38]$$

where $\Delta P_\mu = \Delta P_T - \Delta P_\gamma$ is the pressure drop between the entrance of the preform at $x = 0$ and the region just behind the infiltration front at $x = L^-$. Boundary conditions and thermal equilibria on either side of the composite and the preform are

$$\chi = 0, \qquad T = T_0 \qquad [39]$$

$$\chi = 1, \qquad T_{\chi-1} = T_{\chi-1^+} \qquad [40]$$

$$\chi = 1, \qquad k_c T'_{\chi=1} = k_p T'_{\chi=1^+} \qquad [41]$$

$$\chi \rightarrow \infty, \qquad T = T_f \qquad [42]$$

Equations [40] and [41] are unidimensional versions of Eqs. [22] and [23], respectively, while Eqs. [39] and [42] are boundary conditions. The temperature profile is obtained by solution of Eqs. [36] and [37] subject to these equations and is given by

$$\frac{T_0 - T}{T_0 - T_f} = \frac{\text{erf}\,[A(\chi - \beta)] + \text{erf}\,[A\beta]}{\text{erf}\,[A(1 - \beta)] + \text{erf}\,[A\beta] + [1 - \text{erf}\,(B)]C} \qquad [43]$$

where

$$A = \frac{\psi}{2\sqrt{\alpha_c}}, \qquad B = \frac{\psi}{2\sqrt{\alpha_p}}$$

and

$$C = \sqrt{\frac{k_c c_c \rho_c}{k_p c_p \rho_p}} \; e^{[B^2 - A^2(1-\beta)^2]}$$

in the composite, and

$$\frac{T - T_f}{T_0 - T_f} = \frac{1 - \mathrm{erf}\,(B\chi)}{1 - \mathrm{erf}\,(B) + [\mathrm{erf}\,(A(1 - \beta)) + \mathrm{erf}\,(A\beta)]C^{-1}}$$

[44]

in the preform. A simpler case is that in which conduction through the preform can be neglected, *i.e.*, where $\alpha_p = 0$. The temperature is then uniformly at T_f in the preform and is given in the composite by

$$\frac{T_0 - T}{T_0 - T_f} =$$

$$\frac{A\sqrt{\pi}\,(1 - \beta)\,[\mathrm{erf}\,(A\beta) + \mathrm{erf}\,(A(\chi - \beta))]}{e^{-A^2(1-\beta)^2} + A\sqrt{\pi}\,(1 - \beta)\,[\mathrm{erf}\,(A\beta) + \mathrm{erf}\,(A(1 - \beta))]}$$

[45]

which can also be obtained directly by solving Eq. [36] subject to the boundary conditions

$$\chi = 0, \qquad T = T_0$$

and

$$\chi = 1, \qquad -k_c \frac{dT}{d\chi}\bigg)_{\chi=1} = \frac{\rho_f c_f V_f (T_{\chi=1} - T_f)}{2}\,\psi^2$$

Plots of the temperature profiles given by Eq. [45] for various values of A are shown in Figure 4, using as an example the thermal values of aluminum and alumina fibers.

The conditions described here can be obtained as long as no solid metal forms. This is true when the lowest temperature experienced by the metal is no lower than T_m, the metal freezing point. Because the lowest tem-

perature must be at $\chi = 1$, the condition for validity of this solution is that

$$\frac{T_0 - T_m}{T_0 - T_f} \geq \frac{\mathrm{erf}\,[A(1 - \beta)] + \mathrm{erf}\,[A\beta]}{\mathrm{erf}\,[A(1 - \beta)] + \mathrm{erf}\,[A\beta] + [1 - \mathrm{erf}\,(B)]C}$$

[46]

Otherwise, some of the matrix must solidify.

B. In the Presence of Solidification

When the initial fiber preform temperature, T_f, and the initial metal temperature are sufficiently low to violate Eq. [46], solid metal forms at the infiltration front and remains at the point where it has formed in the form of a coating surrounding the fibers. The remaining liquid flows further downstream, encountering a new set of cold fibers, and solidifies in an analogous manner. Behind the infiltration front, wherever there is solid metal in the presence of liquid metal, the temperature is uniform at T_m. As shown above, the volume fraction solid metal remains fixed wherever it is present. Remelting of the metal thus occurs by the passage of a sharp remelting front created by the influx of liquid metal at $T_0 > T_m$ at $x = 0$. The composite then comprises two zones: a zone where solid and liquid metal coexist in fixed proportions (and where permeability is lowered), extending from the infiltration front to the remelting front, and a zone where the metal is entirely liquid and covers the rest of the composite; these are regions 3 and 1, respectively, in Figure 1. Analysis of the stability of the remelting front which separates the two regions is beyond the scope of this paper; we defer this analysis to a subsequent publication. In this work, we assume for simplicity that the remelting front is planar and located at $\chi = \chi_s$. Figure 5 schematically illustrates this case.
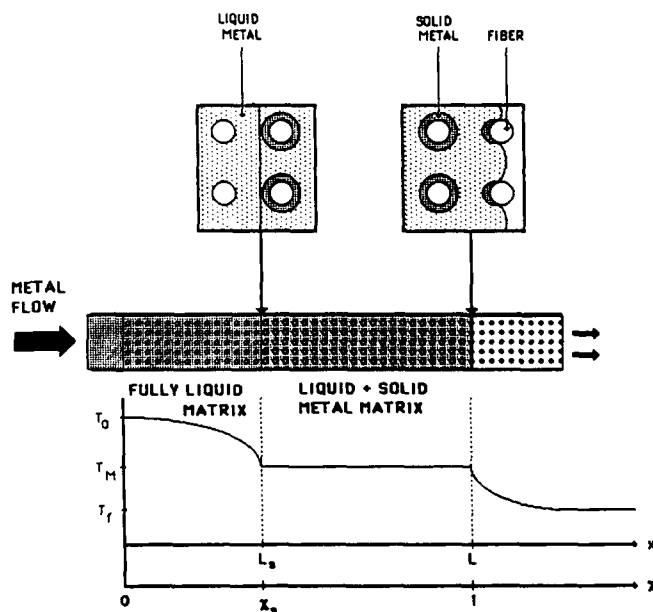
Fig. 5 — Schematic drawing of the temperature profile and composite morphology during infiltration for a case with finite metal superheat and low initial fiber temperature.
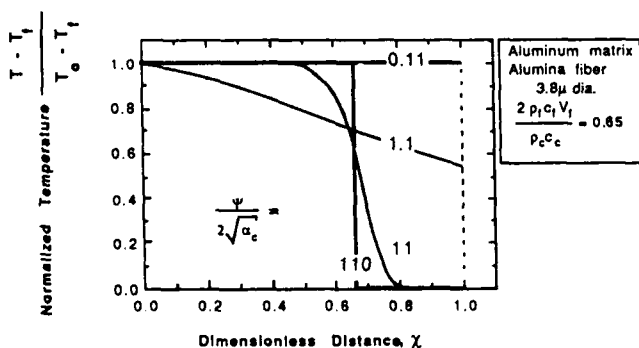

Fig. 4 — Normalized temperature profile within the infiltrated composite with no metal solidification. The aluminum matrix is reinforced with 24 vol pct alumina fibers, and infiltration is perpendicular to the fiber axis, with no conduction of heat in the fiber preform (Eq. [45]).

The position of the infiltration front is now given by

$$\psi = \sqrt{\frac{2K\Delta P_\mu}{\mu(1 - V_f)\left[\dfrac{\chi_s}{K_1} + \dfrac{1 - \chi_s}{K_2}\right]}} \qquad [47]$$

where K_1 is the permeability of the preform with no solid metal present, given by Eq. [25] or [26] with $V_{sf} = V_f$ and $r_{sf} = r_s$, the fiber radius, for flow parallel or perpendicular to the fibers, respectively. The permeability of the preform in the presence of solid metal is represented by K_2, and is given by Eqs. [25] and [26] with

$$V_{sf} = V_f + V_s \qquad [48]$$

and

$$r_{sf} = r_f \sqrt{\frac{V_{sf}}{V_f}} \qquad [49]$$

for flow parallel or perpendicular to the fibers, respectively, where V_s is the volume fraction of the solid metal in the composite, $g_s(1 - V_f)$, where g_s is the volume fraction solid metal in the matrix.

Heat transfer, as before, is governed by Eqs. [36] and [37] in the composite and the preform, respectively, and is subject to the following boundary conditions and thermal equilibria:

$$\chi = 0, \qquad T = T_0 \qquad [50]$$

$$\chi = \chi_s, \qquad T = T_m \qquad [51]$$

$$T' = -\frac{2\rho_m \Delta H V_s A^2 \chi_s}{\rho_c C_c} \qquad [52]$$

where L_s is the position of the remelting front. Also,

$$\chi = 1, \qquad T = T_m \qquad [53]$$

$$\chi = 1, \qquad T' = -\frac{2\rho_m \Delta H V_s B^2}{\rho_p C_p} \qquad [54]$$

$$\chi \to \infty, \qquad T = T_f \qquad [55]$$

Equations [51] through [54] are unidimensional versions of Eqs. [11], [12], [15], and [16], respectively, while Eqs. [50] and [55] are boundary conditions. It is apparent that the two regions, $0 \leq \chi \leq \chi_s$ and $1 \leq \chi \leq \infty$, are only related by the quantity V_s, the volume fraction solid metal in the composite region extending from $\chi = \chi_s$ to $\chi = 1$, and the flow rate of the metal, measured by ψ. It is most convenient to solve in the preform first, where the temperature profile is given by

$$\frac{T - T_f}{T_m - T_f} = \frac{\text{erf}(B\chi) - 1}{\text{erf}\,B - 1} \qquad [56]$$

and V_s is

$$V_s = \frac{(T_m - T_f)\,e^{-B^2}\rho_p C_p}{\rho_m \Delta H B(1 - \text{erf}\,B)\sqrt{\pi}} \qquad [57]$$

In the limit where $\alpha_p = 0$, V_s is given by

$$V_s = \frac{(T_m - T_f)\rho_f c_f V_f}{\rho_m \Delta H} \qquad [58]$$

which could be obtained by simple thermal equilibration of the heat generated by the solidified metal with that needed to heat the fibers up from T_f to T_m at $\chi = 1$.

The temperature profile in the remelted region is given by

$$T_0 - T = \frac{\rho_m \Delta H V_s A \sqrt{\pi}\chi_s}{\rho_c c_c} e^{A^2\chi_s^2 - B^2}$$
$$\cdot \{\text{erf}\,[A(\chi - \beta)] + \text{erf}\,(A\beta)\} \qquad [59]$$

which in the limit where $\alpha_p = 0$, becomes

$$\frac{T_0 - T}{T_m - T_f} = A\sqrt{\pi}\chi_s(1 - \beta)e^{A^2\chi_s^2 - B^2}$$
$$\cdot \{\text{erf}\,[A(\chi - \beta)] + \text{erf}\,(A\beta)\} \qquad [60]$$

We must calculate ψ and χ_s from Eqs. [47] and [51] with the aid of Eqs. [57] and [59] (or Eqs. [58] and [60], if heat transfer in the preform can be neglected). The temperature and the fraction solid in the composite and the preform can then be calculated based on Eqs. [56], [57], and [59] (or Eqs. [56], [58], and [60], if heat transfer in the preform can be neglected).

A particularly simple case is that of no metal superheat with negligible heat conduction in the preform ahead of the infiltration front. The volume fraction solid given by Eq. [58] is then uniformly present in the composite, as described in Figure 6. The permeability within the composite is uniformly equal to K_2, and ψ is given by Eq. [47] with $\chi_s = 0$. Plots of the resulting values of ψ for the infiltration of alumina preforms by pure aluminum are given in Figure 7. It is apparent that the influences of fiber preform temperature and volume fraction are significant.

The influence of conduction through the preform is given for the case of no metal superheat and the same materials system in Figure 8. This is a plot of the ratio of V_s predicted by Eq. [57] (which incorporates the effect of fiber preform conductivity) to V_s predicted by Eq. [58] (which ignores this effect). It is apparent that the ratio is approximately 1 for $B > 1.5$, which for $\psi = 0.01$ m/$\sqrt{s}$ corresponds to $\alpha_p > 10^{-5}$ m^2/s, a value within the range of the thermal diffusivities of metals. Therefore, very conductive preforms or slow infiltration rates are necessary for the influence of heat conduction at the infiltration front into the preform to be perceptible. Consequently, in our illustrative calculations for alumina preforms, we ignore heat conduction through the preform.

Values of χ_s for aluminum infiltrating alumina fibers as above are given in Figure 9, together with temperature profiles for a fixed value of χ_s. The resulting influence of superheat, $T_0 - T_m$, on infiltration kinetics, given in Figure 10 for the same materials system as in Figure 7, is comparatively negligible within a range of superheats of practical interest (i.e., <200 K).
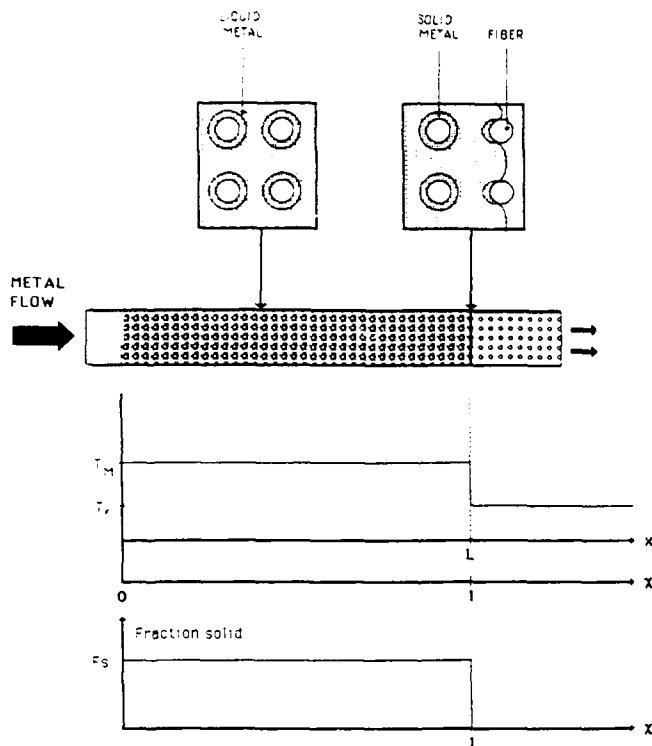
Fig. 6 — Schematic drawing of transverse flow and solidification within the fiber preform for the case of fibers heated significantly below the metal melting point, with no metal superheat and no thermal conduction in the fiber preform.

VI. NONADIABATIC UNIDIRECTIONAL INFILTRATION

In the previous section, we considered heat transfer and fluid flow within a preform thermally isolated from its surroundings; in this section, we consider the additional effect of heat transfer to the surroundings by allowing heat flow to the mold.

Solid metal within the infiltrated preform may now originate from these heat losses to the mold, in addition to thermal exchange with the fibers. Because the case of a pure metal is considered in this paper, the solid forming as a result of heat losses to the mold will grow as a smooth shell progressing inward from the mold surface, as shown by region 2 in Figure 1. The problem is similar to the preceding adiabatic case, except that flow can now occur only within an inner "core" of the sample. To solve this problem, the calculation of a new interface bounding region 2 must be included.

We treat the problem, as in the adiabatic case, for unidirectional infiltration. We add the following assumptions: (1) the mold is thick walled, with a circular cylindrical cavity of internal radius R_i; (2) there is no heat transfer within the mold along the infiltration direction; (3) flow remains essentially unidirectional; and (4) $T_0 = T_m$, $P > 1.5$, and $T_f < T_m$ ($i \cdot$, no metal superheat no heat conduction into the preform; and solid metal forms at the infiltration front).

The infiltrated portion of the preform is now composed of a central core of semisolid metal as before, with a volume fraction solid metal and a permeability given

(a)

(b)

(c)
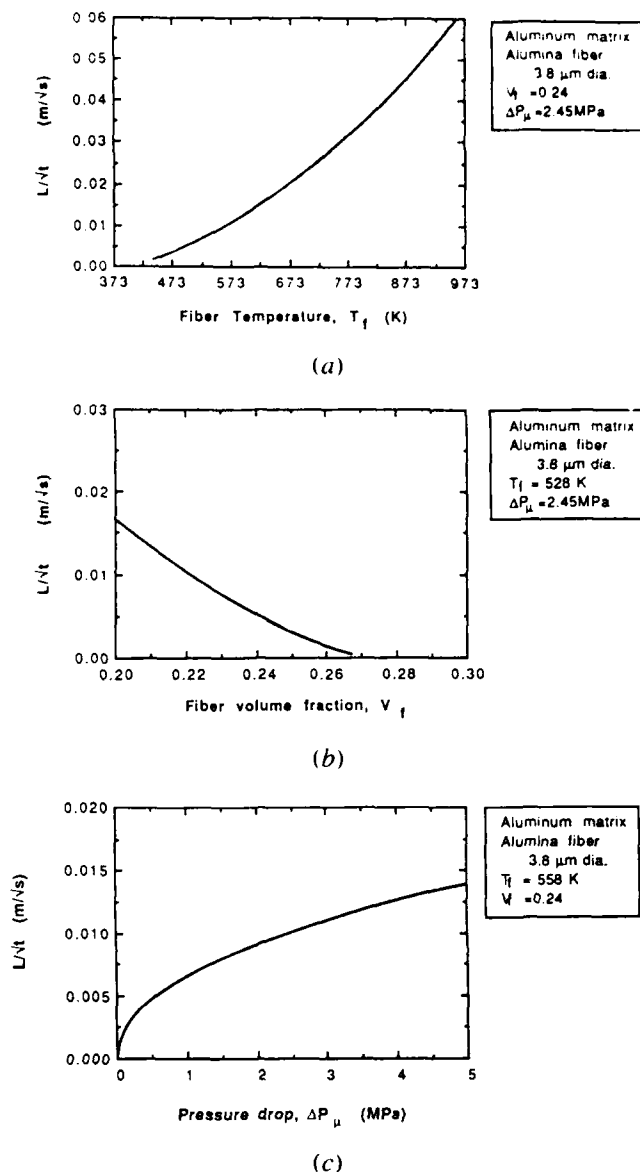
Fig. 7 — Influence of processing parameters on $L/\sqrt{t}$ for infiltration with no metal superheat and matrix solidification during infiltration, depicted in Fig. 6: (a) fiber preheat temperature; (b) fiber volume fraction; and (c) pressure drop. The aluminum matrix is reinforced with 24 vol pct alumina fibers, and infiltration is perpendicular to the fiber axis, with no conduction of heat in the fiber preform (Eqs. [45] and [57] with $\chi_i = 0$).

by Eqs. [58] and [25] or [26], respectively. The outer portion of the infiltrated preform, region 2 in Figure 1, is fully solid and extends from $R = R_c$ to $R = R_i$, where R_c is the radius of the semisolid central core. At any location x along the preform axis, R_c is a decreasing function of time, given by the particular heat loss mechanism into the mold. Figure 11 schematically illustrates the composite during infiltration. According to assumption (2) above, R_c at x is solely a function of the time elapsed, Δt, since the metal first contacted the mold wall at x. This elapsed time, Δt, can be written as

$$\Delta t(x) = t - L^{-1}(x)$$
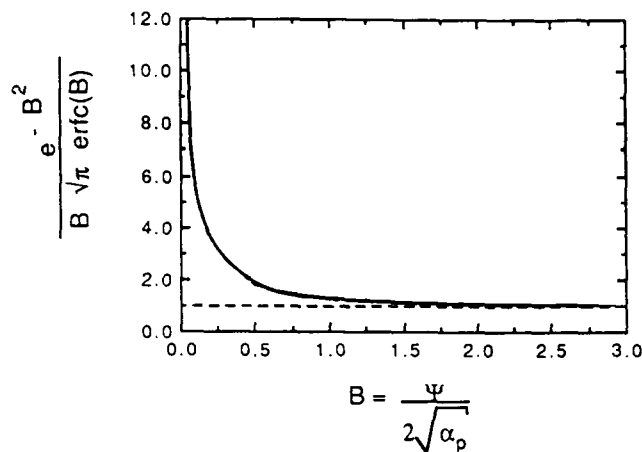
Fig. 8—Plot of the ratio of fraction solid metal with and without taking account of heat conduction into the preform ahead of the infiltration front. for alumina fibers at a volume fraction of 0.24. from a ratio of Eqs. [57] and [58].
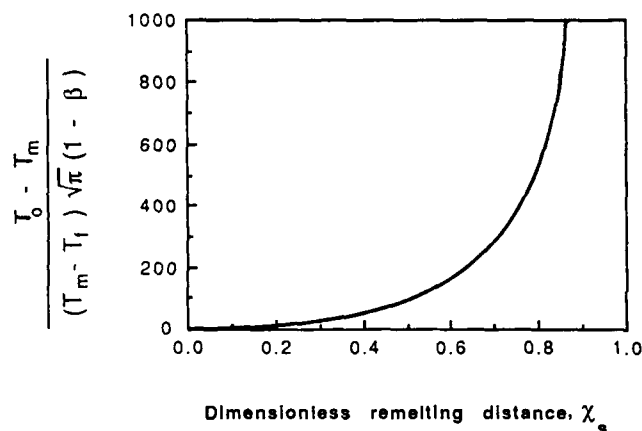
(a)
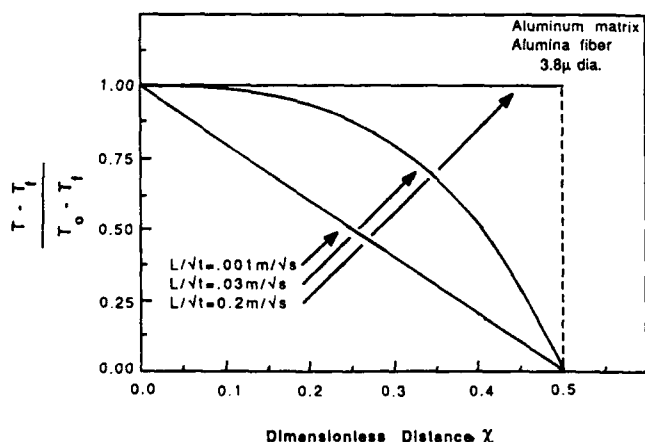
(b)

Fig. 9—(a) Graphical solution for χ_s from Eqs. [47], [51], [58], and [60] for aluminum infiltrating 24 vol pct alumina fibers transverse to the fiber axis for ΔP_μ = 2.45 MPa. (b) Resulting temperature profile in a remelted region extending into 50 pct of the total infiltrated length for the same system and various values of $\psi = L/\sqrt{t}$ from Eq. [60].
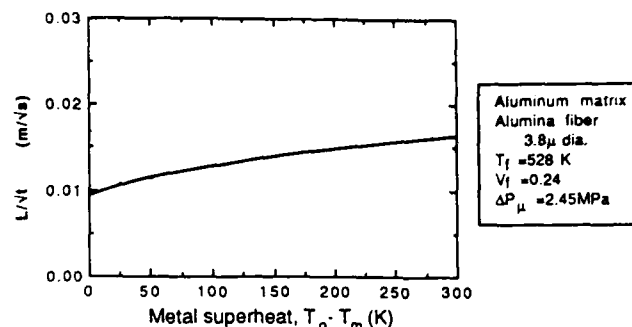
Fig. 10—Dependence of $L/\sqrt{t}$ on metal superheat for alumina fibers infiltrated in cross flow by aluminum. from Eqs. [47], [51], [58], and [60]. and Fig. 9(a).

where $L^{-1}(x)$ is the reciprocal function of the steadily increasing and, hence, bijective function $x = L(t)$. We can thus write

$$R_c(x, t) = R_c[t - L^{-1}(x)] \qquad [61]$$

To satisfy continuity,

$$v_o R_c^2 = (1 - V_f) \frac{dL}{dt} R_i^2 \qquad [62]$$

From Eqs. [61], [62], and [29], after integration from $x = 0$ to $x = L$, we obtain

$$\frac{dL}{dt} \int_0^L \frac{dx}{\left[\frac{R_c(t - L_{(x)}^{-1})}{R_i} \right]^2} = \frac{K \Delta P_\mu}{\mu(1 - V_f)} \qquad [63]$$

The problem is defined with a specification of heat losses at the mold wall, which, in turn, defines $R_c(t)$. When R_c becomes zero (which necessarily occurs first at the preform entrance), choking occurs, and the infiltration process stops. This determines the final infiltration length, L_f.

Solutions of specific cases follow, given as a function of the assumed equation for $R_c(t)$. At this stage, however, it is easily proven (Appendix II) from Eq. [63] that the position of the front at any time during the infiltration process is proportional to the square root of the right-hand side of Eq. [63]. Therefore,

$$L_{(t)} \propto \sqrt{\frac{K \Delta P_\mu}{\mu(1 - V_f)}} \qquad [64]$$
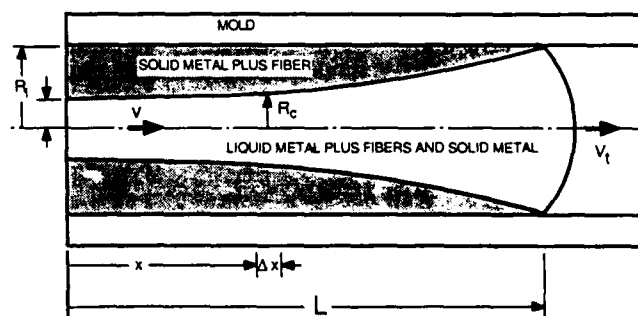
Fig. 11—Schematic cross section of a cylindrical composite during infiltration with external heat losses.

regardless of the heat loss mechanism along the mold surface. This, in turn, implies that the infiltration velocity and final infiltrated length are proportional to fiber radius at constant V_f (Eqs. [25], [26], and [49]).

Simple specific cases for the heat loss mechanism include the following:

(1) External heat loss through a mold of zero thickness with heat transfer limited by convection to the surroundings. In this case, we have[24]

$$\left[\frac{R_c}{R_i}\right]^2 = 1 - \frac{2h_c(T_m - T_e)}{R_i(1 - V_{sf})\rho_m \Delta H} t \qquad [65]$$

where h_c is the global heat transfer coefficient between the metal and the surrounding environment and T_e is the temperature of the surroundings, assumed constant.

(2) External heat loss through a mold of infinite thickness with heat transfer limited by conduction through the mold. In this case, we have

$$\left[\frac{R_c}{R_i}\right]^2 = 1 - \frac{2(T_m - T_i)}{R_i(1 - V_{sf})\rho_m \Delta H} \sqrt{\frac{4\rho'c'k'}{\pi}} \sqrt{t} \qquad [66]$$

where k' is the thermal conductivity of the mold, $\rho'c'$ is the volumetric heat capacity of the mold, and T_i is the initial temperature of the mold.[25]

An example of the effect of external cooling by convection (case (1)) on the infiltration profile for pure aluminum and alumina fibers is given in Figure 12.

VII. CONCLUSIONS

General expressions are given to describe heat and fluid flow during infiltration of a fibrous preform by a pure metal. A solution technique is given for the case of adiabatic unidirectional infiltration into a preform of aligned fibers with constant applied pressure. Some conclusions of engineering significance from the work are as follows:

1. When the fibers are initially at a temperature far enough below the metal melting point to induce solidification of the matrix at the infiltration front, fiber volume fraction and fiber temperature significantly influence infiltration kinetics.
2. The effect of metal superheat is to remelt solid metal that has initially formed between the fibers at the infiltration front. This occurs first at the fiber preform
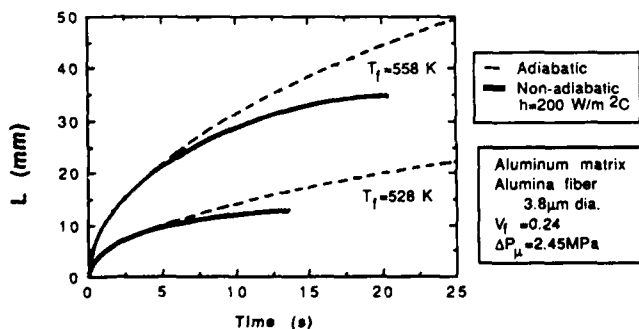

Fig. 12 — Position of infiltration front L as a function of time for alumina fibers infiltrated in cross flow by pure aluminum. Nonadiabatic model, Eqs. [58], [63], and [65]. is shown for one value of h, and is compared to the adiabatic model, Eqs. [47] and [58].

entrance and progresses toward the infiltration front. The analytical solution obtained for this problem indicates a minor role of metal superheat on infiltration kinetics.

3. With no external heat extraction and constant applied pressure, flow through the preform will continue indefinitely if it can initiate. When external heat extraction is present, flow through the preform ceases when solidification from the external heat sink has progressed to the point where the flow channel has closed. This will occur first at the entrance of the fiber preform. The length of penetration when infiltration stops can then be predicted for simple preform geometries. In particular, the dependence of infiltrated length on several parameters, including pressure, can be derived analytically.

4. The effect of thermal losses ahead of the infiltration front is an increase in the amount of solid metal that forms around initially cold fibers. For most fibers of engineering significance, if the infiltration velocity is reasonably high (above about 1 mm/s), this effect can be neglected.

APPENDIX I
Range of validity of assumptions

A. *Darcy's Law*

The range of validity of Darcy's law is usually specified by a range of Reynolds numbers, which for the case of flow through porous media can be defined as

$$Re = \frac{2r_f\rho_m v_o}{\mu V_f} \qquad [Ia]$$

where r_f is fiber radius. There is some agreement on taking the critical Reynolds number to be approximately unity.[26,27] This critical value would be reached, for example, at a flow velocity, v_o, of 1 cm/s in a fiber preform with $r_f = 10\ \mu m$ and $V_f = 0.25$ for an aluminum matrix. However, the range of variation of this critical Reynolds number for cessation of validity for Darcy's law is wide, which seems to indicate that it strongly depends on the geometry of the porous medium.[28]

In unidirectional infiltration with a constant applied pressure, there will always be a period at the start of the infiltration process where Darcy's law does not hold, since the velocity is predicted to be infinite at $t = 0$ (Eq. [34]). The length the metal must travel before the Reynolds number reaches the critical value for Darcy's law to apply is given by

$$L = \frac{r_f\rho_m(1 - V_f)\psi^2}{Re_c\mu} \qquad [Ib]$$

where ψ is defined in Eq. [33]. With values relevant to the system used as an example, $Re_c = 1$, $\psi = 0.01$ $m/\sqrt{s}$, $r_f = 1.9\ \mu m$, and for aluminum, $L = 0.3$ mm.

B. *Negligible Viscous Heat Generation*

The heat dissipated per unit volume in the metal during infiltration can be approximated by the value given in Reference 29 for the volumetric heat dissipation due

to viscous flow at velocity V in a gap, b, between two rotating annuli:

$$S_i = \mu \left(\frac{V}{b}\right)^2 \qquad [Ic]$$

Taking $b \approx r_f$ and $V \approx L/t$, where L is distance infiltrated after time t, the resulting heating rate can be estimated from $S_i = \rho_m c_m \Delta T/t$. The resulting increase in temperature due to flow during t by viscous dissipation can then be estimated as

$$\Delta T = \frac{\mu}{\rho_m c_m} \left(\frac{L}{r_f}\right)^2 t \qquad [Id]$$

For aluminum, $L = 0.01$ m, $t = 1$ s, $r_f = 1.9$ μm, and $\Delta T \approx 0.01$ K, which is negligible.

C. Instantaneous Heat Transfer to the Fibers

A lower limit on the time for heat exchange between metal and fibers can be obtained by assuming that the metal and the fibers exchange heat by conduction. The time required for microscopic temperature equilibration between the fibers and the metal in a volume element ΔV is then of the order of r_f^2/α_f, where α_f is the thermal diffusivity of the fibers, because the fibers are less conductive than the matrix. For alumina fibers with a radius of 1.9 μm, this time is on the order of a microsecond, which is to say that it is quasi-instantaneous with respect to the time scale of the infiltration process.

An upper limit on the time for temperature equilibration can be obtained by assuming that contact between the metal and the fiber is imperfect everywhere, leading to a finite heat transfer coefficient, h, at the interface. This is a conservative assumption, since perfect nonwetting of the fibers by the metal (i.e., a wetting angle of 180 deg) is unusual.[30] A lower limit for h can be estimated by assuming that there is an air gap between the fibers and the metal of a width equal to 10 pct of the fiber radius. Due to the small fiber radius, cooling will be Newtonian, and the resulting time for temperature equilibration can be estimated as

$$\Delta t \approx \frac{\rho_f c_f r_f^2}{10 k_{air}} \qquad [Ie]$$

where k_{air} is the thermal conductivity of air. For alumina fibers with a radius of 1.9 μm, this time is on the order of 50 microseconds, which is still very small compared to the time for infiltration.

APPENDIX II

Proof of Equation [64]

Consider two infiltration experiments, labeled 1 and 2, such that for experiment 2, L is γ times L of experiment 1. The difference between the two experiments is due to a difference in the right-hand term of Eq. [63], while the heat loss kinetics, measured by $R_c(\tau)$, are the same for both experiments. Because $L_2(\tau) =$

$\gamma L_1(\tau)$, $L_2^{-1}(x) = L_1^{-1}(x/\gamma)$. Writing Eq. [63] for experiment 1 gives

$$\frac{dL_1}{dt} \int_0^{L_1} \frac{dx}{\left[\dfrac{R_c(t - L_{1(x)}^{-1})}{R_i}\right]^2} = \frac{K_1 \Delta P_{\mu,1}}{\mu_1(1 - V_{f,1})} = C_1 \qquad [IIa]$$

and for experiment 2, gives

$$\frac{dL_2}{dt} \int_0^{L_2} \frac{dx'}{\left[\dfrac{R_c(t - L_{2(x')}^{-1})}{R_i}\right]^2} = \frac{K_2 \Delta P_{\mu,2}}{\mu_2(1 - V_{f,2})} = C_2 \qquad [IIb]$$

It becomes clear after a change of variables from x' to $x = \gamma x'$ in Eq. [IIb] that C_2 must equal γC_1.

ACKNOWLEDGMENTS

REFERENCES

1. S. Nagata and K. Matsuda: IMONO, 1981, vol. 53, pp. 300-04.
2. S. Nagata and K. Matsuda: Trans. Jpn. Foundrymen's Soc., 1983, vol. 2, pp. 616-20.
3. F.M. Hosking and A.A. Netz: Report No. SAND83-2573, Sandia National Laboratory, Albuquerque, NM, 1983.
4. H. Fukunaga: in Cast Reinforced Metal Composites, S.G. Fishman and A.K. Dhingra, eds., Proc. Conf., Chicago 1988, ASM INTERNATIONAL, Metals Park, OH, 1988, pp. 101-07.
5. H. Fukunaga and K. Goda: J. Jpn. Inst. Met., 1985, vol. 49, pp. 78-83.
6. H. Fukunaga and K. Goda: Bull. JSME, 1984, vol. 27, pp. 1245-50.
7. F. Girot, J.P. Rocher, J.M. Quenisset, and R. Naslain: in Proc. Conf. Eur. MRS, P. Lamicq, W.J.G. Bunk, and J.G. Wurm, eds., Strasbourg, France, 1985, pp. 129-33.
8. J.M. Quenisset, R. Fedou, F. Girot, and Y. Le Petitcorps: in Cast Reinforced Metal Composites, S.G. Fishman and A.K. Dhingra, eds., Proc. Conf., Chicago 1988, ASM INTERNATIONAL, Metals Park, OH, 1988, pp. 133-38.
9. T.W. Clyne: in Proc. 6th Int. Conf. Composite Materials (ICCMVI), F.L. Matthews, N.C.R. Buskell, J M. Hodgkinson, and J. Morton, eds., Elsevier Applied Science, London, 1987, pp. 2.275-2.286.
10. T.W. Clyne and M.G. Bader: in Proc. 5th Int. Conf. Composite Materials (ICCMV), W.C. Harrigan, J. Strife, and A.K. Dhingra, eds., TMS-AIME, Warrendale, PA, 1985, pp. 755-71.
11. T.W. Clyne and J.F. Mason: Metall. Trans. A, 1987, vol. 18A, pp. 1519-30.
12. G.P. Martins, D.L. Olson, and G.R. Edwards: Metall. Trans. B, 1988, vol. 19B, pp. 95-101.
13. W.E. Brittin: J. Appl. Phys., 1946, vol. 17, pp. 37-44.

14. Y.W. Yang, G. Zografi, and E.E. Miller: *J. Colloid Interface Sci.*, 1988, vol. 122, pp. 35-46.
15. G.W. Jackson and D.F. James: *Can. J. Chem. Eng.*, 1986, vol. 64, pp. 364-74.
16. J.E. Drummond and M.I. Tahir: *Int. J. Multiphase Flow*, 1984, vol. 10, pp. 515-40.
17. A.S. Sangani and A. Acrivos: *Int. J. Multiphase Flow*, 1982, vol. 8, pp. 193-206.
18. E. Behrens: *J. Comp. Mater.*, 1968, vol. 2, pp. 2-17.
19. H. Hatta, M. Taya, and F.A. Kulacki: in *Proc. 5th Int. Conf. Composite Materials (ICCMV)*, W.C. Harrigan, J. Strife, and A.K. Dhingra, eds., TMS-AIME, Warrendale, PA, 1985, pp. 1667-81.
20. W.T. Perrins, D.R. McKenzie, and R.C. McPhedran: *Proc. R. Soc. London A*, 1979, vol. 369, pp. 207-25.
21. S. Nomura and T.-W. Chou: *J. Comp. Mater.*, 1980, vol. 14, pp. 120-29.
22. J.R. Willis: *J. Mech. Phys. Solids*, 1977, vol. 25, pp. 185-202.
23. J. Crank: in *Free and Moving Boundaries*, Oxford Science Publications, Clarendon Press, Oxford, 1984, ch. 3, p. 1011.
24. D.V. Ragone, C.M. Adams, and H.F. Taylor: *Trans. Am. Foundrymen's Soc.*, 1956, vol. 64, pp. 640-52.
25. M.C. Flemings: *Solidification Processing*, McGraw-Hill, Inc., New York, NY, 1974, p. 12.
26. S. Ergun: *Chemical Engineering Progress*, 1952, vol. 48 (2), pp. 89-94.
27. V. Stanek and J. Szekely: *AIChE J.*, 1974, vol. 20 (5), pp. 974-80.
28. A.E. Scheidegger: *The Physics of Flow through Porous Media*, 3rd ed., University of Toronto Press, Toronto, 1974, p. 154.
29. R.B. Bird, W.E. Stewart, and E.N. Lightfoot: *Transport Phenomena*, John Wiley & Sons, New York, NY, 1960, p. 278.
30. N.K. Adam: *The Physics and Chemistry of Surfaces*, Dover ed., Dover Publications, New York, NY, 1968, p. 179.

Infiltration of Fibrous Preforms by a Pure Metal: Part II. Experiment

L.J. MASUR, A. MORTENSEN, J.A. CORNIE, and M.C. FLEMINGS

In a previous paper, a theory was developed to describe the flow of a pure metal into a fibrous preform. This paper presents experimental data to test the results of the theory for pure aluminum flowing into fibrous alumina preforms. An apparatus was designed and built for unidirectional infiltration under constant pressure and carefully controlled temperature parameters. A sensor was also developed to measure the position of the liquid metal in the fibrous preform during the experiment. This technique enabled quantitative comparison of theory and experiment. Experimental data are reported for the infiltration by 99.999 and 99.9 wt pct pure aluminum of SAFFIL alumina fibers fabricated into two-dimensionally random preforms. Fiber volume fraction was varied from 0.22 to 0.26, fiber preheat temperature was varied from approximately 483 to 743 K, and metal superheat was varied from 20 to 185 K. Infiltration pressure was varied from 1 to 4.5 MPa (145 to 650 psi). Agreement between theory and experiment was very good under all the experimental conditions studied for the 99.999 wt pct pure matrix. The impurity level of the metal was found to influence infiltration significantly. The measured preform permeability for 99.9 wt pct aluminum was much lower than that for 99.999 wt pct aluminum.

I. INTRODUCTION

IN a previous paper,[1] analytical solutions were given to describe the unidirectional infiltration of a pure metal into a preform of aligned fibers under the application of a constant pressure. In particular, the influence on infiltration kinetics was shown for the processing parameters, including (a) fiber volume fraction, (b) fiber temperature, (c) metal superheat, and (d) applied pressure. Flow of metal into a fiber preform heated significantly below the metal melting point was shown to result in the solidification of metal around the fibers to form a sheath. Also, it was shown that the effect of metal superheat was to remelt this solid metal sheath at a remelting front separating two regions in the composite. The cessation of fluid flow was shown to be due to solidification from the mold wall progressing inward and closing the flow channel. Calculations were performed to predict the behavior of pure aluminum infiltrating alumina fibers in cross flow under a variety of experimental conditions.

In this paper, experiments are presented to test the results of the foregoing analysis. All experiments were performed with alumina fibers and aluminum metal. The experiments reported here were performed with the fibers initially at a temperature significantly below the metal melting point. This is the case of practical interest for the fabrication of many fiber-reinforced metal components, including, for example, diesel engine pistons.

L.J. MASUR, formerly a Graduate Student with the Department of Materials Science and Engineering, Massachusetts Institute of Technology, is Senior Scientist with the American Superconductor Corporation, Cambridge, MA 02139. A. MORTENSEN, Assistant Professor, J.A. CORNIE, Principal Research Associate, and M.C. FLEMINGS, Professor and Department Head, are with the Department of Materials Science and Engineering, Massachusetts Institute of Technology, Cambridge, MA 02139.
Manuscript submitted June 7, 1988.

II. EXPERIMENTAL APPARATUS AND PROCEDURE

A. Fiber Preform Preparation

SAFFIL* fibers were obtained from Imperial Chem-

*SAFFIL is a trademark of ICI Americas, Inc., Wilmington, DE.

ical Industries, London, England. SAFFIL is a nominally 3-μm-diameter, delta-alumina fiber that is chopped and pressed into disk-shaped preforms. The preform fabrication operation tends to align the fiber axes perpendicular to the pressing direction, resulting in a two-dimensional random arrangement of fibers. The preforms used in this study were 100 mm in diameter by 15-mm thick and featured a nominal fiber density of 24 vol pct.

Cylindrical plugs were cut from the mother preform using a knife-edged cutter 17 mm in internal diameter. These plugs were then tightly fitted into quartz tubes 17 mm in internal diameter and 1 mm in wall thickness. Their orientation was such that metal infiltration was perpendicular to the fiber axes. In these experiments, either two or three plugs were placed atop one another within the quartz tube, resulting in fiber preforms 30 or 45 mm in length. Each plug cut from the preform was weighed to calculate fiber volume fraction; the plugs in any given experiment were always within 0.5 fiber vol pct of one another. A ceramic support rod was placed on top of the preforms to prevent them from moving upward in the quartz tube during infiltration. Figure 1 schematically illustrates the preform preparation process.

Selected preforms (chosen at random for each batch of raw materials) were further characterized by a water permeability test. In this test, a falling head permeability apparatus[2] was used to measure the permeability of the preform to flowing water.
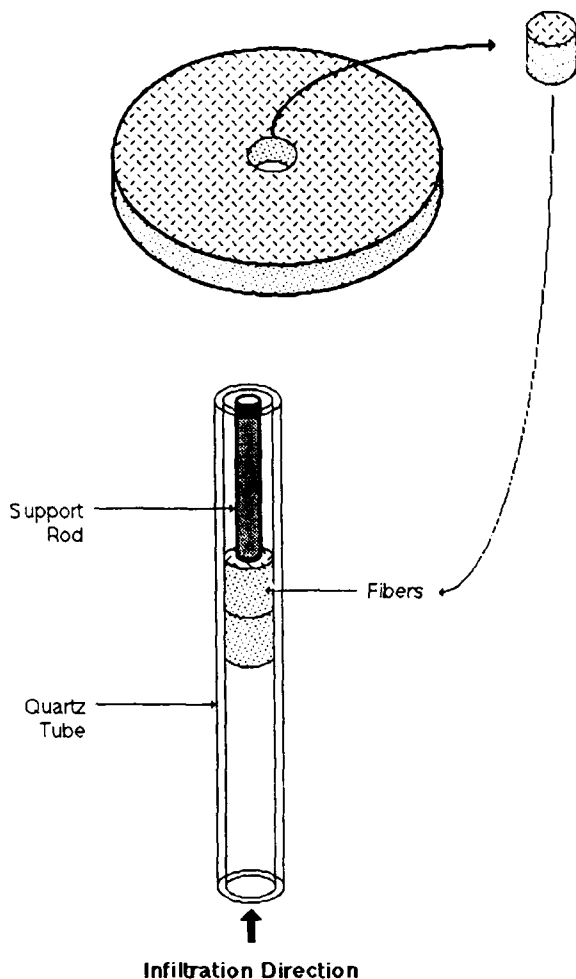
Infiltration Direction

Fig. 1 — Schematic drawing of fiber preform preparation process.

Fig. 2 — Schematic drawing of pressure casting apparatus.

B. Pressure Infiltration Apparatus

Figure 2 is a schematic drawing of the pressure casting apparatus that was constructed for this study. The fiber-filled quartz tube discussed above was secured to the cap of the apparatus with an O-ring fitting, above which was attached a stainless steel tube to act as a chill in the event of overinfiltration. The fibers were heated by a helically wound resistance heater consisting of a 3.2-mm-diameter sheathed heating element wound around, and silver-soldered to, a 15.2-cm-long steel cylinder (1.6-mm wall thickness). The heater assembly was placed over the quartz tube in the vicinity of the fibers; the space between the heater and quartz was filled by a 1.6-mm-thick layer of FIBERFRAX* insulation. Temperature

---

*FIBERFRAX is a trademark of Standard Oil Engineered Materials Co., Niagara Falls, NY.

---

control was maintained with a thermocouple placed between the quartz tube and the heater at the midpoint of the fiber preform length. Temperature differences measured within the furnace over the 45-mm length occupied by the fibers were found not to vary by more than ±3 K.

A second resistance furnace for metal melting was located in the bottom of the pressure vessel portion of the pressure casting apparatus. It measured 11.4 cm in internal
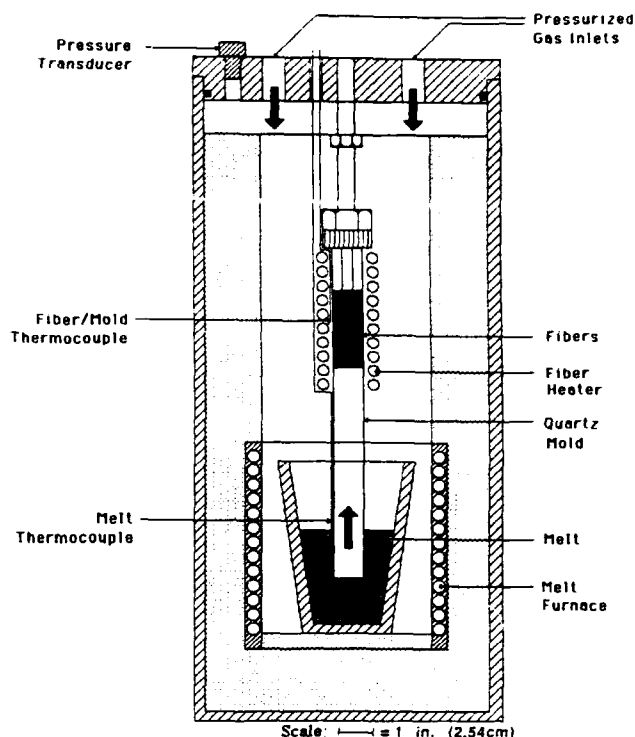
diameter and 15.2 cm in height. Metal, either 99.9 or 99.999 wt pct aluminum, was melted in a thick-walled graphite crucible in air to preserve metal purity.

Pressurization was achieved with nitrogen gas, which was delivered to the apparatus through two inlets *via* two 10.2-mm internal-diameter high-pressure hoses. Fast pressurization of the apparatus ($\approx$1.2 seconds) was achieved by prepressurizing a holding tank, from which nitrogen was released *via* two 10.2-mm orifice ball valves. Thus, the infiltration experiments were conducted at constant pressure over most of their duration, typically of about 10 seconds. This feature of the procedure, combined with the unidirectionality of infiltration, enabled us to use results from calculations presented in Reference 1 to interpret the data.

Compression experiments were performed on the uninfiltrated fiber preform material along the axis of infiltration. These were performed within a heated quartz tube so as to replicate the actual conditions of the infiltration experiments. Strain was measured from crosshead displacement. It was found that preform deformation remained relatively small (<0.03 engineering strain) up to a pressure of about 3.5 MPa, at which the preform started deforming significantly. Therefore, applied pressure was varied from 0 to 3.5 MPa in the infiltration experiments to avoid complications related to preform compression during infiltration. The preform deformation that occurred during infiltration was limited to a strain of only 0.03, which resulted in an imprecision in the volume fraction V_f of less than 0.01.

C. Liquid Metal Position Sensor

A technique was developed to sense the position of the liquid metal front as it advances through the fiber

preform during infiltration. An SiC filament and the molten metal were used as a variable resistor, and as a result of its change in resistance during the experiment, the liquid metal position could be calculated. The filament was a 140-μm-diameter SCS-2 SiC fiber manufactured by AVCO-Specialty Materials Division, Lowell, MA. It is very stiff, which is ideal for specimen preparation, and has a relatively high electrical resistivity ($\approx 10 \Omega$/mm), which is important for resolution of the metal position.

A single SiC filament was inserted through the center of the preform during specimen preparation. The top of the filament above the preform was nickel-plated and attached to the fitting at the top of the quartz tube. The portions of the filament within the preform and extending out the bottom were unplated and allowed to hang free. The interface between the plated and unplated parts of the filament was located exactly at the top of the preform. A load resistor was placed in series with the filament, and a constant potential was applied between the load resistor and the metal crucible, with the molten metal acting as a switch to close the circuit (Figure 3). The potential drop across the SiC filament was recorded as a function of time. As the metal infiltrated the preform, the potential measured across the filament decreased due to the decrease in its effective electrical length, so that by monitoring the potential drop during infiltration, the position of the metal front and its velocity could be determined. Examples of typical infiltration profiles, in terms of infiltration length vs time, are given in Figure 4. The
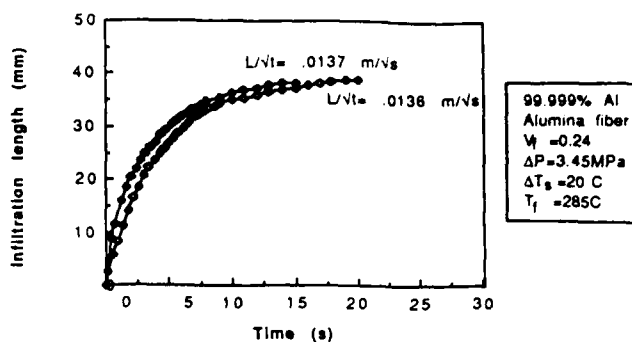
Fig. 4 — Infiltration profiles recorded with the device in Fig. 3 for runs 8 and 9, Table I.

final infiltrated length of most samples was measured independently of the SiC filament and found to deviate from that measured with the sensor by no more than 10 pct.

D. Aluminum-Lead Experiments

A technique was developed for infiltrating a small amount of aluminum followed by molten lead. In these experiments, 2 to 3 g of aluminum were melted and floated on a bath of molten lead. When the system was subsequently pressurized, a small amount of aluminum preceded the lead into the preform. While the aluminum solidified in the preform during infiltration, the lead flowed into those volumes not occupied by solid aluminum. This provided a high-contrast metallographic observation of the volumes where the aluminum first flowed and solidified, because lead is darker than aluminum under the optical microscope.

E. Metallographic Examination

Metallographic preparation of composite samples was achieved by polishing on an automatic polisher with diamond paste on hard synthetic cloth, followed by a final polish with magnesium oxide on a soft billiard-type cloth. Some samples were chemically etched to reveal grains by immersing for 2 to 3 seconds in an etch-pitting solution of 50 ml nitric acid, 47 ml hydrochloric acid, and 3 ml hydrofluoric acid.[13] Observation of the samples under crossed polarizers accentuated the etch pits and readily showed differences in their orientation across different grains.

The purity of the material after infiltration was determined by chemical analyses of samples taken from unreinforced portions of the casting located close to the fiber preform.

III. EXPERIMENTAL RESULTS AND COMPARISON WITH THEORY

A series of 28 infiltration experiments were conducted in this study at various values of pressure, fiber volume fraction, metal superheat, metal purity, and fiber temperature. Experimental conditions are listed in Table I along with measured results.

The total length of flow into the preform, L_f in Table I, was determined from measurement on longitudinally sliced
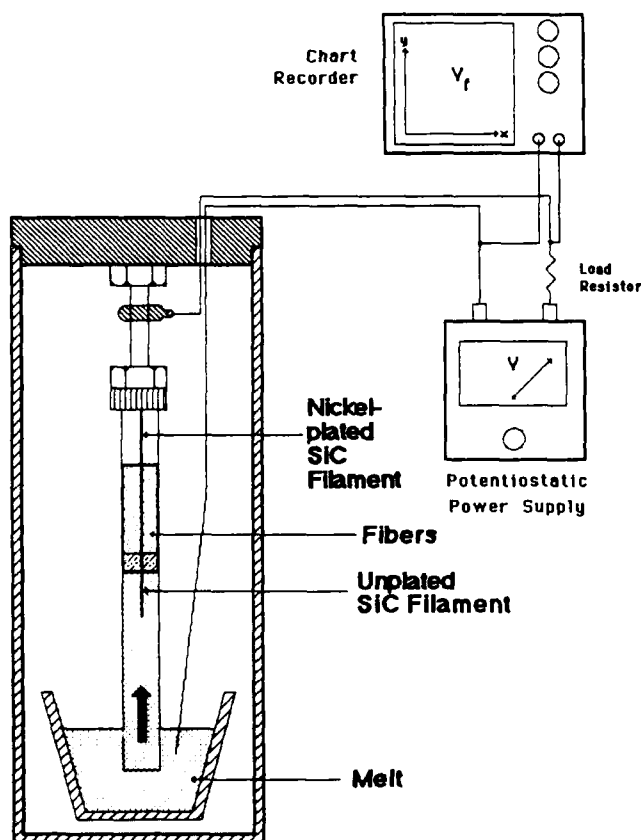

Fig. 3 — Schematic drawing of liquid position measurement technique. An SiC filament detects movement of the liquid metal.

| Run Number	Nominal Metal Purity	Mold Radius (mm)	λ	T_f (K)	ΔP, (MP)	T_0 (K)	$L\sqrt{t} = \psi$ (m/√s)	L_f (mm)	Metal Purity after Experiment (when Analyzed)
1	3N	5.5	0.2.5	1023	0	1023	—	0	—
2	3N	5.5	0.250	983	0	983	—	0	—
3	3N	5.5	0.250	973	0	973	—	0	—
4	3N	5.5	0.250	603	3.59	960	*	23.0	—
5	3N	8.5	0.250	603	3.52	955	0.0144	43.5	—
6	3N	8.5	0.250	575	3.55	959	0.0113	33.5	—
7	3N	8.5	0.240	559	3.42	951	0.0101	20.5	—
8	5N	8.5	0.240	560	3.48	953	0.0137	38.5	99.990 pct
9	5N	8.5	0.240	562	3.48	951	0.0136	39.0	—
10	5N	8.5	0.240	546	3.52	950	0.0129	33.0	—
11	5N	8.5	0.240	530	3.52	953	0.0115	29.5	99.991 pct
12	5N	8.5	0.240	504	3.45	950	*	22.0	—
13	5N	8.5	0.240	741	3.45	948	0.0304	>45	99.987 pct
14	5N	8.5	0.240	483	3.42	943	0.0051	11.5	—
15	5N	8.5	0.240	645	3.45	948	0.0201	>45	99.990 pct
16	5N	8.5	0.235	528	3.42	1180	0.0147	37.0	—
17	5N	8.5	0.245	528	3.31	1011	0.0104	23.0	99.947 pct
18	5N	8.5	0.240	527	3.45	1073	0.0125	33.0	—
19	5N	8.5	0.235	528	3.42	1023	0.0121	30.0	—
20	5N	8.5	0.220	484	3.45	953	0.0144	36.5	—
21	5N	8.5	0.240	558	2.35	953	0.0100	29.0	—
22	5N	8.5	0.240	558	1.30	953	0.0052	10.5	—
23	5N	8.5	0.260	528	3.38	953	0.0070	14.5	—
24	5N	8.5	0.220	529	3.38	956	0.0158	45.0	—
25	5N	8.5	0.240	562	2.28	950	0.0119	34.5	—
26	5N	8.5	0.240	558	4.52	951	0.0141	39.5	—
27	5N	8.5	0.245	560	0.90	948	*	4.0	—
28	5N	8.5	0.240	557	1.73	952	0.0079	21.0	—

3N indicates starting purity of 99.9 pct.
5N indicates starting purity of 99.999 pct.
*Indicates insufficiently long linear portion on L vs $\sqrt{t}$ curve for accurate measurement of slope.

samples. The parameter $L/\sqrt{t} = \psi$, introduced in Reference 1, is also listed. It was determined as described below.

For each run, data such as those in Figure 4 were replotted as L vs $\sqrt{t}$, as shown in Figure 5. In these plots, there was invariably an initial transient of about 1 second during which the slope increased (region I in Figure 5). We attribute this to the transient pressure buildup in the chamber. Following this initial transient, a region II was generally observed in which the slope was constant; lastly, in region III, the slope was observed to decrease with time.

Data for $L/\sqrt{t}$ in Table I represent the slope of curves in region II such as that in Figure 5. This was taken to be the value of $L/\sqrt{t} = \psi$ measured after the steady-state pressure level was reached, but before sufficient solidification from external heat loss occurred to significantly affect flow.

The pressure differential, which drives flow of the metal into the preform, was defined in our previous paper[1] as $\Delta P_\mu = P_T - P_g - \Delta P_\gamma$, where P_T is the applied pressure at the entrance of the preform, P_g is the ambient pressure in the preform at the infiltration front, and ΔP_γ is the pressure drop in the liquid metal due to surface tension. To enable correlation of applied pressure with infiltration kinetics, the capillary pressure drop, ΔP_γ, must be known. According to the theory presented in Reference 1

(Eqs. [47], [51], [58], and [60]), a plot of $\psi^2 = L^2/t$ as a function of ΔP_T (i.e., $P_T - P_g$) should be linear at zero metal superheat, with its intercept on the abscissa axis equal to ΔP_γ (Eq. [47] with $\chi_s = 0$). With a low superheat, such as 20 K for aluminum, the deviation from linearity is small. In Figure 6, L^2/t is plotted for a series
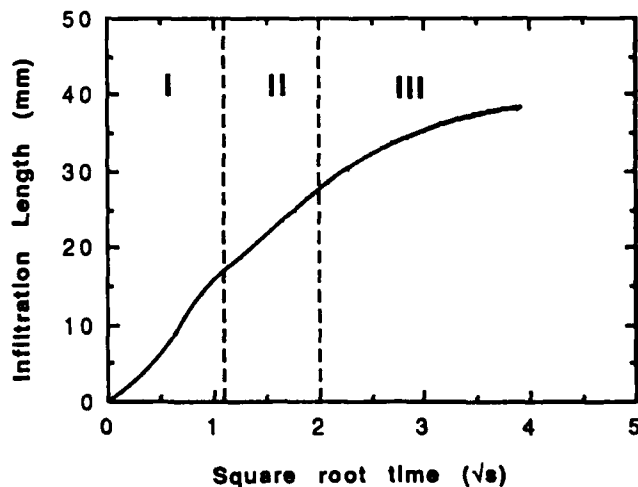

Fig. 5—Typical plot of length vs square-root time showing regions I, II, and III discussed in the text. This particular curve is from run 8, Table I.

of runs with low superheat and identical values of all parameters except for the applied pressure ΔP_t. A straight line through these data points intersects the abscissa at approximately 1 MPa, and this is the value used for ΔP_γ in the calculations that follow. This approximate value is corroborated by the observation that at applied pressures at or below 0.9 MPa, no or very little infiltration of the preforms was observed (Table I, runs 1, 2, 3, and 27). Given the relatively small range of fiber volume fraction explored in this work, we ignore variations in ΔP_γ with fiber volume fraction and use the constant value of $\Delta P_\gamma = 1$ MPa in all applications of equations derived in Reference 1.

Figures 7 through 13 are plots of data from Table I and show comparisons of these data with curves calculated using the analysis of Reference 1. Table II summarizes the values of thermal and physical constants used in the calculations.

Solution of the equations also required a value for the fiber radius, r_f. Fibers in the preforms used in this investigation ranged mostly from 0.75 to 2.5 μm in radius, with a nominal value reported to be ~1.5 μm. In order to assign a single value for fiber radius, we measured the permeability of the preforms to water using standard techniques[2] and calculated the resulting apparent fiber radius from Eq. [26] of Reference 1. This yielded an apparent fiber radius of 1.9 μm, satisfactorily close to the nominal value of 1.5 μm reported by the supplier. Thus, we used $r_f = 1.9$ μm when applying equations derived in Reference 1.

The curves drawn in Figures 7 through 13 were calculated from Eqs. [47], [51], [56], [58], and [60] of Reference 1. The values of fiber volume fraction, fiber temperature, and metal temperature were taken directly from the processing parameters of each experiment (Table I).

The influences of fiber volume fraction and fiber temperature are shown in Figures 8 and 9, respectively. The sensitivity of the kinetics of preform infiltration to fiber volume fraction is a result of the dual role of an increasing fiber volume fraction in decreasing the spacing between fibers and in increasing the amount of solid formed per unit volume of preform. This dual effect significantly decreases the permeability for a relatively small increase in fiber volume fraction.

The effect of metal superheat is shown in Figure 10. Metal superheat is seen to play a minor role in the effect
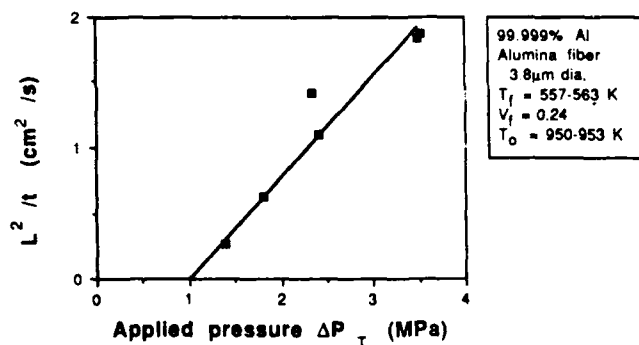
Fig. 6 — Experimental values of infiltration kinetics as a function of total applied pressure.
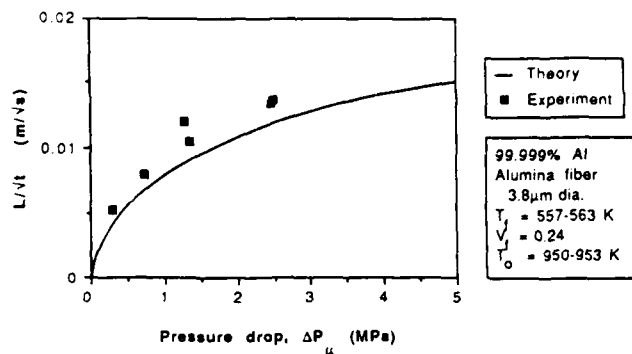
Fig. 7 — Effect of pressure drop on $L/\sqrt{t}$; the theoretical curve drawn is for 20 °C of superheat, and was calculated from Eqs. [47], [51], [58], and [60] of Ref. 1. Experimental data are plotted with the assumption that the capillary pressure drop at the infiltration front is 1 MPa.
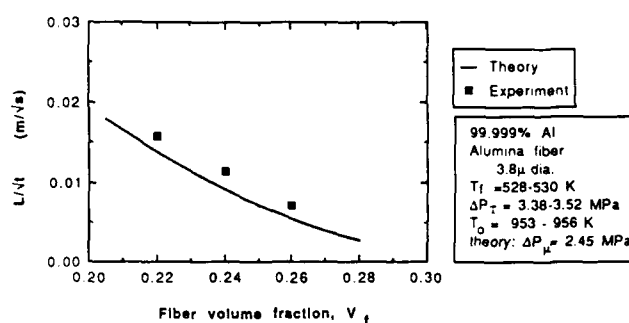
Fig. 8 — Effect of fiber volume fraction on $L/\sqrt{t}$; curve drawn is for 20 °C of superheat.
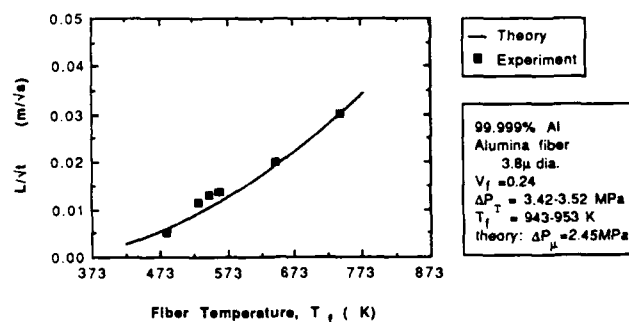
Fig. 9 — Effect of fiber temperature on $L/\sqrt{t}$; curve drawn is for 20 °C of superheat.
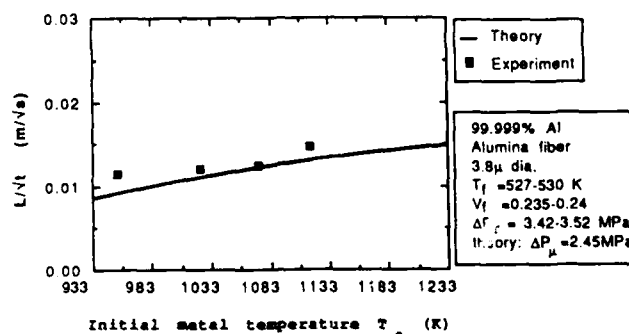
Fig. 10 — Effect of metal superheat on $L/\sqrt{t}$.
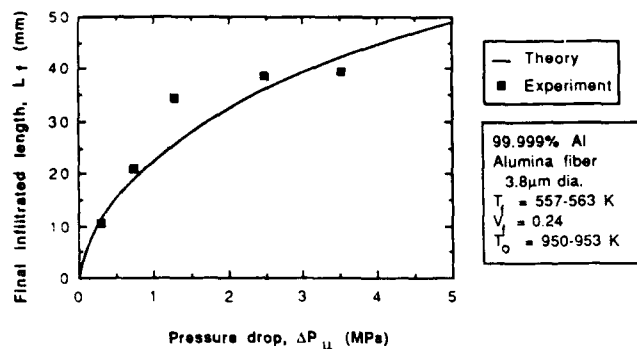
Fig. 11 — Effect of pressure drop on final infiltrated length. Calculations assume $h_c = 200$ W/m^2 K.

Fig. 13 — Effect of fiber temperature on final infiltrated length. Theoretical curve assumes $h_c = 200$ W/m^2 K.

on infiltration kinetics, in agreement with results from our model. This is because to impart a significant effect on overall permeability, a considerable portion of the composite must be remelted. Remelting of aluminum requires a large amount of energy, which is not obtained for metal superheats normally encountered in foundry practice (at most 200 K), so remelting distances are moderate and the effect on infiltration kinetics is minimal.

Using the aluminum-lead experiments as a verification of the role of superheat, the optical micrograph in Figure 14 shows the results for metal with 60 K superheat. Note the existence of a region at the base of the composite where the aluminum was entirely replaced by lead. At the end of the experiment, therefore, this region was entirely liquid; any aluminum which had solidified was remelted. In the central portion of the composite, lead and aluminum coexist in the matrix, indicating that some aluminum was retained by the fibers as the lead flowed past. To be retained by the fibers, this aluminum must have been solid. It is also evident from this figure that fingering occurred at the remelting front (i.e., the planar remelting front was unstable, resulting in cells or "fingers" of fully liquid matrix composite protruding into the partly solid matrix composite), analogous to observations on fluid displacement in porous media.[4]

Indication of a two-zone structure in cast aluminum matrix composites was observed when the superheat was sufficiently high to yield a region of large columnar grains in the upstream portion of the composite (Figure 15). Note that this is also experimental evidence that the fibers do not act as nucleation sites for the growth of solid
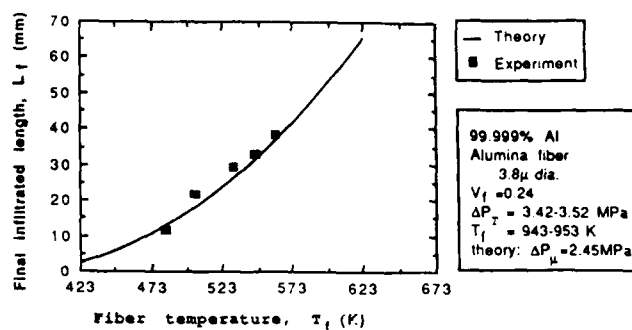
metal. A microstructure taken further downstream in the same sample and in the vicinity of the infiltration front is shown in Figure 16, where many orientations of etch pits in a small volume indicate a fine-grained matrix. This is a consequence of the high nucleation rate achieved by rapid cooling by the fibers at the infiltration front.

The curves of final infiltration length, shown in Figures 11 through 13, were calculated from Eq. [34] of Reference 1. As a first approximation, the external heat loss was assumed to be limited by convection to the surroundings and described by a single heat transfer coefficient, h_c, between the sample and its surroundings at the fiber preheat temperature. Thus, the growth of solid from the mold wall was calculated by Eq. [65] of Reference 1. The best agreement of theory with experiment was obtained by assuming 200 W m^{-2} K^{-1} for h_c. Although agreement with all experimental data using a single value for h_e is satisfactory, a more detailed analysis would be necessary to account for the complexity of heat transfer from the sample to the mold and its surroundings, consisting of successive layers of insulating material, a furnace, and pressurized gas. The value of h_e of 200 W m^{-2} K^{-1} is satisfactory, however, in that it lies between the typical values of 3000 W m^{-2} K^{-1} observed in casting fluidity experiments with aluminum, where all heat was extracted into a quartz mold wall,[5] and 10 W m^{-2} K^{-1} for cooling by natural convection in air.[6] Using the above value of h_e, it is seen that the effects of the processing parameters on L_f mirror those of $L/\sqrt{t}$, with the same experimental agreement with theory. The curves are calculated for the case of no metal superheat; the theory has not been extended to predict the effect of metal superheat on final infiltrated length, which was found experimentally to be small.

The calculation of L_f is based upon the assumption that external heat losses are responsible for the cessation of infiltration. The physical model of solidification from the mold wall is confirmed by a reexamination of the aluminum-lead experiment of Figure 14. Near the mold wall, the matrix is aluminum, indicating complete solidification of the aluminum at the mold wall prior to infiltration by lead. This corresponds to region 2 of the discussion in Reference 1. Figure 14 of this paper is to be compared with Figures 1 and 11 of Reference 1.

The effect of the mold radius is shown experimentally in Figure 17. Note that a change in mold radius does not influence the infiltration profile during the early stages of infiltration, but it does have an influence on the total
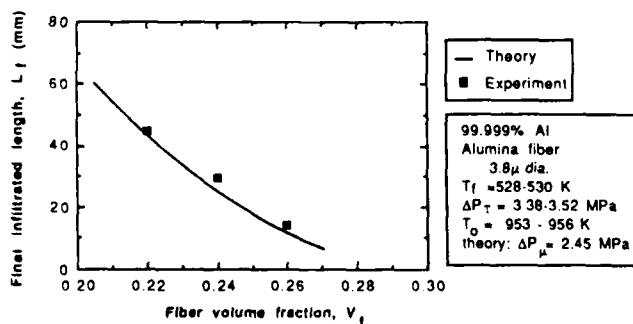

Fig. 12 — Effect of fiber volume fraction on final infiltrated length. Theoretical curve assumes $h_c = 200$ W/m^2 K.

Property	Units	Aluminum[13]	SAFFIL[14]	Quartz[15]	Air[16]
ρ	(kg/m^3)	2.4×10^3	3.3×10^3	2.2×10^3	1.1×10^0
ρC	(J/m^3 K)	2.6×10^6	4.0×10^6	3.1×10^6	1.1×10^3
k	(W/m K)	93	8	2	2.6×10^{-2}
α	(m^2/s)	36×10^{-6}	2×10^{-6}	0.65×10^{-6}	2.4×10^{-5}
$\rho \Delta H$	(J/m^3)	9.5×10^8	—	—	—
μ	(Pa·s)	1.3×10^{-3}	—	—	—

time of flow. Theoretically, the mold radius should influence only the external heat loss kinetics and not the interaction between the metal and fibers which is accounted for in the adiabatic model of Reference 1. Therefore, the slopes of the infiltration profiles during the early stages of infiltration will remain unchanged for the two different mold radii, while the final infiltration lengths will increase as the mold radius increases, as confirmed experimentally by data in Figure 17 for 99.9 wt pct pure aluminum.

Metal purity was noted to have a very strong effect on the infiltration kinetics, as shown in Figure 18. Not only was there a pronounced difference in flow behavior between 99.999 and 99.9 wt pct aluminum, but when repeatedly using a melt of 99.999 wt pct aluminum, a significant effect on infiltration kinetics was detected when the melt purity dropped to only 99.95 wt pct. The effect

of metal purity on results of a vacuum casting fluidity test was studied by Feliu et al.,[7] who reported an 8 pct decrease in fluidity when changing from 99.99 to 99.9 wt pct aluminum. They concluded that the impurities influenced the mode of solidification, which, in turn, affected the drag between the liquid and stationary solid metal. This conclusion has also been supported by observations of the transition from planar to cellular solidification interfaces due to small changes in solute levels.[8] Therefore, it is plausible that the lower purity metal does not initially solidify at the infiltration front in a form that approximates that of a smooth cylinder surrounding the fibers, but solidifies following a different morphology, which is probably more akin to what is observed when an alloy solidifies in the presence of fibers after infiltration.[9,10] These data confirm conclusions in our previous publication[11] on infiltration by 99.9 wt pct aluminum,

Fig. 14—Optical micrograph of a cross section of a sample infiltrated by aluminum followed by lead. Dark regions are lead or fiber, and light regions are aluminum. Infiltration occurred upward. Infiltration parameters were $V_f = 0.23$, 99.9 pct pure Al, $T_f = 608$ K, $T_0 = 993$ K, $\Delta P_f = 3.5$ MPa; sample diameter was 11 mm.

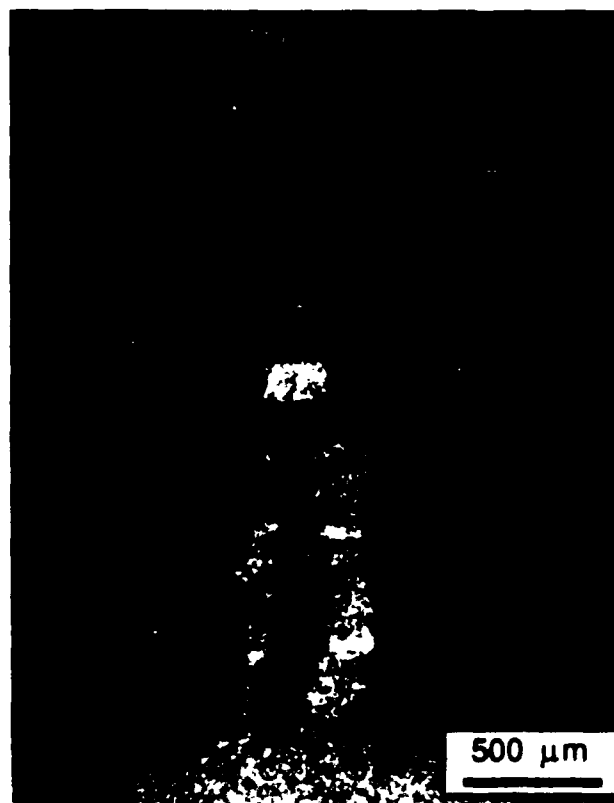Fig. 15—Optical micrograph of the preform entrance region of etch-pitted SAFFIL alumina-fiber-reinforced 99.9 pct pure aluminum matrix composite viewed under crossed polarizers in the optical microscope. Large columnar grains are visible (in white) in this region. The preform entrance is at the bottom of the figure, and infiltration occurred upward. Horizontal striations are due to delamination of the preform.
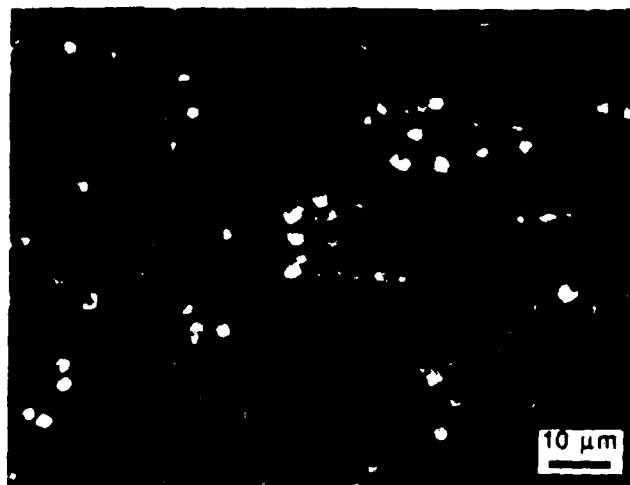
Fig. 16 — Photomicrograph of the same sample as in Fig. 15, viewed as before but at higher magnification. This micrograph was taken farther away from the preform entrance, closer to the infiltration front, above the region in Fig. 15. Here, etch pits display a variety of orientations over a much smaller area of composite (many etch pits are in white and thus distinguishable from fibers and the rest of the matrix), denoting a grain size on the order of 10 μm, close to the infiltration front.

wherein discrepancies between our results and those of Fukunaga *et al.* were attributed to a difference in metal purity.

IV. VALIDITY OF ASSUMPTIONS

In what follows, each of the main assumptions introduced in the theory of Reference 1 is briefly justified for the system investigated here. Table II is a list of the physical and thermal properties for the SAFFIL-reinforced aluminum composites studied in these experiments.

Cross flow through a square array of cylinders: It was observed that even though the infiltration front features numerous fine spikes on a microscopic scale, on a macroscopic scale as measured in these experiments, the infiltration front progresses as a plane, a short distance behind which all pores in the preform are filled. The "slug-flow" assumption of Reference 1 is thus justified.

Data in the review of Jackson and James[12] indicate that the geometry of the fibrous arrays is not a significant factor for the measurements of their permeability as long as flow of the metal is perpendicular to the fiber axes.
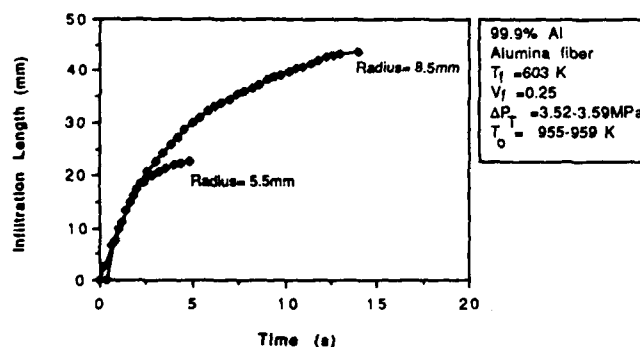
Fig. 17 — Effect of mold radius on infiltration behavior.
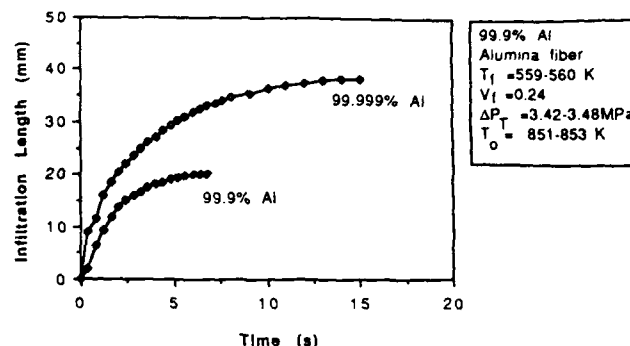
Fig. 18 — Effect of metal purity on infiltration behavior.

This was the case for the vast majority of the fibers in the SAFFIL preforms.

Darcy's law: Throughout this work, it is assumed that Darcy's law describes the flow of metal through the preform. As discussed in Appendix I of Reference 1, this constitutes a valid assumption for Reynolds numbers less than 1. In these experiments, the maximum velocity measured is on the order of 0.01 m/s. This yields a Reynolds number on the order of 0.08, clearly within the region of validity of Darcy's law.

Negligible heat transfer ahead of the infiltration front: The effect of thermal losses ahead of the infiltration front is described in detail in Reference 1. Referring to Figure 8 of the same reference, this effect is significant only when the value of B (defined in Eq. [43]) falls below unity. For the values of $\psi = L/\sqrt{t}$ encountered in experiments reported here, B is always greater than 10. The effect of heat transfer ahead of the infiltration front is therefore negligible for all the experiments considered in this work.

Negligible temperature gradients over the composite sample diameter perpendicular to the infiltration direction in the presence of external cooling: We assume that the rate of heat extraction at the mold wall is limited by convection to a surrounding medium at temperature T_f, the initial fiber temperature. The Biot number gives a measure of the significance of temperature gradients within the composite, defined as:

$$\mathrm{Bi} = \frac{h_e R_i}{k_c}$$

where h_e is the interfacial heat transfer coefficient between the metal and mold, R_i is the inside radius of the mold, and k_c is the thermal conductivity of the composite. The assumption of negligible temperature gradients across the sample diameter is consistent with the value for h_e derived from experimental data, which yields $\mathrm{Bi} = 0.03$.

V. SUMMARY AND CONCLUSIONS

1. An apparatus was designed and built for the infiltration of molten metal into porous preforms under controlled processing conditions. The apparatus utilized pressurized gas to cause infiltration under a constant applied pressure.

2. A sensor was developed to measure the flow of liquid metal through a porous preform composed of non-conductive material. This sensor was used for quantitative measurements of infiltration kinetics.

3. Quantitative agreement of theory with experimental values of infiltration kinetics and final infiltrated length has been shown under a variety of processing conditions. For example, it was shown that an increase in fiber volume fraction of only 10 pct from 0.22 to 0.24 caused a drop in infiltration length of 46 pct, and an increase in fiber temperature by 10 pct from 523 to 553 K increased infiltration length by 35 pct. The effect of applied pressure on infiltration length is parabolic after correction for the capillary pressure drop at the infiltration front; doubling the pressure that drives fluid flow results in a $\sqrt{2}$ increase in infiltrated length.

4. Metal superheat induces a gradual remelting at the preform entrance of solid previously formed. This mechanism was verified by metallographic observation of experiments performed with the immiscible aluminum-lead system. The technique also provided experimental verification for solidification from the mold walls, which is the mechanism for cessation of infiltration.

5. The effect of metal purity on infiltration was extremely pronounced. A decrease in purity from 99.999 to 99.9 wt pct resulted in a decrease in infiltration length of 50 pct. This observation is interpreted by assuming that the impurity level affects the mode of solidification; the assumption that the metal solidifies as a smooth sheath surrounding the fibers is no longer consistent with infiltration kinetics.

6. These experimental results provide confirmation of the analysis of infiltration of metal matrix composites presented in Reference 1. Therefore, it is suggested that physical models for the infiltration process of three-dimensional shapes proposed in that work can be used with some degree of confidence in the analysis of more complex preform and mold geometries. Numerical techniques would be required for solution of most of these cases.

ACKNOWLEDGMENTS

REFERENCES

1. A. Mortensen, L.J. Masur, J.A. Cornie, and M.C. Flemings: *Metall. Trans. A*, 1989, vol. 20A, pp. 2535-47.
2. T.W. Lambe and R.V. Whitman: *Soil Mechanics*, S.I. Version, John Wiley & Sons, New York, NY, 1979, p. 281.
3. *Smithells Metals Reference Book*, 6th ed., Butterworth's, London, 1983, pp. 10-27.
4. A.E. Scheidegger: *The Physics of Flow through Porous Media*, 3rd ed., University of Toronto Press, Toronto, 1974, pp. 229-39.
5. M.C. Flemings, F.R. Mollard, E. Niyama, and H.F. Taylor: *Trans. Am. Foundrymen's Soc.*, 1962, vol. 70, pp. 1029-39.
6. J. Szekely and N.J. Themelis: *Rate Phenomena in Process Metallurgy*, John Wiley & Sons, New York, NY, 1971, p. 234.
7. S. Feliu, M.C. Flemings, and H.F. Taylor: *The British Foundryman*, 1960, vol. 43, pp. 413-25.
8. W.A. Tiller and J.W. Rutter: *Can. J. Phys.*, 1956, vol. 34, pp. 96-121.
9. A. Mortensen, J.A. Cornie, and M.C. Flemings: *Metall. Trans. A*, 1988, vol. 19A, pp. 709-21.
10. A. Mortensen, M.N. Gungor, J.A. Cornie, and M.C. Flemings: *J. Met.*, Mar. 1986, vol. 38, pp. 30-35.
11. L.J. Masur, A. Mortensen, J.A. Cornie, and M.C. Flemings: *Proc. 6th Int. Conf. Composite Materials (ICCMVI)*, F.L. Matthews, N.C.R. Buskell, J.M. Hodgkinson, and J. Morton, eds., Elsevier Applied Science, London, 1987, pp. 2.320-2.329.
12. G.W. Jackson and D.F. James: *Can. J. Chem. Eng.*, 1986, vol. 64, pp. 364-74.
13. *Smithells Metals Reference Book*, 6th ed., Butterworth's, London, 1983, pp. 8.1, 14.7, 14.10.
14. Imperial Chemical Industries SAFFIL Data Sheet, 1984.
15. *CRC Handbook of Chemistry and Physics*, 56th ed., 1975, p. F-78.
16. *CRC Handbook of Chemistry and Physics*, 56th ed., 1975, p. F-13.

Intrinsic toughness of interfaces between SiC coatings and substrates of Si or C fibre

A. S. ARGON, V. GUPTA, H. S. LANDIS*, J. A. CORNIE
Department of Mechanical Engineering, Massachusetts Institute of Technology, Cambridge, Massachusetts 02139, USA

The critical energy release rate for separation of SiC coatings from single crystal Si substrates or surfaces of carbon fibres, along their well-defined interfaces can be determined quite accurately from analysis of the spontaneous delamination of coatings under bi-axial stress, when such coatings exceed a critical thickness. Direct evaluations have been made of the specific work of delamination along the interface for SiC coatings from single crystal Si substrates, for both the case of coatings under bi-axial compression, as well as under bi-axial tension. The critical energy release rate for coatings in tension was $5.1 \, \text{J} \, \text{m}^2$, and that for coatings under compression was $5.9 \, \text{J} \, \text{m}^2$. The higher value of the latter is attributed to relative slippage between coating and substrate before lift-off of the former. Corresponding determination of the critical energy release rate for delamination of SiC coatings under bi-axial tension from surfaces of anisotropic Pitch-55 carbon fibres gave an answer of $5.5 \, \text{J} \, \text{m}^2$. These values compare very well with expectations from surface energies of strong solids.

1. Introduction

Relaxation of shear tractions across interfaces and eventual fracture along interfaces are key phenomena affecting the performance of composites reinforced with stiff or less deformable heterogeneities. Particularly, the possibility of controlled delamination along an interface of a reinforcing fibre or platelet before the stresses become too high in them to produce fracture has been recognized for some time as a desirable condition to achieve stable traction-displacement behaviour, and to increase overall toughness. In the composites field, key interface properties are usually measured by simple operational procedures, such as a single fibre pull-out test or a relatively macroscopic interlaminar shear test [1]. There have also been other more indirect techniques, such as the periodic cracking of a brittle fibre embedded in a matrix, plastically extended parallel to the fibre [2], or initiating local interface fractures through very local deformations produced by scratches [3] or hardness indenters [4]. In all of these cases, either only average information is obtained for a delamination process in which, in reality, a front of concentrated stresses and inelastic strain progagate along the interface, or the deformation is even more inhomogeneous and produces local interface separation through the production of a plastic misfit, which requires the solution of local elasto-plastic boundary value problems for the evaluation of the critical interface conditions. In all of these instances, the critical interface tractions that result in separation are not accurately determinable, whilst the fracture toughness of the interface itself is usually shrouded by much excess accompanying deformation, often even

absent in the failure process occurring in the proto-type composite.

In many interface fractures resulting in a clean cleavage-like separation, the critical intrinsic energy release rate G_{co} for separation of the interface (to be referred to here as the *intrinsic interface toughness*), is accompanied by a much larger term, G_p, reflecting the dissipative additional inelastic deformations in the layers immediately adjacent to the separating interface. Whilst this additional work, G_p, can dominate over the toughness G_{co}, the latter still scales the much larger inelastic dissipation work, so that any factor which affects G_{co} is directly reflected in the magnitude of G_p in an amplified manner [5, 6]. In an accompanying communication [6], we have proposed that the toughness of interfaces between protective coatings, such as SiC and fibres such as Pitch-55, can be tailored to initiate controlled delamination to protect the fibre from damage, and thereby act as mechanical fuses. There, we discussed an experimental technique based on the double cantilever beam to measure the overall specific fracture work $(G_{co} + G_p)$ of model composite interfaces. Here, we will discuss special techniques on how the much smaller, but key, intrinsic toughnesses G_{co} of interfaces can be measured, which must be governed to control composite properties.

2. Intrinsic mechanical properties of interfaces

2.1. Toughness of coating – substrate interfaces

During the study of vapour deposition of SiC coatings on various substrates, it became clear that the intrinsic toughness of an interface between a thin coating and

* Present address: General Telephone and Electronics Laboratory, Waltham, Massachusetts, USA.

a more massive substrate is directly measurable through the controlled delamination of the coating from the substrate during the relief of the residual stresses in the coating. Such delaminations and their potential for interface toughness measurement were recognized earlier by Evans and Hutchinson [7] for surface layers under residual compression. Here, we will demonstrate how this technique can be generalized and used for intrinsic interface toughness measurement in cases where the coating is either in residual tension or residual compression, on both model systems as well as on actual prototype interfaces between SiC coatings and Pitch-55 fibres. Before we present the details of such interface toughness determinations, it is necessary to discuss some essential details of the coating process which clarifies the origin of the residual stresses.

2.2. Vapour deposition of SiC coatings

Amorphous hydrogenated thin films of SiC were deposited on Pitch-55 fibres and on Si single crystal wafers using a plasma-assisted chemical vapour deposition (PACVD) process, the details of which are discussed [8]. It was observed that the processing parameters, especially the ion bombardment energy play a critical role in determining the unique physical and mechanical properties of the SiC deposits. These processing parameters could be adjusted to obtain the necessary toughness properties for the interfaces to optimize their desirable mechanical fuse action discussed in the accompanying communication [6].

Preliminary observations made on such PACVD coatings of SiC on Pitch-55 fibres indicated that in the as-deposited form, the coatings entrap a large concentration of hydrogen, which leaves the coatings under substantial residual compressive stress. When such coated fibres are incorporated into actual metal matrix composites, molten Al must be infiltrated among them at or around 660° C. This releases the entrapped hydrogen and results in poor adhesion of fibres to matrix and in unwanted porosity. To prevent this, coatings are given outgassing treatments at 600° C to remove the hydrogen. If this process is carried to completion in a period of about 30 min at 600° C, the coatings acquire a substantial level of residual tensile stress. Thus, the type and magnitude of the residual stress in coatings is an important element in the proper performance of composites and the factors which influence it are of direct interest.

2.3. Measurement of residual stresses in coatings

The levels of residual stress in SiC coatings applied by the PACVD process were measured through the change of curvature they produce in a 25.4 mm diameter standard Si single crystal wafer with (1 0 0) surfaces and 250 μm thickness when the coating is deposited on the wafer. An initially flat and homogeneous circular disc-shaped Si wafer acquires a convex shape with a coating in residual compression on its top surface, as depicted in Fig. 1b and a concave shape when the coating is in residual tension, as depicted in Fig. 1a. Elementary considerations give readily that the residual

(a) Coating in tension   (b) Coating in compression
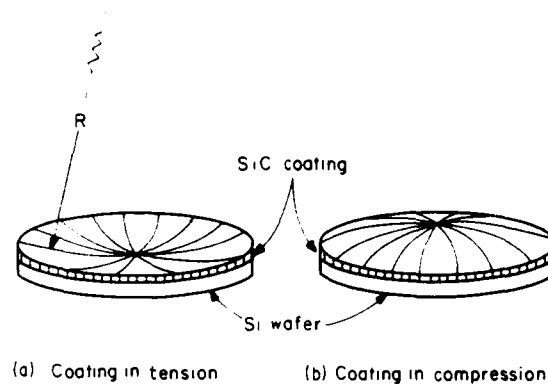
Figure 1 Change of curvature in a circular Si wafer with a thin coating of SiC in bi-axial tension (a), or in bi-axial compression (b).

bi-axial stress σ in the coating depends on the average in-plane elastic modulus E, and the Poisson's ratio v, of the substrate, the thickness of h of the substrate, the thickness t of the coating and, of course, the radius of curvature R of the substrate. Provided that the coating is very much thinner than the substrate, i.e. $t/h \ll 1$, this residual stress is (Appendix 1):

$$\sigma = \frac{E_s h^2}{6(1 - v_s)tR}.$$ (1)

The residual stress is tensile for a positive curvature (concave upward) and compressive for a negative curvature (convex upward) and is not influenced by the elastic properties of the coating. The thicknesses of the coatings were measured using a Dektak II profilometer by masking portions of the Si wafer with a layer of vacuum grease before the coating was applied. When the masked areas were cleaned with a series of rinses of toluene, acetone, methanol and finally ethanol, a sharp surface step emerged at the peripheries of the coated areas left on the wafer. The height of these steps was readily measured by the diamond stylus of the profilometer (under a contact pressure of 25 mg) to an accuracy of 2.5 to 10 nm. Typical coating thicknesses which were measured were between 0.1 to 1.0 μm and were quite reproducible through control of the deposition conditions. The curvatures of the circular disc-shaped wafers with the variously stressed coatings were also measured with the same profilometer. The deformation of the bowed discs during the
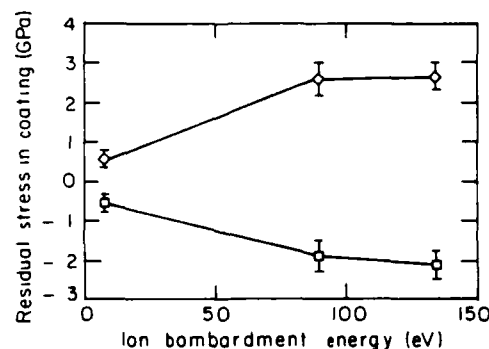
Figure 2 Measured residual stress in a PACVD SiC coating as a function of ion beam energy in both as-deposited hydrogenated coatings (compression) and coatings annealed at 600° C for 30 min (tension). (□) as deposited; (◇) annealed.

1208
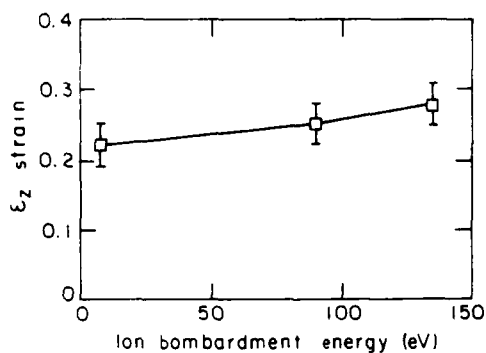
Figure 3 Thickness strain (negative) in hydrogenated coatings upon annealing at 600° C for 30 min.

measurements under the slight pressure of the stylus was negligible.

Since the maximum difference in the Young's modulus in the plane of the (1 0 0) wafer is only 16%, no important differences in curvature were detected in any orientation by the profilometer for coatings of uniform thickness. As shown in Fig. 2, the measured level of bi-axial compression in as-deposited films was found to be independent of the thickness of the deposit, but increased with increasing ion beam energy in the PACVD apparatus. Upon annealing of the as-deposited films for a period of 30 min at 600° C, copious hydrogen gas evolution from the films was observed, which resulted in substantial reduction of film thickness. This thickness reduction also increased with increasing ion beam energy, as shown in Fig. 3, indicating that more energetic ion beams result in more built-in material misfit in the films. Residual stress measurements on the wafers after the 30 min

outgassing treatment at 600° C indicated that in spite of the very large reduction of thickness, the coatings also contract bi-axially and acquire a large bi-axial residual tensile stress. As Fig. 2 shows, the measured bi-axial tensile stresses in the outgassed coatings increase with initial ion beam energy in a manner symmetrical to the compressive stress in the as-deposited coatings. Clearly, these residual stresses at around 2 GPa are exceedingly high (around 0.5% of the Young's modulus of the SiC coating).

2.4. Delamination of coatings from substrates
It was observed that coatings, whether under a compressive residual stress or a tensile residual stress, delaminated nearly spontaneously from the substrate when their thickness exceeded a well-defined critical value. In both cases, delamination was initiated from interface flaws which appeared to be of circular shape and were most probably a result of occasional local surface contamination. The form of delamination in compression differed significantly from that in tension. In the former case for coatings of thickness substantially $< 1 \mu$m, the initially circular delamination patches did not grow. However, when the coating thickness > 1 micron, slow delamination in quasi-static conditions could be observed, which initiated with outward buckling of the coating into one or two fundamental wave lengths, as can be seen in regions A of Fig. 4. These delamination patches grew by development of increasingly complex wrinkling patterns, but rapidly developed a regular delamination front, as shown for the blister at C and for the relatively large blisters in region B of Fig. 4. The blister then grew, often in neutral equilibrium, as residually stressed
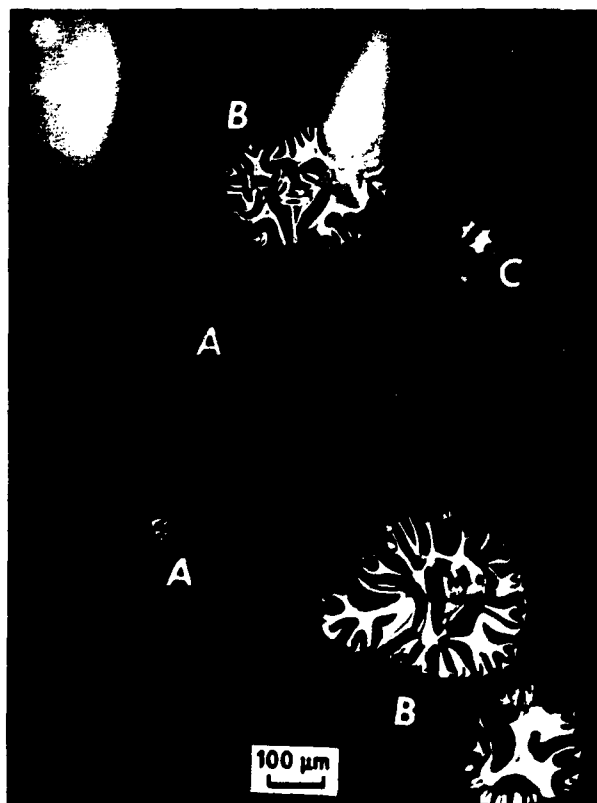
Figure 4 Blisters in the as-deposited coatings of SiC when the coatings are of a critical thickness: (A) blisters just large enough to buckle upwards. (B) large and growing blisters with well-established buckling fronts remaining self similar in growth. (C) smallest regular blister.

10 μm
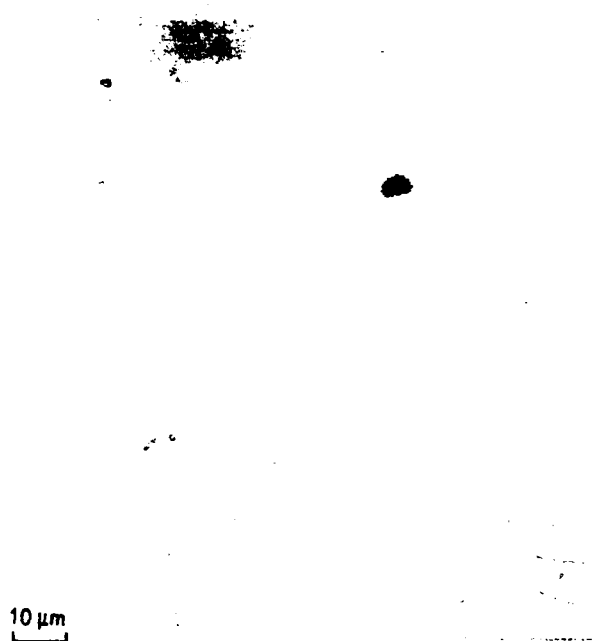
layers fed across the blister periphery into a circumferential strip with regularly spaced radial buckling ridges. In the further radial expansion of the delamination front, the principal buckling wave length in the circumferential strip immediately adjacent to the blister front remained unaltered, as can be discerned from Fig. 4 by comparing the smallest buckled blisters at A with the largest ones at B, as well as with the other intermediate sized blisters shown in the figure. Fig. 4 shows other circular patches, larger than those at A, in which no buckling has occurred. These are likely to be

Figure 6 Delamination of ribbons from substrate, following the through-the-thickness pre-cracking of coatings under bi-axial tension when the coating is thick enough for delamination to begin.

interface flaws, in which the adhesion of the coating to the substrate across the interface has not been fully impaired. No progressive delamination in such regions was observed.

In the outgassed samples, where the residual stress in the coating becomes bi-axial tension, the delamination shows quite different features with increasing thickness of the coating. Three different regimes of delamination have been identified in the coatings deposited under intermediate and high ion beam energies (75 to 150 eV), i.e., those in which the measured residual tensile stress was above 2 GPa. In relatively thin deposits (< 0.2 μm thick) only circular blisters were found by the entrapment of hydrogen gas evolving during the outgassing process. In some instances, particularly for blisters of large radius, the caps of the blisters were found detached from the sample. In samples where the thickness of the coating > 0.2 μm, blister detachment was followed by formation of cracks in the coatings emanating from the edge of the detached blister hole, as shown in Fig. 5. The initially radial cracks become parallel to one of two perpendicular directions once they are about one diameter away from the hole. The straight cracks away from the holes were found to be parallel to the two ⟨1 1 0⟩ directions in the plane of the Si wafer. These directions are the stiffest in the plane of the (1 0 0) wafer, and produce the largest misfit stress, across them in the coating.

In coatings that were thicker than 0.3 μm, delamination fronts spread out along the interface between the coating and the substrate bounded by the parallel pre-cracks in the coatings radiating away from the holes in the mutually orthogonal ⟨1 1 0⟩ directions, as shown in Fig. 6. In samples with even thicker coatings, the

Figure 7 Regular delamination patterns in the form of long ribbons in a coating of more than sufficient thickness for delamination to occur relatively rapidly

delaminated fraction of the interface steadily increases, as in the case of Fig. 7, until at thicknesses $> 0.75 \mu m$, almost the entire coating has delaminated from the substrate, as is shown in Fig. 8.
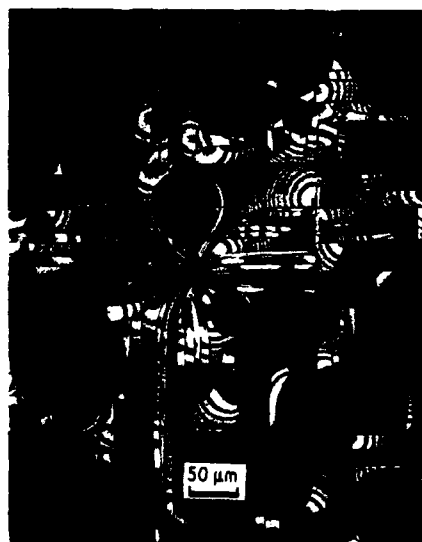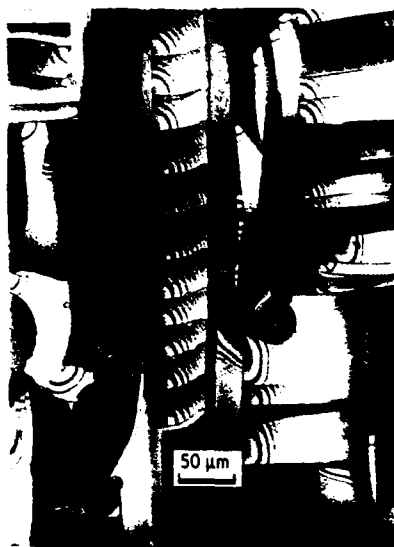
Clearly, the driving force for the delamination in both cases of compressive and tensile residual stresses is the elastic strain energy in the coating. As discussed in section 2.3, the residual stress in the coating depends only on the ion beam energy and the concentration of entrapped hydrogen gas in the coating, that results in the bi-axial material misfit, but not on the coating thickness. Furthermore, as is well known and as we will demonstrate, when the coating is very much thinner than the substrate, nearly all the elastic strain energy of misfit between coating and
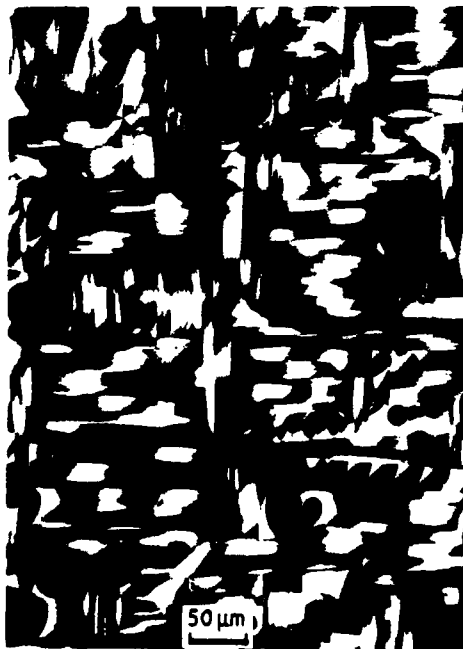
Figure 8 Nearly complete and spontaneous delamination in a coating of 0.8 μm thickness.

substrate is stored in the coating. Thus, as the coating thickness increases the driving force for delamination increases nearly linearly with thickness. In very thin coatings, the stored elastic strain energy is insufficient to provide the required elastic energy release rate necessary to form the interface delamination and no delamination was found to occur in either vacuum or in air. In an intermediate range of thickness, coatings could be preserved intact when stored in a vacuum, but delaminated in time when exposed to the laboratory environment.

With even thicker coatings, delamination occurred very rapidly both in vacuum and in air. Thus, it is expected that the delamination process along the interface is aided by humidity and is subject to static fatigue, well known in silica glasses [9]. This effect, however, will not be pursued further in this communication. We will demonstrate in section 2.6 that the observed delamination phenomenon described previously permits the rather accurate determination of the intrinsic interface toughness between a sharply delineated coating and its substrate, as is the case here between SiC and Si. In addition, the very regular and ribbon-like delamination in the case with tensile residual stresses also permits the determination of the Young's modulus of the amorphous SiC coatings. We discuss this below in the following section in preparation of the developments for interface toughness determination.

2.5. The Young's moduli of amorphous coatings in residual tension

In samples exhibiting the very regular ribbon-like delamination, it was observed that some of the loose ribbons remained perfectly flat upon delamination and in registry with the rectangular slots, in which they underwent the contractile strain resulting from the relief of the material misfit causing the residual stress. A particularly clear example of this is shown in Figs 9a and b. In Fig. 9a, the extent of the delamination ribbon is shown clearly by the bordering parallel cracks in the coating terminating ~ 140 μm below the horizontal crack that initiated the delamination. The termination of the grey region inside the ribbon at the point of termination of the parallel cracks indicates that the extent of delamination in the ribbon is well delineated. The upper portion of the same ribbon, given at a larger magnification in Fig. 9b, shows a well defined gap which represents the overall contraction of the ribbon upon delamination. Observations of this type, which could be made with equal precision at many places on the coating, permitted the accurate determination of the initial bi-axial misfit strain in the coating. The results of such measurements are shown in Fig. 10. They indicated that while the tensile misfit strain was quite large in coatings deposited at low ion beam energy, it was considerably smaller and independent of ion beam energy for energies $> 75 eV$.

Since the residual tensile stress in the coatings resulting from this misfit strain could be measured separately through the measurement of the curvature of the Si wafer before any cracks could develop, as discussed in section 2.3 above, the Young's modulus

Figure 10 Dependence of bi-axial misfit strain on ion beam energy in annealed coatings under bi-axial tension.

Figure 9 Misfit strain in coatings with bi-axial tensile stress is measurable by comparing the relaxed ribbon dimensions with those of the frame into which they initially fitted: (a) long delamination ribbon, (b) displacement of end of ribbon upon relief of misfit strain.

of the coatings could then be calculated from Equation (2):
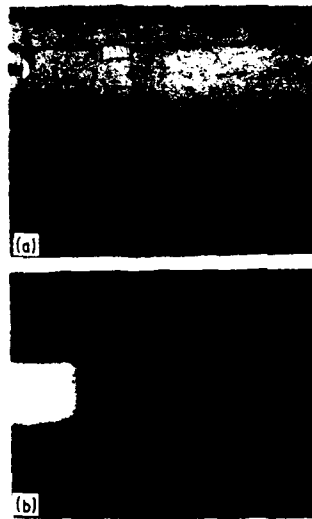
$$E = \frac{(1 - v)\sigma}{\varepsilon_m}.$$ (2)

giving the dependence of bi-axial residual stress σ on the bi-axial misfit strain ε_m provided Poisson's ratio v is known. For an assumed Poisson's ratio of 0.3, the calculated Young's moduli of SiC coatings are plotted in Fig. 11 as a function of the initial ion beam energy. The modulus goes from a rather low value of ca. 16 GPa to ~300 GPa for coatings deposited at energies > 75 eV. The determination of the Young's modulus of coatings having compressive misfit strain require a different procedure.

2.6. Work of separation of interfaces between substrates and coatings with tensile misfit

Although the stress intensity for delamination propagating along interfaces between a coating under tensile residual stress and a massive substrate of different elastic properties is complex and difficult to determine [10, 11], the associated and far more useful critical elastic energy release rate G_{co}, which we have referred to as the intrinsic interface toughness can be readily determined if the crack is constrained to remain in the interface. Thus, considering the elastic energy release from the coating and the substrate in response to a quasi-static extension of the interface crack, the desired energy release rate available from the system can be calculated readily by elementary methods from the theory of circular plates in bending (see Appendix 1) to be:

$$G_{co} = \frac{\varepsilon_m^2 E t}{(1 - v)}\left[1 - 4\left(\frac{1 - v}{1 - v}\right)\left(\frac{E}{E_s}\right)\left(\frac{t}{h}\right)\right]$$ (3)
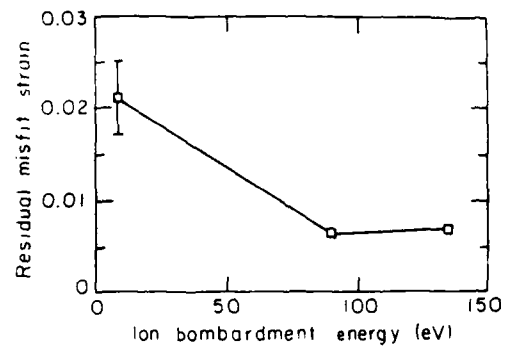
where the second term in brackets gives the fraction of the energy released from the substrate during delamination. In Equation (3), ε_m is the total misfit strain between coating and substrate E, v, E_s, v_s are the Young's moduli and Poisson's ratios of the coating and substrate, respectively, and t and h are the thicknesses of the coating and substrate. For the cases of interest here $t \ll h$, and the total misfit strain is nearly entirely accommodated in the coating. Since σ and E are separately measurable, the energy release rate is calculable uniquely, provided Poisson's ratio of the coating is known. Thus, as the thickness of the coating increases, the available energy from the system becomes larger. At a given threshold thickness t_c of the coating, when the available strain energy is sufficient to provide for the total specific work of delamination in air, such delamination will occur and establishes the intrinsic interface toughness G_{co} in air as:

$$G_{co} = \frac{\sigma^2(1 - v)t_c}{E}$$ (4)

Since the work of delamination in a vacuum will be substantially larger because of the absence of static fatigue, the critical delamination thickness in vacuum for comparable conditions should be proportionally larger. The observed critical thicknesses for delamination in air are shown in Fig. 12, while the calculated specific work of delamination is shown in Fig. 13. Both of these terms depend somewhat on the ion beam energy. The average value of this work of fracture for high ion beam energies is 5.1 J m².
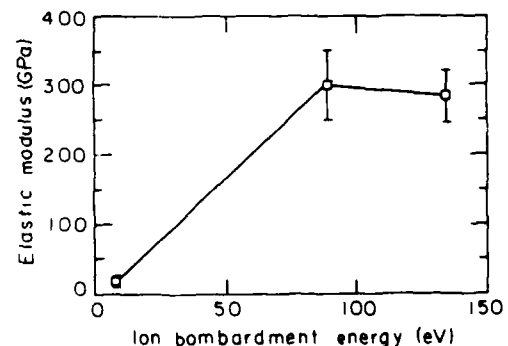
Figure 11 Dependence of Young's modulus on ion beam energy in annealed coatings under bi-axial tension

1212
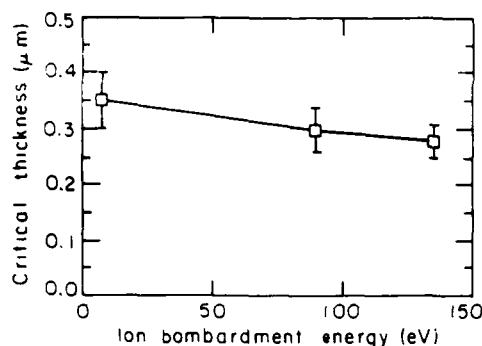
Figure 12 Dependence of critical coating thickness for delamination on ion beam energy in annealed coatings under bi-axial tension.

2.7. Work of separation of interfaces between substrates and coatings with compressive misfit

As is shown in Fig. 4 and Fig. 14a, once a sufficiently large portion of the coating is delaminated from the substrate at an initial flaw, it will undergo some release of elastic strain energy by buckling. After undergoing some early and complex buckling shapes, the delamination process settles down into a self-similar front, seen established for the blister at C in Fig. 4. In this delamination front, (Fig. 14a), bi-axially strained coating feeds in across the circumferential delamination front of the blister and undergoes nearly complete release of the radial stress. In Fig. 15, a blister is seen in Nomarski interference contrast microscopy. It reveals that the blister has an outer ring, which surrounds the buckling front at a radial distance of 5 to 7 μm ahead of it. The nature of this zone between the outer radius of this circular front and the average front of the buckled zone could not be clearly established. Since it could be seen, albeit more faintly, also in ordinary reflected light microscopy, it is attributed to an interference effect between the surface of the semi-transparent coating and the surface of the substrate. This is possible only in the presence of some cohesion impairment. We interpret it as such and propose that it results from relative radial slippage between coating and substrate. This should result then in a differential radial strain $\Delta \varepsilon_r$ and a differential thickness strain $\Delta \varepsilon$, given by:

$$\Delta \varepsilon_r = (1 + v)\varepsilon_m \tag{5}$$

Figure 14 Sketch of idealized circumferential buckling of a delaminating coating in a blister in an as-deposited hydrogenated coating under bi-axial compression: (a) perspective view. (b) buckled coating viewed in the radial direction.

$$\Delta \varepsilon_r = -\frac{v(1 + v)}{(1 - v)}\varepsilon_m \tag{6}$$

Thus, upon a critical radial displacement of the coating toward the interior of the outer front of the blister, cohesion across the interface is completely lost and the remaining tangential stress $\sigma_n (= (1 - v)\sigma)$ is relieved further by the regular circumferential buckling of the film to a wavelength l. The process of delamination with a self similar circumferential buckling mode becomes self-sustaining when for a radial increment of delamination, the difference between the initial elastic strain energy in the coating and that remaining in the regular post-buckling shape is sufficient to provide for the total work of delamination of the interface in this increment.

The key element of the delamination is the principal circumferential buckling wavelength l, which is directly measurable from micrographs. It relates to the initial tangential stress σ that governs it by the Euler buckling relation of thin strips, (see Appendix 2) as:

$$l = \pi t \sqrt{\frac{E}{3(1 - v^2)\sigma(1 - v)}} \tag{7}$$

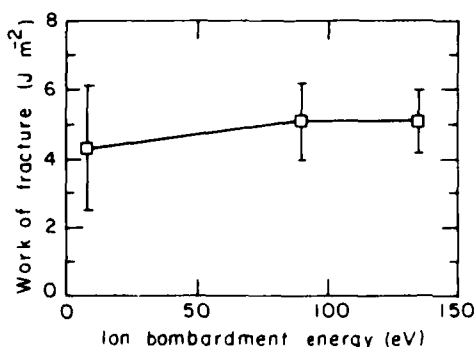*Figure 13* Dependence of critical energy release rate on ion beam energy in annealed coatings under bi-axial tension

Figure 15 A large buckled blister in a coating in the process of undergoing delamination, viewed with the Nomarski interference contrast mode of microscopy. The outer ring surrounding the buckled centre is the zone in which radial slippage occurs to relieve the radial stress.

1213

where E and v are the Young's modulus and the Poisson's ratio of the coating as before, and σ is the initial bi-axial compressive residual stress in the coating. We note parenthetically that since the initial residual stress σ is directly measurable from the curvature of the bent wafer and l from the micrographs, the Young's modulus of the hydrogenated coating in its as-deposited form in the PACVD process is calculable directly from Equation (7).

Since the substrate is massive and nearly inextensional, once strips of coating traverse across the delamination front their initial displacement misfit in the circumferential direction must be completely relieved by the circumferential buckling. This permits calculation of the steady-state post-buckling amplitude z_0, sketched in Fig. 14b as:

$$z_0 = \frac{t}{\sqrt{3(1 - v^2)}} \quad (8)$$

This then permits the calculation of the final elastic strain energy U unit area in the post-buckling shape of the tangential strip, just on the blister side of the delamination front to be (see Appendix 2):

$$U_2 = \frac{\pi^4 E t^5}{9(1 - v^2)^2 l^4} \quad (9)$$

Since the initial elastic strain energy U unit area in the bi-axially stressed coating in the same form of representation is:

$$U_1 = \frac{\pi^4 E t^5}{9(1 - v^2)^2(1 - v)l^4} \quad (10)$$

the elastic strain energy release rate G by this special form of tangential buckling, available to provide for the specific work of delamination of the interface becomes,

$$G = U_1 - U_2 = \frac{v\pi^4 E t^5}{9(1 - v^2)^2(1 - v)l^4} \quad (11)$$

Once again, at a critical thickness t_c, this energy becomes sufficient to provide for the quasi-static propagation of the delamination front in neutral equilibrium in air, establishing the intrinsic delamination toughness of the interface G_{c0} as:

$$G_{c0} = \frac{v\pi^4 E t_c^5}{9(1 - v^2)^2(1 - v)l^4} \quad (12)$$

As a specific case, we consider the delamination blisters of Fig. 4 of a coating deposited at high ion beam energy, expected to have a bi-axial compressive residual stress of $\sigma = 2\,GPa$, as shown in Fig. 2. The critical thickness of this coating was measured to be 1.1 μm, while the average post-buckling wave length l in the circumferential direction was measured to be 20 μm. Assuming as before a Poisson's ratio of 0.3, we calculate first the Young's modulus from Equation (7) to be 116 GPa. Finally, using this value, the critical energy release rate G_{c0} (specific work of delamination) is calculated from Equation (12) to be 5.9 J m². This is 14% higher than the average value calculated from the delamination of the coatings under tensile residual stress and well within the scatter of measurements of
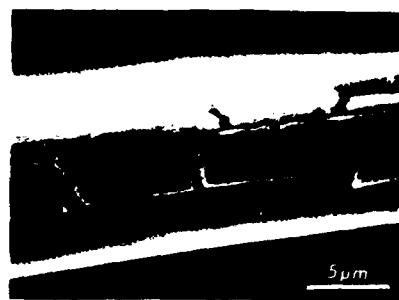
Figure 16 An SEM micrograph of a fragmented and delaminated annealed coating of critical thickness of SiC on a Pitch-55 fibre. The misfit strain is determinable from the gaps between the flakes

that experiment. Thus we conclude that the intrinsic toughness of the interface between SiC and Si is uninfluenced by the dehydrogenation that converts the coatings from having negative misfit to positive misfit.

3. Toughness of interfaces between SiC coatings and Pitch-55 fibres

The total work of delaminating a SiC coating from a Pitch-55 carbon fibre can also be determined by a technique very similar to that used for a system of Si wafer and SiC coating under tensile misfit strain. Fig. 16 shows a SEM micrograph of an outgassed fibre with a SiC coating of 0.33 μm thickness, initially deposited under conditions of low ion beam energy. The coating showed some small through the thickness cracks, but no delamination during several weeks of storage in air after the regular outgassing treatment of 30 min at 600°C. When it was examined again after several months of further storage in laboratory air with the usual level of relative humidity, in the vicinities of 60%, copious delamination of the SiC coating was found, as shown in Fig. 16. The initial bi-axial misfit strain ε_m between the coating and the fibre could be determined from the ratio of the average gap size between flakes to the dimensions of the flakes. With knowledge of this, and the assumption that the Young's modulus of the coating was the same as that for similar coatings on Si wafers deposited under the same ion beam conditions, the total energy release rate per unit area of interface could be determined from the sample.

An elementary misfit analysis presented in more detail in Appendix 3 gives the intrinsic interface toughness G_{c0} of the interface to be

$$G_{c0} = \frac{\varepsilon_m^2 E t_c}{2}\left(\frac{F}{H^2}\right) \quad (15)$$

where ε_m is the bi-axial misfit strain between coating and fibre, E the Young's modulus of the coating, t_c the thickness of the coating, and F and H are complicated functions of ratios of Young's moduli and the coating thickness to fibre radius given as:

$$F = 2(1 - v) + \left[(3 - 5v)\left(\frac{E}{E_s}\right)\right.$$

$$\left. + 6(1 - v)\left(\frac{E}{E_s}\right)\right]\left(\frac{t}{R}\right)$$

$$+ \left[(1 - 2v)\left(\frac{E}{E_i}\right)^2 + 4(1 - v)\left(\frac{E}{E_i}\right)^2 \right.$$

$$+ 2(4 - 7v)\left(\frac{E}{E_i}\right)\left(\frac{E}{E_i}\right)\left.\right]\left(\frac{t}{R}\right)$$

$$+ 2\left[(1 - 2v)\left(\frac{E}{E_i}\right)\left(\frac{E}{E_i}\right)\left(\frac{E}{E_i} + \frac{2E}{E_i}\right)\right]\left(\frac{t}{R}\right)^2 \tag{14}$$

$$H = (1 - v) + \left[(1 - 2v)\left(\frac{E}{E_i}\right)\right.$$

$$+ 2(1 - v)\left(\frac{E}{E_i}\right)\left.\right]\left(\frac{t}{R}\right)$$

$$+ 2(1 - 2v)\left(\frac{E}{E_i}\right)\left(\frac{E}{E_i}\right)\left(\frac{t}{R}\right)^2 \tag{15}$$

In Equations (14) and (15), $(E\,E_i)$ and $(E\,E_i)$ are the ratios of the Young's modulus of the coating to the transverse modulus of the fibre and the axial modulus of the fibre respectively; v is the Poisson's ratio of both the fibre and the coating (assumed to be the same) and $t\,R$ is the ratio of the thickness of the coating to the fibre radius.

As a specific example, we evaluate the critical energy release rate of the coating related to the case of Fig. 16 of a coating applied to a fibre under low ion beam conditions in the PACVD apparatus. This should result in a coating with Young's modulus of $E = 16\,\mathrm{GPa}$. The initial misfit strain, as measured from the gaps between the fragments of the coatings was found to be $\varepsilon_m = 2.7 \times 10^{-3}$ in the axial direction. Since the axial and radial Young's moduli E_a and E_r of the fibre were 385 GPa and 14 GPa respectively, $E\,E_r = 1.14$ and $E\,E_a = 4.16 \times 10^{-2}$. Furthermore, thickness of the SiC coating was $0.33\,\mu m$ and the fibre radius $5\,\mu m$, giving $t\,R = 6.6 \times 10^{-2}$. Thus, for assumed Poisson's ratios of 0.3, the values of the functions F and H can be calculated to be 1.53 and 0.734 respectively. This gives for the intrinsic interface toughness $G_{ic} = 5.5\,\mathrm{J\,m^{-2}}$, which is very close to the corresponding value measured for the delamination of the interface between SiC and a Si substrate.

4. Discussion

We have demonstrated that the spontaneous delamination phenomenon of thin misfitting coatings from their substrates can be used very effectively to determine the toughness of the interface between them. When the elastic strain energy per unit area due to misfit in the coating begins to exceed the intrinsic interface toughness, i.e., the specific work of separation of the coating from the substrate along the interface, the coating delaminates from the interface flaws. Since no instability is involved, the delamination, once started, can propagate under quasi-static conditions. Observations indicate that the critical thickness of a coating for delamination in vacuum is larger than the corresponding thickness for delamination in laboratory air with the usual levels of relative humidity. Thus, a static fatigue or stress

corrosion cracking effect appears to be present in the delamination. This aspect of the delamination still needs to be studied further.

When the coatings are in residual tension, the delamination occurs in a sequence of events, beginning with cracking of the coating in long parallel rows, followed by delamination of the ribbons of coating between the parallel cracks. Since the substrate Si wafers had $\{100\}$ plane surfaces in which the two orthogonal $\langle 110 \rangle$ directions are 16% stiffer than the $\langle 100 \rangle$ directions, the resulting larger misfit stresses in the $\langle 110 \rangle$ directions produce these orthogonal pre-cracks in the coatings. The misfit strain could be measured quite accurately from the relaxed size of the delaminated loose ribbon lying flat in the rectangular cavity of pre-cracking. This, together with the independent measurement of the residual tensile stress through the curvature of the sandwich of coating and substrate, permitted the determination of the elastic modulus of the coatings, which is essential for the determination of the energy release rate.

When the coatings are in residual compression in the hydrogenated state, immediately upon coating, the delamination exhibited rather unusual and hitherto unreported forms. When the coating exceeded the critical thickness required to provide the energy release rate, delamination occurred by the enlargement of blisters having self similar circumferential fronts, in which first, the radial stress appears to be released by translation of the coating relative to the substrate in the radial direction by an amount

$$\Delta u_r = \Delta r \Delta \varepsilon_r \tag{16}$$

where Δr is the width of the radial stress release zone of about $5\,\mu m$ thickness, shown in Fig. 15, and $\Delta\varepsilon_r$ is the radial strain difference between coating and substrate in this zone, given by Equation (5). For the typical case considered in section 2.7 above, where for a residual compressive stress of 2 GPa and a coating modulus of 116 GPa, giving an initial misfit strain of 1.21×10^{-2}, the relative displacement in the inner border of the radial stress release zone is obtained to be ca. 60 nm. The degree of reduction of shear traction in this radial zone is unknown. We consider it to be substantially reduced, but the coating is still attached to the substrate even after a relative slippage of hundreds of interatomic distances. If this interpretation is indeed correct, it must be concluded that for flat interfaces, there is little reduction of the cohesive strength of an interface due to large relative shear displacements across it. Although this is quite natural for flat grain boundaries, it is surprising for the interfaces between crystalline Si and amorphous SiC. Finally, however, as the relative displacements across this strip mount, small departures from flatness should produce normal stresses acting across the interface to produce full delamination and the quite regular circumferential buckling that is so readily apparent. It is interesting to note that the buckled blisters require only one independent measurement for the complete solution of the problem. Considering that the thickness of the coating and the wavelength of

the circumferential buckling are readily determinable by microscopy, only the residual compressive stress in the coating needs to be measured separately by measuring the radius of curvature of the sandwich of Si wafer and SiC coating. The Young's modulus of the coating can be determined from Equation (7), making the energy-release rate determinable uniquely from Equation (12).

The measurement of real interest for metal matrix composites, however, is the interface toughness between a SiC coating and a Pitch-55 carbon fibre, which could be determined by a similar analysis, provided the modulus of the coating depends only on the energy of the ion beam and not on any other property of the substrate or condition of deposition. This point needs to be verified further by additional experiments with planar surfaces of Pitch-55 type material in thin strips permitting residual stress measurement by curvature change. Meanwhile, in the absence of this information, the determined interface toughness of 5.5 J m² is, within experimental error, identical to that between SiC and Si. Furthermore, in the latter case, there was no effect on the interface toughness of substantial residual stresses in the plane of the coating, whether tensile or compressive. The overall average value of the interface toughness for the three experiments is 5.5 J m². It is interesting to compare this overall interface toughness with fundamental expectations. In the absence of any inelastic deformation the intrinsic toughness of an interface should be:

$$G_{io} = \chi_1 + \chi_B - \chi_{iB} \qquad (17)$$

where χ_1 and χ_B can stand for the surface free energies of SiC (A), and Si or C (B), and χ_{iB} for the interface energy of one or the other pair of Si SiC or C SiC. Considering more specifically the pair of Si SiC we note that $\chi_{Si} = 1.24$ J m² [12], while no information is available for χ_{SiC} and $\chi_{Si\,SiC}$. Taking χ_{SiC} as $\chi_{Si}(E_{SiC} E_{Si})$ as a zero order approximation, we obtain for $\chi_{SiC} = 2.53$ J m². Furthermore, guessing for $\chi_{Si\,SiC}$ a value of 1.00 J m², we obtain for $G_{io} = 2.77$ J m². This is only about one half of what was measured. Although it is possible that interface slippage can be responsible for the difference in energy, this does not fully account for the observations. The delamination remains on the interface and does not veer into the substrate or the coating, where the intrinsic toughness levels would appear to be lower. Thus, on the basis of the above estimates we must conclude that either our measurements still contain an error of a factor of 2 or that the effective fracture toughness of the two substrates are actually higher than twice their respective surface energies. It is likely that a combination of these two explanations is responsible for the observations.

Acknowledgements

1216
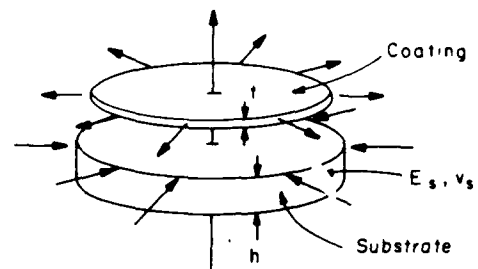
Figure 17 Misfit between coating and substrate in round disc

Appendix 1. Residual stress measurements in thin coatings and interface toughness from coatings in tension

Consider a thin circular wafer with (100) plane surfaces, having a thickness h, an in-plane isotropic modulus of E, and a Poisson's ratio of v. An amorphous isotropic coating of thickness t of SiC with modulus E and Poisson's ratio v is attached to the substrate. Due to the condition of deposition, the coating incorporates a bi-axial misfit strain ε_m, which we take to be tensile. This puts it under a state of residual tensile stress $\sigma_t (= \sigma_m)$, which is of interest. As all elastic misfit problems, the solution is obtained by detaching the coating from the substrate, as shown in Fig. 17 and considering the deformations necessary to attach them together again. Thus, considering the coating to be so thin as to be under a uniform stress σ, by equilibrium, the substrate would be subjected to a compressive stress $\sigma (t\,h)$ and a bending moment per unit length of periphery of:

$$M = (\sigma_t t)(t + h)\,2 \qquad (A1)$$

This bending moment produces a spherical curvature in the substrate wafer given by:

$$\frac{1}{R} = \frac{M}{D(1 + v)} \quad \therefore \quad D = \frac{E h^3}{12(1 - v)^2} \qquad (A2)$$

and a surface strain at the interface of:

$$\varepsilon_s = \frac{h}{2R} \qquad (A3)$$

The average compressive stress in the wafer produces an average radial compressive strain of:

$$\varepsilon_r = \frac{(1 - v)\sigma_t t}{hE} \qquad (A4)$$

The sum of all radial strains at the interface in the coating and the substrate must be equal to the initial misfit strain ε_m:

$$\varepsilon_m = \frac{(1 - v)\sigma_t}{E} + \frac{(1 - v)\sigma_t t}{hE} + \frac{t(t + h)h\sigma_t}{4D(1 + v)} \qquad (A5)$$

where the first term is the radial strain in the coating.

Thus:

$$\sigma = \left[(1 + \cdots) \frac{1}{E} - 4(1 + \cdots) \frac{1}{E}\left(\frac{t}{h}\right) \right.$$

$$\left. + \frac{3(1 - v)}{E}\left(\frac{t}{h}\right)^2 \right] \sigma, \qquad (A6)$$

On the other hand, from Equation (A2), the bi-axial stress σ in the coating is:

$$\sigma = \sigma_r = \frac{E h^2}{6t(1 - v)(t - h)R} \approx \frac{E h^2}{6t(1 - v)R}\left(1 - \frac{t}{h}\right) \qquad (A7)$$

Thus, through the measurement of the radius of curvature of the bent wafer, the residual stress in the coating is determinable from Equations (A7).

The elastic strain energy stored in the sandwich of stretched coating, and compressed and bent substrate is determinable in a straightforward way from the theory of thin circular plates. The strain energy in the coating is determinable from Equation (A7).

$$\frac{(1 - v)\sigma^2 t}{E} \qquad (A8)$$

In the substrate, the elastic strain energy is partly in bending, of a magnitude of:

$$\frac{3(1 - v)t^2}{E h}\left(1 + 2\left(\frac{t}{h}\right)\right)\sigma^2 \qquad (A9)$$

and partly in compression, of a magnitude of:

$$\frac{(1 - v)h}{E}\sigma^2\left(\frac{t}{h}\right)^2 \qquad (A10)$$

Thus, the total elastic strain energy, U is the sandwich is the sum of all three terms, which for quantities including second order terms is:

$$U = \frac{\varepsilon_m^2 E t}{(1 - v)}\left[1 - 4\frac{(1 - v)}{(1 - v)}\frac{E}{E}\left(\frac{t}{h}\right) \right] \qquad (A11)$$

where the total misfit strain is:

$$\varepsilon_m = \frac{\sigma(1 - v)}{E}\left[1 + 4\frac{(1 - v)}{(1 - v)}\frac{E}{E}\left(\frac{t}{h}\right) \right] \qquad (A12)$$

In Equation (A11), the second term in the brackets is the fraction of the energy contributed to the total through the bending and compression of the substrate. For $t/h \ll 1$, this contribution is clearly negligible. This gives for the elastic energy release rate in delamination

$$G_{co} = U \approx \frac{\varepsilon_m^2 E t}{(1 - v)} \qquad (A13)$$

which was used in the interpretation of results.

Appendix 2 Interface toughness from buckled blisters

As explained in the text, the coating inside a blister lifts off through the propagation of a circumferential buckling front with a characteristic circumferential wavelength of l.

Initially, under bi-axial compression, the stresses in the coating are:

$$\sigma = \sigma = \frac{E}{(1 - v)} \cdot \frac{l}{(1 - v)} \cdot \frac{l}{(1 - v)} \qquad (A14)$$

where E and v are properties of the coating, and ε_m the total misfit strain.

Upon traverse of the outer fringe of the blister through an element of coating, the radial stress is fully released; this reduces the tangential stress down to:

$$\sigma_u = E \qquad (A15)$$

As the element of coating traverses through the buckling front, it undergoes a characteristic Euler buckling that responds to the new level of tangential stress, and establishes a circumferential buckling wavelength of

$$l = \pi t \sqrt{\frac{E}{3(1 - v^2)\sigma_u}} \qquad (A16)$$

In the post-buckling shape, circumferential line elements in the coating become longer by an amount of $l\varepsilon_m$ over a wavelength of buckled coating

$$\Delta l = l\varepsilon_m = \frac{\pi^2 t^2}{3l(1 - v^2)} \qquad (A17)$$

This establishes the amplitude of buckling along a circumferential line element. Thus, in reference to Fig. 14b:

$$\Delta l = \int_0^l \left(\sqrt{1 + \left(\frac{dz}{d\phi}\right)^2} - 1 \right) d\phi = \frac{\pi^2 z_0^2}{l} \qquad (A18)$$

for a sinusoidal buckling shape:

$$z = z_0 \sin\left(\frac{2\pi\phi}{l}\right). \qquad (A19)$$

giving for the amplitude:

$$z_0 = \frac{t}{\sqrt{3(1 - v^2)}} \qquad (A20)$$

The final elastic strain energy in the post-buckling shape per unit width in the radial direction is:

$$U_f = \int_0^l \frac{M^2}{2EI}\,d\phi \quad \therefore M = EI\frac{d^2z}{d\phi^2} \qquad (A21)$$

giving

$$U_f = \frac{4EI\pi^4 z_0^2}{l^3} = \frac{\pi^4 E t^5}{9l^3(1 - v^2)^2} \qquad (A22)$$

The initial elastic strain energy in the bi-axially strained coating per strip of unit width and length l is:

$$U = \frac{(1 - v)\sigma_u^2 l t}{E} = \frac{\pi^2 E t^5}{9(1 - v^2)^2(1 - v)l^3} \qquad (A23)$$

where

$$\sigma_u = \frac{\pi^2 E t^2}{3(1 - v^2)(1 - v)l^2} \qquad (A24)$$

the initial tangential stress was substituted to obtain the final result. Finally, the energy release rate (per
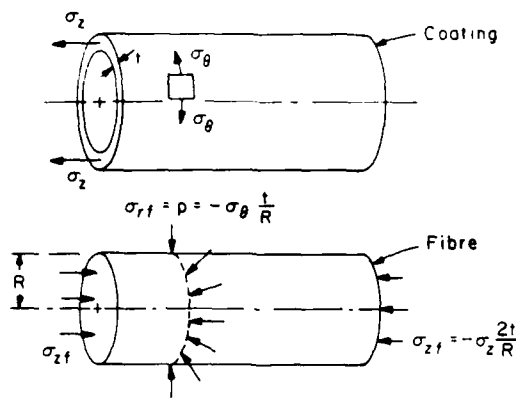
Figure 18 Misfit between coating and fibre.

unit area of coating) is obtained by subtraction of (A9) from (A10), and dividing by t:

$$G_{co} = \frac{v\pi^4 E t^5}{9(1 - v^2)^2(1 - v)t^4} \qquad (A25)$$

Appendix 3 Interface toughness of coatings on Pitch-55 fibres

Consider a Pitch-55 type fibre of radius R with an axial modulus E_z, a radial modulus E_r, and Poisson's ratio v with an isotropic coating of thickness t, with a modulus E and Poisson's ratio v, having a total tensile bi-axial misfit strain ε_m relative to the fibre. As indicated in Fig. 18, we take the unknown misfit stresses in the coating to be σ_θ and σ_z, and since $t/R \ll 1$ will be the case, neglect radial stresses. The corresponding *stresses in the fibre that result from equilibrium are* given in the figure.

By straightforward analysis, the strains in the coating and the fibre are:

$$\varepsilon_{\theta c} = \sigma_\theta E - v\sigma_z E \therefore \varepsilon_{zc} = \sigma_z E - v\sigma_\theta/E \qquad (A26)$$

$$\varepsilon_{\theta f} = -(1 - v)t\sigma_\theta E_r R + 2vt\sigma_z E_z R \qquad (A27)$$

$$\varepsilon_{zf} = 2vt\sigma_\theta E_r R - 2t\sigma_z E_z R \qquad (A28)$$

The matching of the fibre to the coating requires:

$$\varepsilon_{\theta c} - \varepsilon_{\theta f} = \varepsilon_m \therefore \varepsilon_{zc} - \varepsilon_{zf} = \varepsilon_m \qquad (A29)$$

This gives by elementary methods:

$$\sigma_\theta = \frac{\varepsilon_m E}{H}\left[1 + 2\left(\frac{E}{E_z}\right)\left(\frac{t}{R}\right)\right] \qquad (A30)$$

$$\sigma_z = \frac{\varepsilon_m E}{H}\left[1 + \frac{E}{E_r}\left(\frac{t}{R}\right)\right] \qquad (A31)$$

where

$$H = (1 - v) + \left[(1 - 2v)\frac{E}{E_r} + 2(1 - v)\frac{E}{E_z}\right]\left(\frac{t}{R}\right)$$

$$+ 2(1 - 2v)\left(\frac{E}{E_r}\right)\left(\frac{E}{E_z}\right)\left(\frac{t}{R}\right)^2 \qquad (A32)$$

The elastic strain energy in the fibre and coating per unit length are:

$$U_f = (\sigma_{\theta f}\varepsilon_{\theta f} + \sigma_{zf}\varepsilon_{zf} \, 2)\pi R^2 \qquad (A33)$$

$$U_c = (\sigma_\theta^2 + \sigma_z^2 - 2v\sigma_\theta\sigma_z)\pi Rt/E \qquad (A34)$$

By elementary methods, using the results above, the total elastic strain energy unit length of fibre can be readily obtained as:

$$U = \frac{\pi R t \varepsilon_m^2 E}{H^2} F \qquad (A35)$$

where

$$F = 2(1 - v) + \left[(3 - 5v)\left(\frac{E}{E_r}\right)\right]$$

$$+ 6(1 - v)\left(\frac{E}{E_z}\right)\right]\left(\frac{t}{R}\right) + \left[(1 - 2v)\left(\frac{E}{E_r}\right)^2\right.$$

$$+ 4(1 - v)\left(\frac{E}{E_z}\right)^2 + 2(4 - 7v)\left(\frac{E}{E_r}\right)\left(\frac{E}{E_z}\right)\right]\left(\frac{t}{R}\right)^2$$

$$+ 2(1 - 2v)\left(\frac{E}{E_r}\right)\left(\frac{E}{E_z}\right)\left(\frac{E}{E_r} + 2\left(\frac{E}{E_z}\right)\right)\left(\frac{t}{R}\right)^3 \qquad (A36)$$

This gives finally the energy release rate per unit area of interface, if delamination were to occur at the interface to completely unload both fibre and coating:

$$G_{co} = U \, 2\pi R = \frac{\varepsilon_m^2 EtF}{2H^2}. \qquad (A37)$$

This was used to evaluate the results of cracking and delamination of coatings from fibres.

References
1. K. L. MITTAL, in "Adhesion Measurement of Thin Films, Thick Films, and Bulk Coatings", edited by K. L. Mittal, ASTM STP 640 (American Society for Testing and Materials, Philadelphia, 1978) p. 5.
2. T. S. CHOW, C. A. LIU and R. C. PENWELL, *J. Polymer Sci.* **14** (1976) 1305.
3. J. AHN, K. L. MITTAL and R. H. McQUEEN, in "Adhesion Measurement of Thin Films, Thick Films, and Bulk Coatings", edited by K. L. Mittal, ASTM STP 640 (American Society for Testing and Materials, Philadelphia, 1978) p. 134.
4. S. S. CHIANG, D. B. MARSHALL and A. G. EVANS, in "Surfaces and Interfaces in Ceramic and Ceramic Metal Systems", edited by J. Pask and A. G. Evans (Plenum Press, New York, 1981) Vol. 14, p. 603.
5. J. R. RICE, in Proceedings of First International Conference on Fracture, Sendai, Japan, Vol. 1, edited by T. Yokobori, T. Kawasaki and J. L. Swedlow (The Japanese Society for Strength and Fracture of Materials, Sendai, Japan, 1965) p. 309.
6. V. GUPTA, A. S. ARGON and J. A. CORNIE, *J. Mater. Sci.* to be published.
7. A. G. EVANS and J. W. HUTCHINSON, *Intern. J. Solids and Structures* **20** (1984) 455.
8. H. S. LANDIS, Amorphous Hydrogenated Silicon Carbide by Plasma Enhanced Chemical Vapor Deposition for Metal Matrix Composite Applications, PhD thesis, Department of Materials Science and Engineering, M.I.T., Cambridge, Massachusetts, USA (1987).
9. S. W. FREIMAN, in "Glass Science and Technology", edited by D. R. Uhlmann and N. J. Kreidl (Academic Press, New York, 1980) Vol. 2, p. 21.
10. J. R. RICE and G. S. SIH, *J. Appl. Mech.* **32** (1965) 418.
11. M. COMNINOU, *ibid.* **44** (1977) 631.
12. J. J. GILMAN, *J. Appl. Phys.* **31** (1960) 2208.

Interfaces with controlled toughness as mechanical fuses to isolate fibres from damage

V. GUPTA, A. S. ARGON, J. A. CORNIE
Massachusetts Institute of Technology, Cambridge, MA 02139, USA

A source of inadequate performance of metal matrix composites has been the loss of strength due to the reaction layers between the fibre and the surrounding metal matrix. Here, we propose that the traditional diffusion barrier coatings on the fibre can be utilized to serve as mechanical fuses to isolate the impinging reaction zone cracks by interface delamination. Requirements on the interface strength and toughness for the specific tailoring of the fibre-coating interface are given. Special problems associated with the graphite–aluminium system are identified. A double cantilever beam experiment has been developed to measure the work of separation of thin coatings (0.1 to 0.3 μm) from bulk substrates. This test has been successfully applied to measure the work of fracture of the interface between a planar pyrolytic graphite substrate with the same chemistry and closely related microstructure as that of the 10 μm Pitch-55 graphite fibre and SiC coatings on them. A value of 60 J m^{-2} was obtained for the critical energy release rate for the PG–SiC interface. Additional measurements of energy release rates in thin layers of glue used to model the aluminium matrix and in PG itself, have given values which account for the high toughness of the main interfaces through the accompanying inelastic deformation work in the glue and the PG while the crack travels along the interface.

1. Introduction

Composite materials are tailored combinations of materials constructed to exploit the desirable properties of the component parts, while minimizing their weaknesses. The points of particular interest are the attainment of high stiffness and strength under both monotonic and cyclic loading, and other improvements in associated properties, such as desired levels of thermal expansion, damping capacity, resistance to environmental attack; all at minimum weight and acceptable cost.

Since composites combine a multiplicity of component material parts, they contain a high volume density of interfaces. The proper performance of composites in service puts extreme and often conflicting demands on these interfaces. In all of our considerations here, we will view composites as heterogeneous media having a relatively coarse microstructural scale, for which the elastic or plastic properties of the heterogeneities are governed by representative volume elements on a much finer scale. This implies that individual phases can be considered as continua, and that they interact with each other only through their interfaces. Thus, the consideration of choice is micromechanics, from which other macroproperties are assumed to be obtainable.

In normal service, interfaces are required to transmit full traction to assure that reinforcing phases such as fibres are fully load bearing to enhance the stiffness of the composite and to promote redundant deformations in a ductile matrix that can markedly increase the overall deformation resistance in it. The difference in the deformation resistance between fibres and matrix results in the development of stress concentrations across the interfaces. These concentrations can initiate cavitation and incipient fracture phenomena, which sooner or later become unstable and result in the premature termination of service by overall fracture. When such fracture is inevitable, it is desirable that as much dissipative work be associated with it as possible to result in tough and energy absorbing structures. Whether that toughness has the clear characteristics of being associated with the propagation of a single crack, and carrying conventional implications of fracture toughness, or is more diffuse and widespread over the entire structure is important in design, but of secondary consideration here. In all of these terminal phenomena, overall instability can be delayed by the systematic decoupling of the reinforcing elements that are on the verge of becoming critically stressed. To the extent that this can be successfully accomplished, subcritical damage can be spread over large volume elements, to result in a quasi-plastic response of the entire composite on the large scale. This desired systematic decoupling of the reinforcing fibres or other heterogeneities can be accomplished by controlling the terminal properties of interfaces, to have them act as mechanical fuses at appropriate predetermined levels of critical tractions. Such fine tuning or "tailoring" of interface properties is in principle possible, but requires a high degree of understanding of both the micromechanics of interfaces and the factors that affect their cohesive strength and overall fracture toughness.
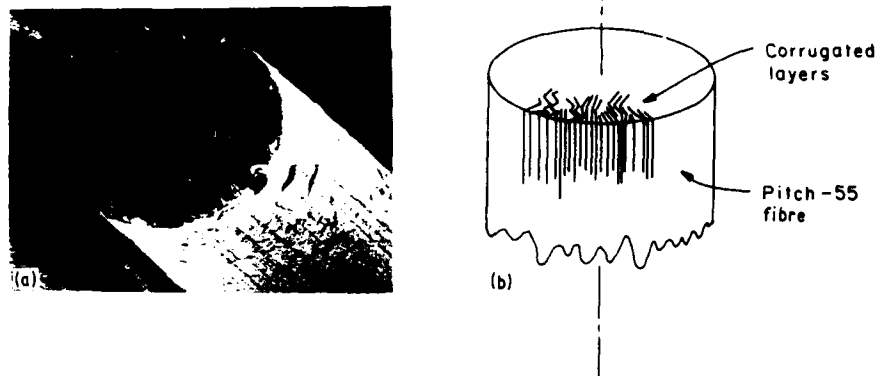
Figure 1 (a) Morphology of a 10 μm diameter Pitch-55 fibre revealed on a transverse fracture surface. (b) idealized fibre morphology as a set of corrugated parallel planes running parallel to the fibre axis. The fibre yield strength is expected to be low in longitudinal shear.

In metal matrix composites, where chemical reactions are also possible between the fibres and the metal matrix, forming reaction product layers along interfaces, the positive material misfit that often accompanies such reactions can initiate cracks in the fibres. To protect the fibres from such reaction damage, it is customary to provide them with non-reactive coatings. Since such coatings are introduced on the fibres under carefully controlled conditions, they can also offer the opportunity for tailoring the strength and toughness of their interfaces with the fibre, to achieve the mechanical fuse action discussed above to isolate damage. Such damage may have originated either among neighbouring fibres, and is transmitted across the matrix to the fibre, or it may have been generated by reaction products forming on the outer interface between the matrix and the protective coating.

We report here the results of a combined experimental and theoretical study on such key interfaces between the fibres and their protective coatings. It should be emphasized that the concept of using such interfaces as mechanical fuses is a very general one, and in principle, could be applied to any composite system. However, in this study, we focus on its application to metal matrix composites.

2. Interface mechanics
2.1. Metal matrix composite systems
For metal matrix composites, a large number of fibre and matrix systems have been explored. For structural applications at intermediate temperatures, the light metals of aluminium, titanium, and magnesium have been under primary consideration as matrices. While beryllium has most attractive properties in its own right, even without any reinforcement, it has not received much attention because of the difficulties associated with its processing. Of these, aluminium has been the matrix most widely considered. As a fcc metal, it exhibits exceptional ductility, and has a large number of well developed alloys with impressive properties. Of the various fibres used to reinforce aluminium, such as, boron, Al_2O_3, SiC, and carbon, the one that will be of primary interest to this investigation is the system of meso-phase pitch base fibres obtained from spun polymer precursors by a sequence of carbonization (1000 to 2000°C) or graphitization (2000 to 3000°C) treatments. Such pitch base fibres have axial fibre Young's moduli that range from 100 to 500 GPa with increasing molecular orientation, increasing long-period of crystalline domains, and increasing density (1.9 to 2.2 g cm^{-3}). In graphitized form, their tensile strengths are of the order of 2 GPa and relatively independent of their stiffness [1]. Fig. 1a gives the microstructure of a Pitch-55 (axial modulus 55×10^6 psi = 385 GPa) fibre, as viewed in a cross section across the axis. The fibres are typically of 10 μm in diameter, and are predominantly available in 500 to 10 000 filament yarns. The long axial grooves along the external cylindrical surface and the microstructure of the transverse section indicate that the principal morphology of the fibre is in the form of randomly corrugated and densely packed lamellae, oriented parallel to the fibre axis. This suggests an idealized fibre morphology, shown in Fig. 1b, with "planes of weakness" terminating roughly at right angles in the external surface. The consequence of this fibre morphology is a very low transverse modulus (14 GPa for the Pitch-55 fibre), and correspondingly low transverse tensile strength as well, estimated to be around 75 MPa on the basis of the usual correlation between modulus and strength. The particular morphology of the fibre also results in low shear stiffness and shear strength in longitudinal shear response to stresses σ_{zr} and $\sigma_{z\theta}$. Although this has no important consequence in the normal service of the composite; it can have important beneficial effects in the spreading of damage. Pitch-55 fibres have a density of 2.0 g cm^{-3}. The major advantage of Pitch-55 fibres is their chemical inertness due to high carbon content, high density, and high crystallinity. In the case of metal matrix composites for space structures, the attractions of this are the combination of properties which promote thermal dimensional stability, i.e., high Young's modulus, low and negative coefficient of thermal expansion, and high thermal conductivity.

The fibres are usually provided with a SiC coating of roughly 0.2 μm thickness, applied by a plasma-

assisted chemical vapour deposition process (PACVD) to isolate them from the matrix. The properties of such SiC coatings and means for their placement have been investigated by Landis *et al.*, and will be reported by them elsewhere [2]. Such coatings can be under substantial biaxial misfit stresses, dependent upon their structure and levels of entrapped hydrogen. These misfit stresses are compressive in the asdeposited form of the coatings, but can be relieved and even turned into tensile stresses upon thermal treatment. They are usually either maintained at zero or slightly compressive levels. The coatings are generally amorphous and have isotropic Young's moduli of about 300 GPa.

As discussed earlier, the overall mechanical properties of the composite are critically dependent on the properties of the key interfaces between the fibre and coating. The general mechanics, and in particular, the problems associated with Gr–Al systems involving the fibre-coating interactions are of a generic nature, and are potentially applicable to many other composite systems as well.

2.2. Fibre–matrix interaction

In composites, certain conflicting requirements must be satisfied by the interfaces between fibre and matrix. First, in a successful composite, it is important to decouple the fibre from the matrix during fracture, so as to prevent planar, low energy absorbing fractures. In fact, fibre fracture at random levels, followed by fibre pull out is desirable. This demands that the interfacial strength should not be too high. On the other hand, adequate interfacial strength is required to provide good transverse properties to the composite. Hence, in order to tailor the interfaces to desired properties, for them to act as mechanical fuses, it is necessary to bound the interface strength and toughness.

2.3. Transverse behaviour and lower bound to the interface strength

The interface strength is probed directly when the composite is stressed in the transverse direction. Hence, the interface strength should be high enough, so that transverse service stresses can be transferred to the fibre. The complexity of the stress field at the interfaces in a bundle of fibres has required that the transverse loading problem be approached chiefly with numerical techniques. The interfacial stresses developed under transverse tensile loading in composites of Pitch-55 fibres in pure aluminium matrices has been studied to a considerable extent by Zywicz [3]. Fig. 2, relating to his work, shows the geometry of a typical close-packed array of Pitch-55 fibres surrounded by an aluminium matrix. The relevant results for our consideration are given in Table I, where the stress concentrations in purely elastic and elastic-plastic behaviour of the aluminium matrix are summarized as a function of volume fraction of fibres for two different modes of tensile loading in the transverse direction, i.e., σ_{xx}, in the close-packed direction and σ_{yy}, mid-way between the close-packed directions.
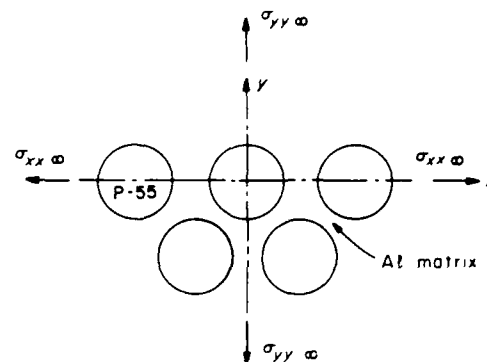
Figure 2 A hexagonal packing of aligned fibres in a metal matrix. The transverse plastic resistance differs in the *y* direction from that of the *x* direction.

The table shows that since the transverse modulus of the fibres is less than that of the aluminium, the fibres have actually a deficiency in load carrying capacity in purely elastic behaviour of fibres and matrix, resulting in a stress concentration in the matrix. This, however, is changed when the matrix can undergo plastic deformation, and can continue to load the fibres by plastic drag. Thus, for an equivalent plastic strain of even as small as 0.01, interface stress concentrations ranging from 1.14 to 2.40 appear on the cylindrical fibre surface, depending on fibre volume fraction and are governed by the equivalent plastic resistance of the matrix. Based upon what the equivalent plastic resistance of the matrix is, i.e., whether the matrix is pure aluminium or an aluminium alloy, the results in Table I provide a lower bound for the required interface strength, i.e.,

$$\sigma^*_{\text{I(lower bound)}} > k\sigma_{Tx}. \tag{1}$$

where k is the maximum stress concentration factor, and σ_{Tx} is the desired transverse strength of the composite.

2.4. Controlled delamination of coatings and upper bound to the interface strength

The nature of the interface cracking problem is of particular interest, as depicted in Fig. 3, which shows a schematic view of a crack in a SiC coating, terminating on the interface between the coating and the Pitch-55 fibre. The crack could alternatively have resulted from a matrix strain concentration produced by fractures in the surrounding fibres, a surface notch, or as shown in the figure, by a reaction product produced

TABLE I Transverse stress concentration for Pitch-55 fibres in an aluminium matrix*

Elastic stress concentration factors k			
V_f	0.4	0.6	0.8
$\sigma_{r_{max}}$ σ_{xx}	0.44	0.56	0.74
$\sigma_{r_{max}}$ σ_{yy}	0.60	0.82	1.04

Elastic–plastic ($\bar{\varepsilon} = 0.01$) stress concentration factors $k^\dagger$			
$\sigma_{r_{max}}$ $\bar{\sigma}$	1.14	1.55	2.40	(σ_{xx})
$\sigma_{r_{max}}$ $\bar{\sigma}$	1.14	1.14	1.33	(σ_{yy})

*Zywicz [3].
†$\bar{\sigma}$ is the Mises equivalent stress.
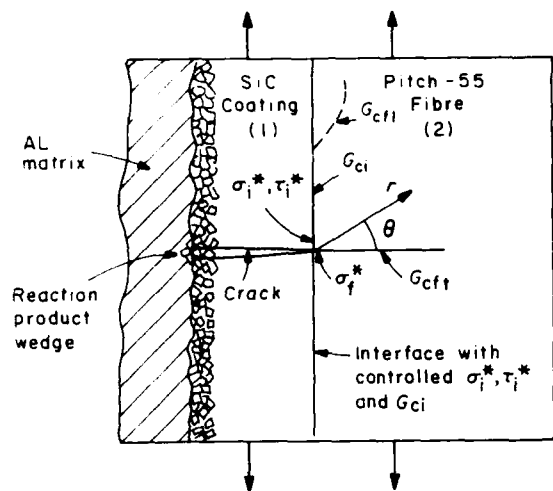
Figure 3 Sketch showing a potential form of mechanical probing of a fibre by a crack in the coating pried open by a misfit wedge produced by a coating-matrix reaction. To protect the fibre, controlled delamination at the interface is desired.

misfit wedge propping the flanks of the crack open. In all these cases, the principal concern is to protect the fibre from fracturing by penetration of the main crack into the fibre. This is to be achieved by decoupling the fibre at the interface between the coating and the fibre by producing either normal or shear failure at the interface using the concentrated interface stresses $\sigma_{rr}(\pi/2)$ or $\sigma_{r\theta}(\pi/2)$. The crack deflection process along the interface requires the following conditions to be satisfied by the stress field near the tip of the crack:

(a) The ratio of the fibre tensile strength σ_f^* to the interface cohesive strength σ_i^* should be greater than the ratio of the elastic crack tip stresses probing the plane across the fibre to the stress probing the interface to separate it in tension, i.e., the ratio of $\sigma_{\theta\theta}$ (at $\theta = 0$) to σ_{rr} (at $\theta = \pi/2$). This will lead to the delamination of the interface in tension, provided that such te ,ile stress can be achieved. This condition leads to ; , upper bound for the interface cohesive strength.

(b) The ratio of the fibre tensile strength to the interface shear strength τ_i^* should be greater than the ratio of $\sigma_{\theta\theta}$ (at $\theta = 0$) to $\sigma_{r\theta}$ at the interface (i.e., at $\theta = \pi/2$). This will ensure the separation of the interface in shear, and bounds the interface shear strength. When the ratio of the interface cohesive strength to the interface shear strength is less than the ratio of $\sigma_{\theta\theta} \cdot \sigma_{r\theta}$ at the interface, tensile separation will be preferred. Alternatively, for two possible directions of growth of the crack, i.e., across the fibre as opposed to along the interface, if the ratio of the energy release rate for growth across the fibre, to growth along the interface is less than the ratio of the work of fracture G_{cft} of transversely across the fibre to work of separation of the interface G_{ci}, then the fracture will follow the interface.

(c) The work of separation of the interface G_{ci} in any appropriate combination of separation across $\sigma_{\theta\theta}$ and $\sigma_{r\theta}$ along the interface should be less than the work of fracture G_{cft} of the fibre in the longitudinal direction for the crack to continue to travel along the interface.

Thus, it is of interest to determine the stress r and

σ_{rr} acting across the interface for a crack terminating at right angles on the interface, and establish the energy release rates that result when the crack branches into the interface to relieve these stresses. Furthermore, it is of interest to compare these energy release rates with the release rate for a crack going into the fibre.

Upon the initial successful diversion of the delamination crack along the interface, continued preferential delamination, as opposed to the crack entering the fibre, requires in addition, knowledge of the stress intensity associated with cracks lying on the interface, to satisfy the condition under (c) above.

Although knowledge of these stresses and energy release rates for cracks terminating on the interface or lying along the interface in these bi-material problems should be quite useful for purely elastic behaviour, it will be clear that additional considerations will be necessary to understand the interface behaviour, when plastic deformation in the fibre or in the matrix outside the coating accompanies the propagation of the delamination crack.

For isotropic bi-material media with a crack terminating at right angles on the interface, a very useful solution has been provided by Swenson and Rau [4] for the Mode I loading of such a crack. As these authors show, such cracks have a singularity which differs fundamentaly from that of cracks in homogeneous media, with singularity exponents either larger or smaller than 0.5, depending upon whether the crack is in the stiffer or the more compliant medium. The principal result of their analysis for the changes in stress intensification around the crack tip in a bi-material with semi-infinite extent is reproduced in Fig. 4 for plane strain, Mode I loading, as a function of the shear modulus ratio for a pair of materials having the same Poisson's ratios of 0.3. It is to be noted that, when the crack is in the stiffer medium, as would be the case of interest in this study with a crack in the SiC coating, the intensification of delaminating tensile stress $\sigma_{\theta\theta}(\pi/2)$ decreases, while the delaminating shear stress $\sigma_{r\theta}(\pi/2)$ increases with increasing shear modulus ratio μ_1/μ_2. In fact, when μ_1/μ_2 exceeds 10, the opening mode stress $\sigma_{\theta\theta}(\pi/2)$ across the interface drops to zero, while the magnitude of $\sigma_{r\theta}(\pi/2)$ has doubled. It is to be noted that in the case of interest here, the ratio between the modulus of the SiC and the axial modulus of the fibre is 1.17, and thus differs only marginally from the isotropic case. This implies that the ratio of the opening mode stress $\sigma_{\theta\theta}(\pi/2)$ across the interface to that in the fibre, i.e., $\sigma_{\theta\theta}(\pi/2)/\sigma_{\theta\theta}(0)$ is roughly 0.35 (as is the ratio $\sigma_{r\theta}(\pi/2)/\sigma_{\theta\theta}(0)$). We note, however, that the Pitch-55 fibre is intensely anisotropic and has a transverse modulus that is only 4% of the axial modulus. Thus, it can be expected that the fibre can readily flex in the transverse direction to release the transverse normal stress $\sigma_{\theta\theta}(\pi/2)$; perhaps completely. This indicates that decoupling the fibre from the coating may prove to be quite difficult, particularly if the interface has no means of responding plastically in shear. Clearly, a full solution of this bi-material problem with the anisotropy of the fibre fully taken into account is necessary.
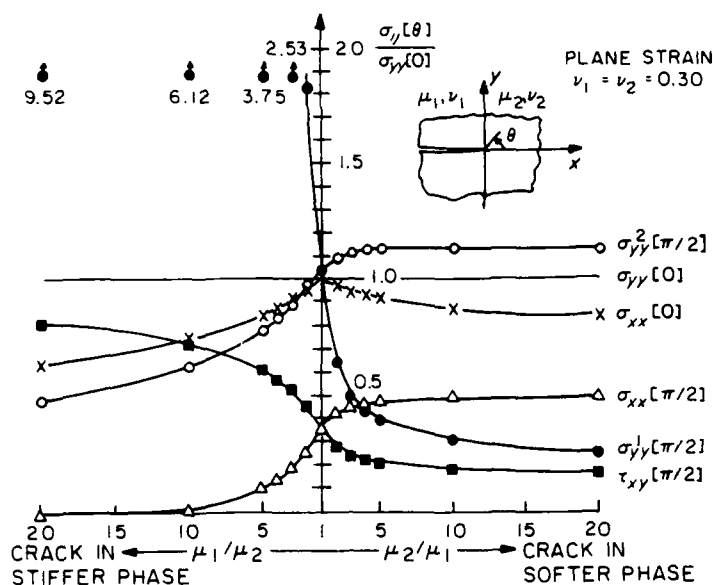
2034

Figure 4 The effect of shear modulus ratios on crack tip stresses for a crack in one medium ending perpendicularly on the interface, under plane strain loading (from Swenson and Rau [4], courtesy of Pergamon Press)

The associated bi-material problem of a crack lying in the interface of two elastic media that would be required to follow the path of the delamination crack has been considered by a number of investigators [5, 6], and reliable solutions are now available. Incorporation of plastic response of one or both of the two materials is also presently being explored [7]. Solutions of this type, however, will be necessary not only for the problem of continued propagation of delamination cracks, but also in the final interpretation of experimental measures of interface toughness, as we describe below.

3. Control and measurement of toughness of interfaces

3.1. General strategy

To use the interface between the fibre and its coating as a reliable mechanical fuse to protect the fibre from damage, requires both control of interface strength and toughness in processing, as well as reliable methods of measuring such strength and toughness. The process of producing high quality coatings of SiC on Pitch-55 fibres and other substrates with the desired properties of interfaces by plasma-assisted chemical vapour deposition has been discussed by Landis *et al.* [2]. The actual tailoring of the properties of these interfaces between coating and substrate to place them between the required lower and upper bounds discussed above, is still in progress, and will be reported in the future. Here, we will discuss primarily the procedures developed for the measurement of interface properties. Of these, the interface cohesive strength and shear strength are difficult to measure, since they will be very sensitive to imperfections and are not likely to be of great value in governing the mode of the delamination of the interface to protect the fibre. For this latter purpose, the work of separation across the interface will be of greater value. From fundamental considerations, it is expected that the actual fracture work of an interface could be dependent on the mixture of the modes that are forcing it apart, i.e., the mixture of the applied

Mode I and Mode II, to which the interface crack is subjected. However, since the nature of the singularity related to interface cracks separating two dissimilar materials with some plastic response, under any mode of loading is presently not available, we have concentrated attention on the development of reliable and reproducible methods of measurement of the fracture work of an interface by the most convenient means possible. In this quest, however, two limiting approaches have been distinguished. The interfaces which are of interest are expected to be relatively sharply defined along a steep material gradient between the coating and the fibre. The decohesion should then follow along a smooth surface, and have the appearance of a typical cleavage fracture. Thus, the actual intrinsic toughness G_{co}, i.e., the energy release rate necessary for the decohesion is expected to be in the range of only 3 to $5 \, J \, m^{-2}$, which is typical for a cleavage-like fracture in hard inorganic solid. On the other hand, the energy release rate G_c for an actual interface delamination in a composite is likely to be very much larger, because of the presence of accompanying inelastic deformation in the fibre and in the matrix surrounding the fibres. In such fractures where the eventual separation process is of a cleavage type, the additional energy release rate G_p that is associated with the surrounding inelastic dissipations will be scaled by the intrinsic toughness of the interface G_{co} [8], i.e.

$$G_c = G_{co} + G_p = G_{co}(1 + K) \qquad (2)$$

where

$$K = G_p/G_{co} \qquad (3)$$

Therefore, in spite of the much larger dissipations associated with delaminations of interfaces in composites, the fundamental interface property to be controlled is the interface toughness G_{co}, which is expected to be related directly to the reversible work of separation of the interface by the well known relation

$$G_{co} = \chi_{SiC} + \chi_C - \chi_i \qquad (4)$$

2035

where γ_{sc} and γ_c are the surface free energies of SiC and carbon and γ_i is the interface energy of SiC and carbon. Hence, in the control of the fuse-like action of the interface between coating and fibre, the reliable measurement of G_{ic} and how it may be affected by the processing conditions is of vital importance. Nevertheless, of almost equal importance is the measurement of the interface toughness in the actual composite itself.

In what follows, we will discuss the methods developed to measure the overall toughness G_c of the interface in systems very similar to those of the actual composite. The special methods necessary to measure the intrinsic toughness of the interface are discussed in a separate communication [9].

3.2. Measurement of critical energy release rates G_c of interfaces in composites

Measurement of interface fracture work is not a new problem in thin film and coating technology. The literature is replete with practical techniques for the measurement of some average properties of thin film or coating interfaces, recently reviewed by Mittal [10]. Here, we shall develop some special considerations and procedures necessary for the accurate measurement of interface fracture work.

The preferred test for the determination of interfacial properties should measure the state of adhesion directly using simple fundamental procedures of mechanics relatively free of artifacts relying on complex models, based on unverifiable assumptions. For example, in the scratch test [11], the process of scratch formation is complex and cannot be readily explained in terms of pure models. Furthermore, there is no preferential failure at the film–substrate interface, and the size and shape of the stylus can influence the mode of failure in an undeterminable manner. In the periodic cracking technique utilized by Chow, Liu and Penwell [12] and by Davutoglu and Askay [13], the complex state of stress at the edge of the film in contact with the substrate is not taken into account. More detailed stress field modelling, such as that carried out by Yang and Freund [14] using sliding stress intensity factors, are necessary. The indentation technique of Chiang, Marshall, and Evans [15], requiring the presence of the interface in the vicinity of a plastic zone, is also based on a fairly complicated model, and does not measure the interface work of fracture directly. On the other hand, the double cantilever beam test provides a simple

and direct method to measure the total adhesive fracture work, and has been used earlier by Gilman [16] quite effectively to measure the work of cleavage fracture of bulk materials. However, we have modified it to measure the work of fracture of thin film interfaces in systems structurally and chemically resembling those in the metal matrix composite itself.

4. Interfaces in model composite systems

4.1. The pyrolytic graphite SiC interface

An important prerequisite in the control of interface properties, such as tensile cohesive strength and the work of fracture, is that these properties should be measurable and the effectiveness of the crack deflection process should be demonstrable.

It would be best to perform experiments on actual interfaces in composites but is very difficult because of the very small diameter of the fibre (c.a. $10 \mu m$). Therefore, it is desirable that the experiments be performed on similar planar interfaces on a larger scale. This requires finding material available in bulk, having the same chemical and morphological characteristics as that of the fibre, which can then be adopted for macroscopic testing procedures.

For this purpose, pyrolytic graphite was chosen as a first approximation to the Pitch-55 fibres. Pyrolytic graphite (PG) is obtained by vapour phase deposition of pure carbon in a temperature range of 1900 to 2500°C. It has a density of 2.2 g cm^{-3}, which is approaching the theoretical density of graphitic carbon, i.e., 2.28 g cm^{-3}. It grows in polycrystalline, nearly planar spherulitic forms in a layer-like manner, but with a great degree of anisotropy in the growth direction across which it is very compliant and weak. Its isotropic Young's modulus in the growth planes is 28.5 GPa, and in the growth direction across the layers is only 7 GPa. Fig. 5 shows the basis of modelling of the fibre surface with PG. The surface of PG parallel to the c axis resembles the surface of the Pitch-55 fibre. It has the same chemistry as Pitch-55, a somewhat higher density, and rather similar anisotropic morphology that resembles that of the Pitch-55 fibres, as viewed in the circumferential direction. However, the analogy is quantitatively quite different. The Pitch-55 fibres have a stiff direction modulus 13.5 times that of PG, but a compliant direction modulus that is only 2 times that of PG. Thus, the fibres are both far more
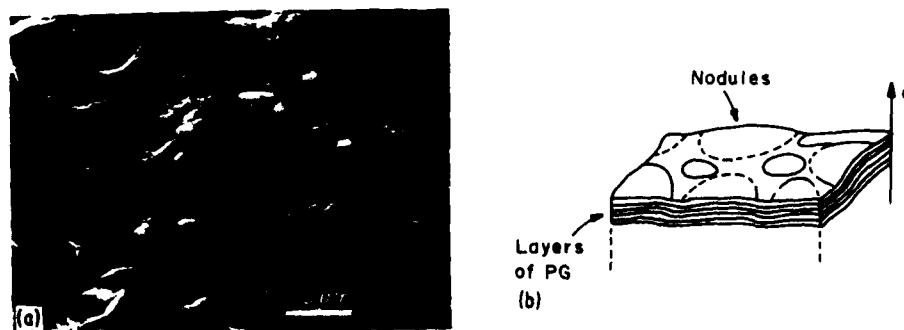

Figure 5 (a) Scanning electron micrograph of the morphology of a smooth layer plane perpendicular to the "c" axis in pyrolitic graphite showing nodules. (b) idealized rendering of the layer planes in PG.
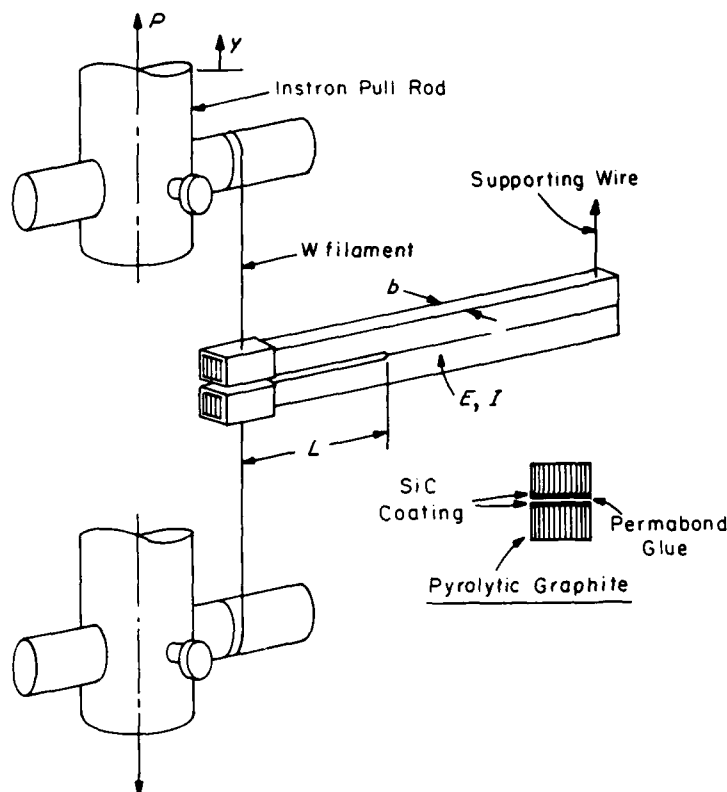
anisotropic and far stiffer than the PG. Nevertheless, experimentation of relative interface properties and general response of coating on carbon substrates are more readily investigated on PG than on individual Pitch-55 fibres, and permit simulation of coating-substrate interactions in bulk.

4.2. The double-cantilever beam experiment

This experiment was designed to measure the work of separation of a SiC coating of 0.1 to 0.5 μm thickness, deposited on a planar PG substrate. The specimen consists of strips of PG of 6.3 mm width, 3.2 mm thickness, and 150 mm length with the layer planes oriented perpendicular to the surface, as shown in Fig. 6. The surfaces of these strips with the given orientation of the planes were metalographically polished in a Syntron vibratory polisher. These polished surfaces were then coated with SiC of near stoichiometric composition, using a plasma-assisted chemical vapour deposition process. The coated strips were annealed at 600° C in a vacuum oven in order to relieve the residual stresses inside the films. Two of these coated strips were then bonded together using a very tough Permabond glue (ESP 109 and 110) over 75 mm of their length, so as to create an initial crack of 75 mm between the two strips. This laminate assembly was heated to 200° C to cure the glue. As will become clear below, the glue layer between the two strips has mechanical properties close to those of pure aluminium.

A schematic diagram of the test apparatus is shown in Fig. 6. The free ends of the graphite strips were connected to tightly fitting metal cages, which were then connected to the Instron machine load train, as shown in the figure. Load was transferred to the free ends of the cantilever strips by 200 μm thick tungsten

wire. This wire was made taut prior to the testing, using a pin and a set screw arrangement, shown in the figure. The double cantilevers were pulled apart with a cross-head speed of 0.5 mm min $^{-1}$. A plot of load against load point displacement was obtained. By initial selection of components, stable testing conditions were obtained, requiring that the unloading stiffness of the specimen is substantially less than the stiffness of the testing machine.

Treating the arms of the crack as cantilever beams and using simple beam theory, the bending force F at the time of the crack propagation can be related to the fracture work of the interface G_c, through the Griffith criterion by means of the formula

$$G_c = F^2 L^2 / EIb \qquad (5)$$

where L is the initial crack length, I the moment of inertia, b the width, and E the modulus of elasticity of the PG strips.

4.3. Double cantilever experimental results

Since the glue and the interface between the glue and the SiC coating is tougher than the interface between PG and SiC coating, the crack preferentially propagates along the latter interface. In some instances, the crack was found to initiate in the glue layer, but jumped to the less tough interface between SiC and PG. In such cases, the portion of the force–crack length curve pertaining to this type of propagation was not considered. Scanning electron microscopy, such as Fig. 7 of the fracture surface clearly shows the plane of the crack and the regions where the crack deviated from the interface, dipped inside the glue, and came back to the PG–SiC interface. Additional stereo-images of the fracture surface helped to establish better these
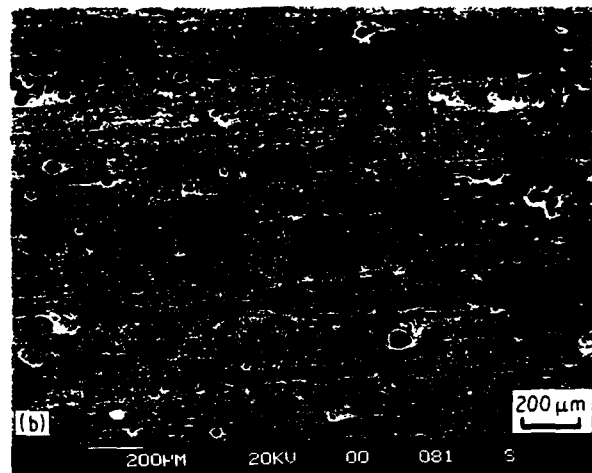
2037
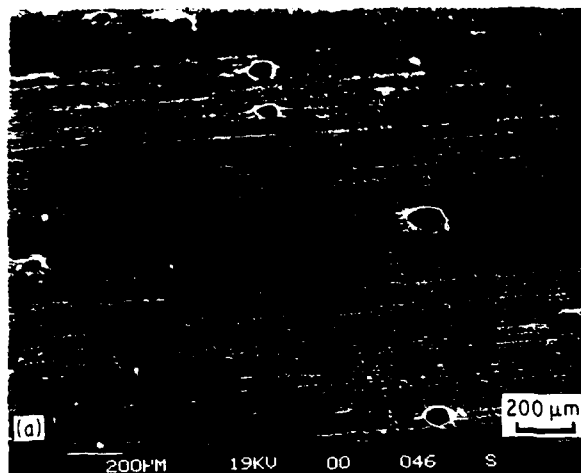
Figure 7 A SEM micrograph of the fracture surface between a SiC coating and a PG substrate having its surface parallel to the c axis of the PG. The crack propagation direction was parallel to the surface markings. (a) fracture surface viewed toward PG, (b) viewed toward SiC and glue layer

occasional deviations of the crack path. Fig. 8 shows an example of such a stereo pair. These observations established that the area of the fracture surface through the glue is only a small fraction (about 0.1) of the total fractured area along the interface. To make corrections for such deviations, to obtain the actual energy release rate along the PG SiC interface, it is necessary to measure the fracture toughness of a comparably thin glue layer. This was accomplished by bonding two high strength steel strips together with the same glue of the same thickness, and prying the strips apart in a double-cantilever beam experiment. This gave a critical energy release rate $G = 244 \text{J m}^{-2}$ for the glue layer, which was used in making the desired corrections.

Fig. 9 shows a typical load extension curve for a crack running along the planar interface between SiC and PG. Three drops in the curve indicate three stable jumps ahead of the crack. The average value of the fracture work G (the critical energy release rate) for the interface determined from such experiments, and incorporating corrections for deviations of the path through the glue gave a value of $60 \mp 6.85 \text{J m}^{-2}$.

The quoted value of the critical energy release rate G along the interface obtained from the double cantilever beam experiment is quite high when compared to an expected level of 3 to 5 J m^{-2}, based on interface energy for hard inorganic solids. These high values must incorporate additional inelastic dissipation when the crack runs along the interface between SiC and PG. Thus, the crack also probes the PG and the glue on both sides, and forces them to undergo plastic relaxation. It is known that the tensile yield strength of the glue is 64 MPa, while the intra-laminar shear strength of the PG is 52 MPa, which translates into a Mises tensile yield strength of 90 MPa. As a crude first approximation we consider the interface cracking to occur in a conventional homogeneous material under small scale yielding conditions, thus we can estimate the inelastically affected layer depth h of material near the fracture surfaces from the well known linear elastic fracture mechanics relation of

$$h = \frac{1}{2\pi} \frac{G}{(1 - v^2) Y \varepsilon} \qquad (6)$$

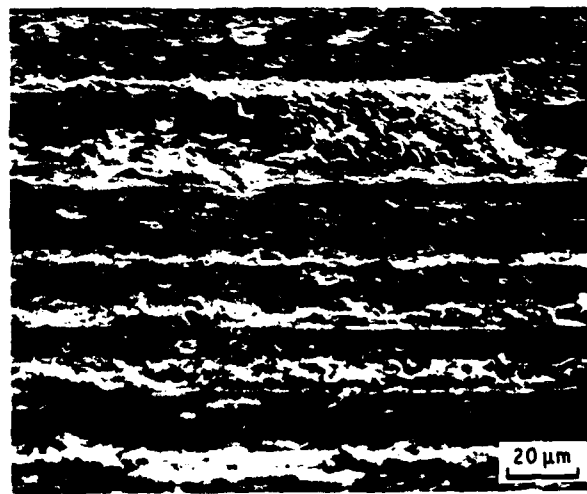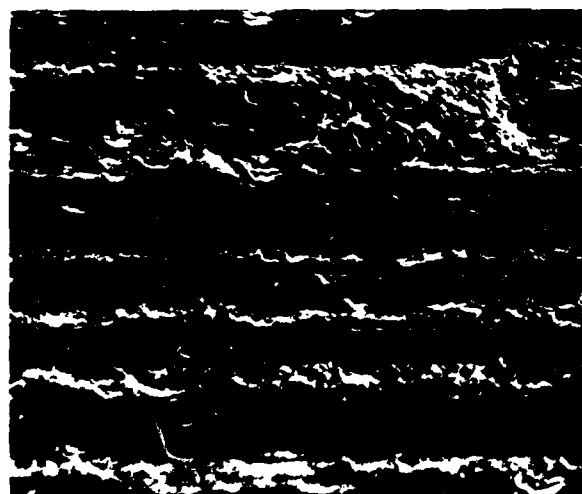where $G = 60 \text{J m}^{-2}$ is the measured work of fracture,

Figure 8 A stereo-pair of SEM micrographs of the fracture surface between a SiC coating and PG substrate. The crack propagation direction was parallel to the markings
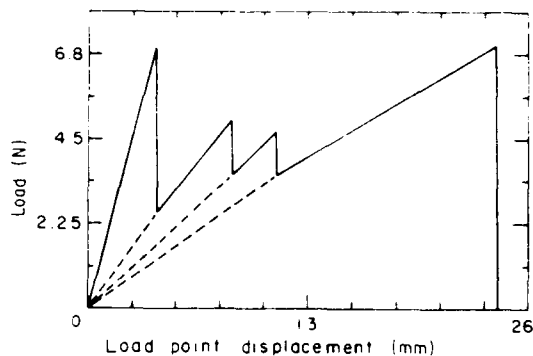
2038

Figure 9 A typical load (displacement) curve recorded in a double cantilever beam experiment, showing three quasi-stable extensions of the crack before it finally ran unstably. Calculated $G = 64$ J m⁻².

Figure 11 Sketch showing the three possible paths of a crack running parallel to an interface between SiC and PG

Y the tensile yield strength of the equivalent homogeneous material (take $Y = 71$ MPa as the average for the glue and the PG), ϵ_y is the elastic strain at yield (~ 0.02 for the glue and ~ 0.013 for the PG, take 0.015), and ν Poisson's ratio (≈ 0.3). Evaluation of this expression gives a layer depth of about $10\,\mu$m. As a similar first approximation, the plastic work per unit area of fracture, locked-up in the crack surface layers of thickness h, should be of the order of $2\beta Y\epsilon_y h$, where β, which is a constant of integration involving the plastic strain gradient into the surface in the deformed layers, is expected to be in the range of 2 to 3 (take 2.5). With the above choices for Y, ϵ_y and h, we estimate the dissipative component G_p of the energy release rate to be 53 J m⁻², or quite close to what was measured.

In order to gain more confidence in the above explanations, the critical energy release rate for fracture of the PG in the same orientation as in the above tests (i.e. with its weak planes oriented perpendicular to the fracture surface and running parallel to the crack growth direction) was also measured using the double cantilever beam experiment. The measured average value of $G_c = 136$ J m⁻² is about twice as large as the critical energy release rates measured for cracks propagating along the PG-SiC interface. Scanning electron microscopy of the fracture surfaces of the PG, as shown in Fig. 10, revealed the layered structure of PG and indicated considerable roughness in the forms of steps between lamina. The measured difference in

Figure 10 A SEM micrograph of the fracture surface in PG running transverse to the smooth layer planes

fracture work between the PG-SiC interface and the PG substrate itself is quite large, indicating that the preferred delamination path should indeed be along the PG-SiC interface, as was observed.

The toughness of the glue layer is worth more consideration. As mentioned above, the thin glue layer exhibited a critical energy release rate at fracture of the order of 244 J m⁻², and has a flow stress equal to 64 MPa. This is close to the yield strength of unalloyed aluminium, which, however, in bulk form, exhibits energy release rates in plane strain fracture nearly two orders of magnitude higher, with deformation zones being correspondingly thicker. However, when tested in confined spaces in thin layers, the fracture work of aluminium is likely to be no larger than what was found for the glue. This indicates that the glue in many respects acts as a good model for the aluminium matrix in the prototype composite. Therefore, we conclude that the double-cantilever beam experiment for the fracture work of the PG-SiC interface, being surrounded by a glue layer and a PG substrate, mimicks the behaviour of the actual composite of SiC coated Pitch-55 fibres in an unalloyed aluminium matrix. Table II summarizes all the measured overall critical energy release rates for fracturing along the interface and in the PG as well as in the glue along paths shown in Fig. 11. From these measurements of the properties of the PG-SiC interfaces, we conclude that the overall energy release rates G_c are indeed made up of an intrinsic component G_{co} and a much larger plastic dissipation component G_p in the surrounding material, as discussed in connection with Equation 2, but that G_{co} is still the fundamental quantity which sets the scale of the overall fracture work.

Therefore, for the purpose of monitoring the toughness properties of the tailored interface, it is essential to find reliable means of measuring the intrinsic toughness level G_{co} alone. In a separate communication [9], we discuss how this intrinsic work of separation of the coatings from its substrate can be measured under nearly ideal conditions of quasi-static delamination of residually stressed coatings under the driving force of the locked-in strain energy of the

TABLE II Total specific fracture work or critical energy release rate

Fracture path	G_c (J m⁻²)
PG-SiC interface	62.4 ± 6.8
Permabond glue	244
Pyrolytic graphite	136

coating, which produces only negligible inelastic effects in the substrate.

5. Discussion

The delamination, or fracture toughness of interfaces play a key role in all composites, but particularly so in metal matrix composites, where unwanted reactions between the matrix and the fibre can produce reaction products with material misfit that can severely damage the fibre. This was observed in elegant experiments of Metcalf [17] in the boron fibre aluminium system. Since during the production of composites processing histories that give proper wetting of fibres by the molten matrix and good adhesion are often in conflict with conditions to limit reaction damage, the proposal has been made here to separate functions of proper wetting from careful control of interface mechanical properties. This can be accomplished by tailoring the desired mechanical properties of the interface between the protective coating and the reinforcing fibre, while accepting some wetting related reaction damage between the matrix and the outer surface of the protective coating of the fibre. When properly controlled, this permits the pedigreed key interface between the coating and the fibre to act as a mechanical fuse to decouple the fibre from its surroundings by initiating delamination along it.

In this communication, we have discussed techniques for the measurement of the fracture work of such interfaces in simulated conditions of local environments representative of those in the composite itself. The double cantilever beam experiment that was used to measure the fracture work in symmetrical sandwiches of PG–SiC–glue–SiC–PG showed that very substantial inelastic deformation in the PG and the thin glue layer accompanies the apparent cleavage-like separation of the interface between the PG and the SiC. Since the PG has qualitatively similar inelastic behaviour and morphology to that of the Pitch-55 fibres, and the glue has similar yield behaviour to that of a pure aluminium matrix in the composite, the toughness measurements reflect behaviour that can be expected from the composite itself. Direct meaningful measurement of fracture work of interfaces between SiC coatings and Pitch-55 fibres in prototype composites have so far not been carried out.

Clearly, additional developments are necessary both for the measurement of intrinsic toughness of interfaces, and for the analysis of interface cracks with accompanying inelastic behaviour in the surrounding matrix and fibres. In a separate communication, we present new developments on the measurement of intrinsic toughness of interfaces [9].

References

1. R. BACON, in Proceedings of Conference on "Metal and Ceramic Matrix Composites Processing", vol. II, p. 23 (US Dept. of Defense, Columbus, Ohio 1984). (limited circulation)
2. H. S. LANDIS, V. GUPTA and J. A. CORNIE, to be published.
3. E. ZYWICZ, SM Thesis, Dept. Mech. Eng. M.I.T., Cambridge, Massachussets (1986).
4. D. O. SWENSON and C. A. RAU, Jr., *Int. J. Fracture Mech.* 6 (1970) 357.
5. J. R. RICE, *J. Appl. Mech.* 110 (1988) 98.
6. Z. SUO and J. W. HUTCHINSON, to be published.
7. C. F. SHIH and R. J. ASARO, *J. Appl. Mech.* submitted.
8. J. R. RICE, in "Proceedings of the First International Conference on Fracture", Vol. I edited by T. Yokobori, T. Kawasaki and J. L. Swedlow (The Japanese Society of Strength and Fracture of Materials, Sendai, Japan, 1965) p. 309.
9. A. S. ARGON, V. GUPTA, H. S. LANDIS and J. A. CORNIE, *J. Mater. Sci.* in press.
10. K. L. MITTAL, in "Adhesion Measurement of Thin Films, Thick Films, and Bulk Coatings", edited by K. L. Mittal, STP640 (American Society for Testing and Materials, Philadelphia, 1978) p. 5.
11. J. AHN, K. L. MITTAL and R. H. McQUEEN, ASTM STP 640 (American Society for Testing and Materials, Philadelphia, 1978) p. 134.
12. T. S. CHOU, C. A. LIU and R. C. PENNELL, *J. Polym. Sci.* 14 (1976) 1305.
13. A. DAVUTOGLU and A. I. AKSAY, in "Surfaces and Interfaces in Ceramic and Ceramic-Metal Systems", edited by J. Pask and A. G. Evans, "Materials Science Research, Vol. 14 (Plenum Press, New York, 1981) p. 641.
14. W. YANG and L. B. FREUND, "Shear Stress Concentration Near the Edge of a Thin Film Deposited on a Substrate", to be published.
15. S. S. CHIANG, D. B. MARSHALL and A. G. EVANS, in "Surfaces and Interfaces in Ceramic and Ceramic-Metal Systems", edited by J. Pask and A. G. Evans, "Materials Science Research" Vol. 14 (Plenum Press, New York, 1981) p. 603.
16. A. G. METCALFE, in "Composite Materials: Interfaces in Metal Matrix Composites", Vol. 1, edited by A. G. Metcalfe (Academic Press, New York, 1974) p. 1.

Intrinsic Toughness of Interfaces*

A. S. ARGON, V. GUPTA, H. S. LANDIS† and J. A. CORNIE

Massachusetts Institute of Technology, Cambridge, MA 02139 (U.S.A.)

Received June 1, 1988

Abstract

The intrinsic delamination toughness of interfaces between thin coatings of SiC and substrates of either silicon single crystals or Pitch-55 carbon fibers can be determined accurately in many instances from the analysis of the spontaneous delamination phenomenon of such coatings when they are under residual tension or compression. When the thickness of such stressed coatings reach a critical threshold value, the elastic strain energy of material misfit stored in the coating becomes a driving force for delamination of the coatings in quasi-static equilibrium, starting from defects on the interfaces or edges. The analysis of this phenomenon has given delamination toughnesses for interfaces between SiC coatings and silicon single crystals and Pitch-55 carbon fibers, which range from 5.1 J m^{-2} to 5.95 J m^{-2}. Although somewhat high, these toughness levels are well within a factor of 2 of the expected true intrinsic interface toughnesses for these systems in the absence of any accompanying inelastic deformation.

1. Introduction

Interfaces play a key role in the mechanical behavior of heterogeneous solids. They govern the mode and extent of traction transmission between phases of different elastic and inelastic properties. When local tractions across interfaces reach a critical magnitude, the parting of interfaces initiates microcracks or voids, which transform a previously continuous solid into a discontinuous one, and set the stage for final fracture.

In many aligned fiber reinforced composites, the structural service requirements are almost

entirely met by the volume fraction of stiff and strong, but brittle fibers. The matrix then acts merely to position the fibers in space and to impart to the composite a minimum level of transverse and longitudinal shear properties. It is now well recognized, however, that in such composites, the evolution of sub-critical damage under stress by correlated fiber fractures is governed by the mechanical coupling between fibers through the matrix. When the interfaces transmit all tractions fully and the coupling between fibers is too good, isolated fractures in fibers with small variability in strength tend to spread more readily to surrounding fibers, and hasten the development of a super-critical damage cluster (see e.g. Argon [1, 2]). In such instances, the strength of the composite is often less than the average strength of an unbonded bundle of similar fibers of equal length [2]. Thus, aligned fiber composites can often be made more damage tolerant, by decoupling fractured fibers from their neighbors through controlled delamination of their interfaces. Since many modern reinforcing carbon fibers are provided with protective coatings, it becomes possible to tailor the strength and toughness of the interfaces between coating and fiber to act as mechanical fuses to decouple broken fibers from their surroundings [3]. While considerable inelastic deformation in the surrounding matrix can accompany the propagation of a crack along the interface between the coating and the fiber, the intrinsic toughness of the interface sets the overall scale of the delamination toughness [4]. Thus, in controlling the performance of the composite through the control of the intrinsic interface toughness, it becomes of paramount importance to measure this toughness reliably.

Here, we will report briefly how, under special circumstances, the intrinsic toughness between certain coatings and substrates can be determined unambiguously through the analysis of the phen-

omenon of "spontaneous" delamination of coatings when they are residually stressed. A more detailed discussion of this phenomenon and its potential for interface toughness determination can be found elsewhere [5].

2. Residual stresses in vapor-deposited SiC coatings

Because of its hardness, low density, and chemical stability, SiC is the coating of choice for carbon fibers. It adheres well to carbon fibers and to most metal matrixes in which carbon fibers are used. In the cases to be discussed here, the SiC coatings have been applied by plasma-assist chemical vapor deposition to both Pitch carbon fiber and single crystal silicon substr with (100) plane surfaces. In all instances, the deposited coatings of SiC were found to entrap large quantities of hydrogen gas—apparently in solid solution, resulting in significant incorporation of positive misfit in the plane of the coating, and establishment of biaxial residual compressive stress. When the coatings were applied to thin disk-shaped silicon single-crystal wafers on only one side, the level of these residual compressive stresses could be readily measured from the changed curvature of the disk from the simple relation:

$$\sigma = \frac{E_s h^2}{6(1 - v_s) t R} \tag{1}$$

where R is the spherical radius of curvature of the substrate silicon disk, E_s and v_s its Young's modulus and Poisson's ratio respectively, h its thickness, and t the thickness of the coating. This established that the residual compressive stresses in the as-deposited coatings were independent of the thickness of the coating, but were dependent only on the ion beam energy of the coating process, as shown in Fig. 1. Upon annealing of the coatings at 600 °C for 30 min, the entrapped hydrogen gas producing the positive misfit could be readily driven out, resulting in substantial reduction in coating thickness, but also in the development of substantial net negative biaxial misfit in the plane of the coating and associated biaxial residual tensile stresses. These tensile stresses could be as readily measured by changing curvature of the substrate disks. They too were found to be independent of coating thickness, but dependent on ion beam energy in a symmetrically reverse way for the levels of compressive stress in
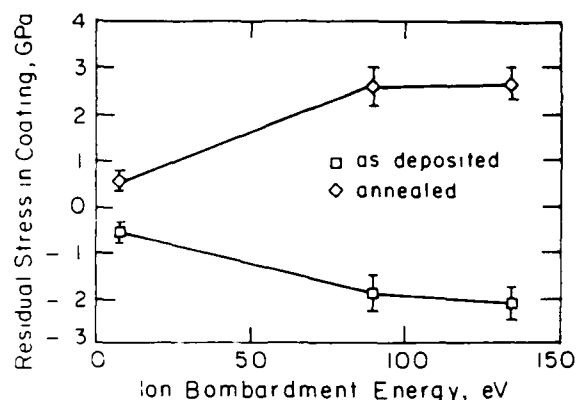
Fig. 1. Measured residual stresses in SiC coatings as a function of ion beam energy of the coating process for as-deposited coatings in compression and annealed coatings in tension.

the as-deposited coatings, as shown also in Fig. 1.

Coatings applied to Pitch-55 carbon fiber in the same manner were of uniform thickness around the circumference of the fiber. Therefore, they did not produce curvature changes in the fibers, but showed identical changes in thickness and other delamination behavior upon annealing, which are presented below. From this, it is concluded that they too were under very similar sets of residual stresses, which also depended only on ion beam energy and not on the thickness of the coatings.

3. "Spontaneous" delamination of coatings

3.1. Threshold thickness of delamination

While thin coatings of submicron thicknesses were found to remain intact on both silicon and carbon fiber substrates for indefinitely long times, regardless of the level or type of the residual stresses, thicker coatings were found to delaminate from the substrates when their thicknesses exceeded a critical level. The forms of this delamination were radically different for coatings in compression from coatings in tension. In both cases, it was observed that when the coatings exceeded a threshold thickness, different in tension from that in compression, the rate of delamination increased with increasing thickness of coatings when the samples were observed in labor.. 'v air. Beyond 'ertain thickness in exces- the threshold :ess, the delamination w .early spontanc non removal of the sample rom the coatir paratus, and happened .. .n in the appa .s in vacuum. This suggests an element of stress corrosion cracking

in the delamination process occurring in laboratory air that needs to be investigated further. This conjecture is reinforced by the observation that coatings with thicknesses in excess of the threshold thickness for long-term delamination in air could be maintained intact when samples were stored in vacuum.

3.2. Delamination of coatings with tensile misfit strain

In annealed coatings with tensile misfit strain on silicon single-crystal substrates, the first form of delamination was the formation of columnar cracks in the coatings, parallel to the ⟨110⟩ directions of the silicon single-crystal substrates. These directions are 16% stiffer in the ⟨100⟩ surface of the crystal than the corresponding orthogonal set of ⟨100⟩ directions. Upon cracking, coatings were found to delaminate in ribbon-shaped slabs, starting from the free ends where parallel coating cracks were arrested by a previously established

crack of the orthogonal family, as shown in Figs. 2(a) and 2(b). In Fig. 2(a), the extent of coating delamination from the substrate is clearly visible from the darker contrast of the ribbon relative to its surroundings. The delaminated ribbon continues to lie flat on the substrate, clearly because the residual tensile stress in it that has been relieved by the delamination was uniform across the thickness. Figure 2(b) shows a gap at the end of the ribbon between it and the upper portion of the surrounding coating which still remains attached to the substrate. These gaps, which could be readily measured at many places, when divided by the length of the delaminated ribbon furnished an independent measure of the initial material misfit strain ε_m. These misfit strains, when divided into the residual tensile stress in the coatings prior to the onset of the delamination, permitted the determination of the Young's modulus of the coatings from eqn. (2) below:

$$E = \frac{(1-v)\,\sigma}{\varepsilon_m} \tag{2}$$

where the Poisson's ratio of the coating was taken to be 0.3, since it could not be measured independently. These measurements established that the Young's modulus of the annealed SiC coatings depended uniquely on the initial ion beam energy of the coating process, as shown in Fig. 3, and indicated that the ion beam energy governs the structure of the coating.

The observations of a well-defined delamination threshold in the thickness of the coatings with tensile misfit indicate that this delamination is driven by the elastic strain energy stored in the coating. In such problems of biaxially stressed
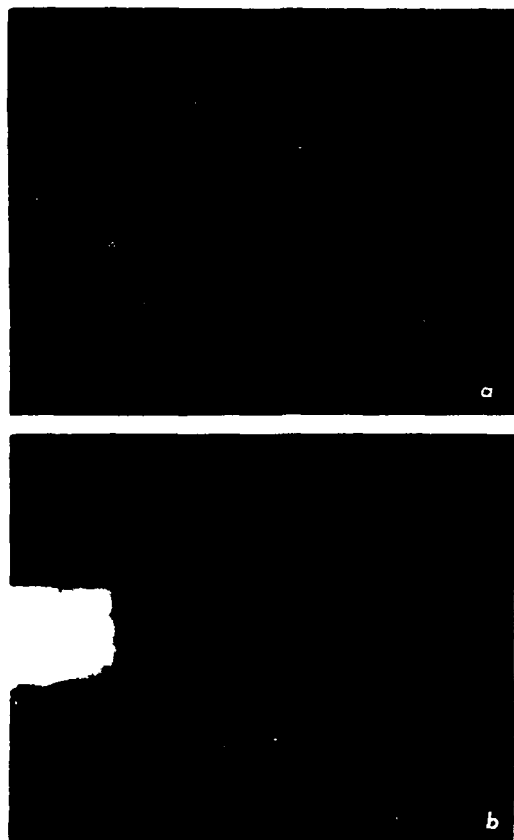
Fig. 2. Example of a ribbon-like delamination of an annealed SiC coating in tension. a low magnification view showing extent of delaminated ribbon. b high magnification view showing the initial tensile material misfit displacement
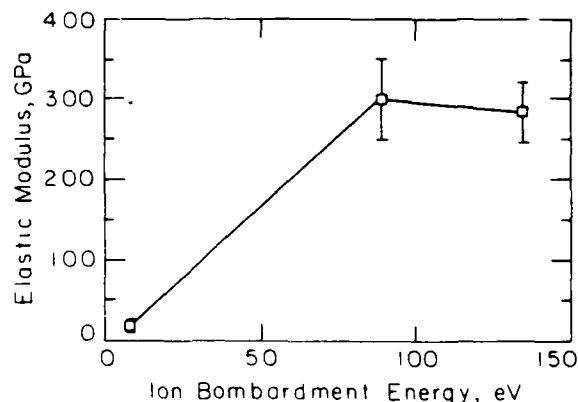
Fig. 3. Dependence of the Young's modulus of SiC coatings in tension, on the ion beam energy of the coating process.

thin coatings resulting from a constant material misfit independent of thickness, the elastic strain energy almost entirely resides in the coating, with only a negligible contribution coming from the much thicker substrate [5]. Thus, for very thin coatings where the elastic strain energy per unit area of the interface is less than the interface toughness, the coating remains intact indefinitely. As the thickness of the coating increases, the available elastic strain energy per unit area increases monotonically until it becomes equal to the intrinsic interface toughness* or energy release rate G_{co}. Then, the coating can delaminate away from the substrate under quasi-static conditions, starting from any interface defect or pre-crack. For thicknesses greater than the critical thickness, the delamination will occur with increasing velocity. From elementary considerations, the G_{co} is given by [5]:

$$G_{co} = \frac{\sigma^2 (1 - \nu) t_c}{E} = \frac{\varepsilon_m^2 E t_c}{1 - \nu}$$

(3)

where σ, ε_m, E, ν, t_c are respectively the biaxial residual tensile stress, the biaxial material misfit strain, the Young's modulus, the Poisson's ratio, and the critical (threshold) thickness—all of the coating. This interface toughness, determined from evaluation of eqn. (3) is shown in Fig. 4. It is found from here that the interface toughness is constant, within experimental error, and does not depend on ion beam energy. Its average value is 5.1 J m^{-2} for coatings in residual tension.

3.3. Delamination of coatings with compressive misfit strain

In the as-deposited coatings, the residual stress is compressive, as stated above. There too, the elastic strain energy stored in the coating per unit area of the interface increases monotonically with thickness of the coating. The delamination of these coatings from the substrate, however, exhibits a very different form. Here, it is found that coatings of considerably greater thickness remain attached intact to the substrate. When they reach a new critical thickness in the range of 1.0 μm, they are found to separate by forming a blister which lifts off the substrate in a regularly buckled form, as shown in Fig. 5, where a number of blis-

---

*Although unconventional, we use the word toughness here for G_{co} in preference to "specific work of fracture" or "critical energy release rate".
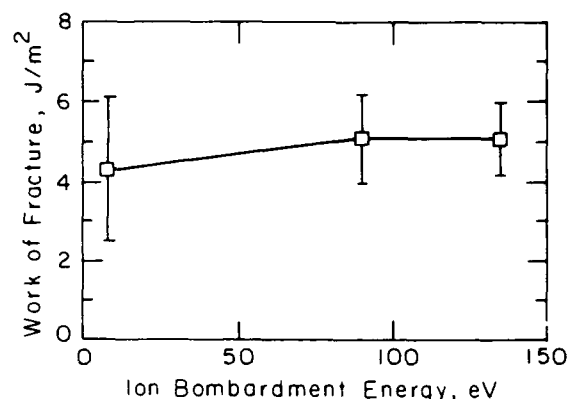
Fig. 4. Interface toughness as a function of ion beam energy.
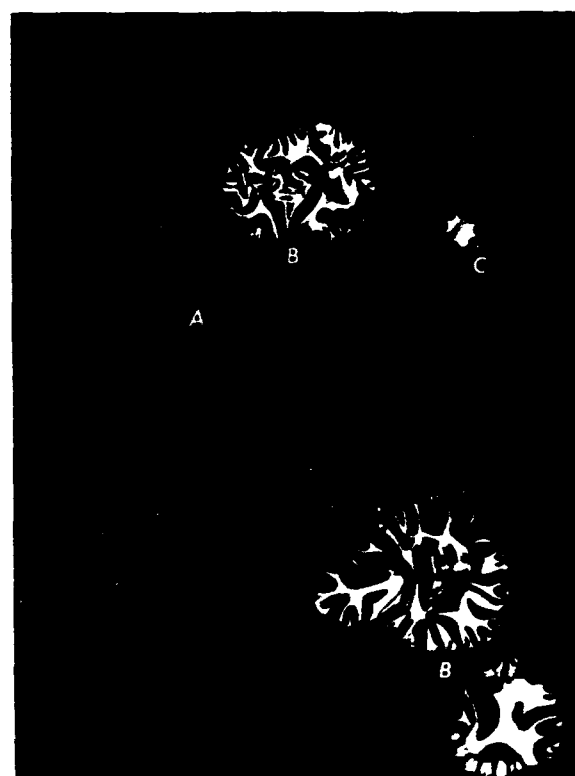
Fig. 5. Delamination blisters in an as-deposited coating in biaxial compression: A smallest size blister just lifting off, B large blisters growing radially outward, with a self-similar and regular circumferential buckled form, C a blister just large enough to assume a regular circumferential buckled shape.

ters in various stages of separation can be seen. At A, the blisters are just large enough to produce two half waves of vertical buckling; at B, large blisters have settled into a form where they propagate radially outward in quasi-static equilibrium, with a self-similar circumferential buckling

wavelength l. This wavelength appears just established in the small blister shown at (C).

Detailed observations of the growth of the blister with Nomarski interference contrast microscopy showed that, as the blister front advances radially outward, first the radial residual stress is relieved, apparently by slippage of the coating radially inward over a process zone of several μm in width. This is followed by the partial relief of the circumferential stress by the formation of the circumferential buckles, with a wavelength l, that depends on the initial biaxial residual compressive stress σ given by eqn. (4) below [5]:

$$ l = \pi t \left\{ \frac{E}{3(1 - v^2)\sigma(1 - v)} \right\}^{1/2} \tag{4} $$

In eqn. (4), E is the Young's modulus of the coating, t its thickness, and v its Poisson's ratio, which we take to be 0.3. Since the residual compressive stress can be measured independently from the curvature of the substrate attached to the coating, and l can be measured from the micrographs, such as Fig. 5, the modulus of the coating can be calculated from eqn. (4). When this was done for a coating of 1.1 μm threshold thickness with a measured l of 20 μm, and residual compressive stress of 2 GPa, E was found to be 116 GPa.

Further elementary analysis of the remaining elastic strain energy U_f per unit area of interface in the post buckled shape of the coating establishes it to be [5]

$$ U_f = \frac{\pi^4 E t^5}{9(1 - v^2)^2 l^4} \tag{5} $$

In the same fundamental parameters, the initial strain energy per unit area of interface prior to the formation of the blister is [5]

$$ U_i = \frac{\pi^4 E t^5}{9(1 - v^2)^2(1 - v)l^4} \tag{6} $$

At the critical threshold thickness t_c, the difference between (6) and (5) should provide for the intrinsic toughness G_{co} of the interface, i.e.

$$ G_{co} = \frac{v\pi^4 E t_c^5}{9(1 - v^2)^2(1 - v)l^4} \tag{7} $$

Evaluation of typical cases already referred to above gave an interface toughness of $G_{co} = 5.95$ J m^{-2}, which is 14% higher than the value determined for coatings in residual tension. This difference is attributed to the additional and possibly different dissipative work of slippage between coating and substrate during the release of the radial stress.

3.4. Delamination of coatings from Pitch-55 carbon fibers

The same phenomenon of spontaneous delamination of SiC coatings with tensile misfit was found also with Pitch-55 carbon fibers. When such fibers were coated followed by the annealing treatment of 600 °C for 30 min, the coatings were found to remain stable and intact, if their thicknesses were less than 0.33 μm for coatings deposited at low ion beam energy. When coatings with thickness slightly exceeding this thickness, having the above process history, were left in laboratory air with the usual relative humidity of 60% for several months, they were found to undergo copious and complete delamination by cracking and flaking, as shown in Fig. 6.

The initial biaxial misfit strain ε_m between coating and fiber could again be determined from the ratio of the average gap size between flakes to the average dimension of the flakes. With this information, and the assumption that the modulus of the coating in tension is given uniquely by Fig. 3 as being a function of only the ion beam energy, and the further assumption that the Poisson's ratio remained at 0.3, the threshold elastic strain energy of the coating per unit area could be calculated and equated to the fracture toughness of the interface to simply result in [5]

$$ G_{co} = \frac{\varepsilon_m^2 E t_c}{(1 - v)} \tag{8} $$

Fig. 6. Flakes of delaminated SiC coatings on a Pitch-55 carbon fiber.

82

for coating thickness to fiber radius ratio $t/R \ll 1$. Evaluation of these results for a typical case of coating with a modulus of 16 GPa threshold thickness of 0.33 μm, and misfit strain of 2.7×10^{-2} on a fiber with a radius of 5 μm, the interface toughness was calculated to be $G_{co} = 5.47$ J m^{-2}. This is quite close to the value of 5.1 J m^{-2} determined for the SiC/Si pair.

4. Discussion

The phenomenon of spontaneous delamination of coatings under residual stress from more massive substrates occurs quasi-statically when the elastic strain energy of misfit per unit area equals the intrinsic work of separation of the coating from the interface. The analysis of the conditions of such delamination provides the much-needed information on the intrinsic toughness of the interface. Apart from small differences between the various modes of separation presented above, the interface toughness is independent of the state of stress in the coating. Furthermore, the toughness of the interface between SiC coatings and carbon fibers is also quite close to that measured for the SiC/Si pair.

Observation of such delamination events is not new. Evans and Hutchinson [6] have reported somewhat similar delamination phenomena for interfaces between surface layers and substrates in microelectronics components, but observed a rather different process in the delamination of the layers in compression, which was less informative.

It must be noted that the simplicity of the phenomenon reported above results from the sharply defined nature of the interface, and the condition that the interface toughness is evidently less than the toughness of either the coating or the substrate, so that delamination cracks remain in the interface and do not wander into either of the two adjoining materials.

Under these conditions, furthermore, where the elastic strain energy of misfit is overwhelmingly stored in the coating, the nature of the stress intensity at the tip of the interface crack must be even more complicated than the complex stress intensities and their associated oscillatory tractions that have been extensively discussed in the literature [7-9]. Clearly, in this case, the singular component of the stress field ahead of the crack must be of very short range and, while it must be of opposite sign for the two cases of tensile and

compressive misfit, the delamination remains in the plane of the interface. A clue to this unique behavior is likely to be the Nomarski interference contrast microscopy observation noted above and discussed in more detail elsewhere [5] that, at least in the case of the enlargement of the compression blister, the delamination may be preceded by some slippage in the interface prior to lift off of the coating. This may also account for the magnitudes of the interface toughness that have been obtained. Thus, in the absence of any dissipative work, the toughness of an interface must be:

$$G_{co} = \chi_A + \chi_B - \chi_{AB} \qquad (9)$$

where χ_A and χ_B are the surface energies of components A and B, and χ_{AB} the specific interface energy between A and B. Although good measurements of either the surface energies of silicon, or SiC, or their interface energy do not exist, a simple estimate can show that the measured interface toughnesses are considerably in excess of what could be expected. The surface energy of silicon measured by Gilman [10] in cleavage experiments is 1.24 J m^{-2}. If the surface energy of SiC is estimated to be higher in the ratio of the Young's moduli of SiC to silicon, i.e. by a factor of 2.04, it should be 2.53 J m^{-2}. Thus, considering the interface energy between silicon and SiC to be somewhere of the order of 1 J m^{-2}, it is clear that the measured interface toughnesses are about twice what might be expected from eqn. (9). Clearly, therefore, even in this very short-range crack tip stress field, as it propagates along the interface, additional dissipative work is done which we propose is expended by some relative slippage between coating and substrate prior to lift off of the coating.

On the whole, however, we conclude that the interface toughnesses that we have reported are quite meaningful and that the spontaneous delamination experiment can be used within these limitations to monitor changes of interface adhesion in tailoring the properties of interfaces in the quest of making tougher and more damage-tolerant composites.

tional support also came from the MIT Consortium for Processing and Evaluation of Metal and Ceramic Matrix Composites.

References

1 A. S. Argon, in H. Herman ed., *Treatise on Materials Science and Technology*, Academic Press, New York, 1972, p. 79.

2 A. S. Argon, in L. J. Broutman and R. H. Krock eds., *Composite Materials: Fracture and Fatigue*, Academic Press, New York, 1974, p. 253.

3 V. Gupta, A. S. Argon and J. A. Cornie, *J. Mater. Sci.*, in the press.

4 J. R. Rice, in T. Yokobori et al. eds., *Proc. 1st Int. Conf. on Fracture*, Japanese Society for Strength and Fracture of Materials, Sendai, Japan, 1965, p. 309.

5 A. S. Argon, V. Gupta, H. S. Landis and J. A. Cornie, *J. Mater. Sci.*, in the press.

6 A. G. Evans and J. W. Hutchinson, *Int. J. Solids Struct.*, 20 1984 455.

7 J. R. Rice and G. S. Sih, *J. Appl. Mech.*, 32 1965 418.

8 M. Comninou, *J. Appl. Mech.*, 44 1977 631.

9 J. W. Hutchinson, M. E. Mear and J. R. Rice, *J. Appl. Mech.*, 54 1987 828.

10 J. J. Gilman, *J. Appl. Phys.*, 31 1960 2208.

Intrinsic toughness of interfaces between SiC coatings and substrates of Si and carbon fiber

A. S. Argon, V. Gupta, H. S. Landis*, and J. A. Cornie

Massachusetts Institute of Technology
Cambridge, MA 02139, U.S.A.
* Now with GTE Laboratories, Waltham, MA, U.S.A.

ABSTRACT

When properly tailored, the interfaces between reinforcing fibers in composites and their protective coatings can act as mechanical fuses to decouple damaged fibers from their surroundings and prevent low energy absorbing early fractures. The intrinsic fracture toughness of these interfaces, which is the key element that must be optimized to achieve decoupling is often difficult to measure.

Here, we report on how this intrinsic toughness can be measured through the analysis of the spontaneous delamination phenomenon that occurs when coatings are under a residual stress and the elastic strain energy of material misfit stored in the coatings per unit surface exceeds the intrinsic interface toughness. Through such analysis the intrinsic delamination toughness of interfaces between SiC coatings and substrates of Si single crystals and Pitch-55 type carbon fibers has been found to be on the average 5.5 J/m^2. This value is within a factor of 2 of the expected intrinsic toughness. The slight excess is attributed to slippage between the coating and the substrates during the delamination lift-off of the coating.

1. INTRODUCTION

In many aligned fiber reinforced composites, the structural service requirements are almost entirely met by the volume fraction of stiff and strong, but brittle fibers. The matrix then acts merely to position the fibers in space and to impart to the composite a minimum level of transverse tensile and longitudinal shear properties. It is now well recognized, however, that in such composites, the evolution of sub-critical damage under stress by correlated fiber fractures is governed by the mechanical coupling between fibers through the matrix. When the interfaces transmit all tractions fully and the coupling between fibers is too good, isolated fractures in fibers with small variability in strength tend to spread more readily to surrounding fibers, and hasten

the development of a super-critical damage cluster (see, e.g., Argon, 1972; 1974). In such instances, the strength of the composite is often less than the average strength of an unbonded bundle of similar fibers of equal length (Argon, 1974). These composites can often be made more damage tolerant, by decoupling fractured fibers from their neighbors through controlled delamination of their interfaces. Since most reinforcing carbon fibers are provided with protective coatings, it becomes possible to tailor the strength and toughness of the interfaces between coating and fiber to act as mechanical fuses to decouple broken fibers from their surroundings (Gupta, et. al. 1988). While considerable inelastic deformation in the surrounding matrix can accompany the propagation of a crack along the interface between the coating and the fiber in a composite, the intrinsic toughness of the interface sets the overall scale of the delamination toughness (Rice, 1965). Thus, in controlling the performance of the composite through the control of the intrinsic interface toughness, it is essential to be able to reliably measure this toughness.

Here we discuss how under special circumstances, the intrinsic toughness between certain coatings and substrates can be unambiguously determined through the analysis of the phenomenon of "spontaneous" delamination of coatings when they are residually stressed. A more detailed discussion of this phenomenon and its potential for interface toughness determination can be found elsewhere (Argon, et. al., 1988).

2. SPONTANEOUS DELAMINATION OF COATINGS

2.1 Coatings. SiC is used widely as a coating material for carbon fibers. It is hard, of low density, and adheres well both to the fibers and to most metal matrixes. In the present study, the SiC coatings have been applied to substrates by a plasma assisted chemical vapor deposition process (PACVD). Two substrates were used for study: single crystal Si wafers of 1 mm thickness with (100) plane surfaces and Pitch-55 type carbon fibers of 10 μm diameter. Because of substantial quantities of hydrogen entrapment during the PACVD process the as-deposited SiC coatings were under substantial residual compressive stress. The entrapped hydrogen could be removed readily by annealing the coatings at 600C for 30 minutes. This produced substantial reduction in coating thickness and resulted in a large residual tensile stress in the coating. When the coatings were applied to only one face of the circular Si single crystal wafers, the residual stresses σ in the coatings produced substantial curvature changes in the wafers which could be determined readily from the simple expression:

$$\sigma = \frac{E_s h^2}{6(1 - \nu_s)tR} \tag{1}$$

where R is the spherical radius of curvature of the substrate Si disk, E_s, ν_s are the Young's modulus and Poisson's ratio of the substrate, h its thickness, and t the thickness of the coating. This established that the residual tensile or compressive stresses in the coatings were independent of the coating thickness but depended only on the ion beam energy. Both tensile and compressive stresses were in the neighborhood of 600 MPa for low ion beam energies of around 10 e.V. They monotonically rose with

ion beam energy to about 2 GPa at 90 e.V., and remained at this level for larger ion beam energies (Argon et. al., 1988).

Coatings applied to Pitch-55 type carbon fibers in the same manner were uniform in thickness around the circumference of the fiber. Therefore, they did not produce curvature changes in the fibers, but showed identical changes in thickness and delamination behavior upon annealing that had been demonstrated by the Si wafers. From this it was concluded that they too were under very similar sets of residual stresses which too depended only on the ion beam energy and not on the thickness of the coatings.

2.2 Threshold thickness of delamination. While thin coatings of low sub-micron thicknesses were found to remain intact on both Si and carbon fiber substrates for indefinitely long times, regardless of the level or type of the residual stresses, thicker coatings were found to delaminate from the substrates when their thicknesses exceeded a critical value. The forms of this delamination were radically different for coatings in compression than from coatings in tension. In both cases, it was observed that when the coatings exceeded a threshold thickness, different in tension from that in compression, the rate of delamination increased with increasing thickness of coatings when the samples were observed in laboratory air. Beyond a certain thickness in excess of the threshold thickness, the delamination was nearly spontaneous upon removal of the samples from the coating apparatus, and happened even in the apparatus in vacuum. This suggests an element of stress corrosion cracking in the delamination process occurring in laboratory air that needs to be investigated further. This conjecture is reinforced by the observation that coatings with thicknesses in excess of the threshold thickness for long term delamination in air could be maintained intact when samples were stored in vacuum.

2.3 Delamination of coatings with tensile misfit strain. In annealed coatings with tensile misfit strain on Si single crystal substrates, the first form of delamination was the formation of columnar cracks in the coatings, parallel to the $< 110 >$ directions of the Si single crystal. These directions are 16% stiffer in the (100) surface of the crystal than the corresponding orthogonal set of $< 100 >$ directions. Upon cracking, coatings were found to delaminate in ribbon shaped slabs, starting from the free ends where parallel coating cracks were arrested by a previously established crack of the orthogonal family, as shown in Fig. 1. In the figure, the extent of coating delamination from the substrate is clearly visible from the darker contrast of the ribbon relative to its surroundings. The delaminated ribbon continues to lie flat on the substrate, because the residual tensile stress that has been relieved by the delamination was uniform across the thickness. The thicknesses of the gaps at the ends of retracted ribbons upon delamination could be readily measured at many places and permitted the determination of the initial material misfit strain ϵ_m. These misfit strains, when divided into the residual tensile stress in the coatings prior to the onset of the delamination, permitted the determination of the Young's modulus of the coatings from Eqn. (2) below:

$$E = \frac{(1 - \nu)\sigma}{\epsilon_m}, \tag{2}$$

where the Poisson's ratio of the coating was taken to be 0.3, since it could not be measured independently. These measurements established that the Young's modulus

271

of the annealed SiC coatings depended uniquely on the initial ion beam energy of the coating process. It was 16 GPa for an ion beam energy of 10 e.V. and rose monotonically to 300 GPa at an ion beam energy of 90 e.V. whereupon it remained constant for higher ion beam energies (Argon et. al., 1988).

The observations of a well-defined delamination threshold in the thickness of the coatings with tensile misfit indicate that this delamination is driven by the elastic strain energy stored in the coating. In such problems of biaxially stressed thin coatings resulting from a constant material misfit independent of thickness, the elastic strain energy almost entirely resides in the coating, with only a negligible contribution coming from the much thicker substrate (Argon, et. al., 1988). Thus, for very thin coatings where the elastic strain energy per unit area of the interface is less than the interface toughness, the coating remains intact indefinitely. As the thickness of the coating increases, the available elastic strain energy per unit area monotonically increases until it becomes equal to the intrinsic interface toughness (or energy release rate) G_{co}. Then, the coating can delaminate away from the substrate under quasi-static conditions, starting from any interface defect or pre-crack. The delamination proceeds in the interface and shows no tendency to veer off into the substrate or break into the coating. From elementary considerations, the G_{co} is given by (Argon, et. al., 1988):

$$G_{co} = \frac{\sigma^2(1-\nu)t_c}{E} = \frac{\epsilon_m^2 E t_c}{(1-\nu)},$$ (3)

where $\sigma, \epsilon_m, E, \nu, t_c$ are in order: the bi-axial residual tensile stress, the bi-axial material misfit strain, the Young's modulus, the Poisson's ratio, and the critical (threshold) thickness – all of the coating. It was found from here that the interface toughness is constant, within experimental error, and does not depend on ion beam energy. Its average value was 5.1 J/m^2 for coatings in residual tension.

2.4 Delamination of coatings with compressive misfit strain.

In the as-deposited coatings, the residual stress is compressive, as stated above. There too, the elastic strain energy stored in the coating per unit area of the interface increases monotonically with thickness of the coating. The delamination of these coatings from the substrate, however, exhibits a very different form. Here, it is found that coatings of considerably greater thickness remain attached intact to the substrate. When they reach a new critical thickness in the range of 1.0 μm, they are found to separate by forming a blister which lifts off the substrate in a regularly buckled form, as shown in Fig. 2, where a number of blisters in various stages of separation can be seen. At (A), the blister is just large enough to produce two half waves of vertical buckling, at (B), large blisters have settled into a form where they propagate radially outward in quasi-static equilibrium, with a self-similar circumferential buckling wave length. This wavelength appears just established in the small blister shown at (C). Observations of the growth of such blisters with Nomarski interference contrast microscopy showed that the buckled blister front is preceded by a narrow radial process zone which appeared to result from an interference effect between the top surface and the interface of the semi-transparent coating. From this, it was concluded that the actual lift-off by buckling of the coating is preceded by radially inward slippage of the coating over this process zone of several microns in width. It was assumed that this slippage relieved

the radial stress in the coating entirely. This was followed by partial relief of the circumferential stress by the formation of the circumferential buckles, with a wavelength ℓ, that depends on the initial bi-axial residual compressive stress σ given by Eqn. (4) below:

$$\ell = \pi t \sqrt{\frac{E}{3(1 - \nu^2)\sigma(1 - \nu)}}. \tag{4}$$

In Eqn. (4) E is the Young's modulus of the coating, t its thickness, and ν its Poisson's ratio, which was still taken to be 0.3. Since the residual compressive stress can be measured independently from the curvature of the substrate attached to the coating, and ℓ can be measured from the micrographs, such as Fig. 2, the modulus of the coating can be calculated from Eqn. (4). When this was done for a coating of 1.1 μm threshold thickness with a measured ℓ of 20 μm, and residual compressive stress of 2 GPa, E was found to be 116 GPa.
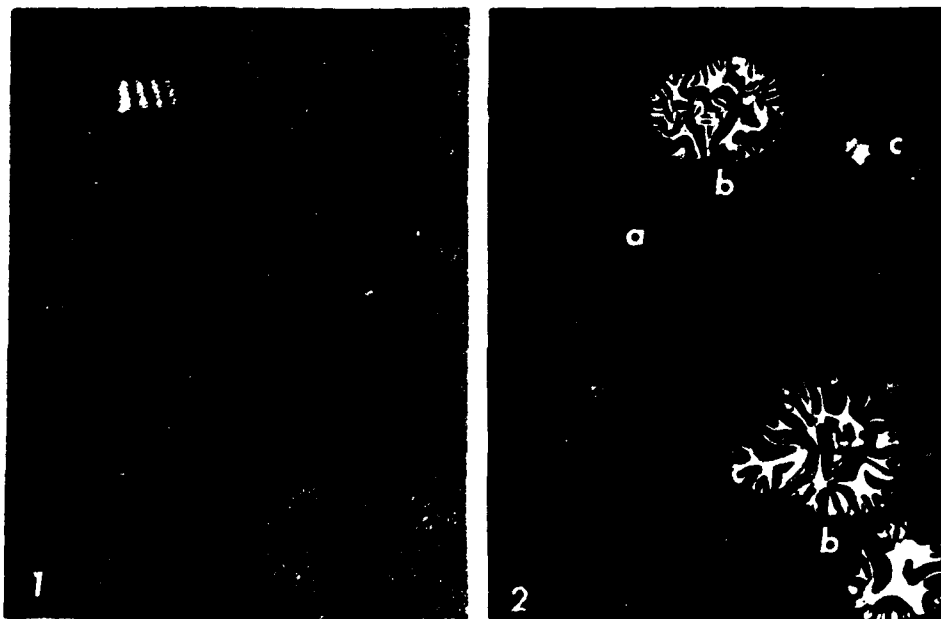
Figure 1: An example of ribbon-like delamination of an annealed SiC coating in tension on a Si single crystal substrate.

Figure 2: Delamination blisters in an as-deposited coating in bi-axial compression: (a) smallest blister just lifting off, (b) large well-established blisters growing radially outward with self-similar and regular circumferential buckled form, (c) a blister just large enough to assume a regular circumferential buckled shape.

273

Further elementary analysis established the remaining elastic strain energy, U_f per unit area of interface in the post buckled shape of the coating, and the initial strain energy U_i, per unit area, expressed in the same fundamental parameters to be:

$$U_f = \frac{\pi^4 E t^5}{9(1 - \nu^2)^2 \ell^4}; \qquad (a)$$

$$U_i = \frac{\pi^4 E t^5}{9(1 - \nu^2)^2 (1 - \nu)\ell^4}. \qquad (b) \qquad\qquad (5)$$

At the critical threshold thickness t_c, the difference between (5b) and (5a) should provide for the intrinsic toughness G_{co} of the interface (Argon, et. al., 1988), i.e.:

$$G_{co} = \frac{\nu \pi^4 E t_c^5}{9(1 - \nu^2)^2 (1 - \nu)\ell^4}. \qquad\qquad (6)$$

Evaluation of typical cases already referred to above gave an interface toughness of $G_{co} = 5.95 \ J/m^2$, which is within experimental error equal to the interface toughness of the coatings in residual tension.

2.5 Delamination of coatings from Pitch-55 type carbon fibers.

The same phenomenon of spontaneous delamination of SiC coatings with tensile misfit was found also with Pitch-55 type carbon fibers. When such fibers were coated followed by the annealing treatment of 600C for 30 minutes, the coatings were found to remain stable and intact, if their thicknesses were less than 0.33 μm for coatings deposited at low ion beam energy. When coatings with thickness slightly exceeding this thickness, having the above process history were left in laboratory air with the usual relative humidity of 60% for several months, they were found to undergo copious and complete delamination by cracking and flaking, as shown in Fig. 3.

The initial bi-axial misfit strain ϵ_m between coating and fiber could again be determined from the ratio of the average gap size between flakes to the average dimension of the flakes. With this information, and the assumption that the modulus of the coating in tension is given uniquely by the previously established connection between modulus and ion beam energy, and the further assumption that the Poisson's ratio remained at 0.3, the threshold elastic strain energy of the coating per unit area could be calculated and equated to the fracture toughness of the interface to simply result in (Argon, et. al., 1988),

$$G_{co} = \frac{\epsilon_m^2 E t_c}{(1 - \nu)}, \qquad\qquad (7)$$

for coating thickness to fiber radius ratio $t/R \ll 1$. Evaluation of these results for a typical case of coating with a modulus of 16 GPa, threshold thickness of 0.33 μm, and misfit strain of 2.7×10^{-2} on a fiber with a radius of 5 μm, the interface toughness was calculated to be $G_{co} = 5.45 \ J/m^2$. Within experimental error, this is also the same as the interface toughness between Si and SiC.

274
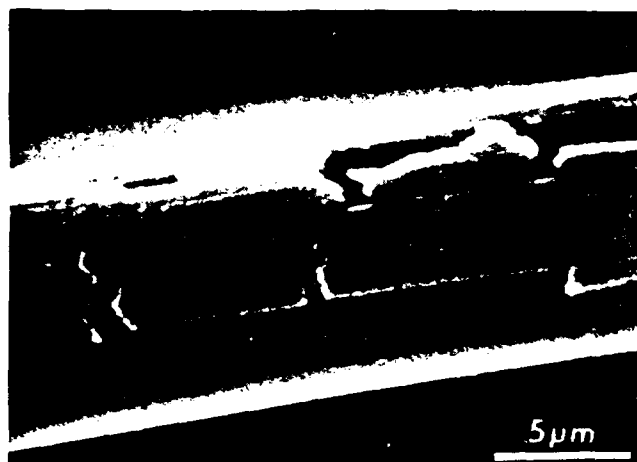
Figure 3: Flakes of delaminated SiC coating on a Pitch-55 type carbon fiber.

3. DISCUSSION

The phenomenon of spontaneous delamination of coatings under residual stress, from more massive substrates occurs quasi-statically when the elastic strain energy of misfit per unit area equals the intrinsic work of separation of the coating from the interface. The analysis of the conditions of such delamination provides the much needed information on the intrinsic fracture toughness of the interface. Apart from small differences between the various modes of separation presented above, the interface toughness was found to be around 5.5 J/m^2, independent of the state of stress in the coating, and the same for the Si/SiC and C/SiC pairs.

Observation of such delamination events is not new. Evans and Hutchinson (1984) have reported somewhat similar delamination phenomena for interfaces between surface layers and substrates in micro-electronics components, but observed a simpler and less informative mode of delamination for layers in compression.

It must be noted that the simplicity of the phenomenon reported above results from the sharply defined nature of the interface. Under these conditions, where the elastic strain energy of misfit is overwhelmingly stored in the coating, the nature of the stress intensity of the singular field at the tip of the interface crack, which is thought to be complex and associated with oscillatory tractions (Rice and Sih, 1965; Comninou, 1977; Hutchinson, et. al., 1987), must also be of very short range.

A clue to this unique behavior of extensive stable delamination along the interface is likely to be the Nomarski interference contrast microscopy observation of a narrow process zone preceding the delamination, at least in the case of the enlargement of the compression blister, prior to lift off of the coating. It is likely that such process zones also precede the delamination of coatings in tension. We have interpreted these zones as being due to plastic slippage of the coating on the substrate. This may also account

275

for the magnitudes of the interface toughness that have been obtained. Thus, in the absence of any dissipative work, the toughness of an interface must be:

$$G_{co} = \chi_A + \chi_B - \chi_{AB},\tag{8}$$

where χ_A and χ_B are the surface energies of components A and B, and χ_{AB} the specific interface energy between A and B. Although good measurements of either the surface energies of Si, or SiC, or their interface energy do not exist, a simple estimate can show that the measured interface toughnesses are considerably in excess of what could be expected. The surface energy of Si measured by Gilman (1960) in cleavage experiments is 1.24 J/m^2. If the surface energy of SiC is estimated to be higher in the ratio of the Young's moduli of SiC to Si, i.e., by a factor of 2.04, it should be 2.53 J/m^2. Thus, considering the interface energy between Si and SiC to be somewhere of the order of 1 J/m^2, it is clear that the measured interface toughnesses are about twice of what might be expected from Eqn. (8). Clearly, therefore, even in this very short range crack tip stress field as it propagates along the interface additional dissipative work is being done which we propose is expended by some relative slippage between coating and substrate prior to lift off of the coating.

Nevertheless, we conclude that the interface toughnesses that we have reported are quite meaningful and that the spontaneous delamination experiment can be used within these limitations to monitor changes of interface adhesion in tailoring the properties of interfaces in the quest of making tougher and more damage tolerant composites.

ACKNOWLEDGMENT

REFERENCES

Argon, A.S. (1972). Fracture of Composites. In: Treatise on Materials Science and Technology. Edited by H. Herman (Academic Press, New York), 79-114.

Argon, A.S. (1974). Statistical Aspects of Fracture. In: Composite Materials: Fracture and Fatigue. Edited by L. J. Broutman, and R. H. Krock (Academic Press, New York), 5, 153-190.

Argon, A.S., Gupta, V., Landis, H. S., and Cornie J. A. (1988). Intrinsic Toughness of Interfaces Between SiC Coatings and Substrates of Si or C Fiber. Submitted to J. Mater. Sci.

Comninou, M. (1977). The Interface Crack. J. Appl. Mech. 44, 631-636.

Evans, A.G. and Hutchinson, J. W. (1984). On the Mechanics of Delamination and Spalling in Compressed Films. Intern. J. Solids Structures, 20, 455-466.

Gilman, J. J. (1960), Direct Measurements of the Simple Energies of Crystals, J. Appl. Phys, 31, 2208-2218.

Gupta, V., Argon, A.S., and Cornie, J.A. (1988). Interfaces with Controlled Toughness as Mechanical Fuses to Isolate Fibers from Damage. Submitted to J. Mater. Sci.

Hutchinson, J.W., Mear, M.E., and Rice, J.R. (1987). Crack Paralleling an Interface Between Dissimilar Materials. J. Appl. Mech., 109, 828-832.

Rice, J.R. (1965). An Examination of the Fracture Mechanics Energy Balance from the Point of View of Continuum Mechanics. In: Proceedings of the First International Conference on Fracture. Edited by T. Yokobori et. al. (The Japanese Society for Strength and Fracture of Materials, Sendai, Japan), Vol. 1, 309-340.

Rice, J.R. and Sih, G. S. (1965). Plane Problems of Cracks in Dissimilar Media. J. Appl. Mech., 32, 418-423.

A High Resolution Transmission Electron Microscopy Study of SiC-coated Graphite Fiber–Aluminum Composite

Q. LI J. MEGUSAR, L. J. MASUR and J. A. CORNIE

Department of Materials Science and Engineering, Massachusetts Institute of Technology, Cambridge, MA 02139 (U.S.A.)

Received August 16, 1988; in revised form February 27, 1989)

Abstract

An SiC-coated graphite fiber–aluminum composite was processed by plasma-enhanced chemical vapor deposition (PECVD) of silicon carbide followed by aluminum pressure infiltration. A high resolution transmission electron microscopy study of this composite was carried out, with emphasis on a detailed characterization of the interface structures. Pitch-55 graphite fiber structure was analyzed in both the core and skin regions and it resembles that of turbostratic graphite. The SiC coating deposited by the PECVD technique was fully amorphous. The graphite fiber–SiC interface was characterized as sharp. Pressure infiltration of aluminum into fibers of low initial temperature (621 K) suppressed almost completely formation of a reaction zone between the aluminum and SiC. A mismatch in the coefficient of thermal expansion between the components of this composite leads to dislocation generation in the aluminum matrix. These observations allowed for a detailed evaluation of the processing techniques used, and structural details of the interfacial regions will serve at the same time as a basis for modeling interface properties.

1. Introduction

This study is a part of an ongoing research program on tailoring interface properties in the graphite fiber–aluminum metal matrix composites. Such tailoring should be based on a detailed knowledge of the interface structure and composition and on a thorough understanding of the deformation and fracture processes. In optimizing mechanical behavior of the metal matrix composites, one has to consider a transfer of load from the metal matrix to the reinforcing fibers to maximize strength and, on the other hand, a deflection of crack at the fiber–metal

matrix interface in order to maintain the composite integrity [1]. An additional consideration is the chemical reaction between graphite fibers and aluminum occurring during processing of the composite or during composite exposure to high service temperatures. Formation of an extensive reaction zone is associated in general with interface embrittlement and loss of fiber strength. Coating graphite fibers with a thin layer of SiC provides, therefore, a chemical barrier and it furthermore enables the tailoring of interface structure and properties. Figure 1 is a low magnification transmission electron micrograph showing the graphite fiber, SiC coating and aluminum matrix in the SiC-coated graphite fiber–aluminum metal matrix composite under study.

In this paper, results of a high resolution transmission electron microscopy (TEM) study of the SiC-coated graphite fiber–aluminum composite are presented, with emphasis on a detailed characterization of the interface structures. Results of an *in situ* high voltage electron microscopy study of fracture in this composite have been described elsewhere [2] and they indicate that fracture advances by decohesion of the graphite fiber–amorphous SiC interface. In research in progress [3], plastic strains and the extent of the plastic zone at the aluminum–amorphous SiC interface are being studied during stepwise straining of miniature tensile specimens in an effort to evaluate the interface strength in SiC-coated graphite fiber–aluminum composites. Results on the interface structure and deformation and fracture behavior will serve as a basis for modeling interface properties.

2. Experimental procedures

Processing of the SiC-coated graphite fiber–aluminum composite included coating the graph-

200

Fig. 1. A low magnification transmission electron micrograph showing graphite fiber, SiC coating and aluminum matrix in the SiC-coated graphite fiber-aluminum composite.

ite fibers and pressure infiltration of the metal matrix.

Pitch-55 graphite fibers were coated with a thin layer of silicon carbide by plasma-enhanced chemical vapor deposition (PECVD). The PECVD system used in this work has been described elsewhere [4]. Fibers were first sputter cleaned and then SiC was deposited on the fiber surface using SiH_4 and CH_4 with an argon carrier at flow rates of 4.2, 6.7 and 10.9 standard cubic centimetres per minute (sccm). The total pressure was 6.7 Pa. The radio-frequency conditions were as follows: upper electrode 100 W, lower electrode 50 W and ion bombardment energy 135 ± 15 eV. The substrate temperature was below 373 K. The as-deposited fibers were annealed in vacuum for 0.5 h at 873 K to release hydrogen stored in the SiC coating during deposition.

The SiC-coated graphite fibers were placed bet een two Saffil alumina fiber plugs, forming a preform. The entire sandwich was then placed n a quartz tube and preheated to 621 K. Pure

molten aluminium (99.9 wt.%) at a temperature of 963 K was pressure infiltrated into the preform at 3.6 MPa and held for 1.5 min. Pressure was then released and the infiltrated composite removed. Details of the pressure infiltration technique used have been described elsewhere [5].

Preliminary microstructural characterization was carried out by using a JEOL 200CX transmission electron microscope. High resolution TEM was performed at the National Center for Electron Microscopy (NCEM), UC Berkeley, by using the atomic resolution microscope (ARM). The point-to-point resolution of the ARM is 0.15 nm and it is uniquely combined with a $\pm 45°$ biaxial specimen tilting. TEM discs were prepared by dimple grinding, followed by ion thinning at 4 kV at the temperature of liquid nitrogen.

3. Results and discussion

3.1. Graphite fibers

High resolution TEM has been applied, in addition to X-ray diffraction, in studying the structure of a number of carbon fibers [6]. The general picture that emerged was that of a network of intertwinned ribbons of stacked graphitic sheets with intervening voids. The orientation of the ribbons is usually along the fiber axis. Information about the width, continuity and orientation of the ribbons and the degree of lattice disorder within the ribbons is potentially available directly from the high resolution transmission electron micrographs.

Typical structures of the pitch-55 graphite fibers used in this study are shown in Figs. 2 and 3. They represent a view perpendicular to the graphite fiber axis (transverse structure). The structure shown in Fig. 2 is representative of the skin region of a graphite fiber, while the structure shown in Fig. 3 is characteristic of some areas of the core region.

Fringe images in Figs. 2 and 3 represent the (0002) lattice graphite structure. The spacing of the fringes corresponds to that expected for graphite (i.e. 0.345 nm). These fringes images indicate that the skin region consists of well-oriented, relatively large and nearly perfect crystallites. It is this structure which is of interest in studying the graphite fiber-SiC interface properties. Some areas of the core region, as shown in Fig. 3, exhibit the graphite structure consisting of less well-oriented and less perfect crystallites. Graphite layers are bent or buckled significantly
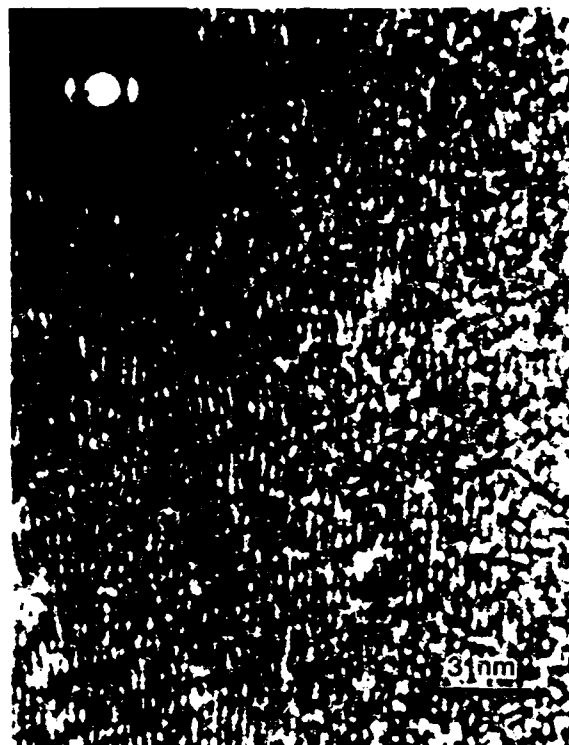
Fig. 2. A high resolution transmission electron micrograph showing the graphite fiber structure characteristic of the skin region.

Fig. 3. A high resolution transmission electron micrograph showing the graphite fiber structure characteristic of some areas in the core region.
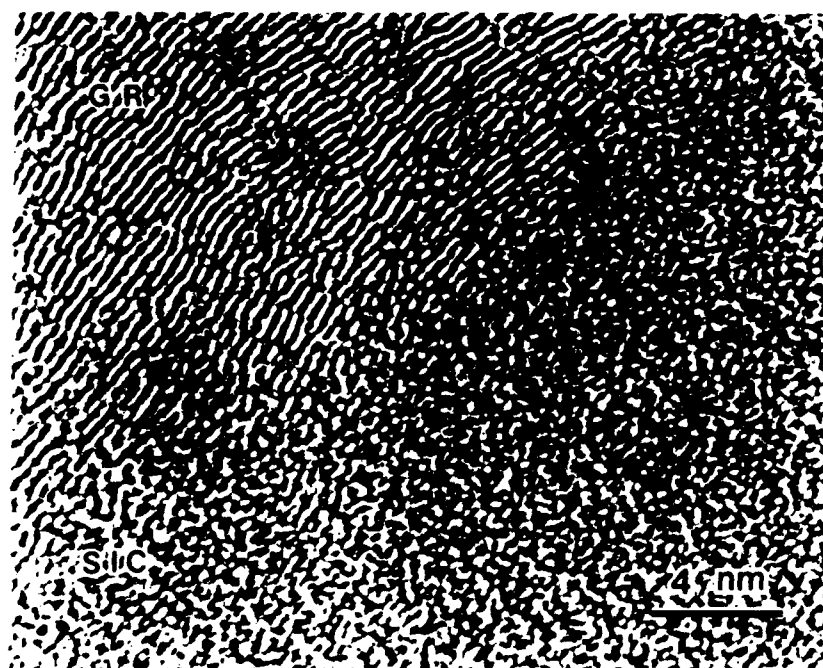
Fig. 4. A high resolution transmission electron micrograph showing the graphite fiber-amorphous SiC interface, with graphite layers aligned parallel to the interface.
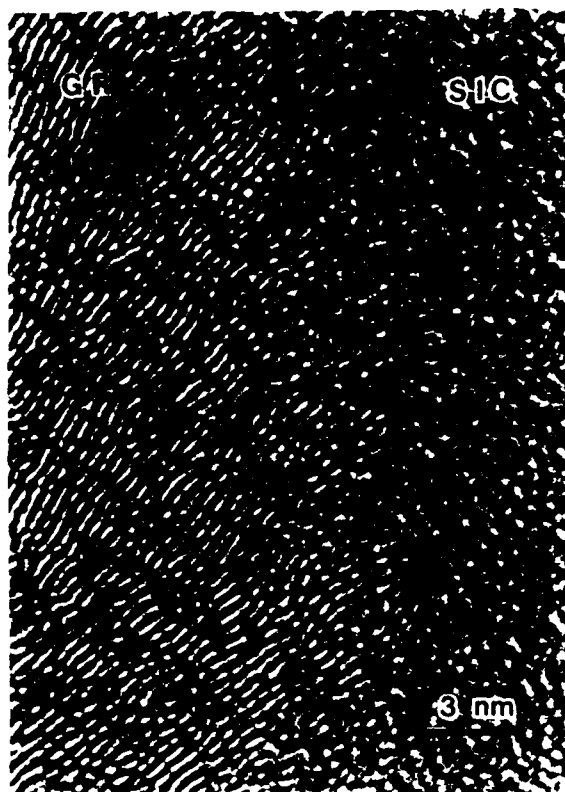
Fig. 5. A high resolution transmission electron micrograph showing the graphite fiber amorphous SiC interface, with graphite layers inclined to the interface

Fig. 6. A high resolution transmission electron micrograph showing the amorphous SiC-aluminum interface lattice fringe image of aluminum

to conform with locally imposed strains. The length of graphite layers is shorter and stacking disorder is more pronounced when compared with the graphite structure of the skin region. The graphite showing such a partially ordered structure is commonly referred to as turbostratic.

The high resolution transmission electron micrographs shown in Figs. 2 and 3 allow a qualitative evaluation of the graphite fiber structure. A precise determination of the graphite layer spacing and a study of stacking disorder and other defects in the graphite structure must be based on a comparison of the above experimentally observed fringe images with computed images based on dynamic theory. This was beyond the scope of the present study.

3.2 Graphite fiber SiC interface

Figures 4 and 5 are high resolution transmission electron micrographs showing two different areas of the graphite fiber SiC interface. They show different orientations of the nearly planar graphite layers with respect to the interface

graphite layers are parallel to the interface in one case (Fig. 4) and inclined to the interface in the other (Fig. 5).

The structure of the SiC coating prepared by PECVD is fully amorphous and the corresponding electron diffraction pattern showed a broad halo around the central spot characteristic of diffuse scattering. The amorphous SiC gives rise to the mottled image contrast characteristic of all amorphous materials. An examination of the free-standing coating of the SiC deposited under identical conditions and annealed for 0.5 h at 873 K revealed lighter and darker regions within the amorphous structure. These are indicative of local variations in density and are most likely related to the variation in deposition energy [4] and to the process of hydrogen release during annealing.

As shown in Figs. 4 and 5, the transition from the graphite fiber to the amorphous SiC coating appears to occur over a rather narrow transition zone. Consequently, the graphite fiber-amorphous SiC interface can be described as sharp

AD-A216 881

UNCLASSIFIED

F/G 11/4   NL
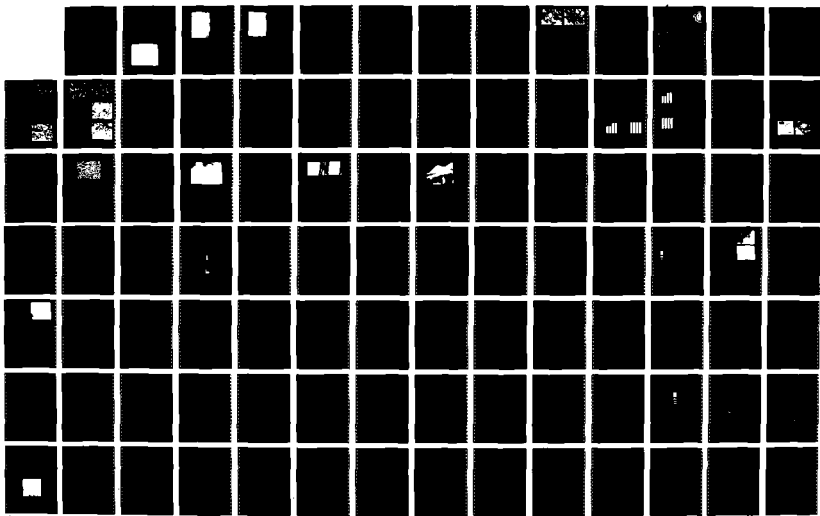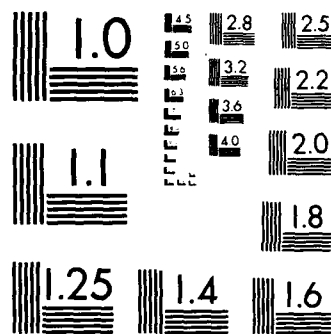
MICROCOPY RESOLUTION TEST CHART

NATIONAL BUREAU OF STANDARDS-1963-A

Such as interface between the graphite fibers and the amorphous SiC coating was expected on the basis of the low temperature nature of the PECVD process. Furthermore, graphite and SiC are refractory materials and the highest temperature to which they had been exposed during composite processing was 963 K over a period of 1.5 min see Section 2.

The orientation of the nearly planar and parallel graphite layers with respect to the amorphous SiC interface was shown to vary from one area of the skin region to another. It has been shown [7] that some crystallites in the skin region of graphite fibers may be misoriented with respect to the fiber axis as well, giving rise to Moiré fringes. A resultant change in the orientation of graphite layers along the amorphous SiC interface and the associated stacking disorder and other defects may have an effect on the cohesive strength of the graphite fiber–amorphous SiC interface.

3.3. Aluminum–SiC interface

Figure 6 is a high resolution transmission electron micrograph of the aluminum–amorphous SiC interface in the SiC-coated graphite fiber–aluminum composite. This micrograph was taken slightly off the 110 orientation. Lattice fringe images formed represent the {111} crystal-lographic planes and their spacing is indicated by the marker.

Figure 7 is a two-dimensional structure image of the aluminum–amorphous SiC interface in the SiC-coated graphite fiber–aluminum composite. It was taken in a 110 orientation. This phase contrast image was obtained by interference of six to eight beams. A close examination of the interface in Fig. 7 indicates that structurally there is an abrupt change from crystalline to amorphous phases and, accordingly, the interface between the aluminum and the amorphous SiC can be defined as sharp. This is in contrast to an atomically diffuse interface in which case the transition from the amorphous to crystalline phase would occur over several atom layers. It is worth noting that the aluminum–amorphous SiC interface shown in Fig. 7 does not exhibit microscopic steps or ledges.

Most of the specimen areas examined showed a sharp transition from the aluminum to amorphous SiC. Some areas, however, showed evidence for formation of a reaction zone. Such an area is shown in Fig. 8, with lattice fringes superimposed on the amorphous (mottled) background. Lattice fringe spacing within the reaction zone (designated as RZ in Fig. 8) was measured by using the built-in calibration standard of the
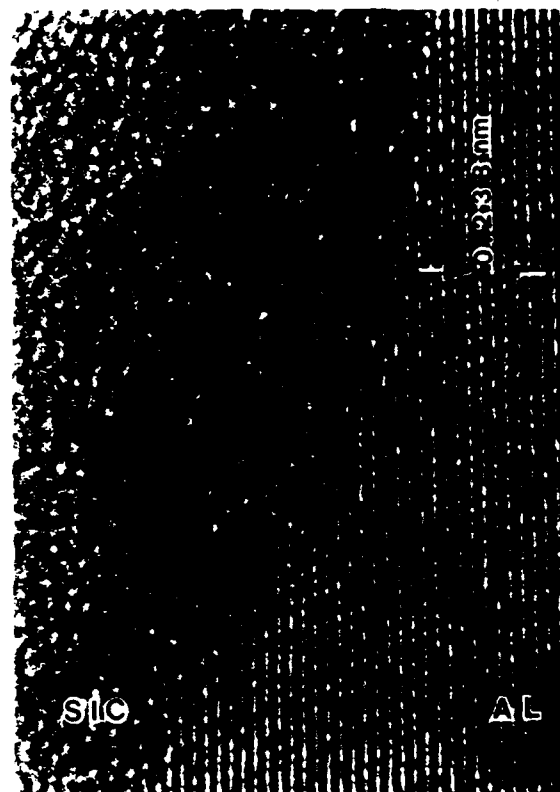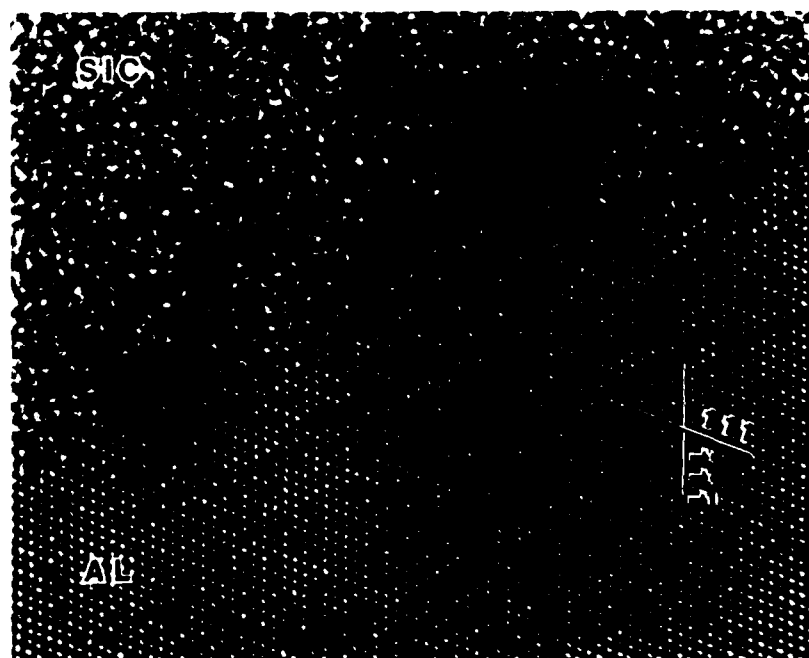

Fig. 7. A high resolution transmission electron micrograph showing the amorphous SiC-aluminum interface two-dimensional structure image of aluminum
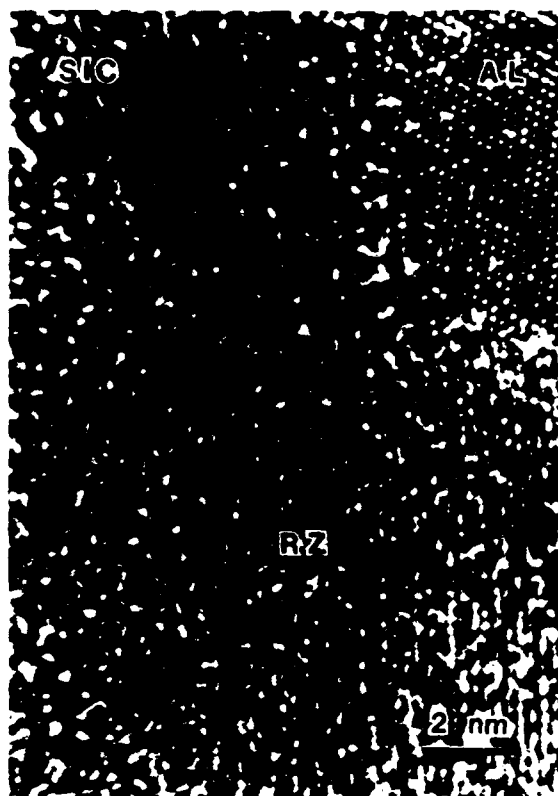
Fig. 8. A high resolution transmission electron micrograph showing a reaction zone at the amorphous SiC-aluminum interface.

aluminum lattice, and its value of 0.278 nm can be compared to that of the (012) spacing of the aluminum carbide (Al$_4$C$_3$). The width of the reaction zone observed was limited and it did not exceed 20 nm. The above high resolution transmission electron microscopy evaluation of the aluminum-amorphous SiC interface indicates that the chosen conditions of the pressure infiltration of graphite preforms with liquid aluminum resulted in an aluminum-amorphous SiC interface which features good bonding and in which, at the same time, formation of the reaction zone has been almost completely suppressed.

Formation of a reaction zone has been typically considered difficult to avoid during composite processing involving an extensive exposure of SiC as continuous or discontinuous reinforcement to liquid aluminum or liquid aluminum alloys. Based on thermodynamic considerations, the Al$_4$C$_3$ reaction zone is expected to form. In preform infiltration processing [8] it is usually desirable to keep temperatures as low as possible in order to minimize chemical reactions between fibers and the matrix. It is possible to infiltrate fibrous preforms held at temperatures significantly below the liquidus of the metal which leads to the formation of some solid metal between the fibers during infiltration. It has been shown [9] that during infiltration of a 99.99% pure Al matrix, SiC fibers can be coated with a layer of solid metal which protects the fibers from chemical degradation. Suppression of a reaction zone between SiC and liquid aluminum in the present study has therefore been ascribed to the combined effects of the high pressure used, the reduced reaction time during pressure infiltration and, most importantly, the choice of the preheating temperature prior to pressure infiltration of the graphite fiber preform with liquid aluminum (see Section 2 for details). Consequently, the pressure infiltration technique, with the preheating temperature of fiber preforms significantly below the liquidus of the metal, shows promise in controlling interface structure and in tailoring interface properties of aluminum metal matrix composites.

An important consideration in developing metal matrix composites is a mismatch in the coefficient of thermal expansion between reinforcing fibers and metal matrix. Such a mismatch may lead to thermal stresses which are induced during cooling from the composite processing temperature. This becomes particularly critical in designing ceramic matrix composites where a mismatch in the coefficient of thermal expansion may lead to microcrack formation. In ductile metal matrices such as aluminum, this mismatch may be accommodated by plastic deformation [10, 11].

In the SiC-coated graphite fiber-aluminum composite there is a large difference (of the order of ten to one) between coefficients of thermal expansion of the aluminum on one hand and the graphite and silicon carbide on the other. Therefore, when the composite is cooled from the processing temperature, misfit strains are sufficient to generate dislocations due to differential thermal contraction at the aluminum-SiC interface. Dislocation generation has been revealed, as expected, by using weak beam electron microscopy. Figure 9 is a (g, 3g) weak beam dark field image of an area in the aluminum matrix near the aluminum-SiC interface showing an extensive dislocation network. Interestingly, as shown in Fig. 7, there is no evidence of dislocations associated with the aluminum-amorphous SiC inter-
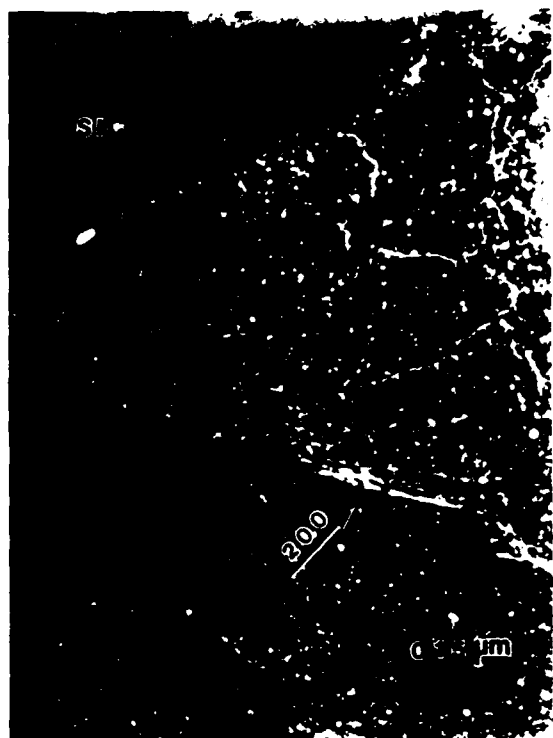
Fig. 9. g, 3g weak beam dark field image of an area in the aluminum matrix near the aluminum-SiC interface.

face, although one would expect that on the basis of a mismatch of the coefficients of thermal expansion between aluminum and silicon carbide. This may be due to dislocation delocalization [12] occurring at the crystalline-amorphous interfaces. It has been shown in particular [12] that lattice dislocations deposited at the crystal aluminum-amorphous Al_2O_3 interface during straining experiments dissociated readily in a short time at room temperature to widths greater than the extinction distance. It is reasonable to assume that the mechanism of dislocation delocalization may be operative in the crystal aluminum-amorphous SiC system as well.

4. Conclusions

The following conclusions can be drawn from this high resolution transmission electron microscopy study of the SiC-coated graphite fiber-aluminum composite.

1 The structure of the pitch-55 graphite fibers resembles that of a turbostratic graphite. The skin region shows the structure which is characteristic of a fully graphitized carbon. Some areas of the core region exhibit a less developed graphitic structure, with graphite layers bent and of shorter length.

2 The structure of the SiC coating deposited by PECVD and annealed for 0.5 h at 873 K to release hydrogen is fully amorphous.

3 The graphite fiber-amorphous SiC interface can be characterized as sharp. Properties of this interface may depend on the relative orientation of graphite layers.

4 The aluminum-amorphous SiC interface was observed to be sharp, with the exception of a few areas where a reaction zone of limited extent was formed. Pressure infiltration, with the preheating temperature of fiber preforms significantly below the liquidus of the metal, therefore shows promise in controlling interface structure and properties of aluminum metal matrix composites. A mismatch in the coefficient of thermal expansion between the components of this composite leads to dislocation generation in the aluminum matrix.

Acknowledgments

References

1 I. Erturk, V. J. Gupta, A. S. Argon and J. A. Cornie, Proc. 6th Int. Conf. on Composite Materials (ICCM-VI), London, Elsevier, Amsterdam, 1987, pp. 2.156-2.168.

2 J. Megusar, O. Li, J. A. Cornie and K. H. Westmacott, Ceram. Eng. Sci. Proc., 9-7-8 1988 1031.

3 O. Li, J. Megusar and J. A. Cornie, unpublished data, 1988.

4 H. S. Landis, Ph.D. Thesis, MIT, Cambridge, MA, 1987.

206

5   L. J. Masur, *Ph.D. Thesis*, MIT, Cambridge, MA, 1988.

6   G. R. Millward and D. A. Jefferson, in P. L. Walker and P. A. Thrower eds., *Chemistry and Physics of Carbon*, Dekker, New York, 1978, pp. 1–82.

7   D. J. Johnson, *Philos. Trans. R. Soc. London, Ser. A, 294* 1980 443.

8   A. Mortensen, J. A. Cornie and M. C. Flemings, *J. Met., 4*

2   1988 12.

9   H. Fukunaga and K. Goda, *J. Jpn. Inst. Met., 1* 1985 85.

10 R. J. Arsenault and N. Shi, *Mater. Sci. Eng., 81* 1986 175.

11 E. Zywicz, *M. S. Thesis*, MIT, Cambridge, MA, 1986.

12 J. S. Liu and R. W. Balluffi, *Mater. Res. Soc. Symp. Proc., 25* 1984 261.

Wetting of Ceramic Particulates with Liquid Aluminum Alloys: Part I. Experimental Techniques

S.-Y. OH, J. A. CORNIE, and K. C. RUSSELL

An experimental technique for evaluation of wettability of solid particulates with liquid metal was developed. Uniformly packed powder specimens were prepared with a tamping device specially made for the present experiment, and wetting tests were conducted by pressure infiltration of liquid Al-alloys into the powder specimens. The threshold pressure for infiltration was used as a measure of wettability. With this technique, wettabilities were measured for 10 μm diameter SiC and B$_4$C particulates by several Al-based alloys. Threshold pressures obtained from this technique showed reproducibility to approximately ± 7 kPa. Microstructures of infiltrated powder specimens indicated planar front infiltration with no disruption of powder compact during infiltration test and virtually no porosity.

I. INTRODUCTION

METAL matrix composites are a family of advanced materials which may have attractive properties including high strength, high specific modulus, low coefficient of thermal expansion, good wear resistance, and attractive high-temperature properties. Composites also offer the opportunity to develop new materials with a unique set of properties that are not available with conventional materials.

Discontinuous particulate or whisker reinforced aluminum alloy composites have a very desirable combination of high specific modulus and strength as well as good thermal stability. Compared with continuous fiber reinforced composites, discontinuous second phase reinforced composites provide improved ductility and reduced anisotropy in mechanical properties. Furthermore, the latter can be subjected to secondary working with conventional techniques, including extrusion and forging. Recently, particulates have been added to continuous fiber-reinforced aluminum alloys to improve both longitudinal and transverse strength.[1]

Casting of metal matrix composites is an attractive processing method since it is relatively inexpensive and offers a wide selection of materials and processing conditions. Good wetting is an essential condition for the generation of a satisfactory bond between solid ceramic phase and liquid metal matrix during casting of composites. In spite of the importance of wettability in the manufacture of composites, relatively few quantitative studies have been conducted and many fundamental questions remain unanswered.

Since the wettability of fine ceramic particulates with liquid metal cannot be measured by such conventional methods as the sessile-drop test or by multiphase equilibrium, the first step of this research work was to develop a reliable and reproducible experimental technique for evaluation of wettability. The new technique is based on uniform packing of ceramic powder cylinders followed by pressure infiltration of liquid metal. Infiltration occurs when the $P \Delta V$ work done by the applied pressure balances the free energy

change due to replacement of the solid:vapor interface by a solid:liquid interface. The threshold pressure for infiltration may be used directly as a measure of wettability or may be converted to work of immersion or to a wetting angle by using a modified capillary force equation.

Two commonly used ceramic particulates, SiC and B$_4$C, and seven different aluminum alloys, pure Al, Al-2 pct Cu, Al-4.5 pct Cu, Al-2 pct Si, Al-4.5 pct Si, Al-2 pct Mg, and Al-4.5 pct Mg, were employed in this study. This paper describes the experimental technique and gives a few typical results. Results of the full study are given in the following paper.[2]

II. BACKGROUND

A. Basic Concepts in Wetting

A liquid will wet a solid phase to a degree dictated by the surface energies of the system. Both spreading wetting and immersional wetting are relevant to the present study.

If a liquid drop rests on a solid substrate, as shown in Figure 1, the wetting angle, θ, characterizes the wetting of solid by liquid. The fundamental relationship between wetting angle and surface energy in equilibrium is given by

$$\gamma_{sv} = \gamma_{sl} + \gamma_{lv} \cos \theta \qquad [1]$$

where γ_{sv} is the surface energy of solid, γ_{sl} is the solid-liquid interfacial energy, γ_{lv} is the surface energy of liquid, and θ is the wetting angle. This equation was first derived by Young,[3] but is often referred to as the Young-Dupré equation.[4] The wetting angle, θ, characterizes the degree of spreading wetting in the system.

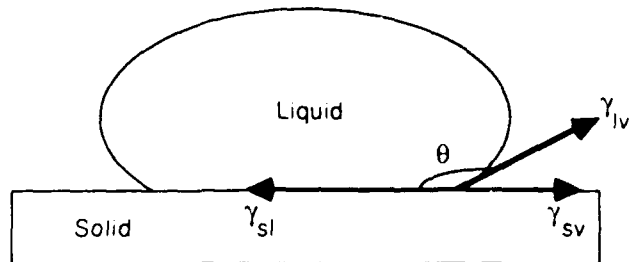Fig. 1 — Schematic diagram of a liquid drop on the solid surface, showing the interfacial forces and wetting angle for a nonwetting system

S.-Y. OH, Research Associate, Department of Materials Science and Engineering, J. A. CORNIE, Principal Research Associate, Energy Laboratory, and K. C. RUSSELL, Professor of Metallurgy and Nuclear Engineering, are with Massachusetts Institute of Technology, Cambridge, MA 02139

When a capillary tube is immersed into liquid, the curved meniscus can either rise or be depressed, depending on γ_{sl} and γ_{lv}. Equilibrium of the liquid column requires a capillary pressure, P, of:

$$P = 2(\gamma_{sl} - \gamma_{sv})/r \qquad [2]$$

where P may be from an applied pressure or from the hydrostatic pressure in the capillary of:

$$P = \rho g h \qquad [3]$$

where r is the radius of the tube, ρ is the density of liquid, g is the force of gravity, and h is the height of the liquid column. Capillary rise is an example of immersional wetting.

When a solid is immersed into liquid, as shown in Figure 2, immersional wetting also occurs. As in capillary rise, the solid:gas interface is replaced by a solid:liquid interface without changing the area of liquid:gas interface. The free energy change or the work performed, W_i, is given by

$$W_i = \gamma_{sl} - \gamma_{sv}. \qquad [4]$$

The work of immersion, W_i, has meaning regardless of the magnitude of wetting angle, θ. However, wetting angle has no meaning where $|(\gamma_{sv} - \gamma_{sl})/\gamma_{lv}| > 1$, i.e., in the cases of perfect wetting or perfect nonwetting.

Equation [4] defines W_i as the change in free energy on immersing the solid in the liquid, so that $W_i < 0$ indicates spontaneous wetting. When $W_i > 0$ the solid (as in Figure 2) would tend to float and must be forced into the liquid.

Capillary rise and pressure infiltration of liquid metal into a solid preform are two practical examples of immersional wetting. Immersional wetting may be affected only by changes in γ_{sl} or γ_{sv} or both. A change in γ_{lv} only is reflected by a change in θ so that $\gamma_{lv} \cos \theta$ remains constant; immersional wetting is not affected.

B. Measurement of Particulate Wettability

Even though the particulate wettability is often of great technical importance, its measurement is quite difficult. Due to the difficulty in performing quantitative wetting
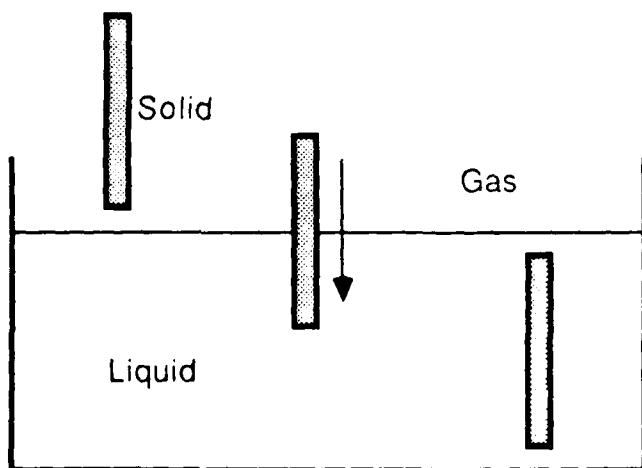
Fig. 2.—Immersion of solid into liquid, illustrating immersional wetting

angle measurements, an ordinal (or ranking) scale was proposed[5] as a measure of wettability of particulates with liquids. A variety of experimental procedures has been described in the literature which in one way or another leads to an ordinal scale of wettabilities. Those procedures either consist of the numerical measurement of certain quantities, such as depth of imbibition, or quantity of infiltrated liquid, which can then be used as an indication of an ordinal wettability score of the system. A repetition of the latter type of test with many pairs of cases will then also provide an ordinal scale. In all these tests the problem of standardization is of utmost importance so that one arrives in every case at a meaningful wettability score.

The work of Bartell et al.[6,7,8] gives quantitative measures of wettability of particulates. They measured the pressure exerted by the organic liquid entering through compacted carbon, silica, glass, or paraffin powder. They obtained the radius of the equivalent cylindrical capillary tube, r, by measuring the pressure set up by a liquid known to wet the particulates completely; i.e., θ is zero. From the displacement pressure to force liquid into a powder compact, the wetting angle was evaluated by using the capillary force equation, Eq. [2]. The value of pressure was reported as quite reproducible.

Another approach to measure the wetting angle of particulates with liquid was introduced by Hackett[9] and others.[7] This method is based on the measurement of the rate of fluid flow through the powder compact, and application of Poiseuille-type equations to the experimental results. However, different researchers used different fluid flow equations with different physical constants.

The concept of the hydraulic radius, introduced by Carman,[10] made the calculation of wetting angle simple. The hydraulic radius, r_h, is defined as

$$r_h = \frac{\text{volume of liquid column in capillary}}{\text{area of wetted surface of capillary}}. \qquad [5]$$

For a compacted powder,

$$r_h = \frac{D \cdot w}{6\lambda(1 - w)} \qquad [6]$$

where D is the average diameter of particulate, w is the void fraction of powder compact, and λ is a geometry factor which depends on the geometry of both particulate and capillary channel. For nonspherical, angular particulates, the value of the geometry factor was determined in experiments with perfect wetting liquids as 1.4, and showed very good fit over a hundredfold variation in particle size.

By combining Eqs. [2] and [6], capillary pressure or threshold pressure for infiltration can be expressed in terms of particulate size and void fraction of powder compact:

$$P = \frac{6\lambda\gamma_{lv} \cos \theta (1 - w)}{D \cdot w} \qquad [7]$$

Equation [7] has two drawbacks. It involves the wetting angle, θ, which is not always defined and the geometry factor, λ, which may be hard to determine. These problems are avoided if wettability is characterized by work of immersion.

Using the concept of immersional wetting at equilibrium, the capillary pressure or threshold pressure for infiltration, P, can be given as:

$$P_c = (\gamma_{sl} - \gamma_{sn})\frac{S}{V} \qquad [8]$$

where S is the surface area of particulates and V is the volume of void, both per unit volume of powder compact.

Various techniques are available to determine the surface area of particulates per unit volume of powder compact, and void fraction is easily calculated. Equation [8] may be inverted to give the work of immersion, $W_i = \gamma_{sn} - \gamma_{sl}$, as

$$W_i = \frac{P_c w}{S'\rho(1 - w)} \qquad [9]$$

where S' is surface area per unit mass of particulate and ρ is the density of particulate.

The work of immersion is thus a quantitative measure of wettability which is independent of particle size and shape, and of void fraction. Thermodynamics of immersion of a solid into a liquid has been reviewed elsewhere[11] by the authors.

The methods discussed above have been used mostly for wetting organics at room temperature. For liquid metals, only a few experiments[12] have been conducted and these were on large particulates with wetting liquid metals. Thus it is necessary to develop a new experimental technique which is accurate at small particle sizes for nonwetting solid ceramic/liquid metal systems.

III. EXPERIMENTAL METHODS

A. Materials

Silicon carbide (SiC) and boron carbide (B₄C) particulates were used in the wetting experiments. These two ceramic particulates are used frequently for the production of particulate reinforced light metal matrix composites due to their low cost as well as attractive physical properties. The SiC and B₄C particulates with average particle sizes of 9.63 and 8.89 μm, and surface areas of 1.0 and 0.8 m^2/g, respectively, were provided by Norton Company.

Seven different aluminum alloys were used as metal matrices: pure Al, Al-2 pct Cu, Al-4.5 pct Cu, Al-2 pct Si, Al-4.5 pct Si, Al-2 pct Mg, and Al-4.5 pct Mg. The 99.99 pct pure aluminum and 99.9 pct pure silicon were purchased from Atlantic Equipment Engineers in Bergenfield, New Jersey and Aremco Products, Inc. in Ossining, New York, respectively. Al-4.5 pct Cu, Al-2.3 pct Mg, and Al-7.5 pct Mg alloys were ordered from Reynolds Metals Company in Richmond, Virginia. Alloys of Al-2 pct Cu, Al-2 pct Si, Al-4.5 pct Si, and Al-4.5 pct Mg were made from the above four master alloys in an electrical resistance furnace.

B. Powder Specimen Preparation

The most critical step in the wetting experiments was to prepare a uniformly-packed powder specimen. Good packing is required to have a planar liquid front and to eliminate channeling during infiltration. The tamping device which was developed for packing the powder into 0.5 cm I.D., 0.8 cm O.D., 13.5 cm long quartz tubes is shown in Fig-
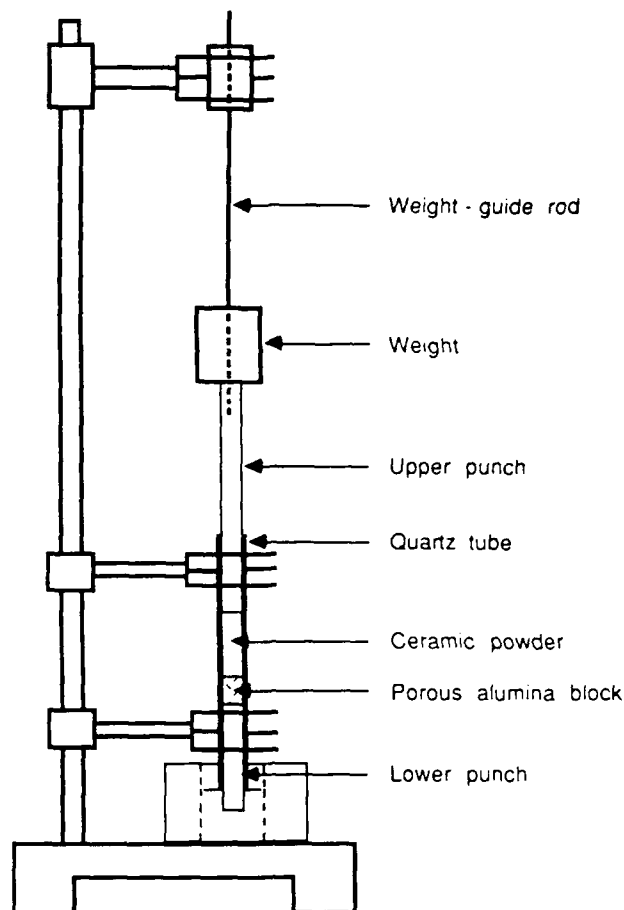
Fig. 3—Sketch of tamping device used to compact powders for infiltration tests.

ure 3. Just above the lower punch inside the quartz tube, a Saffil* paper-wrapped porous alumina block was inserted.

*δ-Al₂O₃ fibers manufactured by ICI.

The Saffil paper was used to close out the gap between filter and quartz tube and to prevent pushing out of powders during compacting and infiltration.

About 0.1 cc of loose powder was placed in the quartz tube; the powder was then subjected to 20 strokes of a 30 g weight from a height of 15 cm. The procedure was iterated until the height of the powder compact reached 3 cm. The measured density of the powder compact was 52 ±1.5 pct of theoretical density of each compound. This relatively low density resulted from the "bridging" of nondeformable angular particulates. After packing, the melt side of the compact was plugged with two layers of 1 mm thick by 5 mm diameter alumina paper. The alumina paper, produced by Zircar Products Inc., in Florida, New York (Cat.# APA-2), is made from Saffil fiber without binder and has 3 pct of theoretical density of alumina. The bottom (powder compact side) of the quartz tube was then capped with aluminum foil and stored in an Ar gas-filled desiccator. Figure 4 shows the SEM images of packed SiC particulates and alumina paper filter.

The outsides of the tubes were coated with ceramic cement (Ceramabond* 590, Aremco Products Inc.) to minimize reaction between the quartz tube and the Al-Mg alloys.

(a)
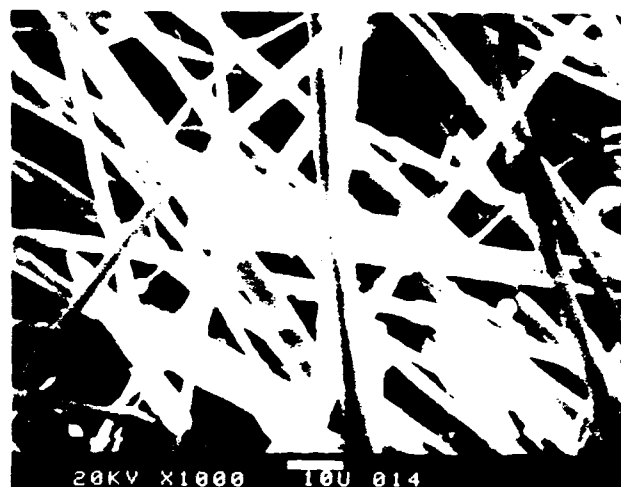
(b)

Fig. 4—SEM micrographs of (a) packed SiC particulates and (b) Saffil paper used as a filter.

After inserting the powder specimens, the desiccator was evacuated for 1 hour and filled slowly with Ar gas up to about 1.1 atmosphere. Before the pressure infiltration test, the desiccator was evacuated one more time for 30 minutes, then filled with Ar gas until the pressure reached about 1.1 atmosphere to prevent influx of air.

C. Pressure Infiltration

The wetting tests were carried out with an apparatus specially designed for this study, shown in Figure 5. The body of the pressure chamber was made of an 18 cm I.D., 19.7 cm O.D., and 27.5 cm long steel cylinder. The cap assembly and bottom portion of the pressure chamber were made of 2024 aluminum alloy. Silicon rubber O-rings were used for sealing between top and bottom and side components.

Each powder specimen was inserted into the melt under an Ar atmosphere and held 5 minutes to achieve isothermal conditions. The quartz tube was inserted in the molten metal (as shown in Figure 5) with the porous alumina block at the top to prevent movement of the powder compact during infiltration. A Saffil paper plug at the bottom of the compact prevented loss of powder and in addition served to skim off Al_2O_3 scum before the melt entered the compact. Pressure was then applied with pressurized nitrogen gas at a rate of 20 kPa/sec up to the predetermined pressure. After a set period of time, normally 5 minutes, the pressure chamber was vented at a rate of 40 kPa/sec. After ventilation of the pressure chamber, the powder specimen was taken out and air-cooled. A typical pressure-time cycle is shown in Figure 6. Infiltration of metal was through the bottom of the compact, as viewed in Figure 5. Low liquid flow rates and hysteresis due to interfacial reactions prevented dewetting after ventilation.

Temperatures of 700, 800, and 900 °C, and three infiltration times were used as experimental variables. Normally, 5 minutes was used as the standard infiltration time, though 2 and 10 minutes were also used to investigate the time dependence of wetting and infiltration.

D. Measurement of Infiltration Distance

After pressure infiltration, the specimens were mounted, sectioned, polished, and the infiltrated distance measured. The threshold pressure was obtained by extrapolating the penetration distance vs pressure curves back to zero penetration. The penetration front was found to be planar to a scale of approximately 1 mm. Polishing difficulties precluded obtaining a micrograph of the interface between infiltrated and noninfiltrated regions. The threshold pressure was either used directly as a measure of wettability or converted to the work of immersion or wetting angle by using the modified capillary pressure equation.

Fig. 5—Sketch of the pressure chamber used for pressure infiltration. The quartz tube containing the packed powder specimen is shown inserted into the melt. A Saffil paper plug is at the bottom and the porous Al_2O_3 plug is at the top.

Fig. 6 — Pressure-time cycle in pressure infiltration test.
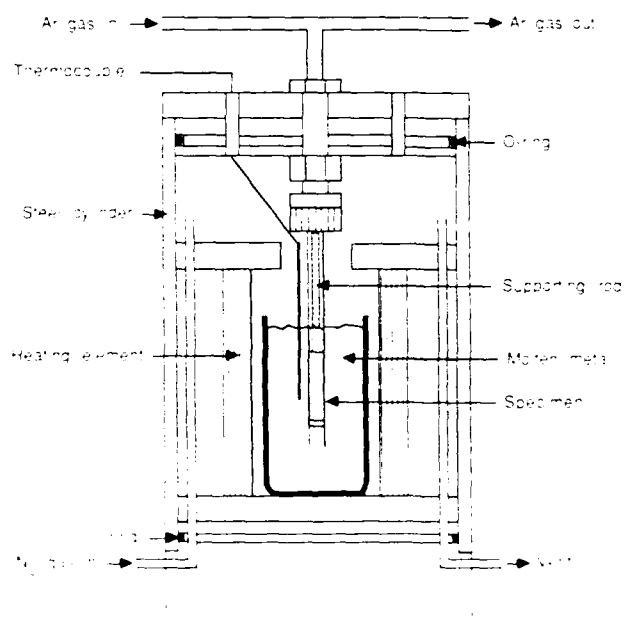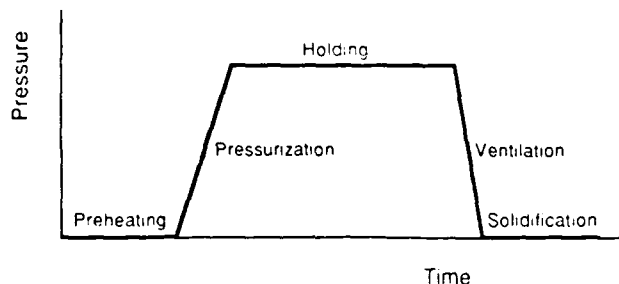
IV. RESULTS AND DISCUSSION

A. Infiltration Behavior

Since wetting was the primary concern of the present work, the experiments were conducted primarily to obtain the threshold pressures for infiltration. As such, the data for infiltration behavior are not sufficient to allow conclusions on the flow behavior of liquid metals into the packed ceramic powder.

Infiltration distances are shown in Figure 7 as a function of applied pressure for SiC and B₄C particulate compacts which were infiltrated with Al-2 pct Mg alloy at 800 °C for 5 minutes. Each data point represents results of a separate experimental run. The linear relationship between the applied pressure and the infiltration distance seems to be typical for nonreactive systems such as SiC/Al-Cu alloy. A linear dependence of infiltration distance on applied pressure was also observed by Fukunaga and Goda[13] when they infiltrated liquid aluminum into a glass fiber preform kept at 600 °C.

The threshold pressure obtained from this experimental technique showed good reproducibility with only ±7 kPa error range.

As shown in Figure 7, the threshold pressure for infiltration in SiC/Al-2 pct Mg system at 800 °C is 565 kPa and the slope of the infiltration distance vs applied pressure of plot is about 0.02 cm/kPa. If hydrostatic equilibrium were obtained, the infiltration distance should have the form:

$$h = \frac{P - P_{th}}{\rho \cdot g} \quad [10]$$

where h is the infiltration distance, P is the applied pressure, P_{th} is the threshold pressure, ρ is the density of liquid, and g is the gravity force. The slope calculated by using Eq. [10], 3.78 cm/kPa, is larger than the experimental result by over two orders of magnitude, which means that equilibrium has not been achieved and infiltration distance is determined by the rate of fluid flow. Since the threshold pressure for infiltration varies with time, it is difficult to predict the infiltration distance as a function of time.

The infiltration behavior of the B₄C/Al-2 pct Mg system at 800 °C, however, is quite different from that of SiC/Al-alloy systems, as shown in Figure 7. The exponential type of relationship between the applied pressure and the infiltration distance is observed when the ceramic/Al-alloy system is reactive, the case for B₄C/Al-2 pct Mg. Details of infiltration behavior will be described by the authors elsewhere.

B. Microstructure of Infiltrated Powder Specimen

The infiltration-tested specimen is composed of 4 different parts: (i) uninfiltrated matrix alloy, (ii) infiltrated Saffil paper, (iii) infiltrated powder compact, and (iv) uninfiltrated powder compact.

The microstructures at the boundaries between metal matrix and Saffil paper and between Saffil paper filter and powder compact in SiC/Al-2 pct Cu system infiltrated at 813 kPa are shown in Figures 8(a) and (b), respectively. As can be seen in the figures, dendritic growth is observed only in the uninfiltrated matrix region. Neither compression nor breakage of Saffil paper was found in the present experiment, although both were reported elsewhere.[14] Also, there was no indication of disruption of the powder compact, especially at the boundary between the Saffil paper filter and powder compact.

A typical microstructure of a SiC powder specimen infiltrated with Al-2 pct Cu alloy at 827 kPa is shown in Figure 9. The microstructure of solidified metal in the infiltrated powder compact differs from that of uninfiltrated metal in several respects: (i) no dendritic growth, (ii) absence of eutectic, and (iii) appearance of Si on SiC particulates.

Optical micrographs revealed that the distribution of particulates is quite uniform with no redistribution during pressure infiltration. The small voids between particulates are evidence of noninfiltration due to a much smaller path than the average size of the capillary channels. Due to the high volume fraction of particulates and high surface-to-volume ratio, a significant amount of SiC was dissolved in the matrix. Details of interfacial reactions are covered in Part II of this article.

V. SUMMARY

1. A pressure infiltration technique was developed to measure the wettability of a packed column of ceramic particulates by a nonwetting liquid metal.

2. The technique was applied to wetting of 10 μm diameter SiC and B₄C particulates with pure molten Al and Al-Cu, Al-Si, and Al-Mg alloys.

3. Threshold pressures for infiltration were measured as a function of time, temperature, and alloy composition with reproducibility of approximately ±7 kPa.

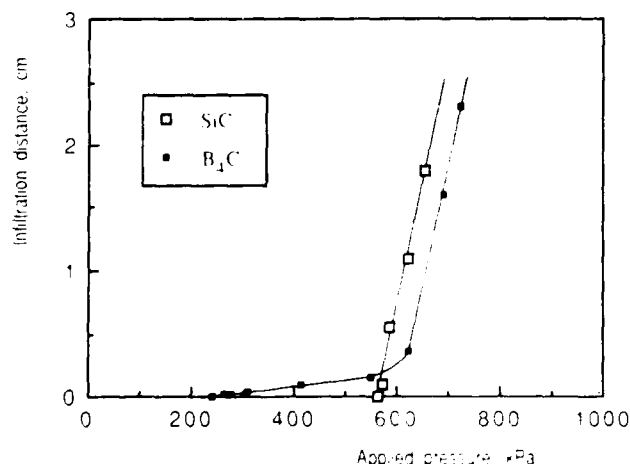4. Microstructures of infiltrated specimens showed planar

Fig. 7 — Variation of the infiltration distance with applied pressure for SiC and B₄C particulate specimens infiltrated with Al-2 pct Mg alloy at 800 °C

(a)

(b)
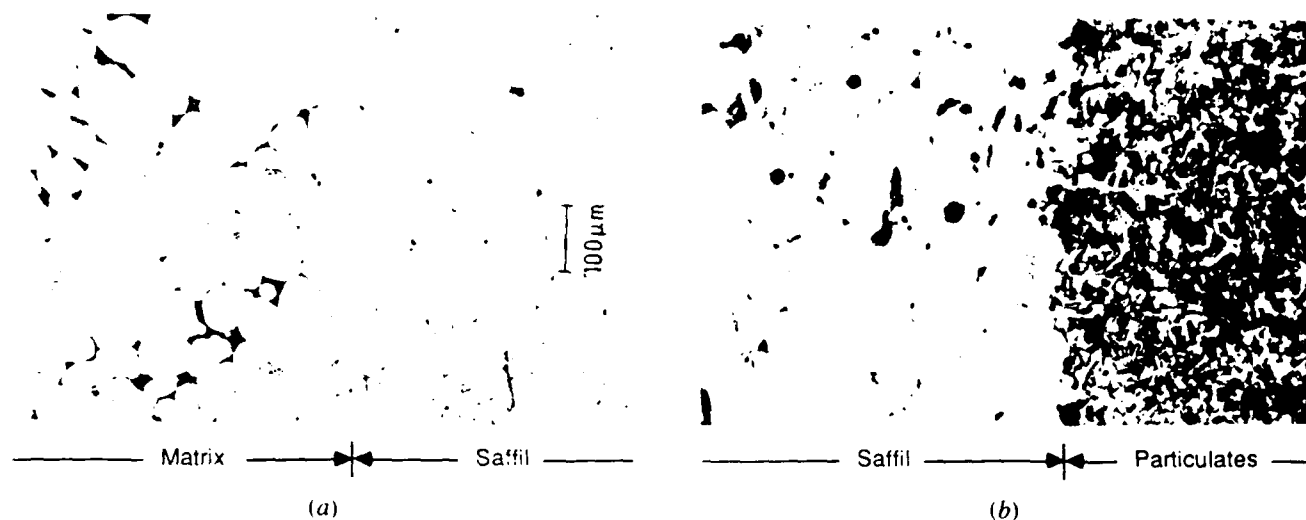
Fig. 8 — Microstructures of SiC particulate specimen infiltrated with Al-2 pct Cu alloy at (a) matrix:Saffil paper boundary and (b) Saffil paper:particulate compact boundary.
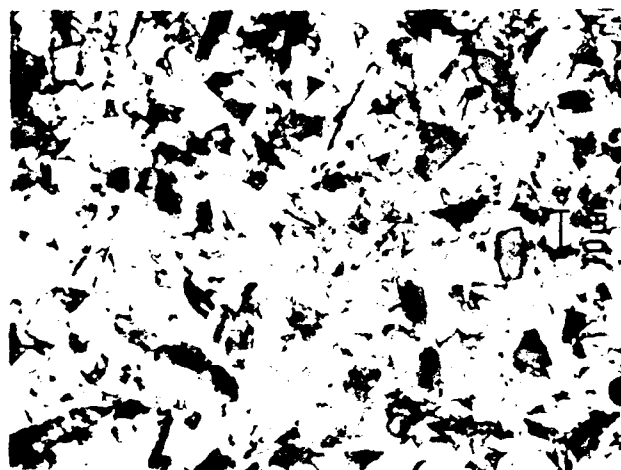
Fig. 9 — Typical microstructures of SiC/Al-2 pct Cu system infiltrated at 800 °C.

front infiltration with uniform distribution of particulates and no disruption during pressure infiltration.

REFERENCES

1. S. Towata, H. Ikuno, and S. Yamata: *J. Japan Inst. Met.*, 1987, vol. 51, pp. 248-55.
2. S.-Y. Oh, J.A. Cornie, and K.C. Russell: *Metall. Trans. A*, 1989, vol. 20A, pp. 533-41.
3. T. Young: *Trans. Roy. Soc.*, 1805, vol. 95, p. 65.
4. A. Dupré: "Théorie Mécanique de la Chaleur", Gauthier-Illars, 1869.
5. A.E. Scheidegger: *The Physics of Flow through Porous Media*, 3rd ed., Univ. Toronto Press, 1974.
6. F.E. Bartell and H.J. Osterhof: *Z. Phys. Chem.*, 1927, vol. 130, pp. 715-23.
7. F.E. Bartell and H.T. Osterhof: *J. Phys. Chem.*, 1928, vol. 32, pp. 1553-71.
8. F.E. Bartell and C.E. Whitney: *J. Phys. Chem.*, 1932, vol. 36, pp. 3115-26.
9. F.E. Hackett: *Trans. Faraday Soc.*, 1922, vol. 17, pp. 160-271.
10. P.C. Carman: *Soil Sci.*, 1941, vol. 52, pp. 1-13.
11. K.C. Russell, J.A. Cornie, and S.-Y. Oh: in *Interfaces in Metal-Matrix Composites*, A.K. Dhingra and S.G. Fishman, eds., AIME, 1986, pp. 61-91.
12. K.A. Semlak and F.N. Rhines: *Trans. AIME*, 1958, vol. 212, pp. 325-31.
13. H. Fukunaga and K. Goda: *Bull. JSME*, 1984, vol. 27, pp. 1245-50.
14. T.W. Clyne, M.G. Bader, G.R. Cappleman, and P.A. Hubert: *J. Mat. Sci.*, 1985, vol. 20, pp. 85-96.

Wetting of Ceramic Particulates with Liquid Aluminum Alloys: Part II. Study of Wettability

S.-Y. OH, J. A. CORNIE, and K. C. RUSSELL

Wetting phenomena in ceramic particulate/liquid Al-alloy systems were investigated experimentally using a new pressure infiltration technique developed by the authors. Studies were performed on two different ceramic particulates, SiC and B$_4$C, with four different liquid aluminum alloy matrices, pure Al, Al-Cu, Al-Si, and Al-Mg. Five major variables tested to study wetting phenomena in ceramic/Al-alloy systems were holding time, melt temperature, alloying element, gas atmosphere, and particulate. Metal:ceramic interfaces were investigated with optical microscopy, SEM, EPMA, and Auger Electron Spectroscopy (AES) in order to understand better the wetting process. The threshold infiltration pressure decreased with temperature as well as with pressurization time for all the ceramic/metal systems. A strong correlation was found between the alloying effect on the threshold pressure and the free energy of formation of oxide phase of the alloying element. More reactive alloying elements were more effective in improving wettability. In air atmospheres, the threshold pressure usually increased markedly as a result of a thick oxide layer formation on the liquid front. Compacts of B$_4$C particulates showed lower threshold pressures than those of SiC particulates. Fracture occurred in a generally brittle manner in infiltrated SiC specimens. AES element profiles on the fracture surfaces showed fast diffusion of Si, and pile-up of C at the metal:SiC boundaries which promoted fracture through the carbon-rich layer. The fracture surfaces of infiltrated B$_4$C specimens indicated plastic deformation, hence a more ductile failure mode.

I. INTRODUCTION

IN metal matrix composites, the primary function of the reinforcements is to support most of the applied load, while that of the matrix is to bind the reinforcements together and to transmit and distribute the external loads to the individual reinforcements. Good wetting is needed to generate a strong enough interface to allow transfer and distribution of load from the matrix to the reinforcements without failure.

However, the wettabilities of ceramic materials with liquid aluminum alloys are poor, *i.e.*, have wetting angles substantially higher than 90 deg even well above the matrix melting temperature. For such systems, application of pressure alone cannot overcome poor wettability in the practical sense due to void formation in the small channels during solidification and debonding during service. Acceptable wettability is thus one of the most important parameters for successful casting of composites.

We report here on measurements of wettability in a pressure infiltration device developed by us. Materials used for this study include 10 μm SiC and B$_4$C particulates, and 4 Al-alloys: pure Al, Al-Cu, Al-Si, and Al-Mg. Major experimental variables were holding time, melt temperature, alloying element, and gas atmosphere. The experimental technique for measuring wettability of ceramic particulates was described in the preceding paper.[1]

II. BACKGROUND

A. Wetting of Ceramic Materials with Liquid Aluminum Alloys

The extremely high oxygen affinity of aluminum makes atmosphere control very important in wetting experiments. The free energy of Al$_2$O$_3$ formation is so high that oxide formation in liquid aluminum alloy systems cannot be avoided without special treatments.

Studies have also been made on the wetting of SiO$_2$,[9-12] SiC,[8,13,14] B$_4$C,[15,16] TiC,[17,18] and TiB$_2$[17,18] by molten aluminum alloys with the sessile drop test. Generally, experimental results show significant differences in wetting angles which are mostly caused by differing experimental conditions, particularly time and oxide formation. For example, John and Hausner[11] showed that a very low wetting angle of Al on Al$_2$O$_3$ could be obtained by maintaining a very low oxygen partial pressure in the system.

In addition to the oxygen partial pressure in the system, holding time and size of liquid metal droplet on the solid substrate may affect the value of wetting angle due to interfacial reactions.

B. Metal:Ceramic Interfaces

Since metal matrix composites are often nonequilibrium systems, there may exist a gradient of chemical potential at the metal:ceramic interface which provides a driving force for interfacial reactions during fabrication or high temperature use. Many investigators[9,12,13,19,20] have suggested that interfacial reactions can promote metal/ceramic wetting.

Although the marked stability of ceramic phases in metal/ceramic systems normally permits only modest mutual solubilities, even small amounts of dissolution can significantly decrease the solid:liquid interfacial energy.

Adsorption is a surface reaction which is concentration, temperature, and diffusivity dependent. The relationship

S.-Y. OH, Research Associate, Department of Materials Science and Engineering, J. A. CORNIE, Principal Research Associate, Energy Laboratory, and K. C. RUSSELL, Professor of Metallurgy and Nuclear Engineering, are with Massachusetts Institute of Technology, Cambridge, MA 02139

between adsorption and temperature, surface energy, and concentration in dilute solutions is given by the Gibbs adsorption equation:

$$\Gamma_B = -\frac{1}{RT}\frac{d\gamma}{d\ln X_B} \qquad [1]$$

where Γ_B is the excess solute concentration at the interface, R is the gas constant, T is the temperature, γ is the surface energy, and X_B is the solute mole fraction. Thus, the greater the adsorption, the more the solute tends to lower the surface energy.

Among the chemical reactions at the metal:ceramic interface, reduction-oxidation (redox) reactions are common. The redox reaction can be represented as:

A (metal) + B (cation in compound)

$\qquad$ = A (cation in compound) + B (metal). [2]
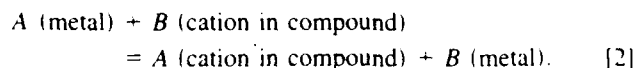
This reaction is reversible and governed by the change in total free energy of reaction. The formation of such complex compounds as spinels or glasses also occurs frequently at the metal:ceramic interface.

Two major types of interaction occur at the interface between a liquid and a solid phase: (i) physical and (ii) chemical. Bonding forces due to physical interactions are typically the order of several kJ/mole, but the bonding forces due to chemical interactions are in the range between tens and thousands kJ/mole.[21] Physical interactions determine the wettability by nonreactive liquids such as water and organics which have tenths of J/m^2 as surface energies. However, chemical interactions are dominant in reactive systems where liquid phases have several J/m^2 as surface energies, and provide most of the bonding energy.

In aluminum alloy matrix composites, interfacial reaction studies have been conducted mainly on oxide systems, such as Al_2O_3,[15,22-25] and SiO_2.[12] Activity in SiC/Al-alloy systems[26-31] has increased rapidly in the past few years.

III. EXPERIMENTAL METHODS

A. Infiltration

Particulates of 9.63 μm SiC or 8.89 μm B_4C were compacted to 52 $\pm$1.5 pct dense 0.5 cm by 3 cm cylinders and pressure infiltrated with one of 7 Al-based alloys. A detailed description of the materials and experimental techniques is given in Part I.[1]

B. Microstructural Analysis

Samples for optical microscopy were prepared by first mechanically polishing with 600 and 1000 grit emery papers, then for 2 minutes each with 6 and 1 μm diamond pastes. Finally, the specimens were polished with 0.05 μm alumina for 30 seconds. Between polishing steps, each specimen was rinsed with ethyl alcohol and ultrasonically cleaned for 10 minutes. Cu-bearing aluminum alloys, Al-2 pct Cu and Al-4.5 pct Cu, were etched with a solution of 4 g $KMnO_4$ and 2 g NaOH in 1 liter of distilled water for 10 seconds, as suggested by Mortensen et al.[32] Other alloys were doubled-etched; with 5 pct HF for 2 to 3 seconds and with same solution as for Al-Cu alloys for 5 seconds. Keller's reagent, a solution of 10 ml HF, 15 ml HCl, 25 ml HNO_3, and 50 ml distilled water, was also used for deep etching.

C. Fracture Surface Preparation

Fracture surfaces of infiltrated powder specimens were analyzed with SEM (AMR or Cambridge) and AES. Since an extensive study on the mechanical properties was beyond the scope of the present work, the specimens were fractured simply clamped in a vise and broken by striking with a hammer. Fractured specimens were coated with approximately 200 Å of gold to give a better image in the SEM. The other halves of fracture specimens were used for AES analysis.

D. Auger Electron Spectroscopy Analysis

Auger electron spectroscopy (AES), using a Physical Electronics Industries Inc., model 590, was used to investigate the surface chemistry of particulates and of the fracture surfaces.

Particulates were embedded in 1 mm thick indium foil and inserted into the analyzing chamber, which was maintained at a pressure of about 10^{-7} Pa. The Auger electron spectroscope was operated at 5 kV and 100 nA. For Ar sputtering, 2 kV and 30 μA/cm^2 were used as electron voltage and beam current.

AES analysis was also performed on fractured specimens in order to determine the chemistry of the metal:ceramic interfacial region. After being fractured by a hammer, the specimens were cut to 1.5 mm thickness. The electron beam conditions included a primary beam voltage of 5 kV and beam current of 100 nA. For depth profile, Ar sputtering was conducted normal to the fracture surface at 4 kV and 70 μA/cm^2.

Depth profiles were obtained by sputtering both in the particulate and in the matrix directions from the fracture surface. The sputtering rate was estimated as 0.1 nm/sec for matrix; the sputtering rates of SiC and B_4C are expected to be much lower.

IV. CHARACTERIZATION OF SPECIMENS

A. Surface Characterization of Ceramic Particulates

The AES profiles which were taken from the as-received SiC and B_4C particulates are shown in Figures 1 and 2, respectively. As seen from the concentration profiles, there were no indications of impurities on the surfaces except small amounts of oxygen.

AES results on the surfaces of SiC and B_4C particulates in uninfiltrated regions before and after infiltration experiments are shown in Figures 1 and 2. Before infiltration, each particulate was preheated for 5 minutes at 800 °C in Ar atmosphere. Including 5 minutes of infiltration time, the particulates were heated for a total of 10 minutes. As can be seen in the AES results, oxygen contents on SiC particulates were reduced during the experiment, while oxygen concentrations of B_4C particulates did not change significantly.

AES results of SiC particulates show that the surface of SiC was cleaned, presumably by reaction of SiC and adsorbed O_2, to form gaseous SiO and either CO_2, CO, or C.[33,34]
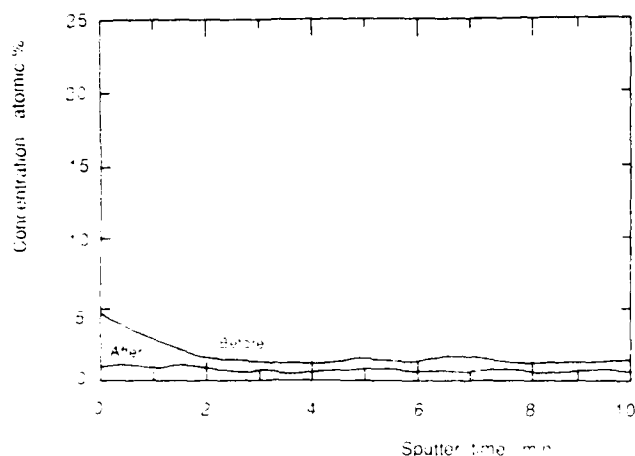
Fig. 1 — AES oxygen concentration profile of SiC particulates before and after infiltration test.

Fig. 3 — Typical microstructure of SiC particulate specimen infiltrated with pure Al at 800 °C.

B. Microstructure of Infiltrated Powder Specimen

A typical microstructure of a SiC powder compact which was infiltrated with pure Al at 724 kPa is shown in Figure 3. In spite of significant amounts of dissolution of SiC particulates, eutectics were seldom found. The eutectics were absent because the pore size in the compact was smaller than the dendrite tip radius characteristic of our cooling rate. Dendritic solidification was thus impossible and the silicon concentration did not reach the level needed for eutectic formation. However, preferential nucleation of Si phase on the particulate surface was found, in agreement with the earlier observations.[34,35,36]

An electron micrograph of a deep-etched SiC/pure Al specimen is shown in Figure 4. The matrix was dissolved in the concentrated Keller's reagent for 30 seconds. The "bridges" in the microstructure are high-Si phases. The serrated surfaces of particulates are evidence of dissolution of SiC on the high-index planes. The concentration of Si in the matrix was measured as about 5 pct with an electron microprobe analyzer. The probe size was too large to obtain a quantitative measurement of the Si content of the bridges.

Different morphologies in the microstructure of top and bottom portions of SiC/Al-2 pct Si samples indicated that the longer metal:particle contact time for the bottom of the powder specimen which was infiltrated first allowed a higher degree of interfacial reaction. In spite of the large variation in the shape of particulates, the matrix microstructures show only a little difference. In the absence of eutectics one would not expect the matrix appearance to vary much with Si content.

Since interfacial reaction rate is a strong function of temperature, it is not surprising to see a variation of microstructure with temperature. Figures 5(a) and (b) show the microstructures of SiC specimens infiltrated with pure aluminum at 930 and 634 kPa at 700 °C and 900 °C, respectively. It is obvious that there was much more interfacial reaction at 900 °C.

A typical microstructure of a B₄C powder specimen infiltrated with pure Al at 758 kPa is shown in Figure 6. Because of the extremely high hardness of B₄C particulates, specimen preparation for metallography was not so successful as with SiC.

Generally, microstructures of infiltrated powder specimens showed almost no porosity and a uniform distribution of particulates.

Fig. 2 — AES oxygen concentration profile of B₄C particulates before and after infiltration test.
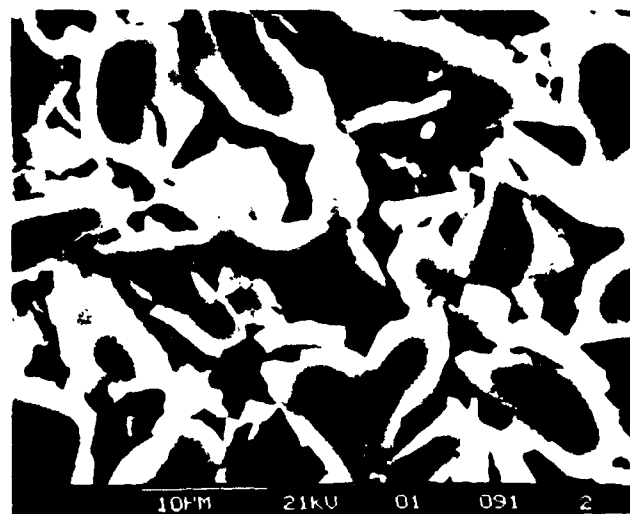
Fig. 4 — SEM micrograph of deep-etched SiC particulate specimen infiltrated with pure Al at 800 °C.
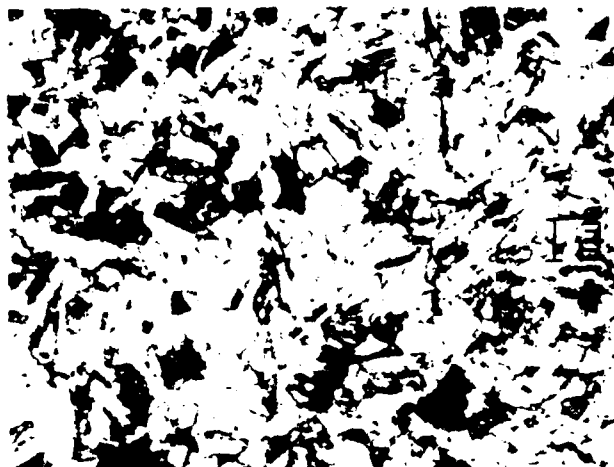
(a)
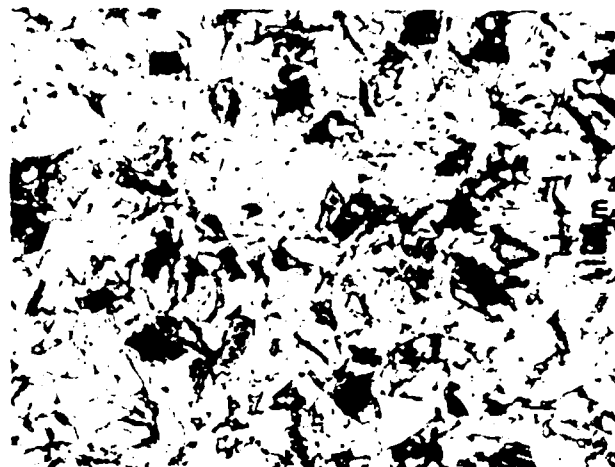
(b)

Fig. 5 — Microstructures of SiC/pure Al system infiltrated at (a) 700 °C and (b) 900 °C.

C. Fracture Morphology

Even though a detailed study of the mechanical properties of infiltrated powder specimens was beyond the scope of the present study, some fracture surfaces of samples broken in bending were examined in order to investigate the metal:ceramic interface. Typical fracture surface morphologies are shown in Figure 7(a) for the SiC/pure Al system, and in Figure 7(b) for the B₄C/pure Al system. The overall fracture morphology of the infiltrated powder specimens was generally unaffected by matrix composition. However, there was a marked difference in the fractographs of different particulate systems, i.e., a more ductile mode in the B₄C/Al-alloy systems. Even though some noninfiltrated regions can be found, debonded interfaces reveal good physical contact between matrix and particulates.

Metal:particulate bonding seems to be weaker for SiC/Al-alloy systems than that of B₄C/Al-alloy systems, as debonding was often found on the fracture surfaces with only a little matrix alloy adhering to the particulate. Fine dimples, indicating ductile fracture, are generally absent from the fracture surface.

(a)

(b)

Fig. 6 — Typical microstructure of B₄C particulate specimen infiltrated with pure Al at 800 °C.

Fig. 7 — Fracture surfaces of (a) SiC particulate and (b) B₄C particulate specimen infiltrated with pure Al at 800 °C.

For B₄C/Al-alloy specimens, Figure 7(b), most of the fracture surface consists of fine, equiaxed dimples, which is indicative of failure by coalescence of microvoids. The process of microvoid formation and coalescence involves considerable localized plastic deformation and requires the expenditure of a large amount of energy, which is an indication of good fracture toughness. However, irregular fracture surfaces due to fine matrix dimples adhering to the B₄C particulates made AES analysis difficult.

V. WETTING PHENOMENA

A. *Effect of Time*

Change of wettability with time is common in solid ceramic/liquid metal systems because several kinetic processes are often involved. The time dependence of the threshold pressure for wetting in SiC and B₄C particulates with liquid aluminum alloys is shown in Figures 8 and 9. Works of immersion, $W_i = \gamma_{sl} - \gamma_{sv}$, are also shown.

Near-equilibrium wettings were achieved in 5 minutes at 800 °C for SiC with pure aluminum, Al-2 pct Si, and Al-2 pct Mg alloys. However, the threshold pressure decreased almost linearly with time for the Al-2 pct Cu alloy.

The time dependence of wetting may be explained in terms of reaction kinetics in ceramic/metal systems. For a system of high reactivity, metal:ceramic interfacial reactions proceed quickly after physical contact between solid and liquid phases. If the reaction products at the interface are stable both chemically and physically, further reaction will be stopped or retarded significantly. Subsequently, the equilibrium wetting occurs in a short time. However, quick wetting equilibrium can also occur in an inert system which does not involve interfacial reactions, such as a water drop on a platinum plate.

In general, wettability is poor and the wetting process is slow for less reactive systems. Therefore, it takes a longer time to reach an equilibrium wetting. Even though SiC/Al-alloy systems are often regarded as chemically inert,[13] a significant amount of dissolution was observed in the present study, as shown in Figures 3 to 5. The high rate of dissolution of SiC in the liquid Al-alloys can be connected to the high surface-to-volume ratio of particulates as well as high Si solubility in Al.

The Al-2 pct Cu and Al-2 pct Si alloys achieved near-equilibrium wetting of B₄C particulates in 5 minutes. For pure aluminum and Al-2 pct Mg alloys, however, the threshold pressures decreased with time, even after 5 minutes.

Chemical reaction-assisted wetting is expected for B₄C particulates in more reactive alloys, such as Al-2 pct Mg. Liquid boron oxide, B₂O₃, exists on the surface of B₄C above 450 °C[?] and enhances wettability through a liquid-liquid reaction when contacted with liquid metal. Cu or Si in aluminum seems to make this chemical reaction less active, probably due to adsorption of the less reactive element, Cu or Si, at the metal:ceramic interface.

Near-linear decreases of wetting angle with time for the SiC/Al system were observed at 980 °C and 900 °C by Köhler[*] and by Halverson et al.,[16] respectively. A linear time dependence of wetting angle was observed in the Al₂O₃/Al system by Brennan and Pask.[11] Achievement of equilibrium wetting in about 5 minutes was reported by

Fig. 8 — Change in threshold pressure and work of immersion with time in SiC/Al-alloy systems.
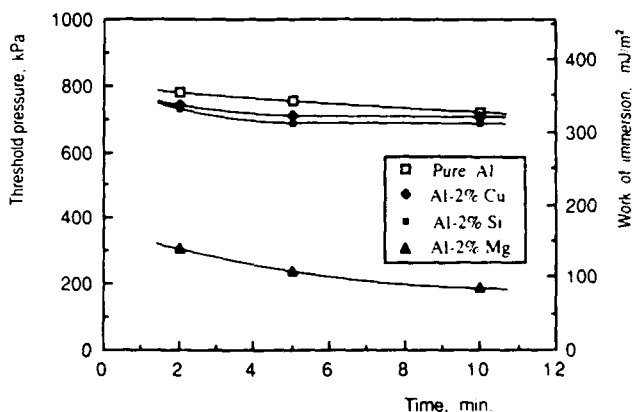
Fig. 9 — Change in threshold pressure and work of immersion with time in B₄C/Al-alloy systems.

Samsonov et al.[37] for the TiC/Al system at 950 °C, and by Ueki et al.[38] for the ZrO₂/Al system at 900 °C.

Breakdown of the oxide layer on the solid ceramic phase either physically or chemically has also been considered as one of the factors affecting the kinetics of wetting.[13,39] Due to the self-cleaning of SiC particulates and liquid oxide layer formation on B₄C particulates, the breakdown of solid oxide films on the ceramic phase is not expected to be a factor in the present systems.

The liquid metal starts infiltration when the applied pressure exceeds the capillary pressure. However, wettability changes with time, mainly due to the reduction of the solid:liquid interfacial energy. If the threshold pressure after time t, $P_{th}(t)$, is smaller than the applied pressure, P_a, infiltration can occur.

Newman's[40] semi-empirical expression for the time dependence of the wetting angle may be applied with minor modification to the time dependence of threshold pressure:

$$P_{th}(t) = P_{th}(eq)[1 + a \cdot \exp(-b \cdot t)] \qquad [3]$$

where $P_{th}(eq)$ is the threshold pressure at equilibrium, and a and b are constants. It was possible to fit our wettability results shown in Figures 8 and 9 to Eq. [3] with constants a, b, and $P_{th}(eq)$ which depend on both matrix composition and particulate type. It is, of course, always possible to fit three data points with a three parameter curve.

B. *Effect of Temperature*

Threshold pressures measured after 5 minutes of holding time for SiC/Al-alloy and B$_4$C/Al-alloy systems are shown as a function of temperature in Figures 10 and 11, respectively, along with works of immersion. As expected, the threshold pressure decreased with temperature for all the ceramic particulate/Al-alloy systems. This effect is thought to be caused partly by changes in surface energies, and partly by faster interfacial reactions at higher temperature.

Variation of threshold pressure with temperature may be due to the different dominant interfacial reactions or kinetics. In many cases, large increases in wettability were observed at 900 °C for ceramic/Al-alloy systems.[3,8,11,39] This behavior has been explained by both the breakdown of oxide film on the ceramic surface[13,39] and by changes in the oxide layer on the liquid metal surface.[3]

Since complex interfacial reactions are involved in the wetting of these ceramic particulates/liquid aluminum alloy systems, it is natural that each system shows a different relationship between wettability and the temperature. We currently lack the knowledge of the physics and chemistry of interfacial reactions required for a detailed explanation of the temperature dependence of wetting in our ceramic/Al-alloy systems.

C. *Effect of Alloying Elements*

There has been no systematic study on the effect of alloying elements on wetting between ceramic and liquid metal. The alloying elements effective in promoting wetting have been found more or less by trial and error.

Figures 8 to 13 show that Mg is the most effective of the alloying elements tested in promoting wetting of both SiC and B$_4$C particulates by aluminum alloys. Conversely, Cu and Si had little or no effect on wettability. Magnesium is especially effective in promoting wetting of B$_4$C. The work of immersion is reduced to 32 mJ/m^2 or, equivalently, the threshold pressure is near zero.

There have been arguments based on the Gibbs adsorption equation, Eq. [2], that small additions of solutes will be sufficient to change the surface energy as long as they can form a monatomic layer at the free surface of liquid or solid:liquid interface. Our experimental results, however, show that the threshold pressure still changes when the solute concentration goes from 2 pct to 4.5 pct.

Liquid aluminum has an extremely high oxygen affinity which makes chemical reactions involving oxygen inevitable at the liquid aluminum:ceramic interface. These interfacial reactions may reduce the interfacial energy of solid ceramic and liquid metal.
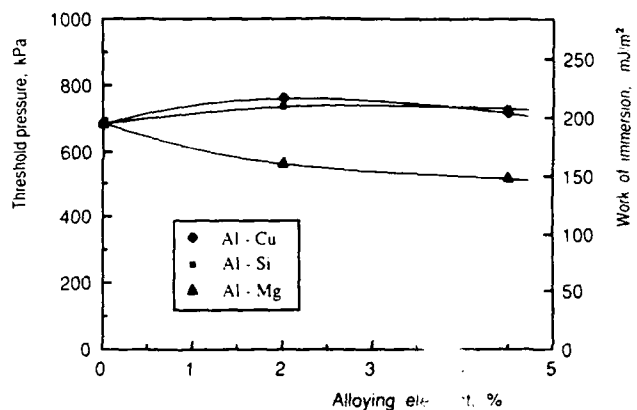
Fig. 10 — Change in threshold pressure and work of immersion with temperature in SiC/Al-alloy systems.
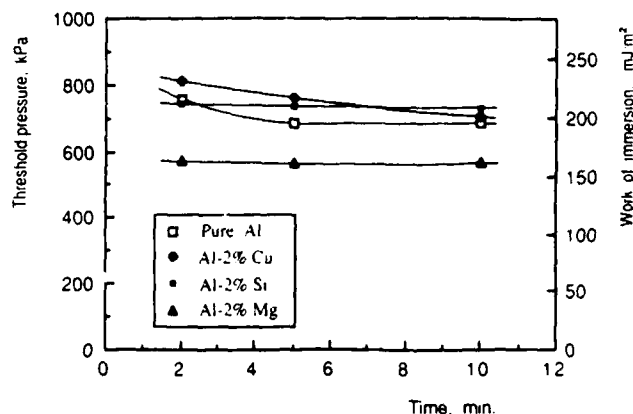

Fig. 12 — Change in threshold pressure and work of immersion with alloying element in SiC/Al-alloy systems.
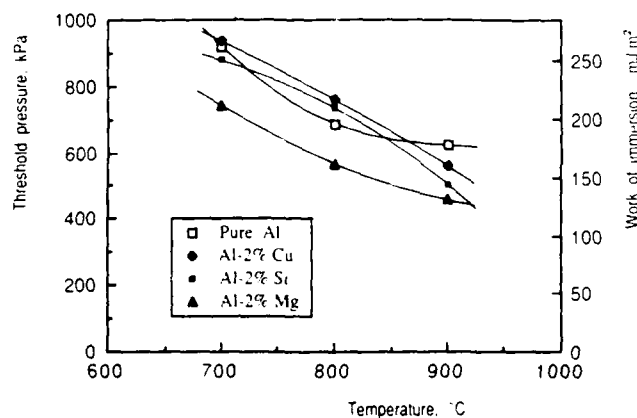

Fig. 11 — Change in threshold pressure and work of immersion with temperature in B$_4$C Al-alloy systems.

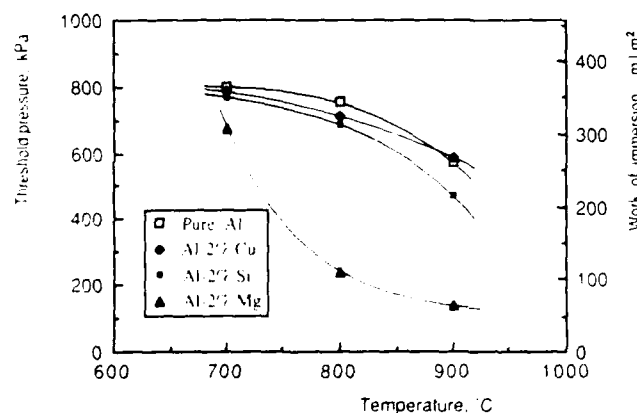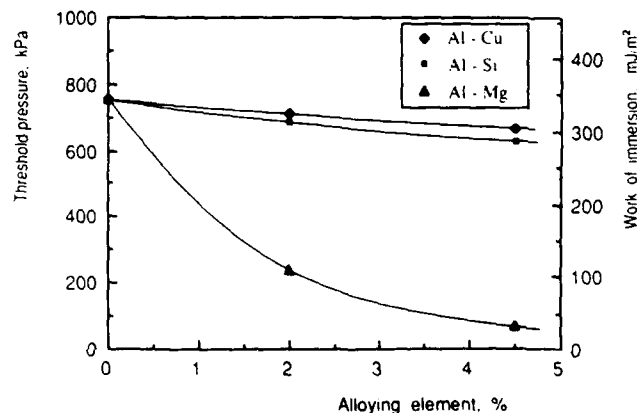Fig. 13 — Change in threshold pressure and work of immersion with alloying element in B$_4$C/Al-alloy systems.

Figures 14 and 15 show the relationship between the free energy of oxide formation of alloying elements and the threshold pressure for wetting in SiC and B$_4$C with aluminum alloys. The free energies of Cu$_2$O, SiO$_2$, and MgO (per mol of gaseous O$_2$) were calculated from JANAF Tables[2] for each infiltration temperature. There is a strong correlation between the free energy of oxide formation and the threshold pressure. The larger the negative values of free energy of formation, the lower the threshold pressures are. However, the effectiveness of alloying varied with temperature and ceramic/metal system.

D. Effect of Gas Atmosphere

The threshold pressures and works of immersion for SiC/Al-alloy and B$_4$C/Al-alloy systems in Ar and air atmospheres are listed in Table I. In most cases, the threshold pressure is greater in air than that in Ar.

An air atmosphere is expected to give greater oxidation of particulates and formation of a thicker oxide layer on the surface of the liquid metal. Obviously, the oxide film on the particulates and the oxide layer on the liquid metal surface change the wetting process as well as wettability.

Since SiO$_2$ has a much lower surface energy, 307 mJ/m^2 1000 °C,[41] than that of SiC, 840 mJ/m^2 at 1200 °C,[39] the wetting angle may increase after oxidation of SiC.
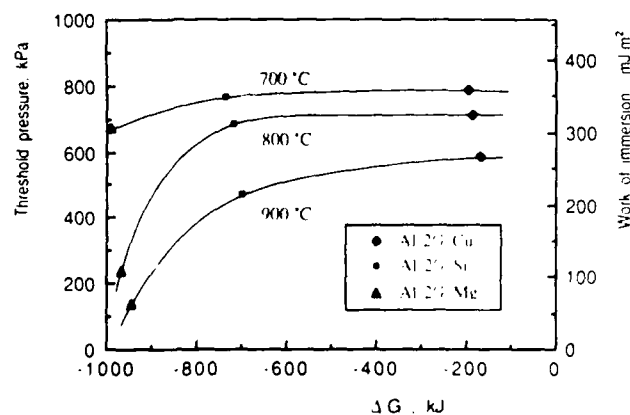
Table I. Threshold Pressure and Work of Immersion for SiC and B$_4$C Particulates in Ar and in Air Atmospheres at 800 °C

System	In Ar		In Air	
	P_{th} (kPa)	W_i (mJ/m^2)	P_{th} (kPa)	W_i (mJ/m^2)
SiC/pure Al	686	197	710	204
SiC/Al-2 pct Cu	759	218	745	214
SiC/Al-2 pct Si	738	212	779	223
SiC/Al-2 pct Mg	565	162	779	223
SiC/Al-4.5 pct Cu	717	206	807	231
SiC/Al-4.5 pct Si	731	210	731	210
SiC/Al-4.5 pct Mg	524	150	731	210
B$_4$C/pure Al	752	344	724	332
B$_4$C/Al-2 pct Cu	710	325	717	328
B$_4$C/Al-2 pct Si	686	314	738	338
B$_4$C/Al-2 pct Mg	241	111	69	32
B$_4$C/Al-4.5 pct Cu	669	306	724	332
B$_4$C/Al-4.5 pct Si	627	287	655	300
B$_4$C/Al-4.5 pct Mg	69	32	69	32

Decreased threshold pressures were observed for some B$_4$C/Al-alloy systems tested in air atmospheres. The decrease in threshold pressure, or increased wettability, is believed to be caused by the formation of a thicker layer of liquid B$_2$O$_3$ on the B$_4$C particulates in an air atmosphere.

VI. INTERFACIAL PHENOMENA

A. Particulates:Atmosphere Reactions

Several studies have been conducted on reactions of SiC with gaseous environments. However, information on the reaction of B$_4$C with gases is scarce. Since the surface characteristics of the solid phase play an important role in wetting, gas-solid reactions should be considered carefully.

The free energies of particulate formation play an important role in interfacial reactions. In spite of some disagreement among different researchers[2,42,43] on SiC, B$_4$C, and Al$_4$C$_3$, it can be estimated that SiC has the most negative value of free energy of formation among the three and that of B$_4$C has the least, making it the least stable. Unlike their carbides, free energies of formation of oxides for Si, B, and Al are very negative, so that both SiC and B$_4$C are very prone to oxidation.

The AES results for SiC before and after infiltration experiment, as shown in Figure 1, show that the surface of SiC was cleaned by the reaction of gaseous SiO formation.

The major oxide on the B$_4$C surface is believed to be B$_2$O$_3$ because of its largest negative free energy of formation. Due to its low melting point, 450 °C,[2] B$_2$O$_3$ on the surface of particulates exists as liquid during the infiltration test.

B. Metal:Ceramic Interface

Ceramic/metal systems are much more stable chemically than metal/metal systems. Therefore, the reactivity at the metal:ceramic interface is usually quite low, generating only a small amount of reaction products. A number of studies[15,17,18,22,29,31,44-53] have been conducted of ceramic:Al-alloy interface phenomena.

Fig. 14 — Relationship between the threshold pressure and free energy of formation of oxide of each alloying element in SiC/Al-alloy systems. Thermodynamic data are from Ref. 2 (per mol O$_2$); free energies were calculated for each infiltration temperature.

Fig. 15 — As for Fig. 14, except for B$_4$C/Al-alloy systems.

The results of Auger analyses performed on a fractured SiC/pure Al specimen obtained by sputtering into the matrix and into the particulate are shown in Figures 16 and 17, respectively. Inside the matrix, the concentration of Al increases rapidly, finally becoming constant. The concentration of C changed in an exactly opposite behavior to Al, as expected. However, the concentration of Si did not change much with sputtering time. This tendency can be explained by fast diffusion of Si after dissolution of SiC particulates, and pile-up of C on the undissolved part of SiC particulates due to its extremely low solubility in Al. Considering the sputtering rate, approximately 0.1 nm/sec, the interfacial region is about 300 Å thick.

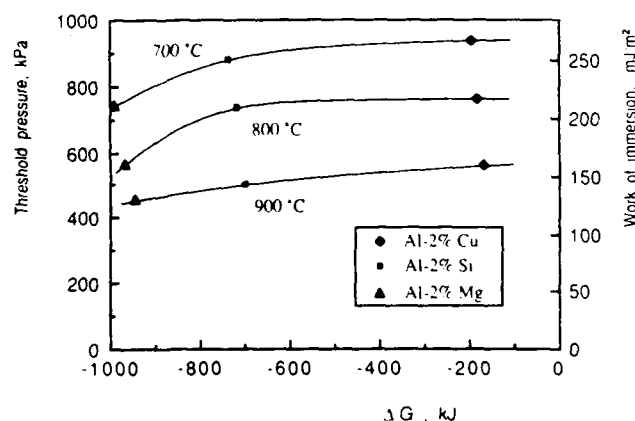In spite of almost zero solubility of B and C in Al, the AES analyses on the fracture surfaces of B_4C/Al-alloy specimens showed similar C profiles as in SiC specimens.

Even though the dissolution of SiC and B_4C were confirmed in various ways, no solid evidence of Al_4C_3 formation was found in the present experiments. This observation may result from the expected extremely small size of Al_4C_3 particles due to short reaction time. Studies[26,29] were made of the reaction of molten aluminum with SiC fibers during short reaction times. Conventional analytic tools including TEM or XRD showed no evidence of Al_4C_3. Of course,
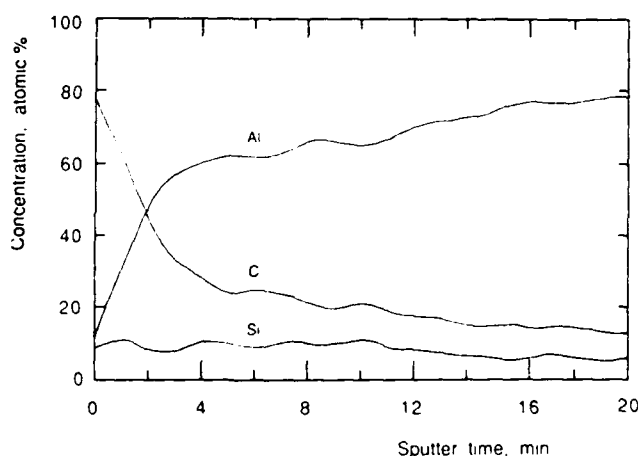
Fig 16—AES element profile for matrix-side from the fracture surface of SiC/pure Al specimen.
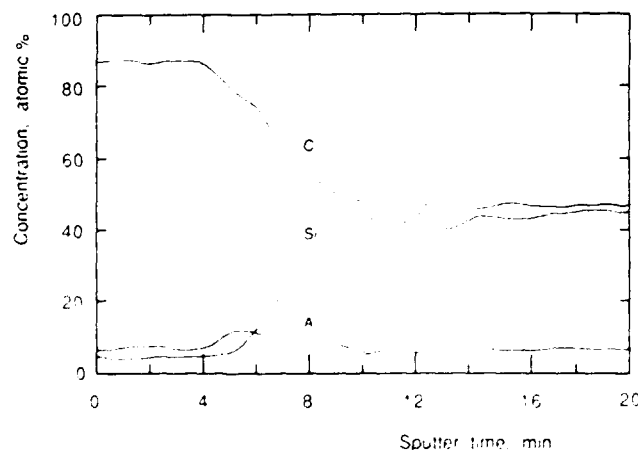
Fig 17—AES element profile for particle-side from the fracture surface of SiC/pure Al specimen

large flakes of Al_4C_3 have been found in the case of long thermal exposure.[27,44]

In general, dissolution of particulates produced a carbon-rich layer at metal:ceramic boundaries where fracture occurred. Due to its slowness, dissolution is believed to commence after infiltration and therefore has little effect on wettability. However, the liquid layer of B_2O_3 is expected to react quickly with liquid aluminum alloys to form oxide compounds, such as $B_2O_3 \cdot Al_2O_3$ and $B_2O_3 \cdot MgO$ during infiltration.

VII. SUMMARY

Five major variables were tested to study wetting phenomena in ceramic particulate/metal systems. Variables include holding time, melt temperature, solute concentration, gas atmosphere, and particulate. The metal:ceramic interfaces were analyzed with optical microscopy, SEM, EPMA, and Auger electron spectroscopy.

The results of this work are summarized in the following statements:

1. The threshold infiltration pressure decreased exponentially with time for all systems, generally approaching the equilibrium value in 5 minutes.
2. The threshold pressure decreased with increasing temperature, probably due to accelerated kinetics of reactions on the solid:vapor, liquid:vapor, and solid:liquid interfaces.
3. Generally, alloying elements which were strong oxide formers were more effective in improving wettability. Mg alloying decreased the threshold pressure in both particulate systems significantly, and Cu and Si had little effect.
4. Threshold pressures were usually higher in air atmospheres as a result of thick oxide layer formation on the liquid front. The decrease of threshold pressure in B_4C/Al-Mg systems in air atmosphere is connected with the formation of a thicker liquid layer of B_2O_3 on the particulates.
5. B_4C particulates showed lower threshold pressures than SiC particulates due to reaction between liquid B_2O_3 and Al alloy.
6. AES element profiles of infiltrated SiC showed fast diffusion of Si and pile-up of C at the metal:ceramic boundary.
7. Fracture occurred in a more or less brittle manner in infiltrated SiC specimens. However, fracture surfaces of infiltrated B_4C specimens showed small dimples which are an indication of plastic deformation. Generally, fracture occurred through the metal:ceramic interfacial region, especially through the carbon-rich layer, which was present on both particulates.
8. The major interfacial reactions affecting wettability are believed to be dissolution of particulates for SiC and liquid:liquid reaction for B_4C particulates.

ACKNOWLEDGMENTS

REFERENCES

1. S.-Y. Oh, J. A. Cornie, and K. C. Russell: *Metall. Trans. A*, 1989, vol. 20A, pp. 527-32.
2. JANAF Thermochemical Tables, 2nd ed., D. R. Stull and H. Prophet, eds., NBS, 1971.
3. J. J. Brennan and J. A. Pask: *J. Am. Ceram. Soc.*, 1968, vol. 51, pp. 569-73.
4. R. D. Carnaham, T. L. Johnston, and C. H. Li: *J. Am. Ceram. Soc.*, 1958, vol. 41, pp. 343-47.
5. J. E. McDonald and J. G. Eberhart: *Trans. AIME*, 1965, vol. 233, pp. 512-17.
6. S. M. Wolf, A. P. Levitt, and J. Brown: *Chem. Eng. Prog.*, 1966, vol. 62, pp. 74-78.
7. J. A. Champion, B. J. Keene, and J. M. Sillwood: *J. Mat. Sci.*, 1969, vol. 4, pp. 39-49.
8. W. Köhler: *Aluminium*, 1975, vol. 51, pp. 443-47.
9. Yu. V. Naidich, Yu. N. Chubashov, N. F. Ishchuk, and V. P. Krasovskii: *Powder Metall. Met. Ceram.*, 1983, vol. 22, pp. 481-83.
10. L. Coudurier, J. Adorian, D. Pique, and N. Eustathopoulos: *Rev. Int. Hautes Tempér. Réfract., Fr.*, 1984, vol. 21, pp. 81-93.
11. H. John and H. Hausner: *J. Mat. Sci. Lett.*, 1986, vol. 5, pp. 549-51.
12. C. Marumo and J. A. Pask: *J. Mat. Sci.*, 1977, vol. 12, pp. 223-33.
13. R. Warren and C.-H. Andersson: *Composites*, April 1984, pp. 101-11.
14. V. Laurent, D. Chatain, and N. Eustathopoulos: *J. Mat. Sci.*, 1987, vol. 22, pp. 244-50.
15. C. R. Manning and T. B. Gurganus: *J. Am. Ceram. Soc.*, 1966, vol. 52, pp. 74-78.
16. D. C. Halverson, A. J. Pyzik, and I. A. Aksay: in *Ceramic Engineering and Science Proceedings*, Am. Ceram. Soc., July-Aug. 1985, pp. 736-44.
17. S. K. Rhee: *J. Am. Ceram. Soc.*, 1970, vol. 53, pp. 386-89.
18. G. A. Yasinskaya: *Sov. Powder Metall. Met. Ceram.*, 1966, vol. 7, pp. 557-59.
19. I. A. Aksay, C. E. Hoge, and J. A. Pask: *J. Phys. Chem.*, 1974, vol. 78, pp. 1178-83.
20. O. B. Kozlora and S. A. Suvorov: *Refractories*, 1976, vol. 17, pp. 763-67.
21. J. V. Naidich: in *Progress in Surface and Membrane Science*, Academic Press, 1981, vol. 14, pp. 353-484.
22. C. G. Levi, G. J. Abbaschian, and R. Mehrabian: *Metall. Trans. A*, 1978, vol. 9A, pp. 697-711.
23. A. Munitz, M. Metzger, and R. Mehrabian: *Metall. Trans. A*, 1979, vol. 10A, pp. 1491-97.
24. I. W. Hall and V. Barrailler: *Metall. Trans A*, 1986, vol. 17A, pp. 1075-80.
25. G. R. Cappleman, J. F. Watts, and T. W. Clyne: *J. Mat. Sci.*, 1985, vol. 20, pp. 2159-68.
26. A. Skinner, M. J. Koczak, and A. Lawley: in *Proc. of the 5th Annual Conference on Composites and Advanced Ceramic Materials*, J. W. McCauley, ed., Am. Ceram. Soc., 1981, pp. 827-40.
27. S. Towata and S. Yamada: *J. Japan Inst. Met.*, 1983, vol. 47, pp. 159-65.
28. T. Iseki, T. Kameda, and T. Maruyama: *J. Japan Inst. Met.*, 1984, vol. 19, pp. 1692-98.
29. S. R. Nutt and R. W. Carpenter: *Mat. Sci. Eng.*, 1985, vol. 75, pp. 169-77.
30. S. R. Nutt: in *Interfaces in Metal-Matrix Composites*, A. K. Dhingra and S. G. Fishman, eds., AIME, 1986, pp. 157-67.
31. S. Inoue, Y. Okuyama, K. Yoshii, and H. Kawabe: *J. Japan Inst. Met.*, 1987, vol. 51, pp. 5-11.
32. A. Mortensen, M. N. Gungor, J. A. Cornie, and M. C. Flemings: *J. Met.*, March 1986, pp. 30-35.
33. G. L. Humphrey, S. S. Todd, J. P. Coughlin, and E. G. King: Bur. Mines Report Invest., No. 4888, July 1952.
34. T. W. Clyne, M. G. Bader, G. R. Cappleman, and P. A. Hubert: *J. Mat. Sci.*, 1985, vol. 20, pp. 85-96.
35. B. P. Krishnan and P. K. Rohatgi: *Met. Tech.*, 1984, vol. 11, pp. 41-44.
36. P. K. Rohatgi, R. Asthana, and S. Das: *Int. Met. Rev.*, 1986, vol. 31, pp. 115-39.
37. G. V. Samsonov, A. D. Panasyuk, and G. K. Kozina: *Sov. Powder Metall. Met. Ceram.*, 1968, vol. 71, pp. 874-78.
38. M. Ueki, M. Naka, and I. Okamoto: *J. Mat. Sci. Lett.*, 1986, vol. 5, pp. 1261-62.
39. B. C. Allen and W. D. Kingery: *Trans. AIME*, 1959, vol. 215, pp. 30-36.
40. S. Newman: *J. Colloid and Interface Sci.*, 1968, vol. 26, pp. 209-13.
41. S. H. Overbury, P. A. Bertrand, and G. A. Somojai: *Chem. Rev.*, 1975, vol. 75, pp. 547-60.
42. F. D. Richardson: *J. Iron Steel Inst.*, Sept. 1953, pp. 33-51.
43. E. T. Turkdogan: U.S. Steel Company, 1970.
44. S. Towata, S. Yamada, and T. Ohwaki: *Tr. Japan Inst. Met.*, 1985, vol. 26, pp. 563-70.
45. A. E. Standage and M. S. Gani: *J. Am. Ceram. Soc.*, 1967, vol. 50, pp. 101-05.
46. H. Mitani and H. Nagai: *J. Japan Inst. Met.*, 1967, vol. 31, pp. 1296-1300.
47. K. Prabriputaloong and M. R. Piggott: *J. Am. Ceram. Soc.*, 1973, vol. 56, pp. 177-80.
48. K. Prabriputaloong and M. R. Piggott: *J. Am. Ceram. Soc.*, 1973, vol. 56, pp. 184-85.
49. K. Prabriputaloong and M. R. Piggott: *J. Electrochem. Soc.*, 1974, vol. 121, pp. 430-34.
50. R. L. Mehan and D. W. McKee: *J. Mat. Sci.*, 1976, vol. 11, pp. 1009-18.
51. A. S. Isaikin, V. M. Chubarov, B. F. Trefilov, V. A. Silaev, and Yu. A. Gorelov: *Met. Sci. Heat Treatment*, 1980, vol. 22, pp. 815-17.
52. A. M. Stoneham: *Appl. Surf. Sci.*, 1982-83, vol. 14, pp. 249-59.
53. F. Delannay, L. Froyen, and A. Deruyttere: *J. Mat. Sci.*, 1987, vol. 22, pp. 1-16.

8816-008

WETTABILITY OF SiC PARTICULATES WITH Zn AND Zn-Al ALLOYS

T. R. Fletcher, J. A. Cornie
Department of Materials Science & Engineering
Massachusetts Institute of Technology
Cambridge, Massachusetts, USA

K. C. Russell
Department of Materials Science & Engineering
Department of Nuclear Engineering
Massachusetts Institute of Technology
Cambridge, Massachusetts, USA

ABSTRACT

The wettability of 8.37 μm SiC particulates with liquid Zn, Zn-4.5Al, Zn-11Al, Zn-27Al, and ZA12 has been studied using pressure infiltration. Threshold pressures for infiltration of compacts of SiC particulates with these metals have been determined experimentally. Works of immersion have been calculated from threshold pressures to obtain a more fundamental measure of wettability.

Figure 1: Schematic diagram of a liquid drop on a solid showing the balance of surface energies and the formation of a contact angle.

REINFORCEMENT OF ZN AND ZN-AL ALLOYS WITH SIC PARTICULATES is expected to improve their strength to weight ratio and dimensional stability while utilizing their advantages of relatively low cost and low processing temperature. Possible applications include transmission gears and other automotive parts. Fabrication of particulate metal matrix composites by casting is potentially one of the most attractive processing routes, but its success depends upon good wettability between the liquid metal and the ceramic particulate. In this paper, wettability has been measured by pressure infiltration of liquid metal through a uniformly packed powder specimen, as was done by S.-Y. Oh et al. for Al-alloy matrix composites with SiC and B4C dispersoids(1).

BACKGROUND

WETTABILITY-Wettability can be simply defined as the ability of a liquid to wet a solid surface. When wetting is complete, the liquid forms an even continuous film over the solid surface. The extent of wetting depends upon the surface energies important in the particular physical setup. For example, the equilibrium configuration of a drop of liquid resting upon a flat solid surface is determined by the balance between liquid-vapor interfacial energy γ_{lv}, solid-vapor interfacial energy γ_{sv} and solid-liquid interfacial energy γ_{sl}, as shown in Figure 1. This balance determines a contact angle between the liquid and solid, which is commonly used as a measure of wettability.

However, wettability can also be measured by the work necessary to immerse a solid in a liquid(2). This method is more appropriate to measurements being made on particulate material. As pictured in Figure 2, the work of immersion is the work done on the system in exchanging a solid gas interface for a solid liquid interface or

$$W_i = \gamma_{sl} - \gamma_{sv} \qquad (1)$$
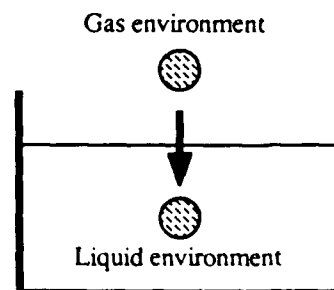
Figure 2: Illustration of immersional wetting for a solid particle. The work of immersion is $\gamma_{sl} - \gamma_{sv}$.

When the infiltration distance of a liquid metal into a particulate ceramic compact is measured as a function of applied pressure at constant time it is found that some non-zero pressure must be applied before infiltration will occur [1]. A threshold pressure for infiltration of fibrous ceramic preforms has also been observed [3,4]. The work of immersion is related to the threshold pressure through the following equation [1,5]:

$$W_i = \frac{P_{th}w}{(1-w)\rho S'}$$

(2)

where w is the void fraction of the compact, ρ the density of the particulate and S' the surface area per unit mass of particulate. The derivation assumes that infiltration takes place reversibly and can be described in simple thermodynamic terms.

FLUID FLOW-The usual way to describe flow through a porous medium is with Darcy's law. For unidirectional flow Darcy's law can be written as:

$$v_0 = \frac{K}{\mu}\frac{dP}{dx}$$

(3)

where v_0 is the superficial velocity of the fluid (the velocity of the fluid as measured by the volumetric flow rate per unit cross sectional area where the cross section is taken perpendicular to the average direction of flow), K is the permeability of the medium, μ is the viscosity of the liquid metal, and dP/dx is the pressure drop at the infiltration front. Gravity effects have been neglected in this formulation. The equation which relates the superficial velocity v_0 to the actual velocity dL/dt in the porous medium by means of the void fraction of the medium w is:

$$v_0 = w\frac{dL}{dt}$$

(4)

Under conditions of constant permeability and constant pressure, Eq. (3) and Eq. (4) can be combined and integrated to obtain the following relationship between infiltration length L, time t, and pressure drop due to viscous drag $\Delta P\mu$:

$$\frac{L}{\sqrt{t}} = \sqrt{\frac{2\Delta P_\mu K}{\mu w}}$$

(5)

When a threshold pressure is necessary for infiltration and caused by capillary effects, $\Delta P\mu$ is equal to the total pressure drop ΔP_T minus the the capillary pressure drop ΔP_γ [3,4]. In this work, ΔP_T is measured experimentally as P_{app}. Therefore, if P_{th} is taken as ΔP_γ, Eq. (5) can be rewritten as:

$$L = \frac{2K}{\mu w}\sqrt{(P_{app}-P_{th})}\sqrt{t}$$

(6)

The parabolic infiltration predicted above has been observed for dynamically monitored infiltration of Saffil alumina fiber preforms with molten aluminum [3,4]. However, static measurements of the infiltration of 10 mm SiC particulates with Al alloys show a linear relationship between L and $(P_{app}-P_{th})$ for a given

holding time at pressure [1]. The linear behavior may be due in part to the dependence of threshold pressure on hold time observed for some alloys [6]. A more thorough investigation of this unusual infiltration behavior is planned.

EXPERIMENTAL METHODS

MATERIALS-The SiC particulates used had a mean diameter by volume percent of 8.37 μm and a surface area of 870 m^2/kg as measured by BET. The Zn used was of 99.99% purity; the Al used to prepare the alloys was of 99.999% purity. The alloys tested were Zn-4.5 Al, Zn-11Al, Zn-27 Al, and commercial alloy ZA12. ZA12 composition limits are: 10.5 to 11.5 Al, 0.5 to 1.0 Cu, 0.01 to 0.02 Mg, 0.005 max Pb, 0.075 max Fe, 0.05 max others (total), with the remainder Zn. The Zn-Al phase diagram is shown in Figure 3.
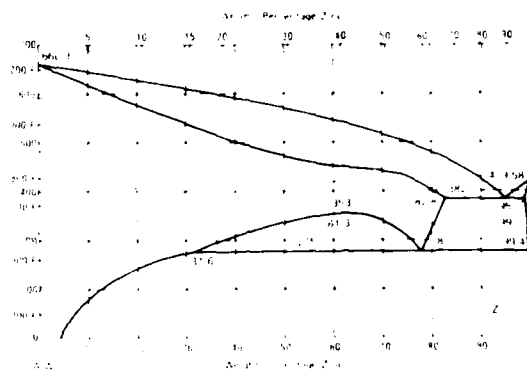
Figure 3: Al-Zn phase diagram (7).

COMPACT PREPARATION-Compacts of approximately uniform density were prepared as described in reference 1. In these experiments, the average compact void fraction,w, was 47% with a standard deviation 1.3%. This w value is similar to that obtained in previous work (1)

PRESSURE INFILTRATION-The device used to perform the pressure infiltration experiments is shown schematically in Figure 4. Each specimen was immersed in the liquid metal and allowed to preheat for about 5 minutes before the chamber was pressurized with N_2 gas. An Ar atmosphere was maintained in the compact during infiltration. After 5 minutes, the chamber was vented , the specimen was removed from the melt and allowed to air cool, and the infiltration length was measured.

22
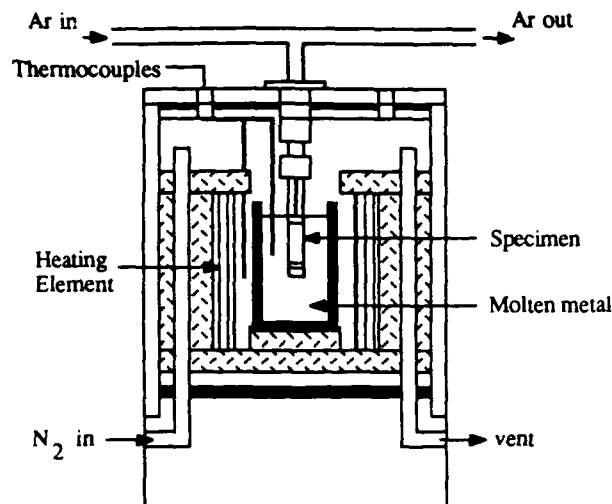
Figure 4: Sketch of the pressure chamber used for pressure infiltration.

a) Linear Fit

Pth = 822 kPa

b) Parabolic Fit

Pth = 847 kPa
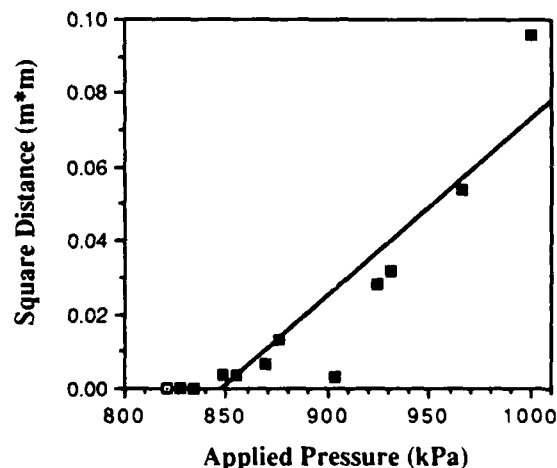
Figure 5: Plots of infiltration distance versus applied pressure for Zn at 645 +/- 5 C.

INFILTRATION RESULTS

A typical plot of infiltration distance versus applied pressure is given in Figure 5. As shown in the figure, the fluid flow behavior is neither perfectly linear nor parabolic. This is partially due to the limitations on infiltration imposed by compact length; with a longer compact it might be possible to observe more of the drop-off in infiltration length at higher pressures characteristic of parabolic infiltration. Some scatter also exists in the data, along with a few points with abnormally low infiltration distances which may be caused by a different mechanism. If the infiltration behavior of Zn alloys is similar to that of Al alloys, infiltration distances may also be influenced by a variation in threshold pressure with holding time. A better measurement of fluid flow behavior would be obtained by measuring infiltration distance as a function of time during the infiltration; development of this kind of dynamic measurement technique for ceramic compacts is in progress.

THRESHOLD PRESSURE AND WORK OF IMMERSION RESULTS

The threshold pressure for infiltration is taken as the intercept of a penetration distance versus pressure curve fitted to the data. Both linear and parabolic fits to non-zero infiltration distances were used in order to determine the difference in predicted threshold pressure. The results are given in Table 1.

Table 1: Threshold Pressures for Zn-Al Alloys

METAL	TEMPERATURE	Pth (LINEAR FIT)	Pth(PARABOLIC FIT)
ZN	545 ^{0}C	841 kPa	872 kPa
	645 ^{0}C	822 kPa	847 kPa
ZN-4.5AL	545 ^{0}C	835 kPa	869 kPa
ZN-11AL	545 ^{0}C	1200 kPa	1200 kPa
	645 ^{0}C	819 kPa	852 kPa
ZA12	645 ^{0}C	830 kPa	857 kPa
ZN-27AL	545 ^{0}C	1210 kPa	1210 kPa
	645 ^{0}C	845 kPa	871 kPa

The difference in absolute values of threshold pressure obtained by linear and parabolic fits for any alloy is less than five percent. In addition, the differences in threshold pressure between alloys are about the same for the two fits. For simplicity, the threshold pressures are taken to be those obtained with a linear fit. These are shown in Figure 6. The uncertainty in intercept associated with curve fitting is such that the differences in threshold pressure among the alloys are probably not significant except for the case of Zn-11Al and Zn-27Al at

545 ^{0}C . These two alloys show a much higher threshold pressure, about 1200 kPa as compared to about 830 kPa. Using 47% as the average compact void fraction and 3217 kg/m^3 as the density of SiC, threshold pressure data has been converted into work of immersion data and displayed in Figure 7. These work of immersion values, about 0.380 J/m^2 for Zn-11Al and Zn-27Al at 545 ^{0}C and 0.263 J/m^2 for the rest of the alloys, are the same order of magnitude of those obtained for Al alloys (6).
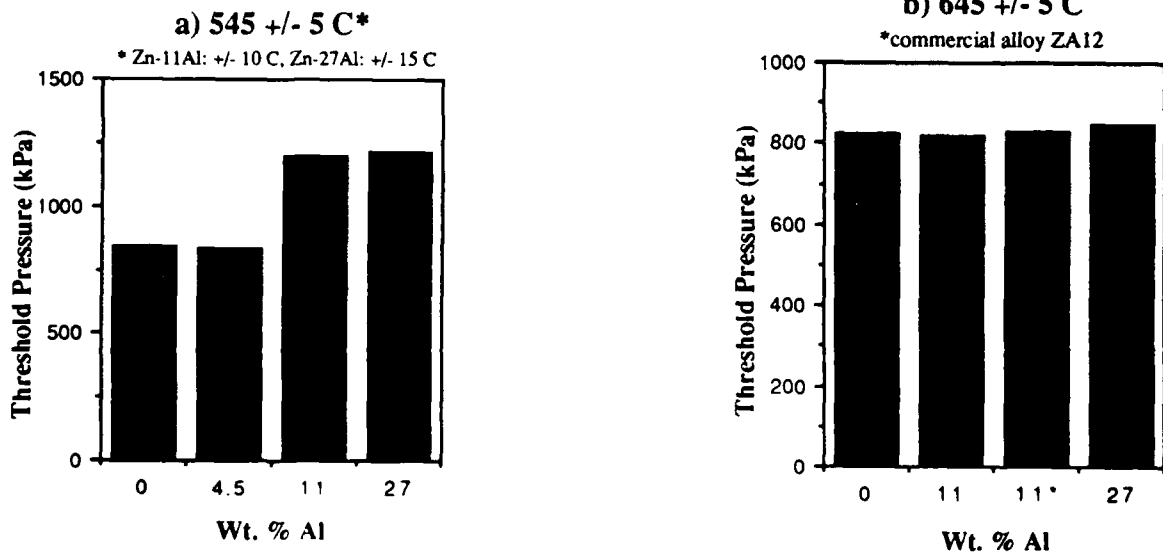
Figure 6: Threshold pressures for Zn-Al Alloys.

Work of Immersion for Zn-Al Alloys

a) 545 +/- 5 C*

*Zn-11Al: +/- 10 C, Zn-27Al: +/- 15 C

b) 645 +/- 5 C

*commercial alloy ZA12

Figure 7: Work of immersion for Zn-Al Alloys.
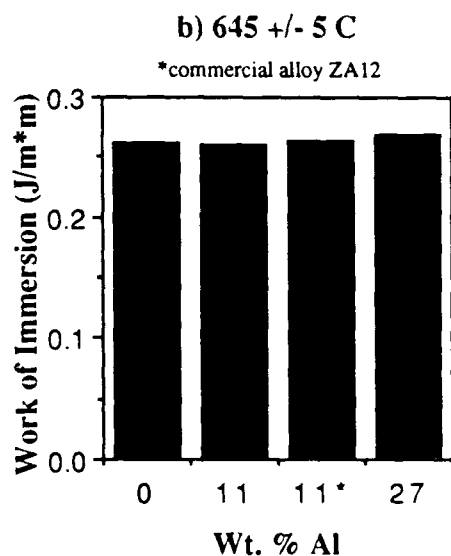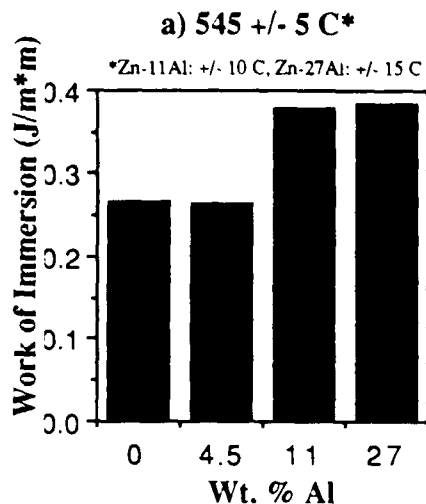
SUMMARY

1. Threshold pressures for Zn at 545 ^{0}C and 645 ^{0}C, Zn-4.5Al at 545 ^{0}C, Zn-11Al at 645 ^{0}C, ZA12 at 645 ^{0}C, and Zn-27Al at 645 ^{0}C are all about 830 kPa. This converts to a work of immersion of 0.263 J/m^2.

2. Threshold pressures for Zn-11Al and Zn-27Al at 545 ^{0}C are about 1200 kPa. This converts to a work of immersion of 0.380 J/m^2.

REFERENCES

1. S.-Y. Oh, J.A. Cornie and K.C. Russell, Met. Trans. A in press.

2. H. J. Osterhof and F. R. Bartell, J. Phys. Chem. 34, (1930), 1399-1411.

3. L. J. Masur, PhD Thesis, Department of Materials Science and Engineering, MIT, February 1988.

4. T. Wong, B.S. Thesis, Department of Mechanical Engineering, MIT, January, 1988

5. A. Mortensen and J.A. Cornie, Met. Trans, 18A (1987), 1160-1163.

6. S.Y. Oh, J.A. Cornie and K.C. Russell, Met. Trans. A in press.

7. "ASM Metals Reference Book", 2nd ed, American Society of Metals, Metals Park, Ohio (1983), p. 481.

INTERFACE CHEMISTRY OF
INORGANIC COMPOSITE MATERIALS

Andreas Mortensen

Department of Materials Science and Engineering
Massachusetts Institute of Technology, Cambridge, MA 02139, USA.

ABSTRACT

Interfaces in metal and ceramic composites differ from interfaces in polymer matrix composites inasmuch as: (i) fiber degradation due to chemical reaction with the matrix at processing temperatures is frequent and (ii) bonding at the interface is generally chemical in nature (i.e. features primary chemical bond formation across the interface). Elementary analysis of requirements placed on the interface for mechanical property optimization indicate that, for toughening by fiber debonding and pull-out, very weakly bonded interfaces are needed. Sufficiently weak interfaces can be obtained by using interfacial layers of materials such as graphite or boron nitride which feature strongly anisotropic chemical bonding. Several tough inorganic composite utilize such interfaces. With large fibers in ductile matrices, however, strong interfaces are desirable if the matrix can provide sufficient resistance to crack propagation.

1. INTRODUCTION

The interface in polymer matrix composites is at this day engineered to a level of sophistication that is rather impressive in comparison with what is generally achieved with inorganic matrix composites. The chemistry of thermosetting polymer resin bonding to hydrophilic glass fiber surfaces via silane coupling agents, as well as the various oxidative treatments that are applied to carbon fibers, have been shown to influence processing and properties of polymer matrix composites to a significant degree via complex chemical tailoring of the bond between the matrix and the fiber (Plueddemann 1974; Hull 1981; Knox 1982; Chawla 1987). Reasons for this state of affairs are numerous and include the head-start research on polymer matrix composites has had, as well as composite processing temperatures that are much lower and do not present fiber-matrix chemical compatibility problems. There are, however, a few other differences between these two types of composites which may point to a slightly different approach in chemical tailoring of the interface for inorganic composites.

Since the volume on interfaces in metal matrix composites edited in 1974 by Metcalfe, no review of interface chemistry nearly as extensive has been published for either metal or ceramic composites, in spite of the fact that such a work would presently be very different in scope and content. Many of the concepts, of the chemical processes, etc. described in that volume still are true and relevant today, such as the recurrent concern with excessive fiber-matrix reactivity in inorganic composites, which places severe restrictions on possible materials systems and processing conditions. New reinforcements, new processing methods and novel characterization

techniques, coupled with a better understanding of the requirements placed on the interface in composites have however emerged since then, justifying a summary of the topic that would be both more extensive, more multidisciplinary and longer: a task much beyond what is attempted here. The present article will therefore seek to briefly summarize in very broad terms where the question stands at present. Specifically, the logic underlying some of the most successful inorganic composites produced to date will be outlined, to provide some indication of how the properties of inorganic composites can be improved by proper chemical engineering of their interface. For simplicity, the discussion is limited to the case of parallel fiber reinforced composites.

2. MECHANICAL REQUIREMENTS AT THE INTERFACE

The first requirement we place on the interface is evidently that the strength of the fibers be preserved. This requirement precludes chemical reactions between the fibers and the matrix that lead to the formation of too thick a reaction layer of low strain to failure, or to the creation of notches on the fiber surface. This requirement, although rather obvious from the point of view of the mechanics of the interface, may be far from obvious from the point of view of processing, as illustrated for example in SiC whisker reinforced RBSN (reaction bonded silicon nitride, Haggerty 1988), Fig. 1. Fiber degradation by chemical reaction with the matrix is still the most frequent cause for poor inorganic composite properties.

Assuming now that fiber strength is preserved, we can place several conflicting requirements on the interface.

2.1. The interface must not be too strong if a strong composite in which toughening mechanisms specific to composite materials and opposing fracture perpendicular to the fibers are to be exploited. This principle has been theoretically and experimentally proven by numerous authors, as summarized in various articles and monographs (Hull 1981; Kelly 1970, 1971; Kelly and Macmillan 1986; Wells and Beaumont 1985 a&b; Evans and McMeeking 1986; Chawla 1987). Resulting fracture energies are very high: polymer matrix composites can feature apparent fracture energies as high as those of unreinforced metals (Ashby and Jones 1980).
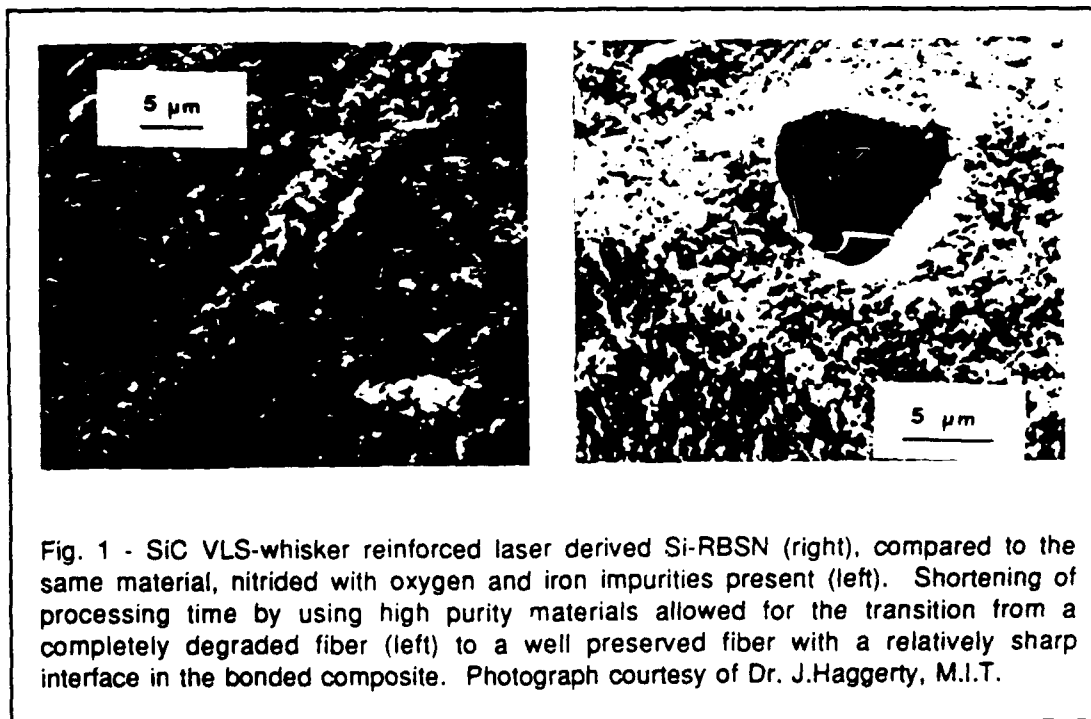
Fig. 1 - SiC VLS-whisker reinforced laser derived Si-RBSN (right), compared to the same material, nitrided with oxygen and iron impurities present (left). Shortening of processing time by using high purity materials allowed for the transition from a completely degraded fiber (left) to a well preserved fiber with a relatively sharp interface in the bonded composite. Photograph courtesy of Dr. J.Haggerty, M.I.T.

The dependence of strength and toughness on the interface varies according to the system and its modeling. One can simplify the role of the interface by consideration of two parameters: the resistance of the interface to initial fracture and its resistance to sliding motion of the matrix against the fiber after debonding. The latter parameter, τ, is mostly a function of physical properties of the interface, in particular its smoothness after debonding. Although τ, as well as other parameters (such as fiber flaw size and distribution) that intervene in composite toughening mechanisms can be varied by chemical tailoring of the interface, the connection between these parameters and interface chemistry is not obvious and has to date not been extensively exploited.

Composite toughening mechanisms are dependent on initiation of debonding at the fiber-matrix interface. Initiation of such debonding has been analyzed by Kendall (Kendall 1975 & 1976; Kelly and Macmillan 1986) in terms of an energy balance, leading to the result that for crack deflection to occur at a planar interface perpendicular to a short crack in an elastically homogeneous material, the fracture energy g_i of the interface must be less than a value given by:

$$\frac{g_i}{g} < \frac{1}{4 \pi (1 - v^2)} \qquad (1)$$

where g is the fracture energy of the material, and v its Poisson ratio. This relation has been modified by Kendall (1975) to account for the effect of crack length as well as differences in modulus accross the interface, all effects resulting in variations of this ratio by a factor significantly less than an order of magnitude. Agreement with experimental work by Kendall (1975,1976) on model samples of rubber was very good. Equation (1) may be an oversimplification of the problem (the effect of elastic inhomogeneity across the interface on crack tip stresses is appreciable, as discussed by Swenson and Rau 1970; Erdogan 1972, Shorshorov, Ustinov, Zirlin and Olefirenko 1979; Erturk, Gupta, Argon and Cornie 1987), but it does indicate that very low values of the interfacial fracture energy g_i are required for crack deflection to occur.

There is little question that for tough brittle matrix composites, these energy absorption mechanisms that are specific to composite materials and rely on weak interfaces are important. With ductile matrix composites, however, the desirability of weak interfaces is less evident since the matrix itself can contribute significantly to the work of fracture by plastic deformation. In W-Cu and B-Al composites, fracture energy has been shown to increase with increasing fiber diameter, matrix volume fraction and matrix ductility. Data clearly indicate that the main contribution to fracture energy in these composites emanates from matrix deformation (Cooper and Kelly 1967; Olster and Jones 1974; Prewo 1976, 1980; McDanells and Signorelli 1976; Kelly and Macmillan 1986). However, most fibers that are present candidates for low cost metal matrix composite reinforcement are rather small in diameter, usually below 20 μm. From data by Cooper and Kelly (1969), the fracture energy of copper reinforced with 50 volume per cent tungsten fibers 20 μm in diameter would be below 10 kJ/m^2, which is already in the low range for metals (Ashby and Jones, 1980). A weak interface for initiation of crack deflection may therefore also be desirable in a large number of fiber reinforced metals of current interest, because fiber diameters are now usually small.

2.2. The interface must not be too weak. This requirement is primarily dictated by the desire to preserve off-axis strength. Otherwise, the composite will fail at the interface, much as the carbon fiber reinforced aluminum sample in Fig. 2. An illustration is provided by comparing the transverse strength of two aluminum matrix composites: one, in which the reinforcement was 35 Vol% *Fiber FP*^{TM} alumina fibers and the matrix Al-3Li, exhibited a transverse strength of 142 MPa with fracture mainly through the matrix, indicating a very strong interfacial bond (resulting
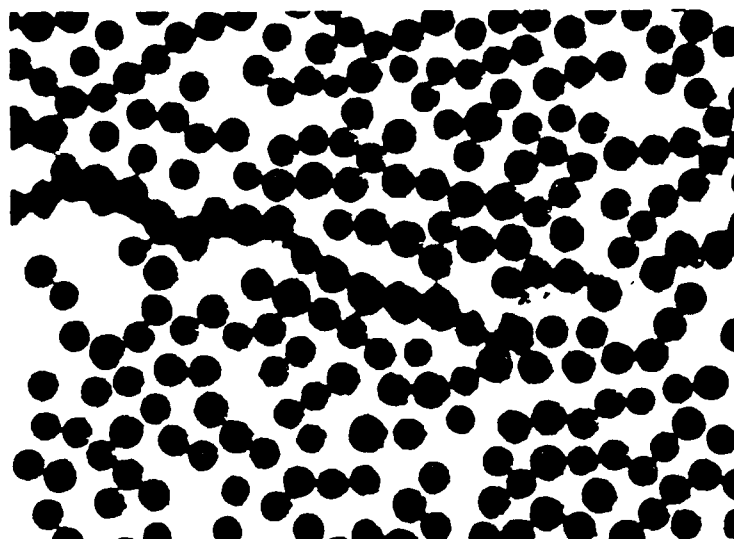
Fig. 2 - Interrupted transverse tension test in Pitch 55 carbon fiber reinforced 2024 aluminum. Fracture initiated at the interface, which is weak in this composite. Average fiber diameter is 10 μm. Photograph courtesy of Prof. T.Erturk, University of Lowell and Dr. J. Cornie, MIT.

from reaction of Li with the Al_2O_3 fibers, Page and Leverant 1985); the other, where aluminum alloys were reinforced with 43 volume percent Pitch 55 carbon fibers, exhibited much lower transverse strengths between 42 and 14 MPa, with fracture mostly through or near the interface as in Figure 2 (Erturk, Cornie and Dixon 1986). Variations of such magnitude can also result from variations in fiber distribution, in particular by suppression of fiber to fiber contact points (Towata and Yamada 1986 a & b), or from differences in matrix strength. Whether fracture takes place along a row of touching fibers as in Fig. 2 or involves some crack propagation through the matrix, analysis of the problem when the interface is weak must again include g_i

(neglecting here any dependence of g_i on crack propagation mode). Low g_i results in low composite transverse strength.

It is realized that the present discussion is centered about a simplified description of the incidence of interface properties on composite strength and toughness. On this most elementary level, however, it is clear that for many inorganic composites, there exists an optimum in the bond strength that is desired at the interface, and that the nature of this optimum will vary significantly with the matrix (assuming fibers are brittle). With matrices unable to contribute significantly to composite toughening, that optimum will be at a very low value of g_i. When the matrix can blunt cracks and increase the work of fracture, a strong interface is desired. Chemical tailoring of the interface will therefore hinge upon attainment of a wide range of values of g_i for the various composites discussed here. It therefore is of interest to address the general character of bonding at the interface in inorganic composites.

3. CHEMICAL NATURE OF INTERFACES

3.1. Sharp interfaces. Interfaces that are sharp on the atomic scale are generally classified into several categories, according to the nature of the bond across the interface. The classification more or less follows that of chemical bonds in general, and distinguishes between physical and chemical bonds. The nature of the bond is important in determining the work of adhesion, i.e. the energy expenditure that is necessary to break the bond at the interface. This

work of adhesion is equal to g_i if the interface is brittle, i.e. if no other energy expenditure is necessary to break the interface.

Physical bonding has been shown to be the principal mechanism for cohesion at the interface formed between numerous substrates and low surface tension liquids such as water and organic solvents. The work of adhesion and wetting angles have been quantified, based on various analyses of van der Waals attraction between two surfaces. Theoretically, the treatment of the bond is well established, and its energy can be calculated by use of the London formula, or more complete continuum approaches that have been reviewed by sever.1 authors (Krupp 1967; Naidich 1981; Adamson 1982; Delannay, Frozen and Deryttere 1986). The resulting bond energy is lower than 0.6 J/m^2, and is temperature independent (Naidich 1981). This type of bond is reversible in that debonding and bond formation can be obtained any number of times at the same interface. Hydrogen bond formation can also be included in this category, since resulting works of adhesion are not much higher than with dispersion forces, and since the bond is also reversible (Pritchard 1969). According to Plueddeman's analysis (1974) of silane sizings on glass fibers, the bond between the silane coupling agent and several types of fiber is of the hydrogen bond type when water is present at the interface, which correlates well with observed mechanical properties of these composites and the fact that the fiber-matrix bond has indeed been observed to be reversible (Hull 1981).

Chemical bonding, on the other hand, involves the formation of primary chemical bonds across the interface. The work of adhesion that results is an order of magnitude or two higher, and is temperature dependent. Extensive experimental data has been gathered to prove that wetting and adhesion between ceramics and metals is strongly dependent on primary chemical bonds that are broken or formed in the process, even in cases where no interfacial reaction products are formed (Pask and Fulrath 1962; Naidich and Kolesnichenko 1964; Naidich 1981; McDonald and Eberhart 1965; Ramqvist 1965, 1966, 1969; Warren 1968; Samsonov, Panasyuk and Kozina 1968; Rhee 1970; Goretzki, Exner and Scheuermann 1971, Pepper 1976; Petzow, Suga, Elssner and Turwitt 1984; Oki, Choh and Hibino 1985; Choh, Kammel and Oki 1987). The nature of the bond itself and hence the work of adhesion vary considerably with the materials forming the interface, and theoretical treatments are thus more system-specific (McDonald and Eberhart 1965; Gubanov and Dunaevskii 1977; Miedema and den Broeder 1979; Warren 1980; Naidich 1981; Delannay et al. 1987).

A contribution to adhesion can arise from electrostatic forces resulting from electron exchange between the two solids (Krupp 1967; Deryagin, Krotova and Smilga 1978). The magnitude of this contribution to the work of adhesion (which could rigorously be viewed as a form of chemical bonding) varies considerably from system to system, and is estimated by Krupp (1967) to be generally negligible because of the high charge densities needed. Experimental work by Mendez, Finello, Walser and Marcus (1982) has, however, demonstrated the importance of electrostatic attraction pressures across an Al/Al$_2$O$_3$/carbon interface.

Whereas for polymer matrix composites, physically bonded interfaces of low adhesion energy are attainable, chemical bonding is generally found with systems and temperatures involved in metal and ceramic matrix composites fabrication. Examples of interfaces where bonding between metals or ceramics can be attributed solely to van der Waals interaction exist, but are rare. These include bonds formed between carbon and metals such as copper, silver, gold, lead or tin that are inert with respect to carbon (Naidich 1981), bonds between sapphire and silver (Pepper 1976), or bonds between ceramic substrates and thin metallic films (Benjamin and Weaver 1959, 1960, 1961, 1963). An example of a sharp boundary across which bonding is chemical in nature is given in Fig. 3. The calculated work of adhesion of the interface between an amorphous silicon carbide coating and a carbon fiber is about 5.5 J/m^2 (Argon, Gupta, Landis and Cornie 1988), clearly higher than can be obtained by physical bonding alone. Another example of a sharp chemically bonded interface can be found with C/Mg composites, where no pull-out was observed in squeeze-cast carbon fiber reinforced magnesium composites, indicating strong bonding at an interface that was sharp when examined in the transmission electron microscope (Diwanji and Hall 1986).
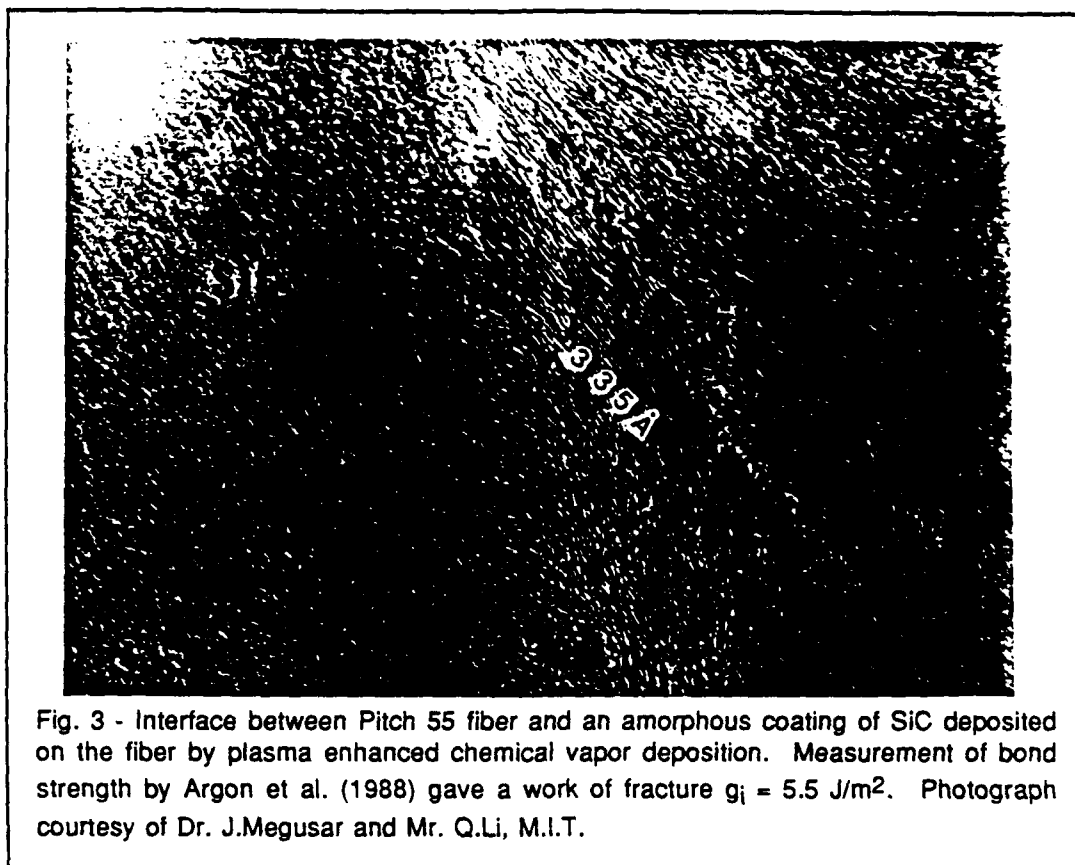
Fig. 3 - Interface between Pitch 55 fiber and an amorphous coating of SiC deposited on the fiber by plasma enhanced chemical vapor deposition. Measurement of bond strength by Argon et al. (1988) gave a work of fracture g_i = 5.5 J/m^2. Photograph courtesy of Dr. J.Megusar and Mr. Q.Li, M.I.T.

3.2. Thicker interfaces. These result from prolonged interaction of the two phases, with formation of diffusion layers or chemical compounds at the interface. As mentioned above, because matrix and reinforcement are generally reactive and their fabrication involves exposure to elevated temperatures, they very often react to some degree. Such interaction will generally result in a strong interface, and may weaken the fiber either through formation of notches (as is the case with aluminum carbide platelet formation on carbon or silicon carbide fibers), or by formation of too thick an interfacial coating of low strain to failure that adheres well to the fiber (Metcalfe 1974; Shorshorov et al. 1979; Ochiai and Murakami 1979 & 1981; Ochiai, Urakawa, Ameyama and Murakami 1980). A comprehensive case by case review of the problem of fiber/matrix reactions is beyond the scope of this article, and references on the subject can be found elsewhere (Metcalfe 1974; Chawla 1987; Mortensen, Cornie and Flemings 1988).

In summary, interfaces in inorganic matrix composites are generally strong because they tend to involve chemical bond formation. Another characteristic is that the bond strength is therefore time and temperature dependent, sometimes even in systems that do not form extended interfacial reaction layers. If the kinetics of chemical bond formation are sluggish, the strength of the interface may then be varied as a function of time, which has in some cases been exploited to control the properties of the composite. Examples of time dependent bond strengths with no concomitant interfacial reaction layer formation include work of adhesion of thin metallic films on ceramic substrates (MacDonald and Eberhart 1965; Benjamin and Weaver 1960, 1961), and electroformed and annealed tungsten-copper composites (Cooper and Kelly 1967; Ochiai et al. 1980). Examples of interfaces featuring time dependent bond strengths in which a reaction layer is formed are, however, much more numerous. A last characteristic of the interfaces in inorganic composites is that in most (but not all, Pepper 1976) cases, bonding is irreversible.

4. CONSEQUENCES FOR COMPOSITE PROPERTY OPTIMIZATION

To obtain debonding at the interface, adopting the simplified analysis of equation (1), it becomes clear that if g is not very high, a very weak interface is indeed necessary to obtain a tough composite. Roughly, g_i should be at least ten times smaller than g, which is low to begin with if we equate this term with the fracture energy of a generally brittle fiber. A lower bound on g_i is given by the work of adhesion at the interface $W_a = \gamma_{fa} + \gamma_{ma} - \gamma_{fm}$, where γ denotes surface energy and subscripts f, a and m denote fiber, ambient atmosphere and matrix respectively. With formation of a chemical bond at the interface, its work of adhesion will be at least on the order of 1 to 10 J/m^2, which is within an order of magnitude of g for most brittle ceramic materials (Kingery, Bowen and Uhlmann 1976; Ashby and Jones 1980). Any ductility in one of the two neighboring phases at the interface will furthermore increase g_i significantly (Petzow, Suga, Elssner and Turwitt 1984). Because most interfaces in inorganic composites comprise a chemical bond, it is unlikely that a satisfactorily low g_i can be obtained without resorting to deliberate tailoring of the interface properties. This can be accomplished by introducing, at the interface, a thin layer of a third phase with low intrinsic toughness, or such that bonding with matrix or fiber will be very weak. Using the relationship

$$g \approx \frac{E\,b}{10} \tag{2}$$

for true brittle fracture toughness where E is Young's modulus and b is the interatomic spacing (Cottrell 1964; Kelly and Macmillan 1986) it is seen that an order of magnitude's difference between g_i and g would require a bond strength within such an interfacial layer that is unusually low for the materials under consideration: the scale over which Young's modulus for inorganic materials varies is hardly more than one order of magnitude (Ashby and Jones, 1980), and b varies over an even smaller range. It seems therefore that the most attractive materials for interface optimization are to be found among those for which the bonding structure is highly anisotropic: graphitic or turbostratic carbon, boron nitride or perhaps sapphire. A thin layer of graphite at the interface, with basal planes oriented parallel to the surface of the fiber, is ideal in that it provides very low bond strength transverse to the interface ($E \approx 10$ GPa; Riggs, Shuford and Lewis 1982), with very high bond strength parallel to the interface ($E \approx 1000$ GPa; Riggs et al. 1982). This layer will be intrinsically weak, and will also be likely to form a weak bond with neighboring phases. Interfacial layers of carbon, either graphitic with basal planes parallel to the interface or in one case, amorphous, have been used in several of the most successful inorganic composites produced to date:

1 - It has been found that the strength of SiC filaments fabricated by chemical vapor deposition on a substrate fiber can be doubled by depositing a thin layer of approximately pure carbon on the surface of the fiber. This finding forms the basis for the remarkable properties of AVCO's SCS series of silicon carbide monofilaments (UTS > 4 GPa). The increase in strength that results from this thin (< 1 μm) layer of carbon has been attributed to the healing effect it exerts on uncoated SiC filament surface defects (Cornie, Suplinskas and DeBolt 1981; Nutt and Wawner 1985). The structure of the fibers and their coating has been investigated in detail by Nutt and Wawner (1985), who found that the carbon layer consisted mostly of pyrolytic type graphite with its basal planes oriented parallel to the fiber surfaces. These fibers thus contain, before incorporation into any matrix, a very weak crack-deflecting surface layer, and should yield elevated values of fracture toughness so long as this layer is not degraded by interfacial chemical reactions with the matrix. With various protective barriers over the carbon layer (most often in the form of carbon-rich Si-C coatings), these fibers have been combined with aluminum alloys (Cornie et al. 1981, Nutt and Wawner 1985), titanium alloys (Naslain, Pailler and
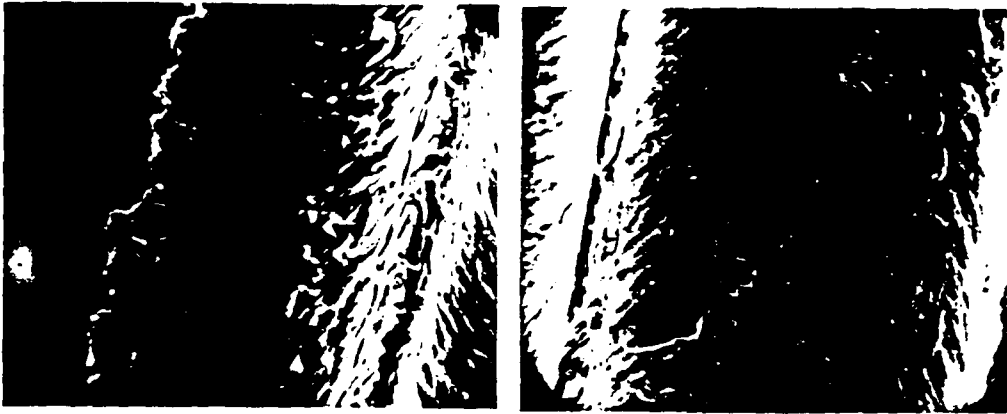
Fig. 4 - Debonded SCS-2 silicon carbide filaments in a cast aluminum alloy 357 matrix composite. The matrix side of the fracture surface (left) is still bonded to a thin crazed layer of the fiber coating, indicating that fracture was through the fiber coating. A denuded fiber from the same sample (right) displays uneven cracking through the SCS coating. ━━━━ 20 μm

Quenisset 1979; Smith, Froes and Cammett 1982; Quenisset, Soumelidis and Naslain 1985; Martineau. LePetitcorps, Pailler and Naslain 1985), titanium aluminide (Brindley 1987), glass matrices (Prewo 1980; Prewo, Brennan and Layden 1986) as well as reaction bonded silicon nitride (Corbin, Rossetti and Hartline 1986). In cases where the carbon layer survived processing, fiber debonding was observed on fracture surfaces, which took place at the interfacial carbon-rich interfacial layer as seen in Fig. 4. In ceramic matrix composites, the presence of this carbon layer resulted in composites with high strength and toughness. In metal matrix composites, such interfacial debonding is, however, less essential for high toughness since matrix ductility can contribute significantly to composite toughening with these rather large diameter filaments (d≈140 μm) .

2 - The structure of carbon fibers varies depending on the diverse heat-treatments that have been used in their production. Detailed examination by transmission electron microscopy of PAN (polyacrylonitrile-derived) carbon fibers heat treated at various temperatures have shown that type I fibers (high modulus, elevated heat treatment temperature) contain a skin layer between 150 and 250 nm thick of highly oriented turbostratic graphite with relatively large crystallite sizes and basal planes parallel to the surface. This skin layer is absent in type II fibers (lower modulus, lower heat treatment temperature; Bennett and Johnson 1979; Johnson 1980). Differences in surface structure, in particular in the type of exposed bonds, influence the initial chemical reactivity of the fibers. Their chemical affinity to oxygen, silicon carbide or aluminum decreases as the modulus of the fibers increases (Amateau and Dull 1977; Baker and Bonfield 1978; Kohara and Muto 1986; Maruyama and Rabenberg 1986; Chawla 1987; Katzmann 1987). This can be explained by a higher degree of perfection in the orientation of basal planes as the modulus of the fiber increases, especially at the fiber periphery where basal planes become more parallel to the surface. As the number of exposed graphite plane edges is reduced, fiber reactivity decreases. After infiltration by aluminum using the TiB process, it has been found that fiber pull-out increases, transverse strength decreases and longitudinal composite strength increases as fiber modulus increases in PAN carbon-aluminum composites (Amateau 1976; Amateau and Dull 1977; Goddard 1978; Shindo 1986; Honjo and Shindo 1986; Shindo and Honjo 1986; Murakami, Nakao, Imataki, Shindo, Honjo and Ochiai 1986). Depositing a layer of pyrolytic carbon on PAN II fibers, thus creating a surface skin similar to that in type I fibers, has been shown to increase fiber strength and to render PAN II fibers essentially similar to PAN I fibers in aluminum: rule of mixtures longitudinal strengths are observed, with increased pull-out and decreased transverse strength. Interpretation of the results is complex and involves

consideration of several phenomena other than the weakness of bonding with and within the outer skin of the carbon fibers: (i) the fibers react with aluminum and the extent of fiber degradation will vary with the orientation of the basal planes at the surface of the fibers; (ii) as the modulus of the fiber is increased, the requirements placed on the interface vary (for a simplistic analysis, combine equations (1) and (2)). Nonetheless, the presence of a layer of carbon with basal planes parallel to the fiber surface, whether initially present in the fibers or deposited onto their surface, has invariably resulted in longitudinal strengths in agreement with rule of mixtures predictions, as well as extensive debonding and pull-out of carbon fibers in aluminum.

3 - In ceramic matrix composites, toughening mechanisms must rely on crack deflection. Weak interfaces are therefore essential for attainment of high longitudinal composite strength and toughness in these composites. Extremely good properties have indeed been achieved on such materials by several authors, in particular by researchers at UTRC, using SiC fibers or whiskers to reinforce several glass or "ceraming" glass matrices (Prewo and Brennan 1980, Brennan and Prewo 1982; Prewo et al. 1986; Brennan 1986, 1987; Prewo 1986,1987). Detailed studies of the interface by Brennan (1986,1987) have shown that achievement of high strength and toughness, with extensive fiber debonding and pull-out, was contingent upon the presence of a thin layer of carbon at the interface which either resulted from fiber-matrix interaction when using non-stoichiometric polymer precursor derived fibers and appropriate matrix compositions, or by deliberate coating of the fibers with carbon. Exposure to air at temperatures at or above 1273 K results in brittle composites, due to degradation of this carbon-rich layer and replacement by a strongly bonded interface (Prewo 1986, Luh and Evans 1987, Grande, Mandell and Hong 1988). Chemical reactions leading to formation of the carbon layer are complex, and result in multilayered interfaces as seen on Fig. 5. The very low values of $g_i \leq 0.4$ J/m^2 measured by Marshall and Evans (1985) on these composites from debond lengths observed after matrix cracking are on the order of the value derived from equation (2) with b = 3.4 Å and E $\approx$ 10 GPa typical of the weak bond in graphite (the carbon rich layer in these composites contains other elements and is reported to be amorphous, however). Use of alumina or silicon nitride reinforcements with similar matrices by the same authors led to brittle failure in the absence of a carbon rich layer (Prewo et al. 1986) *.

Such composite property optimization via a weak interface is not a valid approach for all inorganic composites, however. As pointed out earlier, a price must be paid when using weak interfaces for crack deflection along the fiber, principally in the form of significantly reduced off-axis properties. In several metal matrix composite systems with large fiber diameters, increased interface bond strength has led to increased composite strength and fracture energy, until fiber degradation began due to fiber/matrix chemical reactions (McDanels and Signorelli 1976; Zaboletskii, Salibekov, Kansevich, Lyuttsau and Fadyukov 1978; Naslain et al.1979; Quenisset et al. 1985). In these cases, the limit in permissible interfacial strength is much higher than with composites that rely on crack deflection for longitudinal toughness. Coatings of interest for such composites should mainly aim to preserve the strength of the fibers and facilitate processing of the composite. Numerous examples of such coatings exist, such as the outer Si-C coating on AVCO's SCS fibers (Cornie et al. 1981; Nutt and Wawner 1985). Other approaches to the problem involve slowing down the kinetics of fiber degradation via judicious choice of processing methods. Some fabrication methods use solid metal, preferably coated with its oxide, in conjunction with processing methods that preserve this oxide and use low temperatures. The diffusion bonding process for Al-B is an example (Metcalfe 1974; Hall, Kyono and Diwanji 1987). Other approaches include casting liquid metal around cold fibers, a

---

* With carbon fibers in glass, the differences found in aluminum matrices between high strength and high modulus fibers have not been observed. In fact, the high strength fibers gave somewhat better results in work by Phillips (1974). Phillips interprets these data on the basis of mechanical keying effects with no chemical bond at the interface, due to tensile residual stresses at the interface. This interpretation fits the data nicely, and indicates that differences between the fibers in these composites are probably linked more to their coefficients of thermal expansion than to their interface chemistry.
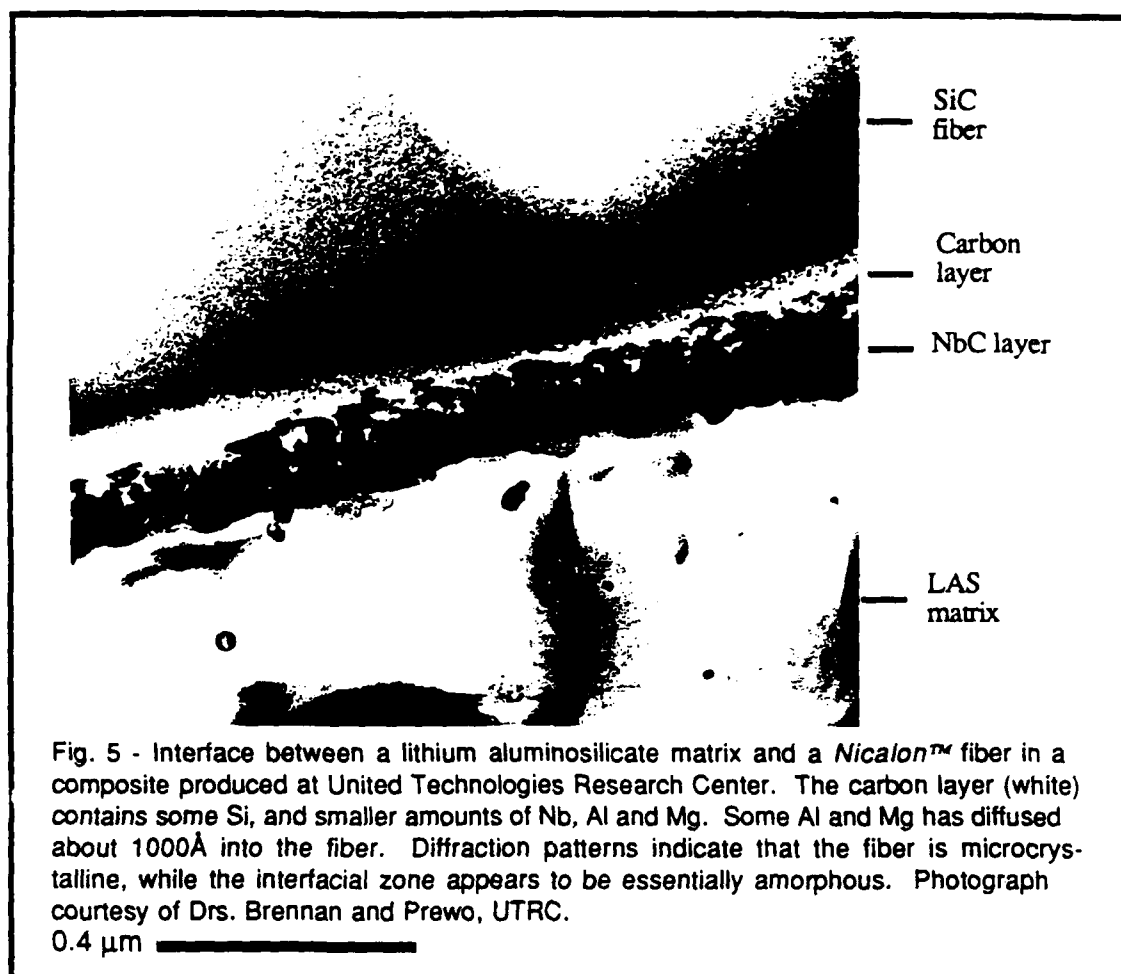
Fig. 5 - Interface between a lithium aluminosilicate matrix and a *Nicalon*™ fiber in a composite produced at United Technologies Research Center. The carbon layer (white) contains some Si, and smaller amounts of Nb, Al and Mg. Some Al and Mg has diffused about 1000Å into the fiber. Diffraction patterns indicate that the fiber is microcrystalline, while the interfacial zone appears to be essentially amorphous. Photograph courtesy of Drs. Brennan and Prewo, UTRC.

0.4 μm ▬▬▬▬▬▬▬▬

method that has been pioneered by Fukunaga and Goda (1985) with 99.99% aluminum and *Nicalon*^{TM} silicon carbide fibers.

It must be emphasized that tailoring of interface chemistry is also strongly dictated by the processing of the composites. For cast composites, for example, wetting of the fiber by the matrix is a critical issue, to lower pressures involved in the process and to fully infiltrate the fiber preform, in particular at fiber contact points (Mortensen and Cornie 1986, Mortensen et al. 1988). Composite processing may in certain instances place requirements on interface chemistry that conflict with optimization of composite properties. For example, chemical reactions between ceramic fibers and molten metals aid wetting, which most often will result in poor composite properties due to fiber degradation or too strong an interface. It is also emphasized that the present analysis of the interface is simple, and that all fundamentally important aspects of processing-structure-property relationships in inorganic composites that are not directly related to interface chemistry have been ignored in this review. Residual stresses in the composite, the complexity of a proper mechanical treatment of the interface, as well as the influence of geometrical distribution of the fibers should all be taken into account in a less concise treatment of the problem.

5. CONCLUSION

For strong and tough fiber reinforced inorganic materials, the interface must presently seek satisfaction of several requirements:

1 - The properties of the fibers must be preserved, i.e. extensive chemical reactions between fiber and matrix must be prevented;

2 - Where fiber debonding is necessary for longitudinal strength and toughness, a weak interface is desirable;

3 - A strong interface is desirable for good transverse properties;

4 - Ease of fabrication, including good wetting of the fibers if the matrix is combined in the liquid state, depends critically on interface chemistry for most economical processing methods.

The criteria to be satisfied will vary, depending on the fiber, the matrix and the application of the composite. There is, therefore, no given set of rules dictating chemical engineering of the interface for optimized properties. However, the bond at the interface is generally chemical in nature, i.e. primary chemical bonds are formed across the interface. This rather general feature of the bond in inorganic composites dictates certain current approaches for interface chemistry control in these composite materials:

(i) where a weak interface is necessary for composite toughness, the strong anisotropy in bonding of certain materials, especially graphite, offers a solution to the problem of crack deflection at the interface. Thin layers of such materials are presently used at the interface of several inorganic composites.

(ii) where the matrix contribution to composite toughness is important, a strong bond is desirable. This category includes that of metal matrix composites with large fibers. In cases where fiber degradation may occur due to chemical reaction with the matrix, protective coatings at the interface and/or careful processing methods are used.

There is at present a surge of interest in the characterization of interfacial properties in inorganic composites (Marshall 1984, Grande et al. 1988, Argon et al. 1988), which will hopefully elucidate on a more quantitative level the requirements we place on the interface. These characterization methods, coupled with a more sophisticated understanding of the interplay between the various processing-structure-property relationships in inorganic composites, will hopefully point to novel ways of controlling and optimizing the interface chemistry of these materials.

ACKNOWLEDGEMENTS

REFERENCES

Adamson, A. W. (1982). Physical Chemistry of Surfaces, 4th edition. (Wiley-Interscience, New-York) Chapter 6.

Amateau, M. F. (1976), Progress in the development of aluminum composites using liqid infiltration technology J. of Composite Materials 10 (1976), 279-296.

Amateau, M. F. and Dull, D. L. (1977) The effect of processing on the transverse strength of graphite-aluminum composites In: Failure Modes in Composites IV Edited by J.A.Cornie and F.W.Crossman, Proc. TMS/AIME Conf. (Chicago Ill.), 336-358.

Argon, A. S., Gupta, V. J., Landis, H. S. and Cornie, J. A., Intrinsic toughness of interfaces between SiC coatings and substrates of Si or C fiber, submitted J. of Materials Science, 1988.

Ashby, M. F. and Jones, D. R. H., (1980) Engineering Materials: An Introduction to their Properties and Applications, (Pergamon, Oxford) pages 32 and 126.

Baker, S. J. and Bonfield,W. (1978) Fracture of aluminium coated carbon fibers *J. of Materials Science* 13, 1329-1334.

Benjamin, P. and Weaver, C. (1959) Condensation energies for metals on glass and other substrates *Proc. Roy. Soc. London* A252, 418-430.

Benjamin, P. and Weaver, C. (1960) Adhesion of metal films to glass *Proc. Roy. Soc. London* A254, 177-183.

Benjamin, P. and Weaver, C. (1961) The adhesion of evaporated metal films on glass *Proc. Roy. Soc. London* A261, 516-531.

Benjamin, P. and Weaver, C. (1963) The adhesion of metals to crystal faces *Proc. Roy. Soc. London* A274, 267-273.

Bennett, S. C. and Johnson, D. J. (1979) Electron-microscope studies of structural heterogeneity in PAN-based carbon fibers *Carbon* 17, 25-39.

Brennan, J. J. and Prewo, K. M. (1982) Silicon carbide fibre reinforced glass-ceramic matrix composites exhibiting high strength and toughness *J.of Materials Science* 17, 2371-2383.

Brennan, J. J. (1986) Interfacial Characterization of glass and glass-ceramic matrix/Nicalon SiC fiber composites Tailoring Multiphase and Composite Ceramics, edited by R.E.Tressler, G.L.Messing, C.G.Pantano and R.E.Newnham (Plenum Publishing Corporation) 549-560.

Brennan, J. J. (1987) Interfacial characteristics of glass-ceramic matrix/SiC fiber composites Interface Science and Engineering 1987 (Lake Placid, N.Y.)

Brewer, W. D. (1982) Metallurgical and tensile property analysis of several silicon carbide/titanium composite systems In: Mechanical Behavior of Metal-Matrix Composites, edited by J.E.Hack and M.F.Amateau (TMS/AIME Proc. Conf. Dallas, Texas), 39-50.

Brindley, P. K. (1987) SiC reinforced aluminide composites *Mat. Res. Soc. Symp. Proc.* 81, 419-424.

Choh, T., Kammel, R. and Oki,T. (1987) Wettability of graphite to liquid aluminum and the effect of alloying elements on it *Zeitschrift für Metallkunde* 77, 286-290.

Corbin, N. D., Rossetti Jr., G. A. and Hartline, S. D. (Jul-Aug. 1986) Microstructure/property relationships for SiC filament-reinforced RBSN *Ceramic Engineering and Science Proceedings* 8, 958-968.

Cornie, J. A., Suplinskas, R. J. and DeBolt, H. (1981)"Surface Enhancement of Silicon Carbide Filament for Metal Matrix Composites", ONR Contract N00014-79-C-0691, Summary Report.

Cooper, G. A. and Kelly, A., (1967) Tensile properties of fibre-reinforced metals: fracture mechanics *J. Mech. Phys. Solids* 15, 279-297.

Cottrell, A. H. (1964) Strong Solids *Proc. Roy. Soc. London* A282, 2-9.

Chawla, K. K. (1987) Composite Materials - Science and Engineering (Springer Verlag).

Delannay, F., Frozen, L. and Deryttere, A. (1987) Review - the wetting of solids by molten metals and its relation to the preparation of metal-matrix composites *J. of Materials Science* 22, 1-16.

Deryagin, B. V., Krotova, N. A. and Smilga, V. P. (1978) Adhesion in Solids (Consultants Bureau).

Diwanji, A. P. and Hall, I. W. (1986) Mechanical properties and the fibre/matrix interface in squeeze-cast graphite-magnesium metal matrix composites Proc. of the Sixth International Conference on Composite Materials ICCM 6, edited by F.L.Matthews, N.C.R.Buskell, J.M.Hodgkinson and J.Morton (Elsevier, London), Vol. 2, 265-274.

Erdogan, F. (1972) Fracture problems in composite materials *Engineering Fracture Mechanics* 4, 811-840.

Erturk, T, Cornie, J. A. and Dixon, R. G. (1986) Interfaces in Metal Matrix Composites edited by A.K.Dhingra and S.G.Fishman, (Proc. Conf. New Orleans TMS/AIME), 239-253.

Erturk,T., Gupta, V. J., Argon, A. and Cornie, J. A. (July 1987) Tailoring interface properes for damage containment in graphite/aluminum metal matrix composites In: Sixth International Conference on Composite Materials ICCM 6, (London) Vol. 2, 156-168.

Evans, A.G., and McMeeking, R.M. (1986), On the toughening of ceramics by strong reinforcements *Acta Metallurgica* 12, 2435-2441.

Fukunaga, H. and Goda, K. (1985), Formation and role of the solidified layer on a fiber during the fabrication of fiber reinforced metal by the liquid process *J. Japan Inst. Metals* 49, 78-83.

Goddard, D. M. (1978) Interface reactions during preparation of aluminium matrix composites by the sodium process *J. of Materials Science* 13, 1841-1848.

Goretzki, H., Exner, H.E. and Scheuermann, W., (1971), Electronic structure of refractory carbides and its relation to wetting Modern Developments in Powder Metallurgy Vol. 4: Processes, edited by H.H.Hausner, Plenum Press, 327-337.

Grande, D. H., Mandell, J. F., Hong, K. C. C., (1988) Fibre-matrix bond strength studies of glass, ceramic and metal matrix composites *J. of Materials Science* 23, 311-328.

metal matrix composites*J. of Materials Science* 23, 311-328.

Gubanov, A. I. and Dunaevskii, S. M. (1977) Adhesion of a metal and an ionic crystal *Sov. Phys. Solid State* 19 (5), 795-797.

Haggerty, J. (1988) MIT, Reaction bonded ceramic matrix composites, private communication.

I.W.Hall, T.Kyono and A.Diwanji, (1987), On the fibre/matrix interface in boron/aluminum metal matrix composites *J. of Materials Science* 22, 1743-1748.

Honjo, K. and Shindo, A. (1986) Interfacial behavior of aluminum matrix composites reinforced with ceramics-coated carbon fibers "Composite Interfaces" Proc of the First Int. Conf. on Composite Interfaces ICCI-1, Cleveland, edited by H.Ishida and J.L.Koenig (Elsevier, North-Holland) ,101-107.

Hull, D. (1981) An Introduction to Composite Materials, (Cambridge Solid State Science Series, Cambridge University Press), Chapters 1&3.

Johnson, D. J. (1980) Recent advances in studies of carbon fibre structure *Phil. Trans. Roy. Soc. London* A294 443-449.

Katzman, H. A. (1987) Fibre coatings for the fabrication of graphite-reinforced magnesium composites *J. of Materials Science* 22 .144-148.

Kelly, A. (1970) Interface effects and the work of fracture of a fibrous composite *Proc. Roy. Soc. London* A319, 95-116.

Kelly, A. (1971) Strengthening Methods in Crystals , edited by A.Kelly and R.B.Nicholson (Applied Science Publishers, London) 473-484.

Kelly, A. and Macmillan, N. H. (190) Strong Solids, third Edition (Clarendon Press, Oxford).

Kendall, K. (1975) Transition between cohesive and interfacial failure in a laminate *Proc. Roy. Soc. London* A344 , 287-302.

Kendall, K. (1976) Interfacial cracking of a composite*J. Materials Science* 11 638-644.

Kingery, W.D., Bowen, H.K. and Uhlmann, D.R.(1976) Introduction to Ceramics, Second Edition, J.Wiley & Sons, N.Y., Chapter 15.

Knox, C. E. (1982) Handbook of Composites, Edited by G.Lubin (Van Nostrand Reinhold) 136-195.

Kohara, S. and Muto, N., (1986) Degradation of PAN-based carbon fibers by molten aluminum Comp '86: Eng. Appl. of New Composites Proc. Conf. University of Patras, 25-29 Aug. 1986.

Krupp, H. (1967) Particle adhesion - theory and experiment *Advan. Colloid Interface Science* 1, 79-110.

Luh, E.Y. and Evans, A.G.(1987), High temperature mechanical properties of a ceramic matrix composite*J. Am. Ceram. Soc.* 70, 466-469.

Martineau, P., Le Petitcorps, Y., Pailler, R., and Naslain, R. (1985) The SiC/Ti metal matrix composites: correlation between the filament composition and the composite thermomechanical behavior In: "Developments in the Science and Technology of Composite Materials" , Proc. First European Conference on Composite Materials ECCM 1, edited by A.R.Bunsell, P.Lamicq and A.Massiah (EACM, Bordeaux), 725-731.

Marshall, D. B., (1984) An indentation method for measuring matrix-fiber frictional stresses in ceramic composites *Comm. of the American Ceramic Soc.*, 67 (12) , C-259-C-260.

Marshall, D. B. and Evans, A. G., (1985) Failure mechanisms in ceramic-fiber/ceramic-matrix composites*J. of the American Ceramic Society* 68 , 225-231.

Maruyama, B. and Rabenberg, L. (1986) Oxidation model of interface reactions in aluminum/graphite composites In: Interfaces in Metal Matrix Composites , edited by A.K.Dhingra and S.G.Fishman, Proc. Conf. New Orleans 1986 (TMS/AIME), 233-238.

McDanels, D. L. and Signorelli, R. A. (1976) Improved impact-resistant boron/aluminum composites for use as turbine engine fan blades In: Failure Modes in Composites III, edited by T.T.Chiao and D.M.Schuster, Proc. Conf.Las Vegas 1976, (TMS/AIME), 27-57.

McDonald, J. E. and Eberhart, J G. (1965) Adhesion in aluminum oxide-metal systems*Trans. Metallurgical Society of AIME* 233 , 512-517.

Mendez, H., Finello, D., Waiser, R. and Marcus, H. L.(1982) Correlation of electronic state and fracture path of aluminum-graphite interfaces*Scripta Metallurgica* 16 , 855-858.

Metcalfe, A.G. (1974) Composite Materials Volume 1 - Interfaces in Metal Matrix Composites, edited by A.G.Metcalfe (Academic Press, N.Y.), Chapters 1 and 3.

Miedema, A.R. and den Broeder, F.J.A. (1979) On the interfacial energy in solid-liquid and solid-solid metal combinations *Zeitschrift für Metallkunde* 70 , 4-20.

Mortensen, A. and Cornie, J.A. (1986), On the infiltration of metal matrix composites*Metallurg.Trans.* 18A, 1160-1163.

Mortensen, A., Cornie, J. A. and Flemings, M. C. (February 1988) Solidification of metal matrix composites

Journal of Metals , 12-19.

Murakami, Y., Nakao, K., Imataki, T., Shindo, A., Honjo, K. and Ochiai, S. (1986) Effect of interfacial conditions of the tensile strength of carbon fiber-6061 aluminum alloy composites Composites '86: Recent Advances in Japan and the United States: Proc. Japan-US CCM3 edited by K.Kawata, S.Umekawa and A.Kobayashi., (Japan Society for Composite Materials), 761-766.

Naidich, Y.V. and Kolesnichenko, G.A. (1964) Investigation of the wetting of diamond and graphite by molten metals and alloys III *Soviet Powder Metallurgy and Metal Ceramics* 1 (19), p.191.

Naidich, J.V. (1981) The wettability of solids by liquid metals *Prog. Surf. Membr. Sci.* 14 , 353-484.

Naslain, R., Pailler, R. and Quenisset, J.-M. (1979) Chapter XV, Introduction aux Matériaux Composites Vol.2 - Matrices Métalliques et Céramiques, edited by R.Naslain , (Éditions du C.N.R.S.), 313-383.

Nutt, S.R. and Wawner, F. E. (1985) Silicon carbide filaments: microstructure *J. Materials Science* 20 1953-1960.

Ochiai, S. and Murakami, Y., Tensile strength of composites with brittle reaction zones at interfaces *J. of Materials Science* 14 (1979) pp.831-840.

Ochiai, S., Urakawa, S., Ameyama, K. and Murakami, Y. Experiments on fracture behavior of single fiber-brittle zone model composites *Metallurg.Trans.* 11A, 525-530.

Ochiai, S. and Murakami, Y. (1981) Theoretical prediction of tensile strength of fibers as a function of thickness of brittle zones on fiber surfaces *Metallurg.Trans.* 12A 1155-1161.

Oki, T., Choh, T. and Hibino, A. (1985) Wettability of aluminium against SiC and the effects of silicon, manganese, iron and copper *J. of the Japan Institute of Metals* 49 , 1131-1137.

Olster, E.F. and Jones, R.C. (1974), Interfaces in Metal Matrix Composites, edited by A.G.Metcalfe, Academic Press, N.Y., Chapter 7.

Page, R. A. and Leverant, G. R. (1985) Relationship of fatigue and fracture to microstructure and processing in alumina fiber reinforced metal matrix composites In: Proc of the Fifth Int. Conf.on Composite Materials ICCM 5, edited by W.C.Harrigan. J.Strife and A.Dhingra (TMS/AIME, San Diego), 867-886.

Pask, J. A., Fulrath, R. M. (1962) Fundamentals of glass to metal bonding VII *J. of the American Ceramic Society* 45 (12), 592-596.

Pepper, S. V. (1976) Shear strength of metal sapphire contacts *J. of Applied Physics*, 47 (3), 801-808.

Petzow, G., Suga, T., Elssner, G. and Turwitt, M. (1984) Nature and structure of metal-ceramic interfaces In: Sintered Metal-Ceramic Composites, edited by G. S. Upadhyaya, (Elsevier Science Publishers, Amsterdam, 3-18.

Phillips, D. C. (1974) Interfacial bonding and the toughness of carbon fibre reinforced glass and glass-ceramics *J. Materials Science* 9 , 1847-1854.

Plueddeman, E. P. (1974) Composite Materials Vol. 6: Interfaces in Polymer Matrix Composites, edited by L.J.Broutman and R.H.Krock (Academic Press) Chapter 6.

Prewo, K. M. (1976) The development of impact tolerant metal matrix composites In: Failure Modes in Composites III, edited by T.T.Chiao and Schuster, Proc. Conf.Las Vegas , (TMS/AIME),1-26.

Prewo, K. W. (1980) The importance of fibres in achieving impact tolerant composites *Phil. Trans. Roy. Soc. London* A294, 551-558.

Prewo, K. M. and Brennan, J. J. (1980) High-strength silicon carbide fibre-reinforced glass-matrix composites *J. of Materials Science* 15 463-468 and 1201-1206.

Prewo, K. M., Brennan, J. J. and Layden, G. K. (1986) Fiber reinforced glasses and glass-ceramics for high performance applications *American Ceramic Society Bulletin* 65 305-313&322.

Prewo, K. M. (1986) Tension and flexural stength of silicon carbide fibre-reinforced glass ceramics *J. of Materials Science* 21 , 3590-3600.

Prewo, K. M. (1987) Fatigue and stress rupture of silicon carbide fibre-reinforced glass-ceramics *J. of Materials Science* 22 , 2695-2701.

Pritchard, W. H. (April 1969) The role of hydrogen bonding in adhesion In: Aspects of Adhesion 6, Proc. Conf. at the City University, London, edited by D.J.Alner (University of London Press), 11-23.

Quenisset, J.-M., Soumelidis, P. and Naslain, R. (1985) Fatigue crack propagation in titanium based 1D composites reinforced by boron, boron carbide and SiC filaments In: "Developments in the Science and Technology of Composite Materials", Proc. First European Conference on Composite Materials ECCM 1, edited by A.R.Bunsell, P.Lamicq and A.Massiah (EACM, Bordeaux), 571-576.

Ramqvist, L. (1965) Wetting of metallic carbides by liquid copper, nickel, cobalt and iron *International Journal of Powder Metallurgy* 1 (4) , 2-21 and (1966) 2 (2) p. 34.

Ramqvist, L. (1969) Preparation, properties and electronic structure of refractory carbides and related compounds

Jernkontorets Annaler 153 159-179.

Rhee, S.K. (1970) Wetting of ceramics by liquid aluminum *J. of the American Ceramic Society* 53 (7) 386-389.

Riggs, D.M., Shuford, R. J. and Lewis, R. W.(1982) Handbook of Composites. edited by G.Lubin, (Van Nostrand Reinhold), 196-271.

Samsonov, G.V., Panasyuk, D. and Kozina, G.K. (1968) Wetting of refractory carbides with liquid metals *Soviet Powder Metallurgy and Metal Ceramics*, 11, 874-878.

Shorshorov, M. Kh., Ustinov, L. M., Zirlin, A. M., Olefirenko, V. I. and Vinogradov, L. V. (1979) Brittle interface layers and the tensile strength of metal matrix composites *J. of Materials Science* 14, 1850-1861.

Shindo, A. and Honjo, K.(1986) Surface treatment of carbon fibers as reinforcements for aluminum matrix composites In: Composites '86: Recent Advances in Japan and the United States: Proc. Japan-US CCM-3, edited by K. Kawata, S. Umekawa and A. Kobayashi (Japan Society for Composite Materials, Tokyo), 767-774.

Shindo, A. (1986) Chemical property of carbon fiber surface and interfacial compatibility of composites In: "Composite Interfaces", Proc of the First Int. Conf. on Composite Interfaces ICCI-1, Cleveland, edited by H.Ishida and J.L.Koenig (Elsevier, North-Holland), 93-100.

Smith, P. R., Froes, F. H., and Cammett, J. T. (1982) Correlation of fracture characteristics and mechanical properties for titanium matrix composites In: "Mechanical Behavior of Metal-Matrix Composites", Proc. Conf. Dallas, edited by J.E.Hack and M.F.Amateau (TMS/AIME, Texas), 143-168.

Swenson, D. O. and Rau Jr., C. A. (1970) The stress distribution around a crack perpendicular to an interface between materials *Int. Journal of Fracture Mechanics* 6, 357-365.

Towata, S.-I. and Yamada, S.-I. (1986-a), Mechanical properties of aluminum alloy composites with hybrid reinforcements of continuous fiber and whisker or particulate Composites '86: Recent Advances in Japan and the United States: Proc. Japan-US CCM-3, edited by K. Kawata, S. Umekawa and A. Kobayashi (Japan Society for Composite Materials, Tokyo), 497-503.

Towata, S.-I. and Yamada, S.-I. (1986-b), Mechanical properties of aluminum alloys reinforced with silicon carbide fibers and whiskers or particulates *Trans. Japan Institute of Metals* 27, 709-716.

Warren, R. (1968) The interaction between liquid platinum and some transition metal carbides *J. of Nuclear Materials* 25, 117-119.

Warren, R. (1980) Solid-liquid interfacial energies in binary and pseudo-binary systems *J. of Materials Science* 15, 2489-2496.

Wells, J. K. and Beaumont, P. W. R. (1985-a) Debonding and pull-out processes in fibrous composites *J.Materials Science* 9 1275-1284

Wells, J. K. and Beaumont, P. W. R. (1985-b) Crack-tip energy absorption processes in fibre composites *J.Materials Science* 9 2735-2749.

Zaboletskii, A. A., Salibekov, S. E., Kansevich, I. A., Lyuttsau, V. G. and Fadyukov, E. M. (1978) Effect of processing factors on some properties of silumin/silicon-carbide-fiber composite materials *Soviet Powder Metallurgy and Metal Ceramics* 17, 51-54.

INFILTRATION OF METAL MATRIX COMPOSITES

Andreas Mortensen
(Department of Materials Science and Engineering, Massachusetts
Institute of Technology, Cambridge, MA 02139, USA)

ABSTRACT

This article constitutes a summary of current research on the infiltration of metal matrix composite materials. A description of fundamentals of the process for a pure metal and a binary alloy is given for the case of unidirectional infiltration. Governing equations, and a method for their solution for constant applied pressure and adiabatic infiltration are discussed. Experimental procedures are outlined and results are compared with theory.

INTRODUCTION

With growing engineering importance of cast metal matrix composites, the problems of infiltration and solidification of a metal within a dense network of fibers or particles (defined herein as a preform) have been gaining in interest and relevance. Much of the pioneering work in this field has been conducted in Japan,[1-5] where the first mass market metal matrix composite component was introduced, a Toyota diesel engine piston selectively reinforced with chopped alumina fibers.

Embodiments of the metal infiltration process are numerous, and range from the squeeze casting process in which pressures as high as 100 MPa are applied on molten metal by a press to force infiltration of a preform, to the simple wicking by capillary forces of a metal into a preform it wets. Several difficulties exist in the process, with two problems prominent: (a) candidate metal matrices such as aluminum or magnesium generally do not wet reinforcements of engineering significance and (b) the two phases often react chemically to a degree that results in loss of potential properties of the composite. These problems are generally solved by two means, respectively the application of pressure to force the metal into the preform and minimization of exposure to elevated temperature during processing.

A most significant result that emanated from the pioneering research that was performed in Japan on the infiltration process is proof that it is possible to infiltrate a preform that is initially held at a temperature below the melting point of a pure metal matrix. This was shown to increase viscous resistance to flow of the metal in the infiltrated portion of the preform due to the formation of solid metal by heat exchange with the cold fibers.[1-4] On the other hand, better composite properties resulted because fiber strength degradation by chemical reaction with the matrix was minimized.[5]

There is thus considerable interplay between solidification and infiltration in metal matrix composites because often the two take place concomitantly. Local thermal history, matrix composition, resistance to fluid flow and microstructure and fiber chemical degradation are all interrelated. Our understanding of infiltration must therefore be global, and must begin with an understanding of the fundamental physical phenomena that govern synergistically the kinetics of infiltration, the resulting microstructure and derivation of optimal processing conditions. The research summarized here addresses the problem from such a global perspective, by focussing on a relatively simple configuration which is both amenable to analytical simplification and detailed experimental investigation. This problem is that of unidirectional infiltration under constant applied pressure.

UNIDIRECTIONAL INFILTRATION: THEORY

Consider the infiltration of a semi-infinite cylinder, axis x'Ox, consisting of a porous material devoid of large pores along its length so that gross channelling of the metal is not observed. Metal enters the preform at position x=0 and time t=0, under pressure P $= P_0$ usually different from the ambient pressure in the preform P_g. Pressure differences within the uninfiltrated preform and within the metal ahead of the preform are generally negligible. When the metal penetrates the preform, the difference between P_0 and P_g is equal to the sum of the capillary pressure drop ΔP_γ across the metal/ambient atmosphere meniscus and the integral ΔP_μ of the pressure gradient along the preform axis needed to sustain flow of the metal through the porous preform:

$$P_0 - P_g = \Delta P_\gamma + \Delta P_\mu \qquad (1).$$

Infiltration will generally be gradual, because the preform is never perfectly homogeneous. A non-wetting metal thus penetrates larger pores first, finer pores later, at a higher pressure in the metal because ΔP_γ is higher where pores are finer. From a practical standpoint, however, pressures far in excess of $P_g + \Delta P_\gamma$ are used to drive the metal to achieve sufficiently high infiltration rates. Generally, therefore, the infiltration front is fairly sharp and can be designated by a single abscissa L. Between x = 0 and x = L, liquid metal is flowing past the fibers and past solid metal if any is present, to feed infiltration at x = L.

We base our analysis of the process on the use of an elementary volume element ΔV that is small on the scale of the casting, but comprises at least several fibers so that variables can be averaged and treated as constants over ΔV: fluid velocity measured by the "superficial" velocity or "seepage" velocity v_0 (a vector of direction given by the average flow direction of the liquid and of magnitude equal to the volume of liquid flowing per unit time through a unit surface cut into the porous medium perpendicular to the average flow direction), temperature T, pressure P, liquid metal composition C_{iL}, solid metal volume fraction f_s, fiber volume fraction V_f, average composition C_i. For this approach to be valid, the reinforcing fibers or particles must be sufficiently fine for temperature and liquid composition equalization within ΔV to be achieved in a very short time compared to the time for infiltration. With particles or fibers usually less than 20 μm in diameter, this is a safe assumption.

Fluid flow within the preform will be governed by Darcy's law, provided the relevant

Reynold's number is less than about one:[6]

$$R_e = \frac{2\, r_f\, \rho_m\, v_o}{\mu\, V_f} \qquad (2)$$

where ρ_m is the density of the metal and μ is the viscosity of liquid metal. This will generally be the case in the infiltration of metal matrix composites due to the fine scale of the reinforcement. Darcy's law then correlates the pressure gradient in the liquid and the superficial velocity. Provided the effect of gravity is nil or negligible, the continuity equation and Darcy's law yield respectively:

$$v_o = (1-V_f)\,\frac{dL}{dt} \qquad (3)$$

$$v_o = -\frac{K}{\mu}\,\frac{dP}{dx} \qquad (4)$$

A relation giving the value of the preform permeability K at each point of the infiltrated preform as a function of the nature of the reinforcement, its volume fraction, and the volume fraction solid metal present f_s is needed. Calculation of K can be based on the Blake-Kozeny approximation or on appropriate relationships derived for the particular preform in question.[8] Of particular interest is the role played by the fraction solid metal f_s present in the composite during infiltration, because the permeability will depend largely upon the solidification morphology of that solid metal phase. This relationship creates a link between the solidification morphology of the metal during infiltration and the kinetics of infiltration.

The heat transfer equation is:

$$\rho_c c_c \frac{\partial T}{\partial t} + \rho_m c_m\, v_o \cdot \frac{\partial T}{\partial x} = \frac{\partial}{\partial x}\left(k_c \frac{\partial T}{\partial x}\right) + (1-V_f)\,\rho_m H\,\frac{\partial f_s}{\partial t} \qquad (5)$$

where $\rho_c c_c$ is the volumetric heat capacity of composite (equal to $\rho_f c_f V_f + \rho_m c_m (1-V_f)$, where $\rho_f c_f$ is the volumetric heat capacity of fibers, $\rho_m c_m$ that of the metal), k_c is the thermal conductivity in the composite, and H the latent heat of solidification of the metal. Heat transfer within the preform is described by Fourier's law of conduction if the contribution of convection of the gas is negligible, which is generally the case. Solute conservation dictates:

$$\frac{\partial\left((1-V_f)\overline{C}\right)}{\partial t} = -\,\mathrm{div}(C_{iL}\, v_o) \qquad (6)$$

where C_{iL} is the concentration of solute i in the liquid metal and C_i the average concentration of solute i in all the metal within ΔV, neglecting density differences between liquid and solid metal. Depending on the solidification mechanism, an additional relationship correlates the average concentration with the liquid metal

composition and fraction solid metal f_s. If diffusion within the solid metal is negligible, this will be the Scheil equation when temperature is locally decreasing, and the equilibrium lever rule if temperature is locally increasing. The composition of the liquid and the temperature in ΔV are linked by the phase diagram if equilibrium is assumed at the solid/liquid metal interface. In the case of a binary alloy, there are thus six unknowns: v_o, P, T, C_{iL}, f_s, and C_i at each position x in the preform and time t. The problem is defined by the relations described above, together with specification of boundary conditions and conservation relationships at sharp metal solidification or remelting fronts. Process parameters are initial fiber temperature T_f, applied pressure $P_o - P_g$, initial metal temperature T_o, reinforcement volume fraction V_f and rate of heat extraction at the mold wall.

There is at least one moving boundary in this problem, the infiltration front. There will in general be other moving boundaries, for example a remelting front separating the region of fully liquid metal extending from x = 0 when the metal is superheated and the region where solid metal exists due to cooling from the fibers.

The presence in this problem of moving boundaries complicates considerably its solution for the most general case. The approach we follow in our treatment is based on the observation that, provided the applied pressure $P_o - P_g$ is constant and the mold walls are adiabatic, the entire problem can be solved by a similarity method whereby position and time are lumped by a Boltzmann transformation into a single parameter χ = x/L with L = $\psi \sqrt{t}$ where ψ is a constant characterizing the kinetics of infiltration. We thus transform the partial differential equations above into ordinary differential equations, and solve for P, T, C_{iL}, f_s, and C_i as functions of χ. For simple cases, we also relax the assumption that mold walls are adiabatic, and solve the partial differential equations above with numerical methods, using the adiabatic solution as a guide. This methodology has several advantages: (a) it allows for relatively simple and general solutions, often in analytical form, of adiabatic infiltration and (b) it allows for separation of effects due to external cooling from those due to the presence of the preform. A complete discussion of the theoretical analysis and its assumptions summarized here is given elsewhere.[7,8]

EXPERIMENTAL PROCEDURE.

Our experiments replicate the situation described above, and allow independent control of the process variables T_f, $P_o - P_g$, T_o and V_f. The matrix metal, pure aluminum or Al-4.5 wt% Cu, is unidirectionally infiltrated into preforms of Saffil™ alumina fibers with a pressure casting apparatus which uses gas pressurized up to 4 MPa, to force molten metal into an evacuated die. Fig. 1 is a sketch of the device. It consists of two main components: the pressure vessel containing the melt furnace and crucible, and the cap, attached to which are the control valves and the die. There are also feed-throughs for thermocouples, power leads, and a pressure transducer. The die is attached to the center of the cap and can be evacuated, vented or pressurized.

To operate the device the cap is placed on the pressure vessel, immersing the bottom of the die in the molten metal. The vessel is then pressurized with nitrogen, forcing the metal up through the die and into the fibers. Gas feed-through lines feature a large diameter, allowing full pressurization in less than 1.2 seconds. The metal and the

fibers do not come in contact until infiltration begins, which enables accurate and independent control of the fiber and metal temperatures. In addition, because of the design of the device, the die need only sustain the compressive stresses imposed by the pressurized gas; heavy-walled metal dies common to other pressure casting apparati are replaced with a quartz tube.
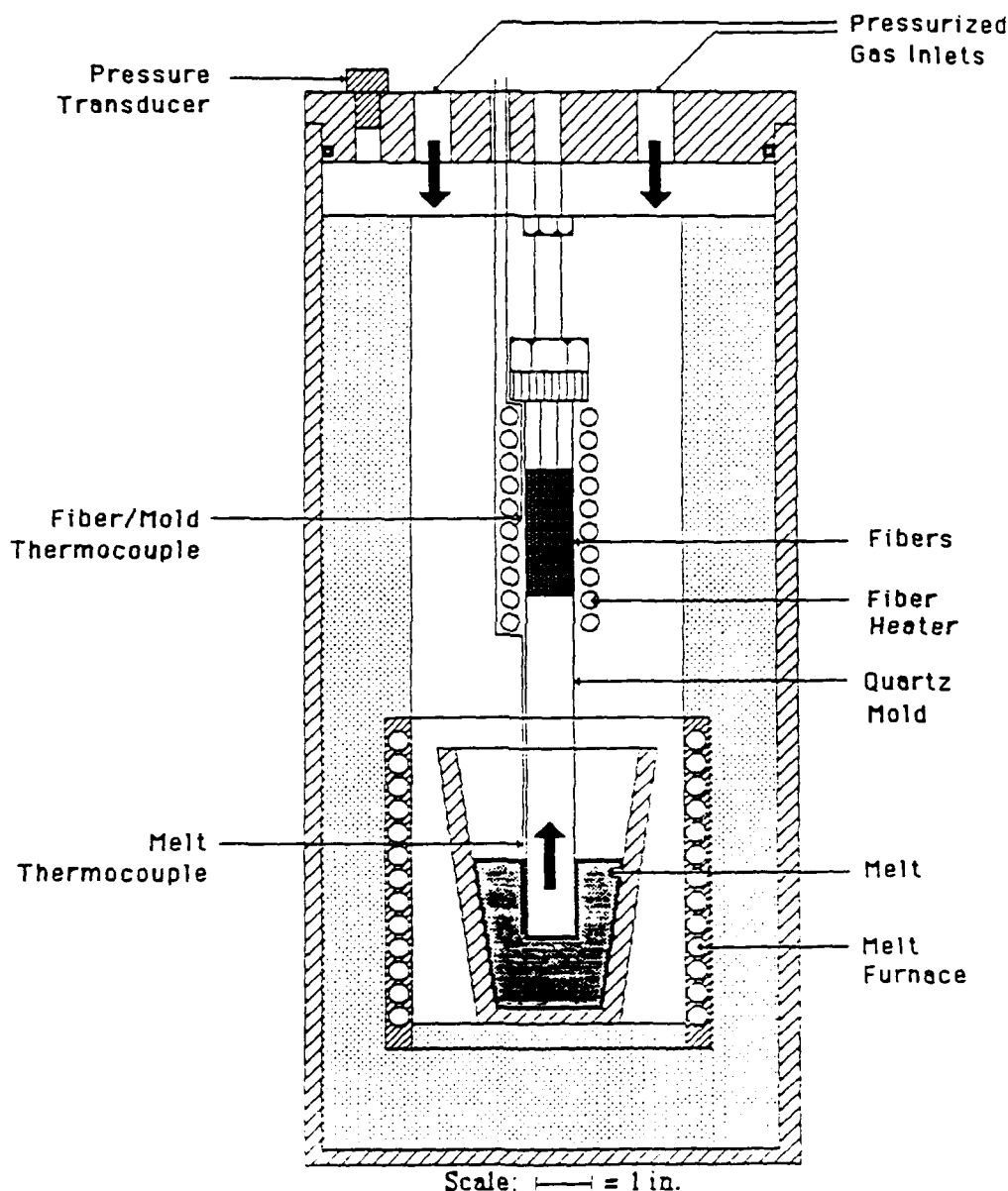
Fig. 1 - Schematic drawing of pressure casting apparatus.

A technique was developed to measure the position of the molten metal front as it moves through the fiber preform during infiltration. This is achieved by inserting a SiC filament between the preform and the quartz tube mold. A potential is applied between the filament and the metal crucible, with the molten metal acting as a switch to close the circuit. A chart recorder then measures the potential drop across the SiC filament over time. As the metal infiltrates the preform, the potential measured across the filament decreases due to the decrease in effective electrical length of the SiC filament.

Monitoring the potential drop during infiltration then allows a calculation of the position of the metal front L as a function of time.

The experimental procedure yields a dynamic measure of infiltration kinetics during infiltration under constant applied pressure, and produces a sample of composite, which can be investigated using conventional metallography and chemical analysis. The relatively planar and well defined infiltration front observed with these preforms and the unidirectionality of the infiltration path simplify considerably analysis of the infiltration process, and the theoretical analysis outlined above can be tested against experimental data.
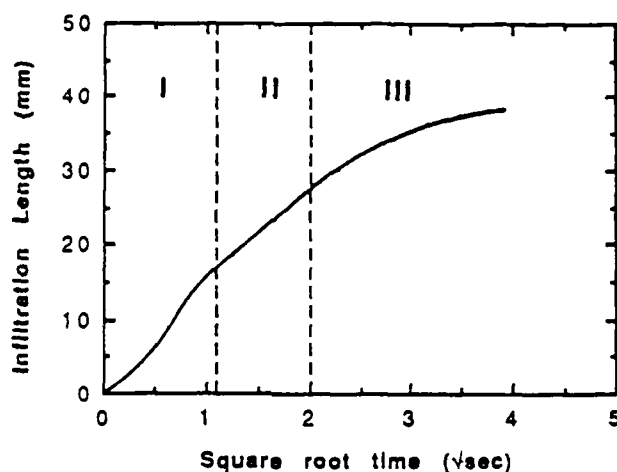
Fig. 2 - Typical plot of infiltration length L versus square-root time measured on an actual infiltration run with a pure aluminum matrix. Region I corresponds to the pressurization transient. In Region II infiltration is adiabatic while in Region III effects due to cooling at the mold wall become noticeable and eventually cause cessation of flow.

The slope in Region II is ψ defined in the text.

We found from our measurement of infiltration front position L versus time that after a short transient due to the finite time for full pressurization of the apparatus (1.2 seconds), infiltration is parabolic as predicted by the adiabatic model, Fig. 2. Later in the infiltration process, infiltration kinetics deviate downwards from the parabolic law, because of external cooling which raises the fraction solid metal in the composite above what is predicted by the adiabatic model. Flow of the metal stops by "choking" when external cooling has caused full solidification of the matrix at any position x along the infiltrated sample.

Adiabatic infiltration is thus observed early in the experiments, and data can be compared with predictions from the adiabatic model. A sample of composite infiltrated under nearly adiabatic conditions can also be obtained if metal flow is suppressed early by suddenly raising the pressure from P_g to P_0 in the preform ahead of the infiltration front. Further details on experimental procedures can be found elsewhere.[9-13]

RESULTS

1 - Case of a pure metal.

In the case of a pure metal, liquid and solid metal can only coexist at the melting point of the metal T_M if equilibrium is assumed at the solid/liquid interface. Therefore, the problem is much simplified, since there can be no heat transfer where solid metal is present, and f_S can therefore not vary continuously in the composite. Furthermore, with a pure metal, composition is no longer an issue, and Equation 6 is irrelevant.

If the initial fiber temperature is above the metal melting point, no solid metal will form, save for solidification due to cooling at the mold walls. The adiabatic problem is then one of uncoupled fluid flow; the infiltration kinetics can be derived first to yield, for unidirectional adiabatic infiltration, the position of the metal front as a function of time. If the initial fiber temperature is below the melting point of the metal, some solid metal will form at the infiltration front to heat the fibers up to the metal melting point by the release of latent heat. In the case of a pure metal, this solid metal must solidify as a sheath surrounding the fibers since solidification is limited by heat transfer to the cold fibers.
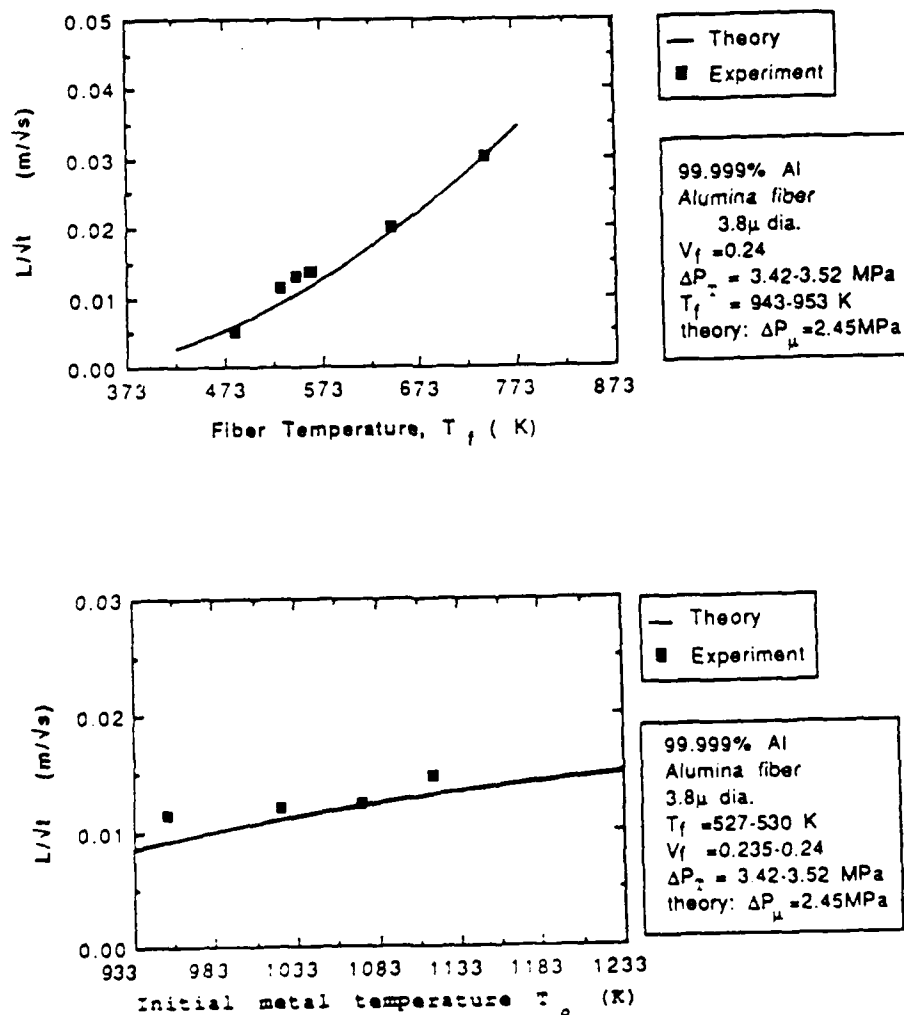
Fig.3 - Effect of initial fiber and metal temperatures on $\psi = L/\sqrt{t}$ for infiltration by pure aluminum.

When heat transfer ahead of the infiltration front is negligible, which will be the case with alumina fibers, for example, the fraction solid metal f_s is simply given by thermal equilibration at the infiltration front:

$$f_s = \frac{\rho_f c_f V_f (T_M - T_f)}{\rho_f H (1 - V_f)}$$

(9)

as was proposed by previous researchers.[1-4] Formation of this solid metal phase will substantially influence the kinetics of infiltration by decreasing the average permeability. Experiments with high purity aluminum have demonstrated the validity of the model, and the physics of infiltration by a pure metal are fairly well understood at present .[7,9-11] A comparison of predicted values of ψ with experimental data from Masur et al.[9] in Fig. 3 shows the very different influence of T_f and T_0, and the level of agreement of data with theory.

2 - Case of an alloy: Al-4.5 wt% Cu.

In the case of an alloy, the problem is more complex with cold fibers than in the case of a pure metal because: (a) solid and liquid metal can coexist over a range of temperatures, making heat transfer possible within the region of semi-solid metal, (b) the morphology of the solidifying metal can no longer be in the form of a sheath surrounding the fibers because solidification is now controlled by solute diffusion and (c) mass transfer must also be accounted for.

Macrosegregation has been shown by Masur et al. to result in the composite after infiltration with Al-4.5 wt % Cu of a preform initially at a temperature below the liquidus of the metal.[10,12] Theoretical analysis of the adiabatic problem, along the lines described above and to be presented in a forthcoming publication,[8] allows prediction of the concentration profile in the composite. The problem is solved for unidirectional adiabatic infiltration with constant applied pressure P_0, based on the equations and methodology given above.
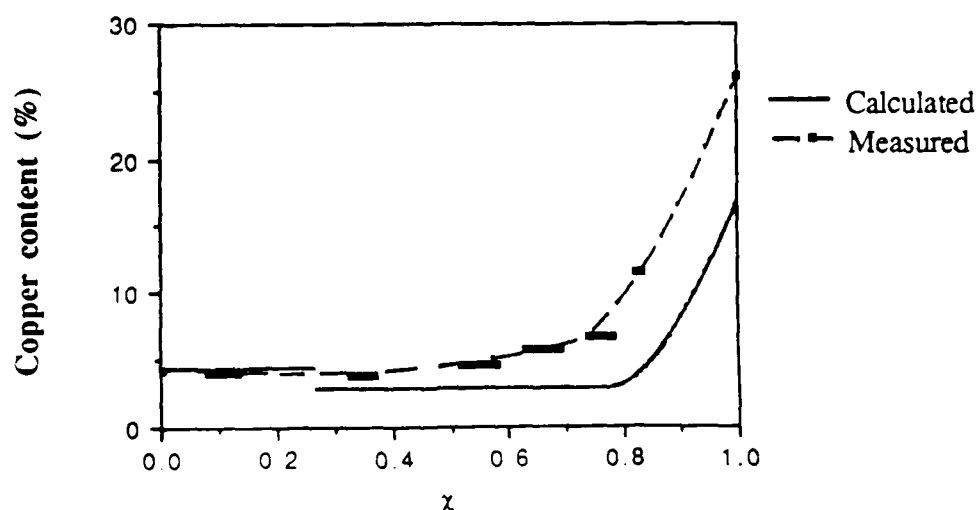
Fig.4 - Comparison of theory and preliminary experimental data for infiltration by Al-4.5 wt% Cu (Véronique Michaud, Ph.D. Thesis, in progress).

It is found that variations in concentration and in fraction solid are predicted within the composite during infiltration, which agree qualitatively with data reported in Reference 12 and quantitatively with preliminary data obtained from wet chemical analysis of slices sectioned from a sample for which most of the infiltration was adiabatic, Fig. 4. A particularly interesting finding from the analysis is that solidification of an alloy during infiltration of a cold preform takes place gradually and as temperature *increases* during progress of solidification.

3 - Measurement of preform wettability.

We found in our work with pure aluminum that by plotting measured values of ψ^2 versus applied pressure $\Delta P_T = P_O - P_g$ as in Fig. 5, a linear correlation was indeed obtained as predicted by theory, with an intercept of the abscissa axis at a pressure different from zero. This we consider, as explained in the beginning of this paper, to be evidence of the capillary pressure drop at the infiltration front which accounts for the difference between applied pressure ΔP_T and the pressure differential across the infiltrated composite which governs the kinetics of infiltration ΔP_μ , see Equation 1. Curves such as that in Fig. 5 therefore allow measurement of the wettability of preforms under conditions that are more relevant to the processing of composites than data from the sessile drop technique. Their interpretation is of course less straightforward than with the sessile drop technique; wetting is measured here under dynamic wetting conditions with concomitant heat exchange between the liquid metal and the ceramic fibers resulting in rapid solidification of the pure matrix.
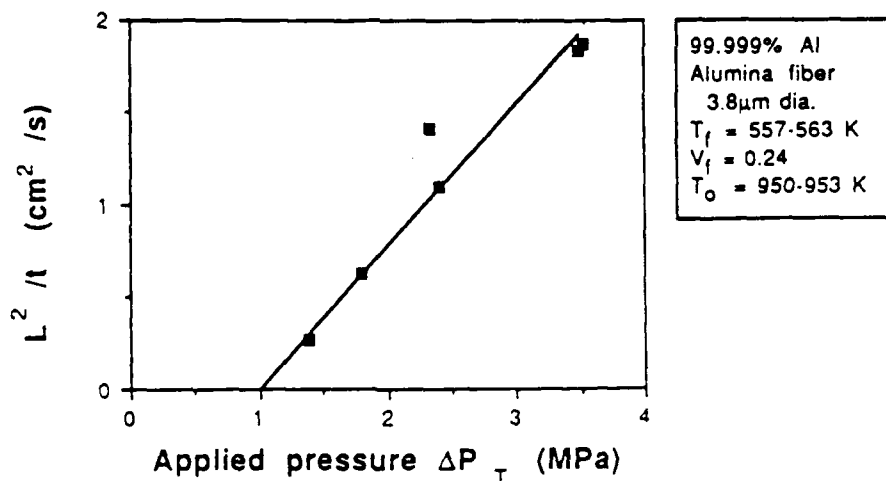
Fig. 5 - Plot of measured values of ψ^2 versus applied pressure showing that the capillary pressure drop is about 1 MPa for alumina preforms infiltrated with pure aluminum at $V_f = 0.24$.

CONCLUSION

Infiltration of a preform with molten metal is analyzed for the case of unidirectional infiltration. For adiabatic unidirectional infiltration under constant applied pressure, solution of the problem can be obtained by a similarity method which simplifies considerably the analysis. Unidirectional infiltration experiments have been performed using a technique which allows for independent control of the various process

variables. Comparison of theory and experiment has been comforting so far, and has allowed measurement of dynamic wettability of preforms by liquid metals.

ACKNOWLEDGEMENTS.

REFERENCES

1. S. Nagata and K. Matsuda, *IMONO*, **53** (1981), 300-304.

2. S. Nagata and K. Matsuda, *Trans. Japan Foundrymen's Soc.*, **2** (1983), 616-620.

3. H. Fukunaga, in *Cast Reinforced Metal Composites*, S.G.Fishman and A.K.Dhingra Eds., Proc. Conf. Chicago 1988, ASM International, (1988), 101-107.

4. H. Fukunaga and K. Goda, *Bull. of Japan. Soc. of Mech. Eng.* **27** (1984), 1245-1250.

5. H. Fukunaga and K. Goda, *J. of Japan Inst. of Metals* **49** (1985), 78-83.

6. S. Ergun, *Chem. Eng. Prog.* **48** (1952), 89-94.

7. A.Mortensen, L.J. Masur, J.A. Cornie and M.C. Flemings, "Infiltration of Fiber Preforms by a Pure Metal Part I: Theory", accepted *Met. Trans. A.*

8. A.Mortensen and V.Michaud, "Infiltration of Fiber Preforms by an Alloy Part I: Theory", work in progress.

9. L.J. Masur, A. Mortensen, J.A. Cornie and M.C. Flemings, "Infiltration of Fiber Preforms by a Pure Metal Part II: Experiment", accepted *Met. Trans. A.*

10. L.J. Masur, "Infiltration of Fibrous Preforms by a Pure Metal", Ph.D. Thesis, Department of Materials Science and Engineering, MIT, February 1988.

11. L.J. Masur, A. Mortensen, J.A. Cornie and M.C. Flemings, Proceedings of the Sixth International Conference on Composite Materials ICCM 6, F.L.Matthews, N.C.R.Buskell, J.M.Hodgkinson and J.Morton Eds., London, Elsevier, 1987, 2.320-2.329.

12. Experimental work by L.J.Masur, cited by J.A.Cornie, A.Mortensen and M.C.Flemings, Proceedings of the Sixth International Conference on Composite Materials ICCM 6, F.L.Matthews, N.C.R.Buskell, J.M.Hodgkinson and J.Morton Eds., London, Elsevier, 1987, pp.2.297-2.319.

Preparation of Boron-Containing Ceramic Materials by Pyrolysis of the Decaborane(14)-Derived [-B₁₀H₁₂·Ph₂POPPh₂]ₓ- Polymer

Dietmar Seyferth,*,† William S. Rees, Jr.,† John S. Haggerty,*,‡ and Annamarie Lightfoot‡

Department of Chemistry and Materials Processing Center, Massachusetts Institute of Technology, Cambridge, Massachusetts 02139

Received June 13, 1988

The pyrolysis of the known polymer [-B$_{10}$H$_{12}$·Ph$_2$POPPh$_2$]$_x$- to give a boron-containing ceramic has been studied. The pyrolysis to 1000 °C gives an amorphous solid in 93% ceramic yield that contains boron, phosphorus, oxygen, and a large excess of carbon. Further studies devoted to this material have served to characterize it with respect to surface area, pore size and distribution, density, grain size, crystalline phases, and elemental composition as a function of temperature up to 2350 °C.

Introduction

Polymer pyrolysis as a route to ceramic materials has received much attention in recent years.[1] This procedure has been applied principally to the preparation of silicon-containing ceramic materials such as silicon carbide, nitride, carbonitride, and oxynitride.[1,2] Much less work has been devoted to the application of polymer pyrolysis to the preparation of boron-containing ceramic materials. The few reports in this area have dealt mostly with boron nitride precursors,[3] and there is only one recent example of the preparation of boron carbide by the preceramic polymer route.[3h]

The development of polymer pyrolysis as a route to ceramics beyond the restricted field of pyrolytic carbon came about as a result of interest in new "high-technology" applications of ceramics with exceptional high-temperature properties such as the carbides, nitrides, and oxides of silicon, boron, aluminum, and the early transition metals. For instance, there is considerable interest in strong ceramic fibers for use in composites, in inert ceramic coatings for materials that are subject to high-temperature oxidation and other forms of corrosion, and in low-loss binders for use in forming ceramic powders into shaped bodies. These applications require a soluble or fusible polymeric precursor that can be spun into fibers and/or that can be used to coat ceramic bodies and powder particles. Also

of interest is the preparation of shaped ceramic bodies by pyrolysis of shaped bodies of such "preceramic" polymers.

The issues that are of importance in preceramic polymer design and preparation have been discussed.[1] The most important *chemical* issues are those of polymer processability, high ceramic yield, and elemental composition. However, there are important *ceramics* issues as well, such

(1) Reviews on preceramic polymers: (a) Wynne, K. J.; Rice, R. W. Ann. Rev. Mater. Sci. 1984, 14, 297. (b) Rice, R. W. Am. Ceram. Soc. Bull. 1983, 62, 889. (c) Seyferth, D. In Transformations of Organometallics Into Common and Exotic Materials: Design and Activation; NATO ASI Series E: Applied Sciences, 141; Laine, R. M., Ed.; Martinus Nijhoff: Dordrecht, 1988; pp 133–154. (d) Seyferth, D.; Wiseman, G. H.; Schwark, J. M.; Yu, Y.-F.; Poutasse, C. A. In Inorganic and Organometallic Polymers; ACS Symposium Series 360; Zeldin, M., Wynne, K. J., Allcock, H. R., Eds.; American Chemical Society: Washington, D.C., 1988; pp 143–155.

(2) (a) Yajima, S. Am. Ceram. Soc. Bull. 1983, 62, 893. (b) Wills, R. R.; Markle, R. A.; Mukherjee, S. P. Am. Ceram. Soc. Bull. 1983, 62, 904. (c) Schilling, Jr., C. L.; Wesson, J. P.; Williams, T. C. Am. Ceram. Soc. Bull. 1983, 62, 912. (d) LeGrow, G. E.; Lim, T. F.; Lipowitz, J.; Reaoch, R. S. Am. Ceram. Soc. Bull. 1987, 66, 363. (e) Laine, R. M.; Blum, Y. D.; Tse, D.; Glaser, R. In Inorganic and Organometallic Polymers; ACS Symposium Series 360; Zeldin, M., Wynne, K. J., Allcock, H. R., Eds.; American Chemical Society: Washington, D.C., 1988; pp 124–142.

(3) (a) Narula, C. K.; Schaeffer, R.; Paine, R. T.; Dayte, A.; Hammetter, W. F. J. Am. Chem. Soc. 1987, 109, 5556. (b) Narula, C. K.; Janik, J. F.; Duesler, E. N.; Paine, R. T.; Schaeffer, R. Inorg. Chem. 1986, 25, 3346. (c) Wada, H.; Ito, S.; Kuroda, K.; Kato, C. Chem. Lett. 1985, 691. (d) Paciorek, K. J. L.; Kratzer, R. H.; Harris, D. H.; Smythe, M. E.; Kimble, P. F. U.S. Patent 4581468, 1986. (e) Paciorek, K. J. L.; Harris, D. H.; Kratzer, R. H. J. Polym. Sci., Polym. Chem. Ed. 1986, 24, 173. (f) Lindemanis, A. E. Mater. Sci. Res. 1984, 17, pp 111–121. (g) Rees, Jr., W. S.; Seyferth, D. J. Am. Ceram. Soc. 1988, 71, C-194. (h) Mirabelli, M. G. L.; Sneddon, L. G. J. Am. Chem. Soc. 1988, 110, 3305.

† Department of Chemistry.
‡ Materials Processing Center.
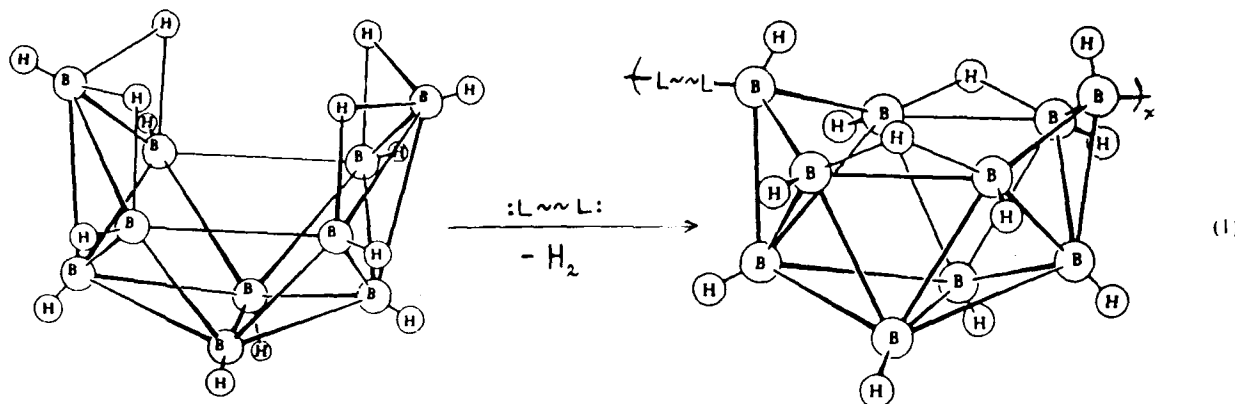
as *control* of porosity and microstructure.

Boron carbide, B_4C, is of considerable interest because of its high thermal stability (mp 2450 °C), high hardness, and resistance to attack at high temperature by many chemicals.[4] The investigation described here had as its objective the synthesis of a polymeric precursor for boron carbide, either as the pure material or as a major component of a ceramic blend.

Results and Discussion

Synthesis and Preliminary Studies. As a starting material for this investigation we chose decaborane(14), $B_{10}H_{14}$, since it is a difunctional molecule with respect to reaction with Lewis bases (:L), forming products of the type $L \cdot B_{10}H_{12} \cdot L$ with concomitant loss of 1 mol equiv of dihydrogen.[5] With difunctional Lewis bases (:L~~L:), linear polymers are formed (eq 1). Decaborane(14)-derived polymers had been prepared some 20 years ago by Parshall[6] and by Schroeder and co-workers,[7] both using diphosphines as the difunctional Lewis bases. In the formation of such $L \cdot B_{10}H_{12} \cdot L$ adducts, monomeric or polymeric, there is no polyhedral rearrangement of boron atoms, the only structural change being relocation of B–H–B three-center, two-electron bonds on going from the nido to the arachno structure.

For detailed investigation of polymer pyrolysis as a route to boron-containing ceramics we chose the $[-B_{10}H_{12} \cdot Ph_2POPPh_2]_x-$ polymer that had been prepared first by Schroeder and co-workers by hydrolysis of $ClPh_2P \cdot B_{10}H_{12} \cdot PPh_2Cl$ with wet benzene in the presence of triethylamine or by reaction of this adduct with $HOPh_2P \cdot B_{10}H_{12} \cdot PPh_2OH$ in the presence of triethylamine.[7a,b] This polymer, an air-stable, white solid with mp >300 °C, is soluble in polar organic solvents such as acetonitrile and *N,N*-dimethylformamide (DMF) and was found to have a molecular weight of 27 000 (light scattering, in *N*-methylpyrrolidone solution). When this polymer was heated to 350 °C, 4 mol equiv of dihydrogen was evolved per $B_{10}H_{12}$ unit, as well as a trace amount of benzene. The residue was insoluble in all organic solvents tried. Pyrolysis at higher temperature was not investigated by Schroeder and co-workers.

We have found that pyrolysis of the $[-B_{10}H_{12} \cdot Ph_2POPPh_2]_x-$ polymer, prepared as described by Schroeder and co-workers, in a stream of argon to 1000 °C at 10 °C/min, gave a black powder as residue in 86% ceramic yield.[8] Elemental analysis of the pyrolysis product, which was amorphous as determined by X-ray diffraction, gave 23.7% B, 57.4% C, 11.5% P, and 0.2% H. Thus this material contains a large excess of free carbon (compare B_4C: calcd 78.26% B, 21.74% C). This was not unexpected since it is known that pyrolysis of phenyl-substituted organosilicon polymers always gives a large excess of carbon in addition to SiC.[9] Exploratory experiments showed the $[-B_{10}H_{12} \cdot Ph_2POPPh_2]_x-$ polymer to be potentially useful as a binder for boron carbide powder and in the formation of shaped ceramic bodies. Accordingly, it was chosen for further, more detailed studies.

The potential utility of this polymer in the formation of shaped ceramic bodies no doubt is due in large part to its extremely high ceramic yield on pyrolysis. However, a disadvantage of this polymer, already noted, is the fact that the solid pyrolysis product contains a large excess of free carbon. We have addressed this problem by forming a composite of the $[-B_{10}H_{12} \cdot Ph_2POPPh_2]_x-$ polymer with the amount of elemental boron powder required to convert this excess carbon to B_4C. (Elemental boron and carbon undergo reaction to form boron carbide at around 1600 °C).[4] Such an experiment (pyrolysis to 1000 °C in argon) gave a ceramic residue that contained 73.2% B, 21.3% C, and 4.18% P. Heating this material to 1500 °C in argon left a residue that now contained 76.9% B, 18.0% C, and 2.6% P. This translates to 87.3% by weight B_4C and 12.7% by weight B if one assumes only the presence of boron and carbon and ignores the small amounts of phosphorus and oxygen still present. Examination of this material by powder X-ray diffraction (XRD) showed the presence of crystalline B_4C.

During the course of this investigation other $[-B_{10}H_{12} \cdot diphosphine]_x-$ polymers were examined for potential utility: those in which the diphosphine is $Ph_2PN=PPh_2CH_2CH_2PPh_2=NPPh_2$[7a,c] and $Ph_2PNHNHPPh_2$. These, however, gave only low ceramic yields (52% and 57%, respectively) on pyrolysis to 1000 °C and thus were not investigated further.

Characterization of Materials. Four types of samples were characterized systematically: as-fired powder (powder) and bar (bulk) samples, in addition to ground powders from either fired bars (ground bulk) or powders (ground powder) derived from the $[-B_{10}H_{12} \cdot Ph_2POPPh_2]_x-$ poly-

(4) (a) Thompson, R. In *Progress in Boron Chemistry*; Brotherton, R. J., Steinberg, H., Eds.; Pergamon: London, 1970; Vol. 2, pp 173–230. (b) Wentorf, Jr., R. H. In *Kirk-Othmer Encyclopedia of Chemical Technology*, 3rd ed.; Wiley: New York, 1978; Vol. 4, pp 126–127.

(5) *Gmelin Handbook of Inorganic Chemistry*, 8th ed.; New Supplement Series, *Boron Compounds 20, Boron-Hydrogen Compounds*; Springer-Verlag: Berlin, 1979; Vol. 54, pp 151–165.

(6) Parshall, G. W. U.S Patent 3035949, 1962.

(7) (a) Schroeder, H. A.; Reiner, J. R.; Knowles, T. A. *Inorg. Chem.* **1963**, *2*, 393. (b) Reiner, J. R.; Schroeder, H. A. U.S. Patent 3141856, 1964. (c) Schroeder, H. A. U.S. Patent 3155630, 1964.

(8) Percent ceramic yield = (wt pyrolysis residue × 100)/(wt pyrolysis charge).

(9) White, D. A.; Oleff, S. M.; Fox, J. R. *Adv. Ceram. Mater.* **1983**, *2*, 53.

Table I. Summary of Crystalline Phases Observed by XRD and EDS Determined Phosphorus Content in Materials Produced from the $[-B_{10}H_{12} \cdot Ph_2POPPh_2]_x-$ Polymer at Various Stages of Processing

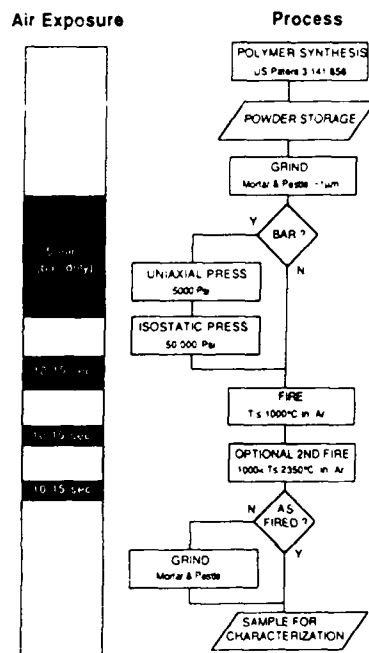| temp, °C	time, h	sample	P (EDS)	rel peak int (XRD)			
				B_4C	C	$B_{13}P_2$	BP
1000	0.5	bulk	yes	0	0	0	0
1500	10.0	powder		62	100	90	0
1500	10.0	bulk	yes	26	70	100	42
1500	10.0	bulk[a]		0	47	65	100
1500	25.0	bulk	yes	62	80	100	9
1500	25.0	bulk[a]		0	70	71	100
1550	0.5	bulk	yes	0	43	100	53
1870	0.5	bulk	yes	42	100	0	0
2090	0.5	bulk	no	18	100	0	0
2350	0.5	bulk	no	9	100	0	0

[a] After ~1 mm removed by surface grinding.

Figure 1. Summary of processing steps and air exposures for the ceramic blend produced from the $[-B_{10}H_{12} \cdot Ph_2POPPh_2]_x-$ polymer.

Figure 2. Growth of B_4C and C crystallite grain sizes, as determined by XRD line broadening, on the exposed surface of a bulk sample of ceramic derived from the pyrolysis of the $[-B_{10}H_{12} \cdot Ph_2POPPh_2]_x-$ polymer in an argon atmosphere after maintaining firing temperature for 0.5 h.

mer. These sample groups (Figure 1) permitted a qualitative determination of the scale over which pores were isolated; they also permitted the effect of diffusion distance on phosphorus and oxygen losses to be investigated.

Crystallinity and Grain Size. X-ray diffraction patterns were made of as-fired powder and the surfaces of bulk samples, both before and after removal of ~1 mm of exterior thickness. The results illustrate some important differences between samples fired as powder and bulk (Table I). A complex crystallization sequence that results in part from the phosphorus residuals is also evident.

No sample showed evidence of crystallinity for firing temperatures below 1500 °C. This is common for the extremely fine, sometimes microcrystalline, structures that result from polymer pyrolysis.[10] Crystalline phases emerged with progressively sharper diffraction patterns with increasing firing temperatures.

After firing at 1500 °C for 10 h, as-fired powder samples exhibited crystalline B_4C, C, and $B_{13}P_2$. Exterior surfaces of bulk samples subjected to the same firing cycle revealed these phases in addition to BP. The BP concentration increased with distance from the outer surface (Table I).

The initial appearance of crystalline BP at 1500 °C in these samples, its subsequent conversion to crystalline $B_{13}P_2$, and finally its disproportionation into solid boron and gaseous phosphorus as firing temperatures exceeded 1500 °C is similar to reported findings for simple mixtures of boron and phosphorus.[4]

Crystalline B_4C was first observed only on the exterior surfaces of bulk samples fired at 1500 °C. Boron carbide and carbon diffraction patterns became well developed for bulk samples only for firing temperatures of 1870 °C and higher. With heating to 2090 °C, B_4C was present throughout the bulk sample. The emergence of a diffraction peak at $2\theta = 44.6°$ with Cu $K\alpha$ radiation ({101} type carbon planes) in the bulk sample fired to 2350 °C is evidence of carbon graphitization.[11] The differences in crystallinity between powder and bulk samples and between the surfaces and interiors of bulk samples probably result from enhanced phosphorus and oxygen losses in the proximity of free surfaces (Table I).

The B_4C and C crystallite sizes on the exposed surfaces of bulk samples were determined by XRD line broadening. Results for samples fired at temperatures between 1500 and 2350 °C for 0.5 h are summarized in Figure 2. Both phases grow continuously to the highest temperature investigated (2350 °C). The maximum observed grain sizes (~50–60 nm) are extremely small by comparison to materials processed by conventional techniques.[12] The BP grain size on the exposed surface of the bulk samples fired at 1525 ± 25 °C decreased from a dimension that was larger than the broadening limit of the X-ray diffractom-

(10) Walker, Jr., B. E.; Rice, R. W.; Becher, P. F.; Bender, P. A.; Coblenz, W. S. *Am. Ceram. Soc. Bull.* **1983**, *62*, 916.

(11) Jenkins. G. M.; Kawamura, K. *Polymeric Carbons—Carbon Fibre, Glass and Char*; Cambridge University Press: Oxford, 1976.

(12) Schwetz, K. A.; Grellner, W. *J. Less-Common Met.* **1981**, *82*, 37.

eter (150 nm) for a 0.5-h heat treatment to 13 nm for a 25-h heat treatment. Internal BP grain sizes also decreased with firing time but were 3–5 times larger than the surface grains. The $B_{13}P_2$ grain size remained constant (9–14 nm) with respect to both time held at 1500 °C and position throughout the bulk sample.

TEM and STEM analyses of internal regions of bulk samples heated at 1500 °C for 10 h revealed four distinct crystalline phases in an amorphous matrix; three had spherical dimensions of ~50 nm, 150–200 nm, and >1 μm, and one was 10 nm × 200 nm needles. The XRD-calculated sizes of $B_{13}P_2$ and BP (13 and 125 nm, respectively) are in general agreement with two of the observed crystalline phases. With the exception of the BP phase, the dimensions of the crystalline phases were uniform throughout the bulk sample volumes.

Composition. Chemical compositions for the $[-B_{10}H_{12}\cdot Ph_2POPPh_2]_x-$ polymer-based materials present at various stages of processing are summarized in the Experimental Section. Energy-dispersive X-ray spectroscopy (EDS) results for qualitative phosphorus content are presented (Table I). Even though the $[-B_{10}H_{12}\cdot Ph_2POPPh_2]_x-$ polymer gives a high yield of solids that include B_4C, it is evident that the pyrolysis product should be carbon rich. The B/C ratios observed for the materials fired as either powder or bulk are higher than those present in the calculated composition of a material resulting from loss of all elements present in the polymer except boron and carbon. Although the ceramic samples were carbon rich, some of the carbon initially present in the polymer was lost during pyrolysis. The determination of a nominal formulation for amorphous materials is not easily carried out. For example, it is not simple to differentiate between an intimate mixture of boron and carbon and boron carbide, when both samples contain the same elemental composition and are amorphous. If we assume that all boron is present as B_4C and the remaining carbon as the free element, then a nominal formulation may be derived for the material. For example, in this manner, the ceramic blend produced by pyrolysis of the $[-B_{10}H_{12}\cdot Ph_2POPPh_2]_x-$ polymer to 2350 °C may be represented as $(B_4C)_{1.0}(C)_{7.0}$ on a molar basis or 39.7% B_4C and 60.3% C on a weight basis. It should be stressed that this is only a *nominal* formulation of this material. It could also contain amorphous phases of nonstoichiometric boron carbide and/or elemental boron. There is not enough information available at the present time to present a realistic formula for the composition of those materials present at intermediate stages of processing. However, at this point several qualitative trends have emerged and will be pointed out. Boron carbide and carbon crystallize from the amorphous blend at ~1500 °C. Oxygen and phosphorus loss is not complete until temperatures greater than 1500 °C are reached.

The effect of the shortened diffusion distances in the powder samples is shown by comparing the phosphorus and oxygen contents of the 1500 °C powder and bulk samples (P: bulk, 11.2%; powder, 0.4%. O: bulk, 6.7%; powder, 2.9%). The effect of increased firing temperature is shown by comparing results obtained at 1000 and 1500 °C for powder samples and those obtained at 1500 and 2300 °C for bulk samples (see Experimental Section). Both shorter dimensions and increased temperature enhance phosphorus and oxygen losses.

EDS analyses of fracture surfaces (Table I) show that all detectable phosphorus is lost from the bulk samples for firing temperatures between 1870 and 2090 °C. EDS X-ray mapping of the internal phosphorus distribution within

A

B |◄—200 nm—►|
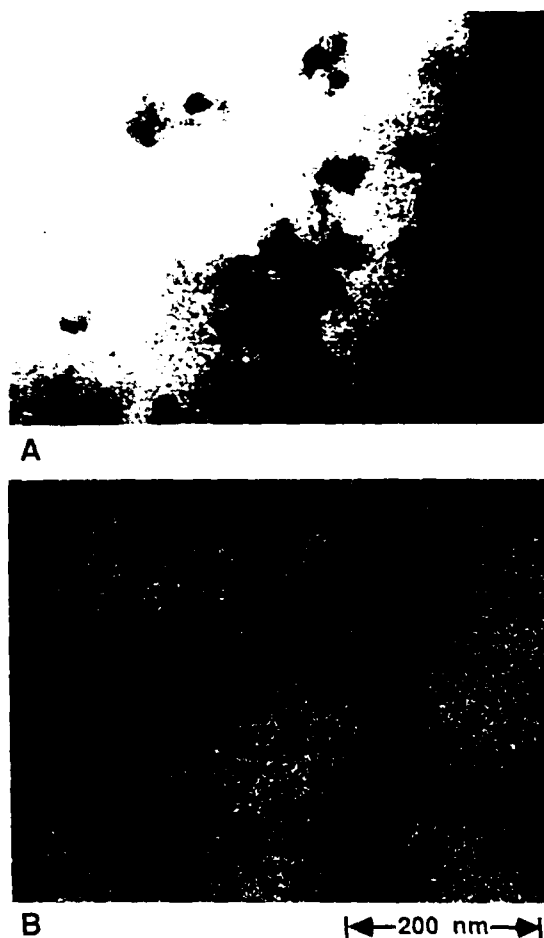
Figure 3. (A) Scanning electron micrograph of an internal cross section of a bulk ceramic sample derived from the $[-B_{10}H_{12}\cdot Ph_2POPPh_2]_x-$ polymer by pyrolysis at 1500 °C for 10 h, showing ~50-nm crystals embedded in an amorphous matrix. (B) X-ray map of phosphorus distribution in the region shown in A. Lighter areas indicate higher concentration.

a bulk sample fired at 1500 °C for 10 h shows that the phosphorus is concentrated in isolated regions, some of which surround the ~50-nm, phosphorus-containing crystallites (Figure 3). Thus, phosphorus segregation occurs on a macroscopic level near exposed surfaces and on a microscopic level near precipitates, in bulk samples.

Oxygen levels found in some fired samples are higher than those predicted from the polymer composition (3.2% O in the polymer). It has not been determined whether the apparent excesses are entirely real or whether they result in part from contamination of the high-surface-area materials during processing and/or chemical analyses. Air exposure during processing was minimized to reduce the contamination of processed samples with atmospheric water vapor and oxygen (Figure 1).

It is not known how oxygen is held in the ceramic blends formed by pyrolysis of this precursor. Boron oxide (mp 450 °C) and phosphorus oxide (mp 580 °C) both melt well below 1000 °C. Boron phosphate, BPO_4, is also a known material. All of these oxygen-containing compounds are either soluble in hot water or easily hydrated. However, an attempt to extract samples of the ceramic material (fired to 1000 °C as a powder) with boiling water did not result in any appreciable weight change of the samples.

The diffuse-reflectance Fourier transform (DRIFT) infrared spectra of powder samples of the $[-B_{10}H_{12}\cdot Ph_2POPPh_2]_x-$ polymer fired to 1000 and 1500 °C each showed broad absorptions at 1104–1406 cm^{-1} (maxima at
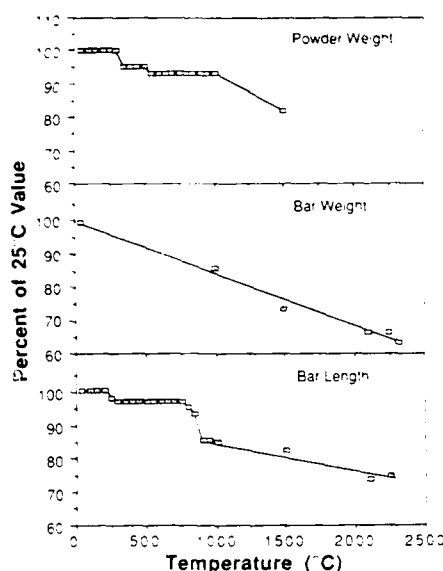
Figure 4. Graph of weight and length changes of the $[-B_{10}H_{12} \cdot Ph_2POPPh_2]_x-$ polymer as a function of temperature.

Figure 5. Graph of density of the material produced by pyrolysis of the $[-B_{10}H_{12} \cdot Ph_2POPPh_2]_x$ polymer as a function of temperature.

Figure 6. Specific surface areas, measured by the BET method, of bulk, ground bulk, powder, and ground powder samples derived from pyrolysis of the $[-B_{10}H_{12} \cdot Ph_2POPPh_2]_x-$ polymer as a function of firing temperature.

1190 and 1302 cm^{-1}; B_4C shows absorptions at 1080 and 1340 cm^{-1}).[13] The absence of DRIFT absorptions attributable to the presence of B-O and P-O bonds,[13] coupled with the water extraction mentioned above, leads us to conclude that the presence of oxygen, as determined by chemical analysis, arises from dioxygen contamination of samples during handling and that oxygen is not present on the surface of the ceramic derived from pyrolysis of the $[-B_{10}H_{12} \cdot Ph_2POPPh_2]_x-$ polymer. Additionally, samples that had been fired only to 1000 °C had absorptions at 2350–3100 cm^{-1} attributed to the presence of residual B-H and C-H bonds. From these data we conclude that processing temperatures above 1000 °C are required for complete removal of all hydrogen-containing moieties.

Density, Surface Area, and Porosity. Weight and length changes observed during firing of the $[-B_{10}H_{12} \cdot Ph_2POPPh_2]_x-$ polymer from 50 to 2350 °C are shown in Figure 4 for powder and bulk samples. The TMA data imply that this polymer does not soften appreciably to either a molten or a semimolten phase over the temperature range studied. The initial TGA weight decrease ($\sim$ 350 °C) arises from loss of H_2 caused by cleavage of B-H bonds and concomitant formation of B-B bonds, as inferred from IR studies of the polymer prior to and after the weight change (decrease in intensity of absorption at $\sim$ 2500 cm^{-1}, relative to other absorptions). Likewise, intermediate weight loss ($\sim$ 550 °C) presumably is due to processes involving cleavage of C-H bonds and concomitant formation of B-C bonds. High-temperature weight loss (>1000 °C) is associated with removal of phosphorus and oxygen. A detailed description of the pyrolysis mechanism for the $[-B_{10}H_{12} \cdot Ph_2POPPh_2]_x-$ polymer to ceramic conversion is beyond the scope of the data available at this time.

Between 1000 and 1500 °C, both powder and bulk samples exhibit the same weight losses as the average rate followed by the bulk samples from room temperature to 2350 °C. This trend is consistent with the loss of the last element-hydrogen moieties, observed in DRIFT data (above). Unfortunately, there is a gap in the TGA data for the bulk samples arising from sample size limitations in the low-temperature TGA. The total weight loss for
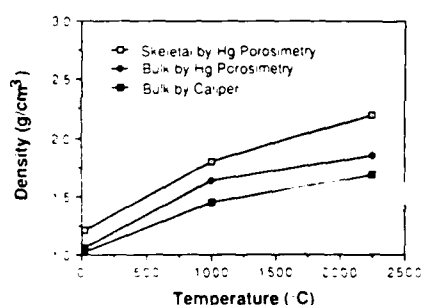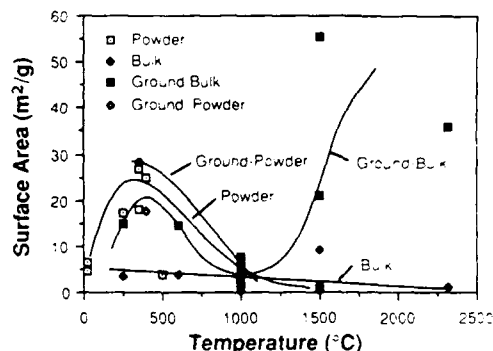
bulk samples between 1500 and 2350 °C corresponds closely to that predicted for the complete loss of the phosphorus and oxygen still present in the material at 1500 °C. The agreement between the room-temperature, 1000 °C, and 1500 °C data points for the powder and bulk samples suggests that the two sample types behaved similarly between room temperature and 1000 °C. However, surface area results discussed below indicate the potential for differences. Below 1000 °C, shrinkage of the bulk samples occurs at two specific temperature levels (250 and 850 °C) which do not coincide precisely with temperatures where weight losses are concentrated in the powder samples. Above 1000 °C, bulk shrinkage persists at a reduced rate.

Densities of bulk samples (measured after cooling to ambient temperature by both calipers and Hg porosimetry) increase continuously with firing temperatures up to 2250 °C (Figure 5). The density of the solid phase including closed pores (skeletal density) increases at a higher rate than the bulk density in the temperature range above 1000 °C. All of these density values are subject to error because of the small sample sizes and irregular shapes. However, the trends and relative values are reproducible. At its maximum, the skeletal density (as determined by Hg porosimetry) reaches $\sim$ 100 % of the theoretical value for a B_4C + C body having the overall nominal composition given above.

The results of BET surface area determinations for powder, bulk, ground bulk, and ground powder samples are summarized in Figure 6. These complex results show that materials fired as powder and bulk differ from one another over the entire range of temperatures investigated. Bulk samples exhibit progressively reduced surface areas from 250 °C to the highest temperature studied (2350 °C). The ground bulk samples show that the reduced surface area does not result from conventional densification mechanisms; rather, internal pores become isolated from

(13) Nyquist, R. A.; Kagel, R. O. *Infrared Spectra of Inorganic Compounds*; Academic: New York, 1971.
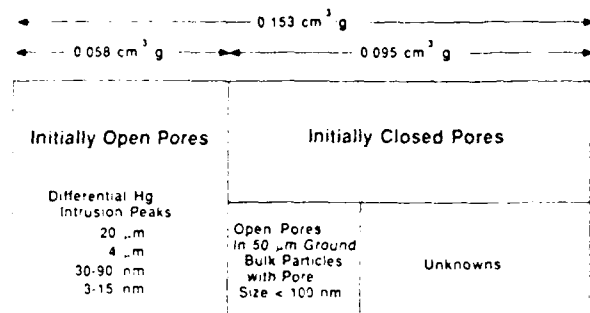
Figure 7. Summary of porosity types found in a sample of the ceramic produced from the $[-B_{10}H_{12} \cdot Ph_2POPPh_2]_x-$ polymer fired in bulk at 1000 °C for 0.5 h. The absolute specific volumes are shown at the top. The results of Hg porosimetry measurements are summarized.

the outer surface. As shown by the ground bulk samples, high-surface-area pores evolve within bulk samples during the initial weight loss up to ~300 °C and then diminish with increasing temperature. Powder, ground bulk, and ground powder samples exhibit similar behavior for temperatures up to ~1000 °C. Surface areas for these three sample types pass through maxima at ~300 °C and then decrease to values exhibited by bulk samples at 1000 °C. Some of the variance between the surface areas of the 1000 °C samples arises from not grinding the samples to the same particle size; the specific area of the ground samples depends on the fraction of total porosity that was exposed to the exterior surfaces of the particles.

For firing temperatures above 1000 °C, the bulk samples show another unusual characteristic. The ground bulk samples reveal that bulk samples again form extremely small, isolated pores at these higher temperatures. BET characterization of the ground bulk samples shows that up to 15% of the initially closed porosity in the bulk samples becomes connected to the exterior surfaces by grinding bulk samples to a particle size of ~50 μm; these pores have a characteristic dimension of less than 100 nm. The total volumes and partition of the pore types in bulk samples after firing to 1000 °C and after grinding (ground bulk) are summarized in Figure 7. These characterizations of the ground bulk samples do not permit estimations either of pores having dimensions greater than 100 nm which are exposed upon grinding or of pores that still remain closed within the ~50-μm particles after grinding.

Channel diameters in the initially open pore structure of bulk samples fired at 1000 °C for 0.5 h were measured by Hg porosimetry; peaks occur at 20 μm, 4 μm, 30–90 nm, and 3–15 nm (Figure 7). SEM photomicrographs show that pores with diameters larger than 2–4 μm result from gross defects (such as entrapment of bubbles or aggregates of several ~5-μm-diameter polymer particles) and that the 30–90-nm pores result from voids, often lenticular, between the original particles that have not completely consolidated by sintering mechanisms. Presumably, these gross defects could be removed by exerting improved control over process variables. The 3–15-nm features probably result from a pore structure that evolves during pyrolysis. The pore size distribution (by number, observed by SEM) on a fracture surface of a 1000 °C bulk sample peaked at nominally 100 nm.

The pore size distribution determined by N_2 adsorption of a bulk sample fired at 1000 °C for 0.5 h revealed pore radii concentrated in two populations that peaked at ~1.5 nm (9% of measured open porosity) and 30 nm (41%). The total open porosity was 8% of the bulk volume. A 2250 °C sample had only 2% open porosity consisting of the smaller characteristic dimension (2–3 nm) pores. These

|◄— 250 μm —►|

Figure 8. SEM micrograph of a sample of the ceramic derived from the $[-B_{10}H_{12} \cdot Ph_2POPPh_2]_x-$ polymer fired in bulk at 1500 °C for 25 h illustrating crack damage originating from an isolated pore.

nitrogen adsorption results agree with the SEM and Hg porosimetry results. TEM micrographs of bulk samples fired at 1500 °C for 10 h reveal features that resemble high number density, spherical pores having ~2-nm diameters. It still must be verified that these features are not damage that resulted from ion thinning.

Much of the weight loss from the $[-B_{10}H_{12} \cdot Ph_2POPPh_2]_x-$ polymer occurs after pores become isolated in bulk samples, whereas pores within the smaller diameter powder samples retain pathways to the exterior surfaces. Isolation of pores before gaseous products have completely escaped presents obvious problems with respect to internal pressures. A photomicrograph of a crack originating from a (presumably isolated) pore within a bulk sample fired at 1500 °C for 25 h is shown in Figure 8. The potential for this type of damage will impose dimensional limits upon parts produced by pyrolysis of fabricated shapes from the $[-B_{10}H_{12} \cdot Ph_2POPPh_2]_x-$ polymer unless firing cycles are identified that do not cause premature closure of pores.

Conclusions

The characterizations described above have demonstrated the feasibility of using the $[-B_{10}H_{12} \cdot Ph_2POPPh_2]_x-$ polymer to produce B_4C-containing material. They also have revealed issues that must be resolved before these materials can compete effectively with conventionally processed bulk materials. Defects in the polymer-derived material include large quantities of free carbon, as well as phosphorus and oxygen residuals, and cracks generated by gas evolution within closed pores. All of these features are much less severe in powder samples, especially those that are amorphous. Thus, intermediate service temperature fibers and coatings are a possible application for this chemistry. The excess carbon may be consumed by the addition of reactive boron to the polymer. Many other feasible chemistries are known, so it is likely that the premature pore closure issue observed with these bulk samples can be controlled with careful processing of alternative chemistries. The extremely small diameter closed porosity should not be a problem for oxidation resistance or mechanical properties.

Experimental Section

General Comments. All manipulations were carried out in

oven-dried glassware under an inert atmosphere (argon or nitrogen) following standard techniques.[14] All solvents were distilled from appropriate drying agents[15] under a nitrogen atmosphere prior to use. Unless otherwise given, all reagents employed were available commercially and were used as received. Twice sublimed decaborane(14) was purchased from Callery Chemical Co., Callery, PA, and used as received. Triethylamine (Aldrich) was distilled from CaH_2 under argon immediately prior to use. Both $B_{10}H_{12} \cdot 2(Ph_2PCl)$ and $B_{10}H_{12} \cdot 2(Ph_2POH)$ were prepared and checked for purity by melting-point analysis (206–208 °C, lit.[16] 212 °C, and 212–215 °C softening, lit.[16] 216 °C softening, respectively). Boron carbide powder (99.5%, <5 µm) was purchased from Cerac and dried at 130 °C for 15 h.

NMR spectra were obtained by using a Varian XL-300 NMR spectrometer, IR spectra on a Perkin-Elmer Model 1430 spectrophotometer. Ceramic analyses were obtained from Galbraith Laboratories, Knoxville, TN, and C and H analyses on nonceramic materials were obtained from Scandinavian Microanalytical Laboratory, Herlev, Denmark. Qualitative content and spatial distribution for phosphorus were determined by using an EG&G Ortec System 5000 EDS attached to a Hitachi S-530 SEM and a Linc LZ5 Series E windowless EDS detector attached to a VG HB5 STEM, respectively.

A hardened stainless steel die was used for forming 1.5 in. × 0.5 in. bars. A Carver laboratory press was used for bar formation. Isostatic bar compaction was carried out in a pneumatically driven oil press with the bars wrapped in Saran Wrap and contained in evacuated, sealed rubber bags. Lindberg tube furnaces with Eurotherm controllers were used for all preparative scale (>1 g) pyrolyses (powder and bulk) to 1500 °C. For pyrolyses to 1000 °C, 1.5-in. o.d. quartz tubes and fused silica boats were used for all samples; for those to 1500 °C, 2.5-in. o.d. mullite tubes and boron nitride boats supported on alumina dee tubes were used; for those to 2350 °C a 1.1-in. o.d. graphite tube furnace and vitreous carbon boats were used. All pyrolyses were carried out under an atmosphere of flowing argon. For experiments to 1000 °C the flow rate was ~6–8 L/h, for experiments to 1500 °C it was ~16–20 L/h, and for experiments to 2350 °C it was ~50–70 L/h.

DRIFT spectra were recorded on an IBM Model IR/85 spectrophotometer. X-ray diffraction patterns were obtained either on a Charles Supper detector and Diano generator instrument or on a Rigaku rotating-anode system. SiC grinding wheels were used to expose internal cross sections of bars for X-ray diffraction.

TMA and TGA measurements were made on a Perkin-Elmer model TGS2 instrument equipped with a Thermal Analysis System 4 controller. In situ TMA data were gathered from ambient temperature to 350 °C; from 350 to 2350 °C measurements were performed on samples that had been heated to the desired temperature and then cooled to ambient. For TGA data, in situ data were obtained for powdered samples from ambient to 950 °C, and mass change data for higher temperatures were collected on bulk samples after they had been heated to the desired temperature and then cooled to ambient conditions. Bulk densities were calculated by using sample mass and caliper-determined volumes. Bulk and skeletal densities as well as pore size distributions were determined by using a Micromeritics Autopore 9220 porosimeter.

Nitrogen adsorption was employed for surface area measurement, as well as an alternative technique for pore size determination. A Quantachrome Quantasorb surface area analyzer and an Omicron Technology Omnisorp 360 instrument were used, respectively, in these adsorption measurements. Powder and bulk samples were characterized as prepared. Bulk samples were broken into pieces consistent with the instrument capacity. Ground bulk and ground powder samples were obtained by grinding bulk and powder samples, respectively, by using an alumina mortar and pestle for about 15 min, until the powder appeared to be uniform. Pore characteristics also were observed

by electron microscopy on fractured or polished specimen surfaces.

Phases and grain sizes were studied by STEM and TEM microscopy and by XRD. A JEOL 200CX instrument was utilized for all TEM and STEM measurements. Two methods were used for TEM sample preparation. Beginning with a thin slice of a ceramic bar, a concave surface was ground into the sample; then it was argon ion milled. The center was perforated to give a circle of the appropriate thickness needed for observation. Alternatively, a bulk sample was powdered, and the resultant powder was deposited on a thin carbon film by dipping the film into a dispersion of the powder in hexane.

Preparation of $[-B_{10}H_{12} \cdot Ph_2POPPh_2]_x -$.[7a] To a suspension of 27.74 g (0.05 mol) of $B_{10}H_{12} \cdot 2(Ph_2PCl)$ and 25.92 g (0.05 mol) of $B_{10}H_{12} \cdot 2(Ph_2POH)$ in 250 mL of benzene was added dropwise with stirring, under nitrogen, a solution containing 10.12 g (0.10 mol) of Et_3N in 250 mL of benzene. After addition was complete, the solution was stirred at reflux for 1 h, cooled to ambient temperature, and filtered in air. The off-yellow solid was washed with 2 × 100 mL of 0 °C acetone, 5 × 100 mL of water, and 5 × 100 mL of 50 °C acetone to give a white powder. Drying for 15 h at ambient temperature and 0.01 mmHg gave 29.14 g (58%) of a free-flowing powder, mp >360 °C. The TGA (to 950 °C at 10 °C/min, argon atmosphere) showed a ceramic yield of 93%. Anal. Calcd for $C_{24}H_{32}OP_2B_{10}$: C, 56.89; H, 6.37. Found: C, 55.94; H, 6.08. $^{11}B\{^1H\}$ NMR (DMSO) 70–30, 24, 18 to –10, –24 to –42 (all br) ppm. $^{31}P\{^1H\}$ NMR (DMF-d_7) 69–72 (br) ppm. $^{13}C\{^1H\}$ NMR (DMF-d_7) 129, 133 ppm (ipso C not observed). ^1H NMR (DMF-d_7) 7.3–8.2 (br, C_6H_5) ppm. IR (nujol) 2540 m, 2520 s, 2500 m, 1376 s, 1110 s, 1005 m, 980 w, 960 s, 914 m, 875 w, 785 w, 742 m, 718 m, 688 m, 641 w cm^{-1}.

Pyrolysis of $[-B_{10}H_{12} \cdot Ph_2POPPh_2]_x -$. A 1.09-g sample of the powdered polymer was placed in two fused silica boats and heated in a quartz tube, under an atmosphere of flowing argon, to 1000 °C at a rate of 10 °C/min, held at 1000 °C for 0.5 h, and allowed to cool to ambient temperature over a period of ~3.5 h. The powdery black residue, 0.937 g (86%), which had shrunk ~24% from the sides of the boat, was amorphous by XRD and had DRIFT absorptions at 2350–3100 and 1104–1406 cm^{-1}, with maxima at 1190 and 1302 cm^{-1}. Anal. Found: B, 23.67; H, 0.2; C, 57.40; P, 11.54. A 0.336-g powder sample of this pyrolysis product was placed in a boron nitride boat and heated in a mullite tube, under an atmosphere of flowing argon, to 1000 °C at a rate of 25 °C/min, held for 1 h at 1000 °C, heated to 1500 °C at a rate of 10 °C/min, held for 10 h at 1500 °C, and cooled to ambient temperature over a period of ~10 h. The residue, 0.274 g (82%), had not visibly changed in appearance; however, a yellow/orange film had deposited on the walls of the pyrolysis tube. Broad diffractions at d = 3.8 and 2.5, indicative of a weakly crystalline material, were observed for B_4C by XRD (JCPDS 35-798, B_4C: d = 2.38, 2.56, 3.78). DRIFT absorptions were present at 1560–1580, 1090–1105, and 780–830 cm^{-1}. Anal. Found: B, 28.9; C, 60.2; P, 0.39; O, 2.88.

Pyrolyses of bulk samples to higher temperatures gave the following results: to 1500 °C, B, 25.16; C, 55.42; P, 11.22; O, 6.66; to 2350 °C, B, 29.15; C, 65.14; P, nil.

General Procedure for the Preparation of Ceramic Composite Bars Using $[-B_{10}H_{12} \cdot Ph_2POPPh_2]_x -$ Polymer as a Binder for Boron Carbide Powder. Weighed quantities of $[-B_{10}H_{12} \cdot Ph_2POPPh_2]_x -$ (0.5 g) and B_4C powder (2.5 g) were mixed and ground for 15 min in an alumina mortar and pestle in an inert-atmosphere box. The samples thus prepared were placed in a 0.5 in. × 1.5 in rectangular die and formed into bars in a Carver laboratory press at 5000 pounds (6667 psi uniaxially), removed to an ambient temperature isostatic press and further compacted to 50 000 psi after being wrapped in Saran Wrap and placed in an evacuated, sealed rubber bag. The uniaxial pressing time duration was ~5 min, and the isostatic pressing time duration was ~15 min. The resulting bar was pyrolyzed in a stream of argon to 1000 °C (10 °C/min heating rate, hold at 1000 °C for 30 min) and allowed to cool to ambient temperature over a period of ~3.5 h. The pyrolyzed sample was handled in an inert-atmosphere box.

For the purposes of this initial screening, a ceramic bar was considered to be "excellent" if it was a uniform, black rectangular monolithic body that had retained its shape (vs the polymer bar before pyrolysis) in all three dimensions without undergoing any

(14) Shriver, D. F.; Drezdzon, M. A. *Manipulation of Air Sensitive Compounds*, 2nd ed.; Wiley: New York, 1986.

(15) Gordon, A. J.; Ford, R. A. *The Chemist's Companion*; Wiley: New York, 1977.

(16) Schroeder, H. A.; Reiner, J. R.; Heying, T. L. *Inorg. Chem.* **1962**, *1*, 618.

discernible shrinkage or bloating above the detectable level of 3–5% and if its strength was such that it could not be broken manually without employing the aid of mechanical means (e.g., a vise and pliers). Such a composite bar prepared by using the $[-B_{10}H_{12}\cdot Ph_2POPPh_2]_x-$ polymer as a binder for B_4C powder was classified as excellent.

Procedure for the Preparation of Ceramic Bars from the $[-B_{10}H_{12}\cdot Ph_2POPPh_2]_x-$ Polymer. A 3.0-g sample of the polymer was finely powdered for 15 min in an alumina mortar and pestle in an inert-atmosphere box and then placed in a 0.5 in. × 1.5 in. rectangular die. Uniaxial pressing in a Carver press to 5000 pounds (~5 min) was followed by ambient temperature isostatic compaction at 50 000 psi (~15 min). The polymer bar thus obtained had the approximate dimensions 0.5 in. × 1.5 in. × 0.25 in.

The weighed and micrometer-measured polymer bar was introduced into a fused silica pyrolysis boat that then was inserted into a quartz tube that had been flushed with argon for 15 min and the end of the tube was connected to an oil bubbler. After ~5 min, the argon flow was reduced from ~100 mL/min to ~20–30 mL/min, and the quartz tube was placed in a Lindberg tube furnace and heated at a rate of 10 °C/min to a temperature of 1000 °C, held at 1000 °C for 0.5 h, and allowed to cool to ambient temperature over a period of ~3.5 h. The ceramic bar was removed to an inert-atmosphere box, weighed, micrometer measured and then subjected to further evaluation or transferred to the appropriate furnace for temperature treatment above 1000 °C. Heating rates for temperatures to 1500 °C were 25 °C/min.

For temperatures above 1500 °C, the heating rate was 17 °C/min.

Preparation and Processing of a Boron Powder/ $[-B_{10}H_{12}\cdot Ph_2POPPh_2]_x-$ Polymer Mixture. The average values of boron $[(23.7 + 28.9)/2]$ and carbon $[(57.4 + 60.2)/2]$ found in the 1000 and 1500 °C samples of fired $[-B_{10}H_{12}\cdot Ph_2POPPh_2]_x-$ polymer powder, 26.3 and 58.8, respectively, were used to calculate the necessary amount of boron required to provide a theoretical boron/carbon ratio of 4/1. Thus, a mixture of 0.80 g of $[-B_{10}H_{12}\cdot Ph_2POPPh_2]_x-$ polymer and 1.40 g of amorphous boron powder (Cerac, 94%, <5 μm) were mixed in an alumina mortar and pestle in an inert-atmosphere box for 15 min. A 2.00-g sample of this mixture pyrolyzed to 1000 °C resulted in 1.83 g (92%) of an amorphous, dull gray-black powder. Anal. Found: B, 73.23; C, 21.34; P, 4.18. Further heating to 1500 °C of 0.512 g of the material thus produced gave 0.476 g (7% weight loss from 1000–1500 °C; overall yield to 1500 °C, 85%) of a metallic, silver-black powder containing crystalline B_4C. Anal. Found: B, 76.88; C, 18.00; P, 2.58.

Non-Polymeric Binders for Ceramic Powders: Utilization of Neutral and Ionic Species Derived From Decaborane(14)

William S. Rees, Jr. and Dietmar Seyferth

Department of Chemistry
Massachusetts Institute of Technology
Cambridge, Massachusetts 02139

ABSTRACT

The pyrolytic conversion of *bis*-Lewis base adducts of decaborane(14), $L \cdot B_{10}H_{12} \cdot L$ (L = neutral monophosphine) and phosphonium salts of the $[B_{10}H_{10}]^{2-}$ anion (e.g., $[Ph_4P^+]_2$, etc.), to ceramic materials has been studied. All species examined served as binders for a variety of non-oxide refractory ceramic powders (e.g., B_4C, BN, BP, $B_{13}P_2$, SiC, Si_3N_4, B, C, AlN).

Non-Polymeric Binders for Ceramic Powders: Utilization of Neutral and Ionic Species Derived From Decaborane(14)

William S. Rees, Jr. and Dietmar Seyferth

Department of Chemistry
Massachusetts Institute of Technology
Cambridge, Massachusetts 02139

1. INTRODUCTION

Binders are used primarily to help ceramic particles adhere to one another [1]. Both the green strength of a ceramic body and its green density are affected by the binder used. Although many types of materials have been employed as binders in ceramic powder processing, organic polymers (e.g., polyvinyl alcohol, polyvinyl butyral, polyethylene, acrylic resins wax emulsions, etc.) have traditionally played an important role as binder formulations. While the use of such materials as binders often results in the achievement of high green body strength and/or high green body density, there also can be some drawbacks resulting from their use. Major problems can be encountered upon firing of the ceramic body due to binder burnout. Cracking of the part results when the temperature range of the binder burnout is narrow, so that most of the volatiles are released practically simultaneously. Not necessarily always a drawback is that during the non-oxidative firing of the ceramic body there can be substantial retention of carbon either due to polymer binder pyrolysis (giving nonvolatile, highly carbonaceous residues) or due to polymer-ceramic surface bond

2

formation, preventing degradative volatilization of the binder [2]. In order to avoid these problems, ceramists more recently have become interested in "low loss" inorganic or organometallic polymeric binders [3]. The polymers of choice are those whose pyrolysis gives a high yield of ceramic residue with the release of a minimum quantity of potentially destructive volatiles. Preferably, this ceramic residue also will be the same material of which the powder is composed, but this is not an essential requirement. By use of such "low loss" binders, one may hope to achieve not only the desired high green body strength and density that organic binders bring, but also one may hope to obtain *ceramic* parts of high strength and density. To date most of the "low loss" organometallic binders that have been investigated have been organosilicon polymers which are used as binders for silicon carbide and silicon nitride powders [4].

In our laboratories we have initiated a program aimed at the development of polymeric precursors for boron-containing ceramic materials: the carbide, nitride and "carbonitride". Successful systems based on known [5] and new [6] polymers involving difunctional Lewis base adducts of decaborane(14) have been developed (Fig. 1). During the course of this research we also prepared and investigated some non-polymeric decaborane(14) derivatives and we report here concerning these and their applications as binders for a variety of non-oxide ceramic powders. As far as binder applications were concerned, we were interested to find out if these non-polymeric boron-containing species might be useful binders for the boron-containing ceramics mentioned above, as well as for elemental boron powder.

3

2. EXPERIMENTAL

2.1. General Comments.

All manipulations were carried out in oven-dried glassware under an inert atmosphere (argon or nitrogen) following standard techniques [7]. All solvents were distilled from appropriate drying agents [8] under a nitrogen atmosphere prior to use. All reagents employed were available commercially and were used as received. All $B_{10}H_{12} \cdot 2L$ complexes and $[B_{10}H_{10}]^{2-}$ salts were prepared by published methods (L = Ph_3P, Ph_2PH, $(n\text{-Bu})_3P$ and $(NMe_2)_2PCl$ [9], L = Ph_2POH, Ph_2PN_3 and Ph_2PNHNH_2 [10], all $[B_{10}H_{10}]^{2-}$ salts [11]). Twice sublimed decaborane(14) was purchased from Callery Chemical Co., Callery, PA and used as received. All compounds prepared were characterized on the basis of their melting points and spectroscopic (IR; ^{11}B, ^{13}C, ^{31}P, ^{1}H NMR) properties and comparison with literature values [9-11]. NMR spectra were obtained using a Varian XL-300 NMR spectrometer, IR spectra on a Perkin-Elmer Model 1430 spectrophotometer. Ceramic analyses were obtained from Galbraith Laboratories, Knoxville, TN.

A hardened stainless steel die in a Carver laboratory press was used for forming 3.75 cm x 1.25 cm bars. Isostatic bar compaction was carried out in a pneumatically-driven oil press with the bars wrapped in "Saran Wrap" and contained in evacuated, sealed rubber bags. Lindberg tube furnaces with Eurotherm controllers were used for all preparative scale (>1 g) pyrolyses (powder and bulk). For pyrolyses to 1000°C, 3.75 cm o.d. quartz tubes and fused silica boats were used; for ones to 1500°C, 6.50 cm o.d. mullite tubes and boron nitride boats supported on alumina dee tubes were used. All pyrolyses were carried out under an atmosphere of flowing argon. For experiments to 1000°C the flow rate was ~6-8 L/h and for experiments to 1500°C it was ~16-20 L/h.

4

X-ray diffraction patterns were obtained either on a Charles Supper detector and Diano generator instrument or on a Rigaku rotating-anode system. TGA measurements were made on a Perkin-Elmer model TGS2 instrument equipped with a Thermal Analysis System 4 controller. For TGA data, *in situ* data was obtained for powdered samples from ambient to 950°C and mass change data for higher temperatures were collected on bulk samples after they had been heated to the desired temperature and then cooled to ambient conditions.

2.2. General Procedure for the Preparation of $B_{10}H_{12}\cdot2L$ Complexes [9].

The preparation of $B_{10}H_{12}\cdot2Ph_3P$ is given as a representative example: A 250 mL Schlenk flask equipped with a stir-bar, gas-inlet tube and a septum was charged under argon with 5.0 g (41 mmol) of $B_{10}H_{14}$, 35 mL of Et_2O and a solution of 25.0 g (95 mmol) of Ph_3P in 150 mL of Et_2O, with vigorous stirring during and for 5 min after addition. The precipitate which had formed was filtered, washed with Et_2O and dried at 100°C/0.1 mm Hg to give a nearly quantitative yield of $B_{10}H_{12}\cdot2Ph_3P$. The complexes where L = Ph_2PH, Ph_2PCl, $(n\text{-}Bu)_3P$, and $(Me_2N)_2PCl$ were all prepared by this general procedure. Those where L = Ph_2POH, Ph_2PN_3 and Ph_2PNHNH_2 were prepared by nucleophilic substitution at phosphorus in $B_{10}H_{12}\cdot2Ph_2PCl$ [10]. The results of their pyrolyses (i.e., their ceramic yields and compositions) are given in Table I.

2.3. General Procedure for the Preparation of $[B_{10}H_{10}]^{2-}$ Salts [11].

The preparation of $[Ph_4P]_2[B_{10}H_{10}]$ is given as a representative example: A solution of 2.00 g of $[Et_3NH]_2[B_{10}H_{10}]$ (6.2 mmol) in 30 mL of 9/1 water/ethanol was added to a solution of $[Ph_4P][Br]$ (6.00 g, 14.3 mmol) in 50 mL of the same solvent mixture in a 125 mL Erlenmeyer flask. After the mixture had been stirred for 5 min, the precipitate was filtered, washed with water, 5 mL of cold (*ca.* -10°C) acetone and,

5

finally, with Et_2O. Drying at 60°C/0.1 mm Hg for 5 h gave a white solid in nearly quantitative yield. The following salts were all prepared by the above general metathesis route: $[Ph_3PMe]_2[B_{10}H_{10}]$, $[n\text{-}Bu_3PMe]_2[B_{10}H_{10}]$ and $[Ph_3P(CH_2)_3PPh_3][B_{10}H_{10}]$. The results of their pyrolyses (i.e., their ceramic yields and compositions) are given in Table I.

2.4. General Procedure for the Preparation of Ceramic Composite Bars Using $B_{10}H_{12}\cdot 2L$ Complexes and $[B_{10}H_{10}]^{2-}$ Salts as Binders for Ceramic Powders (Scheme 1).

One of the three following procedures were used for sample preparation:

A. Weighed quantities (See Table II) of $B_{10}H_{12}\cdot 2L$ or of a $[B_{10}H_{10}]^{2-}$ salt and the ceramic powder were mixed and ground for 15 min in a mortar and pestle in an inert atmosphere box.

B. The $B_{10}H_{12}\cdot 2L$ or $[B_{10}H_{10}]^{2-}$ salt (0.5 g) was dissolved in 50 mL of a solvent (usually acetone) and 2.5 g of ceramic powder was added. The stoppered flask was immersed into a Branson B-220 ultrasonicator containing ~7.5 cm of ambient temperature water and vibrated for 15 min. Afterwards, the solvent was removed at 100°C and 0.1 mm Hg.

C. The $B_{10}H_{12}\cdot 2L$ or $[B_{10}H_{10}]^{2-}$ salt (0.5 g) and the ceramic powder (2.5 g) were suspended in ~75 mL of a non-solvent (usually pentane) in a 100 mL stoppered round bottomed flask. Further processing was carried out as described in B, above.

The samples thus prepared were placed in a 1.25 cm x 3.75 cm rectangular die and formed into bars in a Carver laboratory press at 2,250 kg (4.6×10^7 nt/m^2 uniaxially), wrapped in "Saran Wrap", placed in an evacuated, sealed rubber bag, removed to an ambient temperature isostatic press and further compacted to 3.45×10^8 nt/m^2. The uniaxial pressing time duration was ~5 min and the isostatic pressing

time duration was ~15 min. The resulting bar was pyrolyzed in a stream of argon to 1000°C (10°C/min heating rate, hold at 1000°C for 30 min) and subsequently allowed to cool to ambient temperature over a period of ~3.5 h. The pyrolyzed sample was handled in an inert atmosphere box. The results of the individual experiments are given in Table II.

For the purposes of this initial screening test, a ceramic composite bar was considered to be "excellent" if it met both the criteria of being a uniform, rectangular monolithic body that had retained its shape (vs the polymer composite bar before pyrolysis) in all three dimensions without undergoing any discernable shrinkage or bloating above the detectable level of 3-5%, as well as having a strength such that it could not be broken manually without mechanical means (e.g., a vise and pliers).

3. RESULTS AND DISCUSSION

We began this investigation with the preparation and a study of the pyrolysis of several known monomeric decaborane(14)-Lewis base adducts in which the Lewis base was a trivalent phosphorus compound and also of some phosphonium salts of the $[B_{10}H_{10}]^{2-}$ anion. This initial thrust was due to the fact that the known processable decaborane(14) polymers involved diphosphines as the difunctional Lewis base [12]. Both of these classes of compounds have a high boron content, and this is what is needed in a B_4C precursor. The $B_{10}H_{12}$-Lewis base compounds, written as $B_{10}H_{12} \cdot 2L$ or, to better indicate their structure, as $L \cdot B_{10}H_{12} \cdot L$, are readily prepared by the reaction of $B_{10}H_{14}$ with two molar equivalents of the Lewis base in a suitable organic solvent such as diethyl ether or benzene (Eq. 1).[9] Among the Lewis bases

$$B_{10}H_{14} + 2\,:L \longrightarrow L \cdot B_{10}H_{12} \cdot L + H_2 \qquad (1)$$
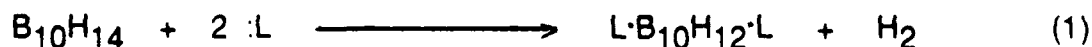
that react with $B_{10}H_{14}$ in this way are amines, phosphines, organic sulfides and nitriles. When an $R_3N \cdot B_{10}H_{12} \cdot NR_3$ adduct is heated, proton transfer from boron to nitrogen occurs and salts of the very stable $[B_{10}H_{10}]^{2-}$ anion, $[R_3NH]_2[B_{10}H_{10}]$, are formed. A wide variety of $[B_{10}H_{10}]^{2-}$ salts can be prepared by cation exchange reactions [11]. Such proton transfer processes had not been demonstrated for phosphine adducts, $R_3P \cdot B_{10}H_{12} \cdot PR_3$, but we have found that they do occur. Thus, when a sample of $B_{10}H_{12} \cdot 2Ph_3P$ was heated to 250°C at 10°C/min under a stream of argon, transformation to $[Ph_3PH]_2[B_{10}H_{10}]$ took place as evidenced by the IR spectrum of the sample after it had cooled to room temperature. A medium intensity band at 2395 cm^{-1}, not present in the *spectrum of the* neutral adduct, was observed. This band may be assigned to ν (P-H) of the $[Ph_3PH]^+$ cation [13].

The $L \cdot B_{10}H_{12} \cdot L$ compounds and $[B_{10}H_{10}]^{2-}$ salts that we prepared and studied are shown in Table I. Of initial interest were the yield and elemental composition of the ceramic residue obtained when they were pyrolyzed to 1000°C in a stream of argon. According to the results in Table I, the precursors can be divided into two classes: (1) those having phenyl groups attached to phosphorus, whose pyrolysis gives a high (> 70%) yield of ceramic residue that contains a large fraction of the carbon present in the precursor, and (2) those that do not contain phenyl groups, whose pyrolysis gives lower yields of ceramic residue. As Table I shows, pyrolysis of powder samples of the various phosphorus-containing compounds or salts under the stated conditions resulted in retention of phosphorus in the residue. However, on further heating to 2350°C under argon, nearly total loss of phosphorus occurred when polymeric precursors such as $-[-B_{10}H_{12} \cdot Ph_2POPPh_2-]-_x$ were pyrolyzed [5].

8

In all examples studied, the ceramic residue from the pyrolysis under argon to 1000°C was amorphous. Firing at 1500°C for 10 h resulted in materials whose powder X-ray diffraction (XRD) pattern showed broad lines indicative of weakly crystalline B_4C-containing material. The ceramic residues derived from the precursors in Table I are all black solids. Those precursors in class (1) above gave freely flowing powders that were quite hard, often scoring the agate mortar used to prepare XRD samples. The precursors in class (2) gave brittle, foamy solids, as might be expected when there is more substantial evolution of volatiles.

The determination of a nominal composition of amorphous materials is merely an accounting game using elemental analysis data. At that point no identifiable crystalline phases are preser Further firing at higher temperatures, as already noted, does cause crystallization, but also can cause changes in elemental composition. By elemental accounting, we assume that all phosphorus in the amorphous material is present as BP. The remaining boron then is assigned to B_4C. This leaves unbound carbon that we assume to be present in its elemental form. Such an accounting gives a molar formulation of 1 B_4C + 0.94 BP + 16 C to the pyrolysis product of $B_{10}H_{12} \cdot 2Ph_3P$, or, on a weight percent basis, 21.2% B_4C, 13.3% BP and 65.5% C. However, we stress that this is only a *nominal* formulation for this material. It is possible that these elements are randomly bound in the amorphous product. A more detailed study of the *crystalline* phases obtained by firing to higher temperatures was made for the $-[-B_{10}H_{12} \cdot Ph_2POPPh_2-]-_x$ polymer [5]. One fact, however, is a certainty in the case of the ceramic products of the pyrolysis of the class (1) precursors in Table I: they contain a substantial amount of free carbon.

The $B_{10}H_{12} \cdot 2L$ adducts and $[B_{10}H_{10}]^{2-}$ salts listed in Table I proved to be useful as binders for B_4C and other ceramic powders such as BN, SiC, $B_{13}P_2$, Si_3N_4 and elemental boron (Table II). Scheme I shows the procedure used. The best results were obtained when the phosphorus-containing ligand had phenyl substituents on phosphorus. This very likely is due to the high ceramic yields obtained in the pyrolysis of the class (1) precursors. Since, in this application, the compounds used as binders are present in the green body to the extent of about 17% by weight (Table II), the excess of carbon in their pyrolysis residue is less of a disadvantage than when the pure precursors are pyrolyzed. Other weight ratios of binder to ceramic powder were investigated, but, in general, the 17% binder content gave the best results. Of the various systems studied (Table II), the one in which $B_{10}H_{12} \cdot 2Ph_3P$ was used as binder for elemental boron powder should be the best in terms of potential useful application. Firing at higher temperature should result in reaction of elemental boron with the free carbon to form boron carbide, a process that is known to take place at around 1600°C [14]. It should be noted that our evaluation of binders as "excellent", "good" and "fair" is based on the degree of shape retention of a fired composite bar as compared to the unfired, pressed composite bar, as well as on a qualitative estimate of strength. Quantitative strength tests were not undertaken for every sample in this orientational study [15].

Covalent, unimolecular compounds, in general, would not be expected to be suitable "low loss" binders due to their volatility at temperatures prior to complete thermal decomposition. In the $L \cdot B_{10}H_{12} \cdot L$ adducts, however, we are dealing with covalent, unimolecular compounds which are converted to nonvolatile salts, $[LH^+]_2[B_{10}H_{10}{}^{2-}]$, by relatively mild heating, so that on further heating no material is

lost except for the volatiles released in the pyrolysis itself. This unique chemistry makes these materials unexpectedly good binders.

REFERENCES AND COMMENTS

1. a) A. C. Pincus and L. A. Shipley, Ceramics Industry, **92**, 106 (1969).

   b) T. Morse, *Handbook of Organic Additives for use in Ceramic Body Formulation,* (Montana Energy and NHD Research and Development Institute, Butte, MT, 1979).

2. R. J. Higgins, W. E. Farnetn, W. E. Rhine and H. K. Bowen, in press.

3. a) K. J. Wynne and R. W. Rice, Ann. Rev. Mater. Sci. **14**, 297 (1984).

   b) R. W. Rice, Amer. Ceram. Soc. Bull. **62**, 889 (1983)

4. a) B. C. Mutsuddy, Ceram. Int. **13**, 41 (1987); Mater. Sci. Monogr. **38A**, 571 (1987).

   b) K. B. Schwartz and D. J. Rowcliffe, J. Am. Ceram. Soc., **69**, C-106 (1986).

   c) G. Saiki, N. Hirai and J. Kondo, Jpn. Kokai Tokkyo Koho JP 63 21,253 [88, 21,253], Jan. 28, 1988; Chem. Abstr. **108**, 172382r; Jpn. Kokai Tokkyo Koho, JP 63 25,276 [88, 25,276], Feb. 2, 1988; Chem. Abstr. **108**, 172384.

   d) K. Saeki and M. Hirano, Jpn. Kokai Tokkyo Koho JP 62, 113,771 [87, 113,771]; Chem. Abstr. **107**, 160168a.

5. a) Seyferth, D.; Rees, Jr., W. S.; Lightfoot, A.; Haggerty, J. S. *Chem. of Materials,* **1989**, *1(1),* in the press.

   b) Lightfoot, A.; Rees, Jr., W. S.; Haggerty, J. S. *Ceram. Eng. and Sci. Proc.* **1988**, *9,* 1021.

   c) Rees, Jr., W. S.; Seyferth, D. *Ceram. Eng. and Sci. Proc.* **1988**, *9,* 1009.

6. a) Rees, Jr., W. S.; Seyferth, D. *J. Am. Ceram. Soc.* **1988**, *71,* C-194.

   b) Seyferth, D.; Rees, Jr., W. S. In *Better Ceramics Through Chemistry III,* Brinker, C. J.; Clark, D. E.; Ulrich, D. R., Eds.; Materials Research Society: Pittsburgh, PA, 1988; pp. 449-454.

7. D. F. Shriver and M. A. Drezdzon, *Manipulation of Air Sensitive Compounds, 2nd ed.* (Wiley, New York, 1986).

8. A. J. Gordon and R. A. Ford, *The Chemist's Companion* (Wiley, New York, 1977).

9. For a discussion of $B_{10}H_{12} \cdot 2L$ complexes see: *Gmelin Handbook of Inorganic Chemistry, 8th Ed., Vol. 54 ,* edited by K. Niedenzu and K.-C. Buschbeck (Springer-Verlag, Berlin, 1979) pp. 151-165.

10. H. A. Schroeder, J. R. Reiner and T. L. Heying, Inorg. Chem. **1**, 618 (1962).

11. For a discussion of salts of the $B_{10}H_{10}^{2-}$ anion, see: E. L. Muetterties and W. A. Knoth, *Polyhedral Boranes* (Dekker, New York, 1968).

12. a) G. W. Parshall, U.S. patent 3,035,949 (May 22, 1962).

    b) H. A. Schroeder, J. R. Reiner and T. A. Knowles, Inorg. Chem., **2**, 393 (1963).

    c) J. R. Reiner and H. A. Schroeder, U.S. patent 3,141,856 (July 21, 1964).

    d) H. A. Schroeder, U.S. patent 3,155,630 (Nov. 3, 1964).

13. J. Weidlein, U. Mueller and K. Dehnicke, *Schwingungsfrequenzen I*, (G. Thieme - Verlag, Stuttgart, 1981).

14. R. H. Wentorf, Jr., *Kirk-Othmer Encyclopedia of Chemical Technology, 3rd Ed., Vol. 4;* (Wiley, New York, 1978) pp. 126-127.

15. A fired composite bar produced as described in Scheme 1 from B_4C and $B_{10}H_{12} \cdot 2Ph_3P$ gave a strength of ~1 x 10^8 nt/m^2. We thank Mr. Garry Garvey of the MIT Dept. of Matls. Sci. for this measurement.

FIGURE 1
STRUCTURE OF -[-B$_{10}$H$_{12}$·diamine-]-$_x$ POLYMERS.
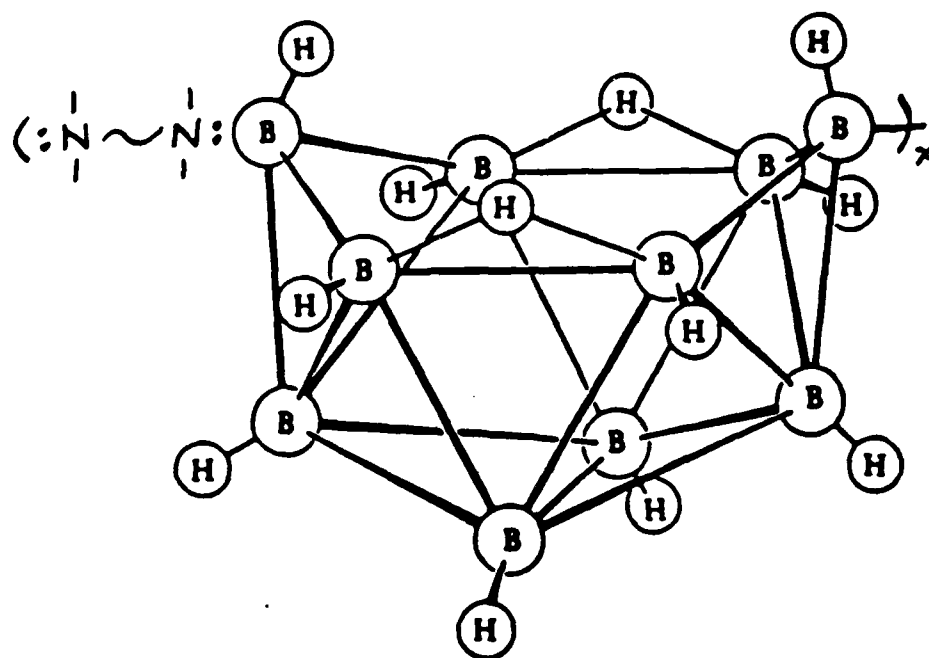
SCHEME 1
PREPARATION OF CERAMIC COMPOSITES UTILIZING DERIVATIVES OF $B_{10}H_{14}$ AS BINDERS FOR CERAMIC POWDERS.

MATRIX[a]   REINFORCEMENT[a]

combine
- A: physical mixture, OR
- B: ceramic powder suspended in solution of binder, OR
- C: mixture in a liquid diluent- neither component in solution

dry (if mixed by B or C)
place in a die
uniaxially form (5,000 lbs)
isostatically compact (50 K psi)

UNFIRED COMPOSITE

pyrolyze (1000°C, 10°C/min, Ar atm)
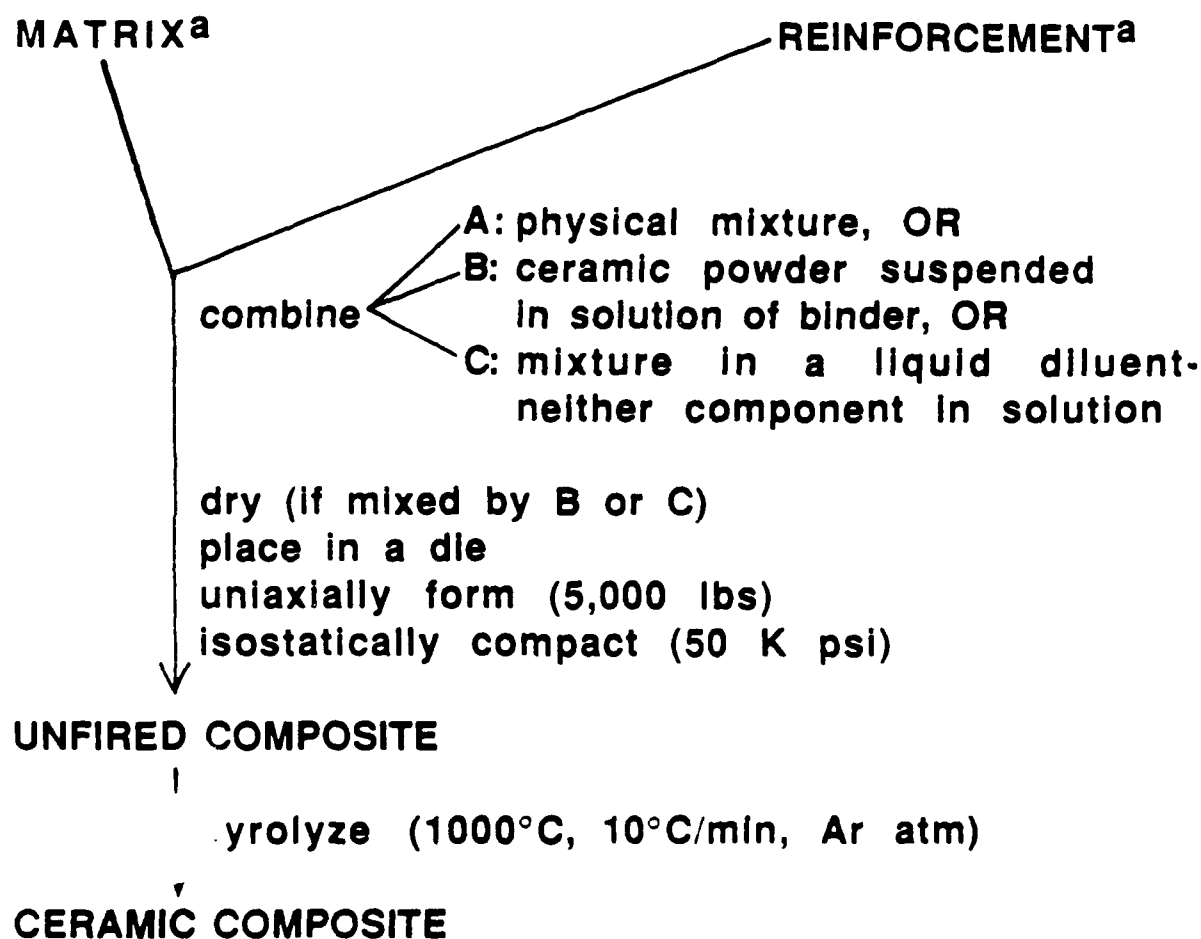
CERAMIC COMPOSITE

[a]Typical binder/ceramic powder ratio is 16.7 wt % binder (matrix)/83.3 wt % ceramic powder (reinforcement).

TABLE I.
PYROLYSIS OF $B_{10}H_{12} \cdot 2L$ ADDUCTS AND $[B_{10}H_{10}]^{2-}$ SALTS.

Compound	Ceramic Yield, %[a]	Ceramic Composition,%			
		B	C	P	Other
$B_{10}H_{12} \cdot 2Ph_2PH$	83	23.17	60.75	13.71	
$B_{10}H_{12} \cdot 2Ph_3P$	86	18.20	69.59	9.88	
$B_{10}H_{12} \cdot 2Ph_2PCl$	73	20.62	57.09	13.17	Cl, 0.02
$B_{10}H_{12} \cdot 2Ph_2POH$	77	21.38	55.65	11.93	O, 10.57
$B_{10}H_{12} \cdot 2Ph_2PN_3$	72[b]				
$B_{10}H_{12} \cdot 2Ph_2PNHNH_2$	71	27.69	43.80	8.20	N, 16.56
$B_{10}H_{12} \cdot 2(n\text{-}Bu)_3P$	58	35.94	46.43	15.34	
$B_{10}H_{12} \cdot 2(NMe_2)_2PCl$	55[b]				
$[Ph_3PMe]_2[B_{10}H_{10}]$	83[b]				
$[Ph_4P]_2[B_{10}H_{10}]$	93	6.87	73.06	13.01	
$[Ph_3P(CH_2)_3PPh_3][B_{10}H_{10}]$	91	15.96	69.33	8.33	
$[(n\text{-}Bu)_3PMe][B_{10}H_{10}]$	68	30.10	49.03	11.96	

[a]Yield to 1000°C at a rate of 10°C/min under an argon atmosphere as determined in a tube furnace on ~1 g samples as follows:

Ceramic Yield = [(wt. residue)/(wt. sample pyrolyzed)] x 100

[b]composition not determined

TABLE II.
$B_{10}H_{12} \cdot 2L$ BINDER EXPERIMENTS WITH 16.7 WEIGHT % BINDER.

L	Ceramic Powder	Mixture Method[a]	Shape Retention[b]	Color
Ph_2PH	B_4C	A	E	Black
Ph_2PCl	B_4C	A	E	Black
Ph_2PNHNH_2	B_4C	A	G	Black
Ph_2POH	B_4C	A	G	Black
Ph_2PN_3	B_4C	A	G	Black
$(NMe_2)_2PCl$	B_4C	A	F	Black
$(n\text{-}Bu)_3P$	B_4C	B	G	Black
Ph_3P	B_4C	B	E	Black
Ph_3P	B_4C	C	E	Black
Ph_2PH	B_4C	B	E	Black
Ph_2PH	B_4C	C	E	Black
Ph_3P	B	A	E	Dark Red
Ph_3P	Si_3N_4	A	E	Gray
Ph_3P	α-SiC	A	G	Dark Gray
Ph_3P	β-SiC	A	G	Dark Gray
Ph_3P	BN	A	G	Gray
Ph_3P	AlN	A	G	Silver/Gray
Ph_3P	BP	A	F	Gray
Ph_3P	$B_{13}P_2$	A	E	Dark Gray
Ph_3P	Rayon	B	G	Black

[a]See experimental section; method A: without solvent; method B: in acetone; method C: in pentane.

[b]Based on the fired ceramic composite bar as compared to the unfired, pressed composite bar. Qualitative order: E = excellent > G = good > F = fair.

Boron-Containing Ceramic Materials Derived from Polymeric Precursors: Material Characteristics

Annamarie Lightfoot, William S. Rees, Jr., and John S. Haggerty

Materials Processing Center
Massachusetts Institute of Technology
Cambridge, MA   02139

Boron-containing ceramics originating from polymeric precursors have been characterized with respect to density, pore structure, phases, grain size, and chemistry at various stages of processing. The evolution of pore structure has been the focus of this study since these characteristics define many properties and maximum permissible sample dimensions for specific processes.

Introduction

The use of polymeric precursors to simultaneously synthesize and form ceramics is an exciting new approach for processing shaped parts of refractory materials. Many oxide and nonoxide materials can be formed into configurations that include monoliths, composite matrices, particulates, fibers, and coatings.

The achievement of microstructural features and qualities conventionally believed important for structural applications is particularly difficult with materials formed by this processing route. Typically the synthesis reactions are accompanied by the evolution of large quantities of product gases that must exit the parts freely often after temperatures have reached levels where densification processes can cause pore closure. In addition to accommodating mass transport through unusually small-scale porosity, volatilization, crystallization, coarsening, and densification processes all must be controlled throughout the entire synthesis processes.

Based on MIT's results with reaction bonded Si_3N_4, these polymer-derived ceramic materials also make possible unique structural materials with a very low specific gravity and high strength. Strengths need not decrease exponentially with porosity if the residual porosity is distributed uniformly in minimum diameter pores.[1] The maximum strengths (≈ 690 MPa) of 75% dense RBSN samples essentially equal those of nominally fully dense alpha-Si_3N_4 when processing defects are eliminated.[2,3] These polymer derived ceramic materials offer the opportunity of distributing residual porosity on an even finer scale than was achieved with RBSN.

Approach

Boron carbide was synthesized by pyrolysis of a polymer with the overall composition and structure $[B_{10}H_{12} \cdot Ph_2P\text{-}O\text{-}PPh_2]_x$. POP is used as a shorthand notation for this chemistry to reflect the P-O-P polymer linkage. This chemistry was selected because the yield of solid product is unusually high ($\approx 93\%$ at 1000°C) and B_4C was a demonstrated reaction product;[4] excess C and both P and O residuals are potential sources of additional phases. The procedures used for producing ceramic powders and bars of this material are summarized in Fig. 1. Processing was carried out in Ar or N_2 atmospheres to the extent that was practical.

The firing temperature was the principal process variable investigated in this series of experiments. Three furnaces were used; selection was based on the maximum firing temperature. Up to 1000 °C, samples were fired in a SiO$_2$-tube furnace with SiO$_2$ boats; a mullite-tube furnace and BN boats were used for the 1000 °-1500 °C range and a graphite-tube furnace and carbon boats for 1500 °-2350 °C. Samples fired above 1000 °C were fired to 1000 °C initially in the SiO$_2$-tube furnace before transfer. All samples were fired in atmospheric pressure Ar.

As-fired powder (pdr) and bar (blk) samples were characterized in addition to ground powders from either fired bars (gnd-blk) or powders (gnd-pdr). These sample groups permitted a qualitative determination of the scale over which pores were isolated.

Densities were measured by bulk, pycnometric (Hg & H$_2$O), and Archimedes techniques. Pore characteristics were measured microstructurally, by N$_2$ adsorption and by Hg porosimetry. Phases and grain sizes were studied by optical, SEM, and TEM microscopy and by X-ray diffraction. Reactions were monitored by TGA and shrinkage by dilatometry up to 900 °C. Weight loss and shrinkage for T > 900 °C were determined from measurements made after cooling to room temperature. Quantitative chemical analyses for B and P were made gravimetrically; O and C contents were determined by combustion. Qualitative P contents and its spatial distribution were also determined by EDS in a SEM.

Results

Crystallinity and Grain Size

X-ray diffraction patterns were made of as-fired powder, surfaces, of as-fired bars, and ground bars. The results in Table I illustrate important differences between powder and bulk samples as well as a complex crystallization sequence that results in part from the P residuals.

Below 1500 °C firing temperatures, no sample showed evidence of crystallinity. As-fired powder samples exhibited B$_4$C, C and B$_{13}$P$_2$ lines for a 1500 °C-10-h firing cycle; bulk samples with the same cycle also showed BP. B$_4$C + C patterns were well developed in the blk-0.5 h samples only after firing temperatures reached 1870 °C. The differences in crystallinity between powder and bulk samples very likely result from relatively high P and O losses from the powder samples (Table II).

The B$_4$C and C crystallite sizes for 0.5-h at a temperature determined by diffraction line broadening are shown in Fig. 2. Both grow continuously up to the highest temperature investigated (2350 °C). The maximum observed grain sizes (≈ 50-60 nm) are extremely small by comparison to normally processed materials.[5] The BP grain size in the blk-1550 °C-0.5-h samples was larger than the X-ray machine broadening limit. TEM analysis showed them to have a 150 nm diameter.

Chemistry

The theoretical chemical compositions for the POP-based materials are summarized in Table II with experimental observations; Table I includes EDS results for P. Even though the POP polymer gives a high yield of solids that include B$_4$C, it is evident that the pyrolysis product should be C rich. The samples were C rich, but all lost some of their C during pyrolysis so their B/C ratios are higher than the polymer or the assumed theoretical composition of the resulting solid. The effect of the shortened diffusion distances in the powder samples is evident by com-

paring the P and O contents and the B/C ratios of the 1500 °C pdr and blk samples
The effect of increased firing temperature is shown in comparing 1000 ° and 1500 °C
pdr samples and 1500 ° and 2300 °C blk samples. Shorter dimensions and increas-
ed temperature enhanced P, O, and C losses. Oxygen levels generally are substan-
tially higher than anticipated from the polymer composition. It has not been deter-
mined whether the apparent excesses are entirely real or whether they result in
part from contaminations of the high surface area materials during chemical
analyses.

EDS analyses of fracture surfaces (Table I) show that all detectable P is lost
from the bulk samples for T > 2000 °C. X-ray mappings of the P distribution on
fracture and saw-cut surfaces of bulk samples show that P is concentrated at open
surfaces within the bulk samples. These surfaces correspond to voids or boundaries
between incompletely coalesced particles.

Density, Porosity, and Pores

The weight and length changes that result from firing the POP materials are
shown in Fig. 3. The chemical reactions responsible for the weight losses up to
1500 °C are discussed in the companion paper on synthesis:[4] in general these result
from losses of H- and C-containing products at 3 specific temperature levels. Below
800 °C. the lengths change at 2 specific temperature levels which do not coincide
with the temperatures where weight losses are concentrated. Above 1000 °C. weight
continues to be lost through undefined molecular mechanisms and shrinkage per-
sists at a reduced rate; the total weight loss in the high temperature domain cor-
responds closely to that anticipated for the complete loss of P and O still present
in the 1500 °C samples.

Densities below 800 °C follow an irregular pattern through the combined weight
loss and shrinkage effects, then increase sharply to near final values between 800 °
and 1000 °C. For firing temperatures above 1000 °C. the bulk densities increase
monotonically as shown in Fig. 4. The density of the solid phase including closed
pores (skeletal density) apparently increases at a higher rate than the bulk density
in the high temperature range. All of these density values are subject to error because
of the small sample sizes and irregular shapes; but, the trends and relative values
are correct. At its maximum, the skeletal density reaches ≈ 85-90% of the
theoretical value for a $B_4C + C$ body having an overall composition given in Table II.

The results of BET surface area determinations are given in Fig. 5 for powder,
bulk, ground-bulk, and ground-powder samples. These complex results show that
materials fired as powders and bars differ from the beginning. Bulk samples isolate
pores progressively from 250 °C to the maximum temperature levels. The gnd-blk
samples show that with high surface area, internal pores evolve within bulk samples
during the initial weight loss up to ≈ 300 °C which are isolated from the outer sur-
face. Powder, gnd-blk and gnd-pdr samples exhibit similar behavior for
temperatures up to ≈ 1000 °C; surface areas pass through maxima at ≈ 300 °C then
decrease to values exhibited by bulk samples. The bulk samples show an unusual
characteristic for firing temperatures > 1000 °C. The gnd-blk samples reveal that
bulk samples form very small, isolated pores at the higher temperatures. BET
characterization of the gnd-blk samples shows that ≈ 1/3 of the initially closed
porosity in the bulk samples becomes open by grinding to ≈ 50 μm particle size
and also has a characteristic dimension less than 30 nm. The total volumes and
partition of the pore types are summarized in Fig. 6 for a 1000 °C Blk sample.
The gnd-blk samples have not been fully characterized so we cannot indicate the
total pore volume made open by grinding nor the volume of pores that still remain

1023

closed within the ≈50 μm particles.

Figure 6 also indicates peak channel diameters revealed by Hg porosimetry in the initially open pore structure of a Blk-1000°C-0.5-h sample. SEM photomicrographs show that pore diameters larger than 2-4 μm result from gross defects such as entrapped bubbles or aggregates of several ≈5 μm diameter polymer particles and the 30-90 nm pores result from lenticular voids between incompletely consolidated particles. The 3-15 nm features result from pores that form during pyrolysis. The pore size distribution (by number) measured on a fracture surface of a 1000°C bulk sample peaked at nominally 100 nm.

The pore size distribution of the blk-1000°C-0.5-h samples determined by N_2 adsorption shows that pores are concentrated in 2 populations: these peak at ≈1.5 nm (9% of measured porosity) and 30 nm (41%). These results agree with the SEM and Hg porosimetry results. Importantly, they show that the high pressures used with Hg porosimetry did not crush the porous solid. TEM analysis of a blk-1500°C-10-h sample revealed features that resemble pores; these high number density spherical features have μ2-nm diameters.

Much of the weight loss occurs after pores become isolated in bulk samples while pores in smaller diameter powder samples retain pathways to the surfaces. Figure 7 shows a typical crack originating from a presumably isolated pore within a bulk sample. The potential for this type of damage will limit part dimensions unless firing cycles are identified that do not cause premature closure of pores.

Conclusions

These characterizations have demonstrated the feasibility of using the selected chemistry to produce B_4C-containing material. They have also revealed issues that must be resolved before these materials can compete effectively with conventionally processed bulk materials. Defects in the POP-derived material include large quantities of free carbon, P and O residuals, and cracks generated by gas evolution within closed pores. All of these features are much less severe in powder samples, especially those that are amorphous. Thus, intermediate service temperature fibers are a possible application for this chemistry. The excess C may be consumed by the addition of reactive B to the polymer. Many other feasible chemistries are known, so it is likely that the premature pore closure issue observed with these bulk samples can be controlled with careful processing of alternative chemistries. The extremely small diameter closed porosity should not be a problem for oxidation resistance or mechanical properties based on our experience with RBSN.

References

J. S. Haggerty, A. Lightfoot, J. E. Ritter, S. V. Nair, and P. Gennari, "Properties of Reaction Bonded Silicon Nitride Made from High Purity Silicon Powder," to be published in *Proc. of Engineering Cer Div*, Am. Ceram. Soc., Cocoa Beach, FL, Jan. 1988.

J. S. Haggerty, J. H. Flint, G. J. Garvey, J-M. Lihrmann, and J. E. Ritter, "High Strength Oxidation Resistant Reaction Bonded Silicon Nitride made from Laser-Synthesized Silicon Powder," pp. 47-54 in *Proc. 2nd Int. Sym. Ceramic Materials and Components for Engines*, eds. W. Bunk and H. Hausner, Gerlag Deutsche Keramische Gesellschaft, Lübeck-Travemunde, W. Germany (1987).

J. S. Haggerty, G. J. Garvey, J. H. Flint, B. W. Sheldon, M. Aoki, M. Okuyama, J. E. Ritter, and S. V. Nair, "Processing and Properties of Reaction Bonded Silicon Nitride and Silicon Carbide made from Laser Synthesized Powders," to be published in *Proc. of Basic Sci. Div*, Am. Ceram. Soc., Orlando, FL, (1987).

W. S. Rees, Jr. and D. Seyferth, "Boron-Containing Ceramic Materials Derived from Polymeric Precursors. Synthesis," to be published in *Proc. of Engineering Cer Div*, Am. Ceram. Soc., Cocoa Beach, FL, Jan. 1988.

K. A. Schwetz and W. Grellner, "The Influence of Carbon on the Microstructure and Mechanical Properties of Sintered Boron Carbide," *J. Less-Common Met.*, **82**, 37-47 (1981).

Table I. Summary of X-ray Diffraction and EDS Results

Temp (°C)	Time (h)	Sample	P (EDS)	Relative peak intensities (XRD)			
				B_4C	C	$B_1_3P_2$	BP
1000	0.5	bulk	yes	0	0	0	0
1500	10.0	powder	—	62	100	90	0
	10.0–	bulk	yes	26	70	100	42
	25.0	gnd-blk	—	6	100	75	98
1550	0.5	bulk	yes	0	43	100	53
1870	0.5	bulk	yes	42	100	0	0
2090	0.5	bulk	no	18	100	0	0
2350	0.5	bulk	no	9	100	0	0

Table II. Summary of Chemical Analyses (percent by weight)

Element	B_4C	Polymer	Theor solid*	1000°Pdr	1500°Pdr	1500°Blk	2300°Blk**
C	21.74	56.86	60.74	52.01	60.21	55.42	65.14
H	0.0	6.38	0.0	—	—	—	—
P	0.0	12.22	13.05	8.69	0.39	11.22	0.0038
O	0.0	3.21	3.43	12.05	2.88	6.66	nd
B	78.26	21.33	22.78	25.30	28.90	25.16	29.15
Total	100.00	100.00	100.00	98.05	92.38	98.46	94.29
B/C	3.6	0.37	0.37	0.49	0.48	0.45	0.45

* Assumes only H_2 is lost during pyrolysis reaction.
** Intermediate results.

Air Exposure

Process

- POLYMER SYNTHESIS
  US Patent 3 141 856
- POWDER STORAGE
- GRIND
  Mortar & Pestle ~1μm
- BAR ?
- UNIAXIAL PRESS
  34 5 MPa
- ISOSTATIC PRESS
  345 MPa
- FIRE
  ≤ 1000 °C in Ar
- OPTIONAL 2ND FIRE
  1000< Ts 2350 °C in Ar
- AS FIRED ?
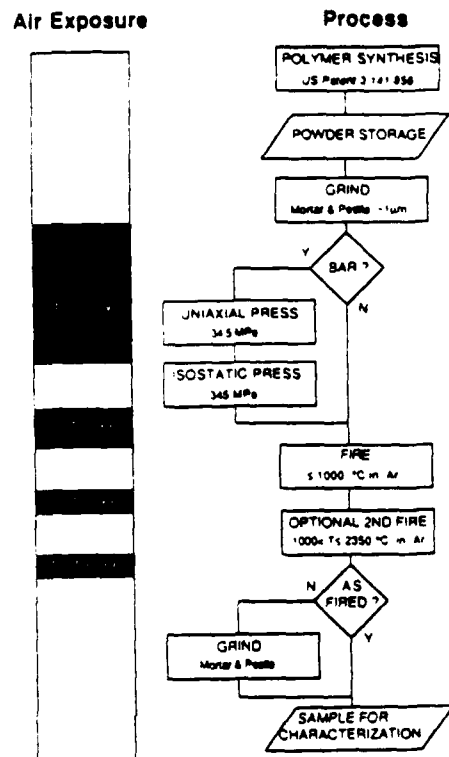- GRIND
  Mortar & Pestle
- SAMPLE FOR CHARACTERIZATION

Fig 1   Summary of processing steps used to make B₄C ceramic from POP polymer precursor Occurrences and durations of exposure to air are shown.
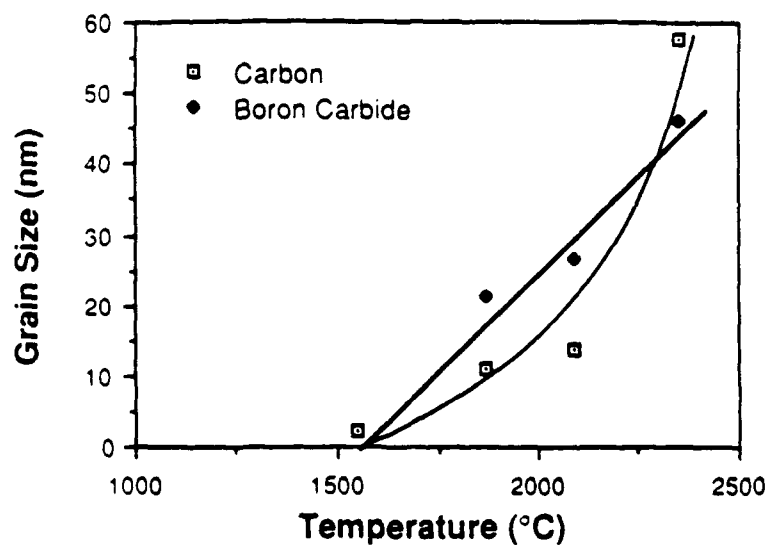
1026

Fig. 2. B₄C and C grain sizes determined by X-ray line broadening as a function of peak firing temperature for 0.5 h exposures in an Ar atmosphere.
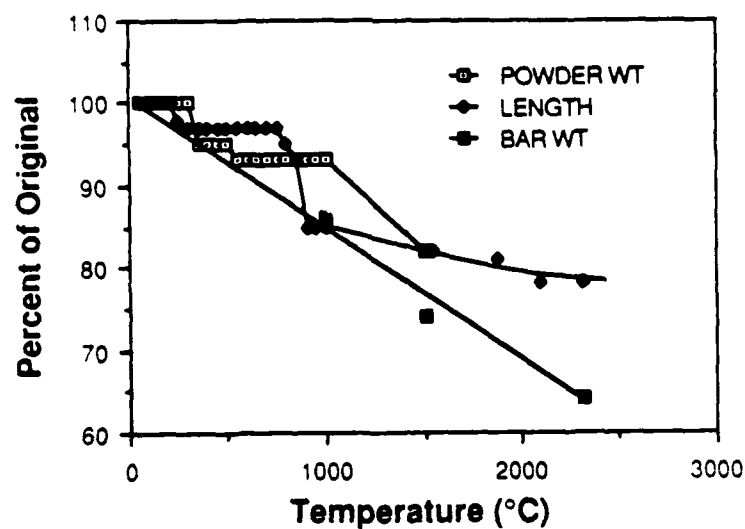

Fig. 3. POP weight losses and linear shrinkage as a function of temperature. Measurements up to 900°C were made in a TGA/dilatometer. Samples fired to higher temperatures were measured after cooling to room temperature.
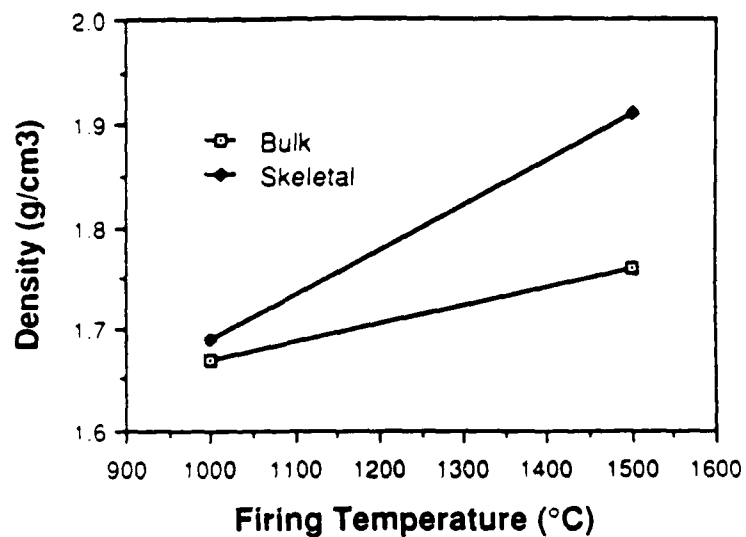
1027

Fig. 4   Bulk and skeletal densities of ceramic material resulting from pyrolysis of POP in Ar as a function of firing temperature.
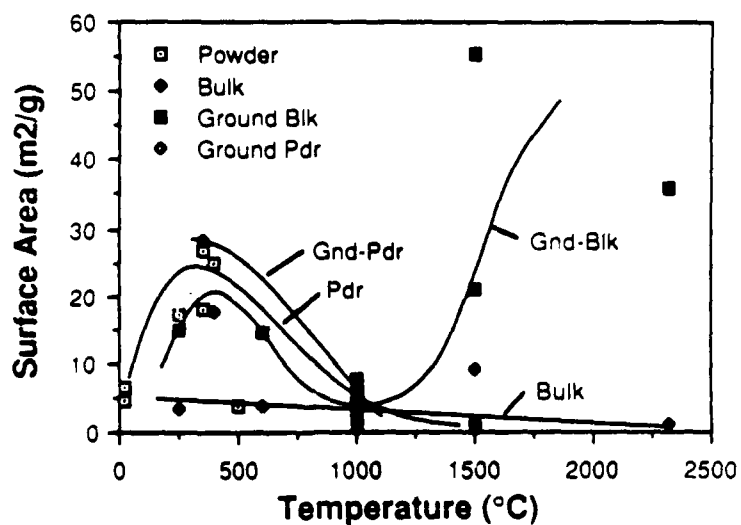

Fig. 5   Specific surface areas of bulk, ground-bulk, powder, and ground-powder POP samples measured by BET as a function of firing temperature

1028

$$\longleftarrow \text{0.153 cm}^3\text{ g} \longrightarrow$$

$$\longleftarrow \text{0.058 cm}^3\text{ g} \longrightarrow \longleftarrow \text{0.095 cm}^3\text{ g} \longrightarrow$$

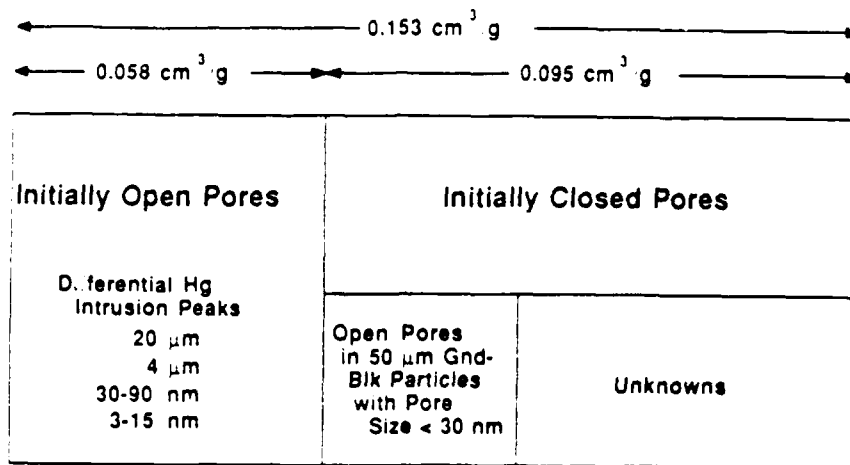| Initially Open Pores	Initially Closed Pores	
Differential Hg Intrusion Peaks 20 µm 4 µm 30-90 nm 3-15 nm	Open Pores in 50 µm Gnd- Blk Particles with Pore Size < 30 nm	Unknowns

Fig. 6   Summary of porosity types in a bulk sample fired at 1000°C for 0.5 h. Absolute specific volumes are shown at the top. The results of Hg porosimetry measurements are summarized.

Fig 7   SEM micrograph of a blk 1500°C 25 h sample illustrating crack damage originating from an isolated pore.

12th Annual Conference on
Composites and Advanced Ceramic Materials

Proceedings of the
12th Annual Conference on
Composites and Advanced Ceramic Materials

David E. Clark
Program Chair

A Collection of Papers Presented at the
12th Annual Conference on
Composites and Advanced Ceramic Materials
Sponsored by the
Engineering Ceramics Division
The American Ceramic Society, Inc.

January 17-22, 1988
Howard Johnson and
Cocoa Beach Hilton
Cocoa Beach, FL

ISSN 0196-6219

Phosphorus-Containing Derivatives of Decaborane(14) As Precursors to Boron-Containing Materials

WILLIAM SMITH REES, JR. AND DIETMAR SEYFERTH

Department of Chemistry
Massachusetts Institute of Technology
Cambridge, MA 02139

A route to soluble boron-containing polymers has been developed. The synthesis and characterization of phosphorus-containing monomeric and polymeric derivatives of $B_{10}H_{14}$ are given. Preparation and characterization of boron-containing ceramic materials from these molecular and macromolecular species are discussed. Success has been achieved in the areas of ceramic fiber and monolith production and in the area of binder applications for composites of advanced ceramic materials.

Introduction

Ceramic materials whose properties are attractive for high technology applications often fail to realize their full potential of usefulness due to an inability to be fabricated into complex, durable shapes.[1] One such class of materials is that of the boron-containing ceramics, e.g., boron carbide, B_4C, boron nitride, BN, boron phosphides, BP, $B_{12}P_2$ and $B_{13}P_2$, aluminum boride, AlB_{12} and boron silicides, B_4Si, B_6Si, and $B_{12}Si$.[2] Boron carbide, one goal of our current effort, is ideally composed of B_{12} icosahedra interstitially linked by three carbon atoms, nominally producing B_4C stoichiometry; however, boron rich phases are also known. Crude boron carbide is prepared by the carbothermal reduction of B_2O_3, with or without added Mg; this material finds its primary use as an abrasive. Pure B_4C can be prepared either directly from the elements ($T > 1600°C$) or by reaction of $BCl_3/CCl_4/H_2$ gas phase mixtures at high temperatures. Material thus prepared has a density of 2.52 g/cm^3, MP of 2450°C, and microhardness of 4.05 GPa. The neutron capture cross section area of the ^{10}B isotope is among the highest known.[3] Thus, its great hardness makes it attractive as ceramic armor plate, whereas its chemical inertness and radiation stability make it a candidate for nuclear applications. It will be appreciated that further development in these areas is inhibited by the inherent brittleness of the material, and lack of a suitable route to prepare it via a processable (i.e., fusible and/or soluble) intermediate.

One method used to increase the fracture toughness (durability) of ceramic materials is to imbed a support of ceramic fibers or powder into a matrix (binder) of ceramic material. The resulting composite is strength reinforced relative to a single component system.[4] In previous work, we have developed polymeric silicon-containing systems whose pyrolytic conversion produces useful ceramic materials, silicon carbide, nitride, "carbonitride," or oxynitride, in high yield.[5-10] We now report the results of an effort to extend the use of preceramic polymers to boron-containing materials.[11,12] The motivation for this work was to

utilize processable materials which give, in general, boron carbide as the major ceramic phase upon pyrolysis. We will limit our current discussion to results obtained with phosphorus-containing molecular and macromolecular species. Three classes of compounds were explored, monomeric $L \cdot B_{10}H_{12} \cdot L$ species, phosphonium salts of $B_{10}H_{10}^{2-}$ and polymers of the general formula $[B_{10}H_{12} \cdot L \sim \sim \sim L]_x$.

Experimental Procedure

General Comments

All manipulations were done in an inert atmosphere (argon or nitrogen) following standard techniques. All solvents were distilled from appropriate drying agents under a nitrogen atmosphere prior to use. All reagents used were available from common suppliers and were used as received. All new compounds were fully characterized by spectroscopic (multinuclear NMR and IR) and analytical data. All compounds had NMR resonances (^{11}B, ^{13}C, ^{1}H, ^{31}P) and ir absorptions that were consistent with their formulated structures. Ceramic analyses were obtained from Galbraith Laboratories, Knoxville, Tenn., and C, H, N analyses on nonceramic materials were obtained from Scandinavian Microanalytical Laboratory, Herlev, Denmark.

NMR measurements were obtained using a Varian XL300 NMR spectrometer. IR measurements were obtained on a Perkin-Elmer Model 1430 spectrometer. DRIFT spectra were recorded on an IBM Model IR/85 spectrometer. TMA and TGA measurements were obtained on a Perkin-Elmer TGS2 equipped with a Thermal Analysis System 4 controller. Lindberg tube furnaces with Eurotherm controllers were used for all bulk pyrolyses. For pyrolyses to 1000°C, 1.5-in. quartz tubes and fused silica boats were used for all samples (bars and bulk); for ones to 1500°C, 2.5-in. mullite tubes and boron nitride boats supported on alumina "dee" tubes were used. All pyrolyses were done under a flowing argon atmosphere, for runs to 1000°C, the flow rate was ≈ 6–8 L/h; for runs to 1500°C it was ≈16–20 L/h.

A stainless steel die was used for forming 1.5- by 0.5-in. bars. A Carver laboratory press was used for uniaxial bar pressing. Isostatic bar pressing was done in a pneumatically driven oil press with the bars contained in evacuated, sealed rubber bags. X-ray powder diffraction spectroscopy was obtained on a Charles Supper detector and Diano generator instrument.

Preparation of $[B_{10}H_{12}(Ph_3P)_2]$

A 250-mL Schlenk flask equipped with a stir-bar, gas inlet tube, and a septum was charged (under argon) with 5.0 g (41 mmol) of $B_{10}H_{14}$, 35 mL of diethyl ether and a solution of 25.0 g (95 mmol) of Ph_3P in 150 mL of Et_2O (with vigorous stirring during and for 5 min after the addition). The precipitate which had formed was filtered, washed with Et_2O, and dried at 100°C/0.1 mm Hg. The complexes where L equals Ph_2PH, Ph_2PCl, Bu_3P, and $(Me_2N)_2PCl$ were prepared by this general procedure. Those where L equals Ph_2POH, Ph_2PN_3, Ph_2PNHNH_2, and Ph_2PNH_2 were prepared as described in ref 13. The results of their pyrolysis (i.e., their ceramic yield and composition) are given in Table I.

1010

Preparation of [Ph₄P]₂[B₁₀H₁₀]

Preparation of [Ph$_4$P]$_2$[B$_{10}$H$_{10}$]

A solution of 2.00 g [Et₃NH]₂[B₁₀H₁₀] (6.2 mmol) in 30 mL 9/1 water/ethanol was added to a solution of [Ph₄P][Br] (6.00 g, 14.3 mmol) in 50 mL of the same solvent mixture, in a 125 mL Erlenmeyer flask. After the mixture had been stirred for 5 minutes, the precipitate was filtered, washed with water, 5 mL of cold (≈ -10°C) acetone and, finally, with ether. Drying at 60°C/0.1 mm Hg for 5 h gave a white solid. The following salts were all prepared by the above general metathesis route: [Ph₃PMe]₂[B₁₀H₁₀], [Bu₃PMe]₂[B₁₀H₁₀] and [Ph₃PCH₂CH₂CH₂PPh₃][B₁₀H₁₀]. The results of their pyrolysis are given in Table I.

Preparation of [B$_{10}$H$_{12}$·Ph$_2$PCH$_2$CH$_2$PPh$_2$]$_x$

To a solution of 300 mg (2.45 mmol) of B₁₀H₁₄ in 50 mL of Et₂O (at 0°C under nitrogen) was added with stirring a solution of 1.0 g (2.5 mmol) of Ph₂PCH₂CH₂PPh₂ in 50 mL of toluene. The reaction mixture was allowed to warm to room temperature and stirred for 20 h. During this time a precipitate formed which was filtered. It was dissolved in acetone and reprecipitated by adding Et₂O. A similar procedure was used in the preparation of [B₁₀H₁₂·Ph₂PC≡CPPh₂]ₓ, (B₁₀H₁₂·Ph₂PCH₂PPh₂)ₓ and [B₁₀H₁₂·Ph₂PCH₂CH₂CH₂PPh₂]ₓ.

Preparation of [B$_{10}$H$_{12}$·Ph$_2$PNHNHPPh$_2$]$_x$

To a suspension of 2.03 g (3.6 mmol) of B₁₀H₁₂(Ph₂PCl)₂ and 2.00 g (3.6 mmol) of B₁₀H₁₂(Ph₂PNHNH₂)₂ in 200 mL of acetone was added with stirring, under nitrogen, 10 mL of Et₃N over a period of 2-3 min at room temperature. The solution became clear and within about 5 min a fine white precipitate appeared. After 2 h the mixture was filtered. The acetone filtrate was evaporated to dryness to leave 4.55 g of light yellow powder. Recrystallization from acetone/diethyl ether gave 3.25 g of white crystals, MP 176–178°C (dec. with gas evolution).

Preparation of Ceramic Bars from Pure [B$_{10}$H$_{12}$·L-L]$_x$ Polymers

The procedure used with [B₁₀H₁₂·Ph₂POPPh₂]ₓ is described as an example.

A 3.0 g sample of the polymer was finely powdered in a mortar and pestle (inert atmosphere box) and then placed in a 0.5- by 1.5-in. rectangular die. Uniaxial pressing in a Carver press to 5 000 pounds (5 min) was followed by ambient temperature isostatic pressing to 50 000 psi (15 min). The polymer bar thus obtained had the approximate dimensions 0.5 by 1.5 by 0.25 in.

The bar was introduced into a fused silica pyrolysis boat which then was inserted into a quartz tube that had been flushed with argon for 15 min. (The end of the quartz tube was connected to an oil bubbler). After ≈5 min, the argon flow was reduced from ≈100 mL/min to ≈20-30 mL/min, and the quartz tube was placed in a Lindberg tube furnace and heated at a rate of 10°C/min to a temperature of 1000°C.

Preparation of Ceramic Composite Bars using B$_{10}$H$_{12}$·2L Complexes as Binders

Three procedures were used for sample preparation:

1. Weighed quantities (See Tables II and III) of B₁₀H₁₂·2L and the ceramic powder were mixed and ground for 15 min in a mortar and pestle.

2. The $B_{10}H_{12} \cdot 2L$ (0.5 g) was dissolved in 50 mL of a solvent (usually acetone) and 2.5 g of ceramic powder added. The stoppered flask was ultrasonicated for 15 min. Afterward, the solvent was removed at 100°C and 0.1 mm Hg.

3. The $B_{10}H_{12} \cdot 2L$ (0.5 g) and the ceramic powder (2.5 g) were suspended in a nonsolvent, usually pentane. Further processing was as in 2. above.

The samples thus prepared were placed in a 0.5- by 1.5-in. rectangular die and pressed in a Carver press to 5 000 pounds uniaxially (6 667 psi), removed to an ambient temperature isostatic press, and further pressed to 50 Kpsi. The uniaxial pressing time duration was about 5 min and the isostatic pressing time duration was about 15 min. The resulting bar was pyrolyzed in a stream of argon to 1000°C (10°C per min heating rate, hold at 1000°C for 30 min). The pyrolyzed sample was handled in an inert atmosphere box. The results of the individual experiments are given in Tables II and III.

A ceramic bar is considered to be "excellent" if it is a uniform, black rectangular bond that has retained its shape (vs the bar before pyrolysis) in all three dimensions without undergoing any discernable shrinkage or bloating above the detectable level of 3–5% and if its strength is such that it cannot be broken manually without the aid of mechanical means (e.g., vise and pliers).

The data in Table III were obtained similarly, but different weight ratios of binder to ceramic powder were used. It would seem that the 0.167 weight fraction of binder used (0.5/0.5 + 2.5) in the Table II experiments gives better results.
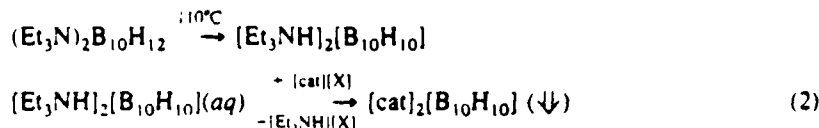
Such bars also were prepared using B_4C powder and $[B_{10}H_{12} \cdot L \cdot L]_x$ polymers as binders, specifically with those in which L-L = POP, PMP, PEP, PPP, and PCCP. All are classified as excellent.

Results and Discussion

Various known boron-containing systems were considered for possible use in this project. The need for the 4:1 boron to carbon ratio in B_4C led us to investigate the chemistry of the higher polyhedral boranes. Among these, $B_{10}H_{14}$ (Fig. 1) is ideally suited for the preparation of polymers. A well-studied reaction of $B_{10}H_{14}$ is the substitution of neutral Lewis bases (electron pair donors) at the 6 and 9 positions, resulting in expulsion of one mole of H_2 and formation of a diadduct, $L \cdot B_{10}H_{12} \cdot L$ (Fig. 2).

$$B_{10}H_{14} + 2L: \rightarrow L \cdot B_{10}H_{12} \cdot L + H_2 \qquad (1)$$
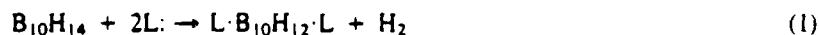
There is no gross polyhedral rearrangement during this reaction, the only structural change being the relocation of the B–H–B three-center, two-electron bridge bonds, upon going from one nido (open) structure to another. There are over 150 such $B_{10}H_{12} \cdot 2L$ complexes reported in the literature.[13] On the whole, they are oxidatively, hydrolytically and thermally stable at ambient conditions. When the Lewis base employed is Et_3N, further reaction can occur upon heating the compound in a solution of boiling toluene to produce $(Et_3NH)_2[B_{10}H_{10}]$ (Fig. 3). This salt readily undergoes cation metathesis in aqueous solution.[14]

$$(Et_3N)_2B_{10}H_{12} \xrightarrow{110°C} [Et_3NH]_2[B_{10}H_{10}]$$

$$[Et_3NH]_2[B_{10}H_{10}](aq) \xrightarrow[-[Et_3NH][X]]{+ [cat][X]} [cat]_2[B_{10}H_{10}] (\downarrow) \qquad (2)$$

A difunctional Lewis base (L~~~L) should react with $B_{10}H_{14}$ to give polymeric species of type $[B_{10}H_{12}\cdot L~~~L]_x$.

$$x\ B_{10}H_{14} + x\ L~~~L \rightarrow x\ H_2 + [B_{10}H_{12}\cdot L~~~L]_x \qquad (3)$$
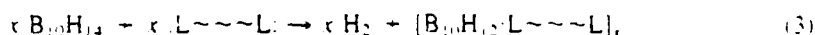
Indeed, several such polymers already had been reported, for which L~~~L was $Et_2PCH_2CH_2PEt_2$,[15] Ph_2POPPh_2 "POP", and $Ph_2PN = PPh_2CH_2CH_2PPh_2 =$ NPPh_2 "PNP".[16-18]

We began our studies with the preparation of a number of $B_{10}H_{12}\cdot 2L$ and $[cat]_2[B_{10}H_{10}]$ complexes (Table I). These can be divided into two classes (1) Those which contain phenyl groups attached to phosphorus, whose pyrolysis (to 1000°C in an argon stream) gives a high (>70%) yield of ceramic residue. This residue contains a large fraction of the initial carbon content of the starting complex (cf., Table I). (This is a general characteristic of phenyl-containing preceramic polymers, see, for instance, refs. 5-10). (2) Those which do not contain phenyl groups attached to phosphorus, whose pyrolysis gives lower (50-70%) yields of ceramic residue. Pyrolysis of powder samples (to 1000°C in an argon stream) resulted in retention of considerable amounts of phosphorus (Table I), however, on further heating to 1500°C, nearly total loss of phosphorus occurred (Table IV) and B_4C was the only X-ray diffracting phase. In all cases, the ceramic residue from pyrolysis to 1000°C was amorphous. For similar experiments on monolithic samples, see the accompanying paper.[19]

These $B_{10}H_{12}\cdot 2L$ and $[cat]_2[B_{10}H_{10}]$ complexes proved to be useful as binders for B_4C and other ceramic powders (SiC, BN, $B_{13}P_2$, Si_3N_4, B; Tables II, III). The best results were obtained when the phosphorus ligand contained phenyl substituents, no doubt due to the high ceramic yields in these systems. Since, in this application, the boron-containing complexes used as binders are present in the composite sample to the extent of ≈ 17 wt% (Table II), the excess of carbon in their pyrolytic char is less of a disadvantage than when the pure complexes (monoliths) are pyrolyzed. The excellent results obtained with boron powder (Table II) hint at a route useful for converting the excess carbon from the binder to B_4C. One known use of B_4C is as a densification aid (with or without added carbon) in silicon-containing ceramic materials; therefore we are encouraged by the results observed in this area (Table II).

Since our major interest was in applications involving ceramic monoliths and/or ceramic fibers (goals not realized with the above monomeric species), and polymeric species had filled these roles in our silicon-containing systems,[5-10] $B_{10}H_{14}$-derived polymers were of interest. In addition to the known POP and PNP polymers, we prepared new $[B_{10}H_{12}\cdot L~~~L]_x$ polymers derived from L~~~L = $Ph_2PCH_2PPh_2$ "PMP", $Ph_2PCH_2CH_2PPh_2$ "PEP", $Ph_2PCH_2CH_2$ CH_2PPh_2 "PPP", $Ph_2PC\equiv CPPh_2$ "PCCP", and $Ph_2PNHNHPPh_2$ "PNNP", and studied their use as "preceramic polymers." Ceramic data (yield and elemental composition) for the pyrolysis products (1000°C, Ar atm) from these macromolecular species are in Table IV. The polymers containing POP, PMP, PEP, PPP and PCCP linkages served well both as binders for B_4C powder and, more importantly, in the production of ceramic monoliths by pyrolysis of shaped polymer bodies. Of these, POP was the most successful and, therefore, chosen as the target of a further, more detailed investigation.

Previous workers had determined the low temperature volatile by-products of the pyrolysis of POP to consist of hydrogen and trace amounts of benzene.[16-18] We have determined the thermogravimetric (TGA wt change) and thermomechan-

ical (TMA/length change) properties of this polymer (Fig. 4). The initial TGA weight loss arises from loss of H_2 caused by breakage of B–H bonds and concomitant formation of B–B bonds, as inferred from ir studies of the polymer prior to and after the weight loss. Likewise, intermediate weight loss is due to processes involving breakage of C–H bonds and formation of B–C bonds. High temperature weight loss is associated with loss of phosphorus. The TMA data imply that no melt phase is present for this polymer over the temperature range studied. By combining TMA and TGA measurements, a composite curve of density versus temperature may be calculated (Fig. 5). These curves have been extended to higher temperatures.[19] The DRIFT (diffuse reflectance Fourier transform infrared) spectra of samples of POP polymer fired to 1000° and 1500°C each showed broad absorptions at 780–830, 1090–1105 and 1560–1580 cm^{-1} attributed to the presence of B–B, B–C and C–C bonds, respectively. Additionally, the 1000°C sample had absorptions at 2850–3000 cm^{-1} attributed to the presence of residual B–H and C–H bonds.

Conclusions

This work has demonstrated the usefulness of phosphorus-containing derivatives of decaborane(14) as precursors for boron-containing ceramic materials. All samples investigated served as binders for B_4C. The results of experiments employing $B_{10}H_{12} \cdot 2L$ compounds and $[P^+]_2[B_{10}H_{10}]$ (P^+ = phosphonium cation) salts in this capacity have been summarized; additionally, some complexes served well as binders for various other ceramic powders. The yield and elemental composition of ceramic materials derived from these molecular species and salts have been given. The best results were obtained when L was a diphenylphosphido derived Lewis base, presumably due to the high ceramic yields observed in these systems. Known and new polymers obtained from reactions of diphosphines with $B_{10}H_{14}$ have been shown to serve as ceramic powder binders, and, in some cases, as ceramic monolith precursors. Results of experiments using organic diamines in a similar manner, to yield either pure BN fibers or $B_4C/BN/C$ fibers and monoliths, are outlined in a separate report.[20]

Acknowledgment

References

[1] H. Kent Bowen. "Advanced Ceramics." *Scientific American.* **255** (4) (1986) 169

[2] R. Thompson. "The Chemistry of Metal Bondes and Related Compounds." in Progress in Boron Chemistry. Vol. 2. R. J. Brotherton and H. Steinberg, ed.. Pergamon. London. 1970. pp. 173–230

[3] R. H. Wentorf. Jr., in Kirk-Othmer Encyclopedia of Chemical Technology. 3rd Ed., Vol. 4. Wiley, New York. 1978. pp. 126–127

[4] "Composite Materials Review." *Composite Materials.* 1987 (9). 54 pp

[5] D. Seyferth. G. H. Wiseman and C. Prud'homme. "A Novel Liquid Silazane Precursor to Silicon Nitride. *J. Am. Ceram. Soc.* **66** [1]. C-13—C-14 (1983)

[6] D. Seyferth and G. H. Wiseman. "High Yield Synthesis of Si_3N_4/SiC Ceramic Materials by Pyrolysis of a Novel Polyorganosilazane." *J. Am. Ceram. Soc.* **67** [7]. C-132—C-133 (1984)

[7] D. Seyferth and G. H. Wiseman. "Preceramic Organosilazane Polymers." U.S. patent 4 482 669 (Nov. 13. 1984)

[1] D. Seyferth, T. G. Wood and Y.-F. Yu, "Method for Forming New Preceramic Polymers for SiC and Si₃N₄/SiC Systems," U.S. patent 4,645,807 (Feb. 24, 1987)

D. Seyferth and Y.-F. Yu, "Method for Forming New Preceramic Polymers Containing Silicon," U.S. patent 4,639,501 (Jan. 27, 1987)

D. Seyferth and Y.-F. Yu, "Method for Converting Si-H Containing Polycarbosilanes to New and Useful Preceramic Polymers and Ceramic Materials," U.S. patent 4,650,837 (Mar. 17, 1987)

K. J. Wynne and R. W. Rice, "Ceramics via Polymer Pyrolysis," Ann. Rev. Mater. Sci., 14 (1984) 297.

[2] R. W. Rice, "Ceramics From Polymer Pyrolysis, Opportunities and Needs—A Materials Perspective," Amer. Ceram. Soc. Bull., 62 (1983) 889

[3] For a complete discussion of B₁₀H₁₂·2L complexes see Gmelin Handbook of Inorganic Chemistry, 8th Ed., Vol. 54, "Boron Compounds B-H Compounds," Part 3, K. Niedenzu and K. C. Buschbeck, ed., Springer-Verlag, Berlin, 1979, pp. 151–165

[4] For a complete discussion of salts of the [B₁₀H₁₀]²⁻ anion, see E. L. Muetterties and W. A. Knoth, "Polyhedral Boranes," Dekker, New York, 1968, 197 pp

[5] G. W. Parshall, "Hydrocarbylphosphinodecaboranes and Fuel Compositions Containing Them," U.S. patent 3,035,949 (May 22, 1962)

[6] H. A. Schroeder, J. R. Reiner and T. A. Knowles, "Chemistry of Decaborane-Phosphorus Compounds III. Decaborane-14-Phosphine Polymers," Inorg. Chem., 2 (1963) 393.

[7] J. R. Reiner and H. A. Schroeder, "Linear Condensation Polymers from Bis(Phosphine) decaboranes," U.S. patent 3,141,856 (July 21, 1964)

[8] H. A. Schroeder, "Novel Polymers From the Condensation of Bis(azidodiarylphosphine)decaborane and Diphosphines," U.S. patent 3,155,630 (Nov. 3, 1964)

[9] Lightfoot, W. S. Rees, Jr. and J. S. Haggerty, "Boron-Containing Ceramic Materials Derived From Polymeric Precursors, Material Characteristics," following paper, this issue

[10] W. S. Rees, Jr. and D. Seyferth, "High Yield Synthesis of B₄C/BN Ceramic Materials by Pyrolysis of Polymeric Lewis Base Adducts of Decaborane(14)," J. Am. Ceram. Soc. in press (1988)

[11] H. A. Schroeder, J. R. Reiner and T. L. Heying, "Chemistry of Decaborane-Phosphorus Compounds. I. Nucleophilic Substitutions of Bis-(chlorodiphenylphosphine)-decaborane," Inorg. Chem., 1 (1962) 618

Table I. Pyrolysis of $B_{10}H_{12}$·2L Adducts and $[P^+]_2[B_{10}H_{10}]$ Salts

Compound	Ceramic Yield (%)[a]	Ceramic Composition (%)[a]		
		B	C	P
$B_{10}H_{12}(Ph_2PH)_2$	83	23.17	60.75	13.71
$B_{10}H_{12}(Ph_3P)_2$	86	18.20	69.59	9.88
$B_{10}H_{12}(Ph_2PCl)_2$	73	20.62 Cl, 0.02	57.09	13.17
$B_{10}H_{12}(Ph_2POH)_2$	77	21.38 O, 10.57	55.65	11.93
$B_{10}H_{12}(Ph_2PN_3)_2$	72			
$B_{10}H_{12}(Ph_2PNHNH_2)_2$	71	27.69 N, 16.56	43.80	8.20
$B_{10}H_{12}(Bu_3P)_2$	58	35.94	46.34	35.94
$B_{10}H_{12}((Me_2N)_2PCl)_2$	55			
$[Ph_3PMe]_2[B_{10}H_{10}]$	83			
$[Ph_4P]_2[B_{10}H_{10}]$	93	6.87	73.06	13.01
$[Ph_3P(CH_2)_3PPh_3][B_{10}H_{10}]$	91	15.96	69.33	8.33
$[Bu_3PMe]_2[B_{10}H_{10}]$	68	30.10	49.03	11.96

[a] Pyrolysis to 1000°C under argon. Ceramic yield $= \dfrac{\text{wt. residue}}{\text{wt. sample pyrolysed}} \times 100$

[b] Compare with B₄C calculated 21.74%C, 78.26%B

Table II. $B_{10}H_{12} \cdot 2L$ Binder Experiments. 16.7% Binder (by weight)

$B_{10}H_{12} \cdot 2L$	Ceramic Powder	Mixture Method*	Color	Shape Retention
$B_{10}H_{12}[(C_6H_5)_2PH]_2$	B_4C	A	Black	Excellent
$B_{10}H_{12}[(C_6H_5)_2PCl]_2$	B_4C	A	Black	Excellent
$B_{10}H_{12}[(C_6H_5)_2PNHNH_2]_2$	B_4C	A	Black	Satisfactory
$B_{10}H_{12}[(C_6H_5)_2POH]_2$	B_4C	A	Black	Good
$B_{10}H_{12}[(C_6H_5)_2PN_3]_2$	B_4C	A	Black	Satisfactory
$B_{10}H_{12}\{[(CH_3)_2N]_2PCl\}_2$	B_4C	A	Black	Fair
$B_{10}H_{12}[(C_4H_9)_3P]_2$	B_4C	B(pentane)	Black	Good
$B_{10}H_{12}[(C_6H_5)_3P]_2$	B_4C	B(acetone)	Black	Excellent
$B_{10}H_{12}[(C_6H_5)_3P]_2$	B_4C	C(pentane)	Black	Excellent
$B_{10}H_{12}[(C_6H_5)_2PH]_2$	B_4C	B(acetone)	Black	Excellent
$B_{10}H_{12}[(C_6H_5)_2PH]_2$	B_4C	C(pentane)	Black	Excellent
$B_{10}H_{12}[(C_6H_5)_3P]_2$	B	A	Dk. red	Excellent
$B_{10}H_{12}[(C_6H_5)_3P]_2$	Si_3N_4	A	Gray	Excellent
$B_{10}H_{12}[(C_6H_5)_3P]_2$	α-SiC	A	Dk. gray	Good
$B_{10}H_{12}[(C_6H_5)_3P]_2$	β-SiC	A	Dk. gray	Good
$B_{10}H_{12}[(C_6H_5)_3P]_2$	BN	A	Gray	Satisfactory
$B_{10}H_{12}[(C_6H_5)_3P]_2$	AlN	A	Silver/Gray	Good
$B_{10}H_{12}[(C_6H_5)_3P]_2$	BP	A	Gray	Fair
$B_{10}H_{12}[(C_6H_5)_3P]_2$	$B_{12}P_2$	A	Dk. gray	Excellent
$B_{10}H_{12}[(C_6H_5)_3P]_2$	Rayon	B(acetone)	Black	Good

*Solvent or diluent used in sample preparation

Table III. $B_{10}H_{12} \cdot 2L$ Binder Experiments (other weight fractions of binder)

$B_{10}H_{12} \cdot 2L$ (g)	Ceramic Powder (g)	Mixture Method	Color	Shape Retention
$B_{10}H_{12}[(C_6H_5)_3P]_2$ (3.0)	None	A	Black	Good
$B_{10}H_{12}[(C_6H_5)_3P]_2$ (0.1)	B_4C (2.9)	A	Black	Fair
$B_{10}H_{12}[(C_6H_5)_3P]_2$ (0.1)	B_4C (2.9)	B(acetone)	Black	Fair
$B_{10}H_{12}[(C_6H_5)_3P]_2$ (0.1)	B_4C (2.9)	C(pentane)	Black	Fair
$B_{10}H_{12}[(C_6H_5)_3P]_2$ (0.25)	B_4C (2.75)	A	Black	Satisfactory
$B_{10}H_{12}[(C_6H_5)_3P]_2$ (0.25)	B_4C (2.75)	B(acetone)	Black	Satisfactory
$B_{10}H_{12}[(C_6H_5)_3P]_2$ (0.25)	B_4C (2.75)	C(pentane)	Black	Satisfactory
$B_{10}H_{12}[(C_6H_5)_2PH]_2$ (0.1)	B_4C (2.9)	A	Black	Fair
$B_{10}H_{12}[(C_6H_5)_2PH]_2$ (0.1)	B_4C (2.9)	B(acetone)	Black	Fair
$B_{10}H_{12}[(C_6H_5)_2PH]_2$ (0.1)	B_4C (2.9)	C(pentane)	Black	Fair
$B_{10}H_{12}[(C_6H_5)_2PH]_2$ (0.25)	B_4C (2.75)	A	Black	Fair
$B_{10}H_{12}[(C_6H_5)_2PH]_2$ (0.25)	B_4C (2.75)	B(acetone)	Black	Fair
$B_{10}H_{12}[(C_6H_5)_2PH]_2$ (0.25)	B_4C (2.75)	C(pentane)	Black	Fair

Table IV. Phosphorus-Containing Polymers Investigated as Ceramic Precursors

Polymer Linker*	Ceramic Yield to 1000°C	Elemental Analysis of Ceramic		
		B	C	P
O	93	25.30 O, 12.05	52.01	8.69
O'	NA	28.90 O, 2.88	60.21	0.39
N = PPh₂CH₂CH₂PPh₂ = N	52	22.75 N, 0.14	56.31	12.46
CH₂CH₂	92	22.52	45.78	11.25
C≡C	69	20.05	59.15	14.59
NHNH	57	Not determined		

*All polymers have the structural formula $[B_{10}H_{12} Ph_2P—linker—PPh_2]_x$.
'Sample pyrolyzed to 1500°C.
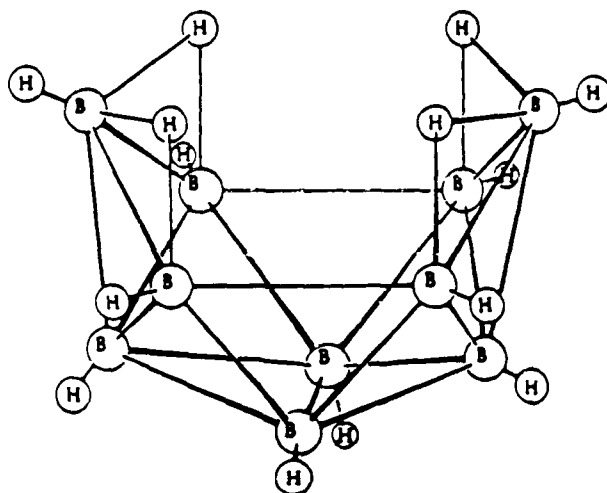
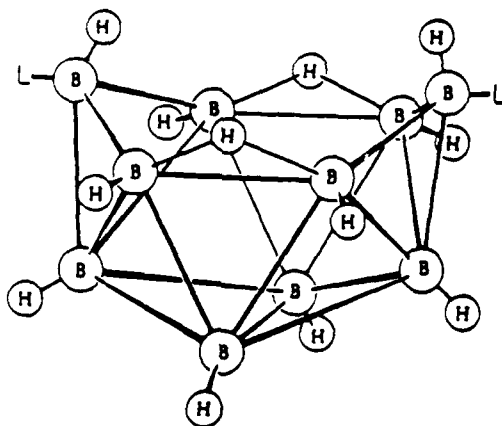Fig. 1. Structure of decaborane(14), $B_{10}H_{14}$.

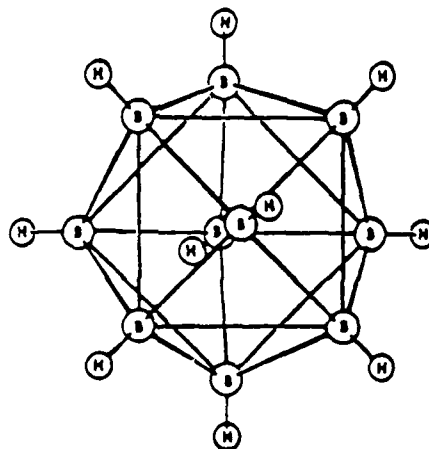Fig. 2. Structure of the $B_{10}H_{12} \cdot 2L$ complexes.
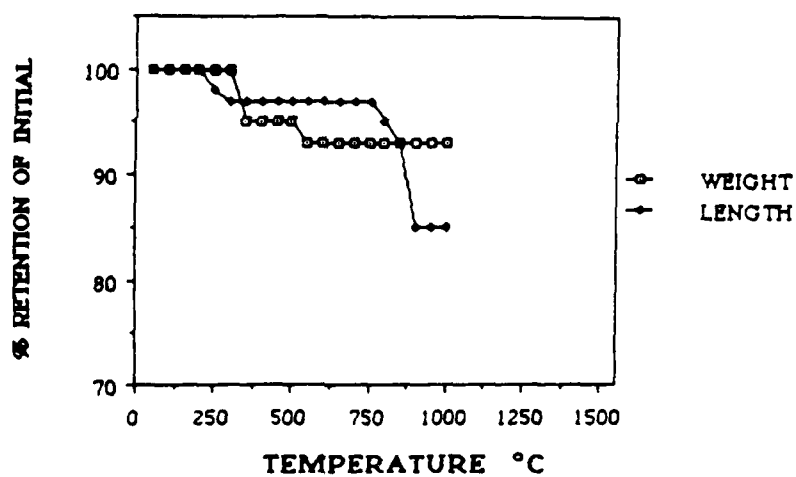
Fig. 3. Structure of $B_{10}H_{10}^{2-}$.

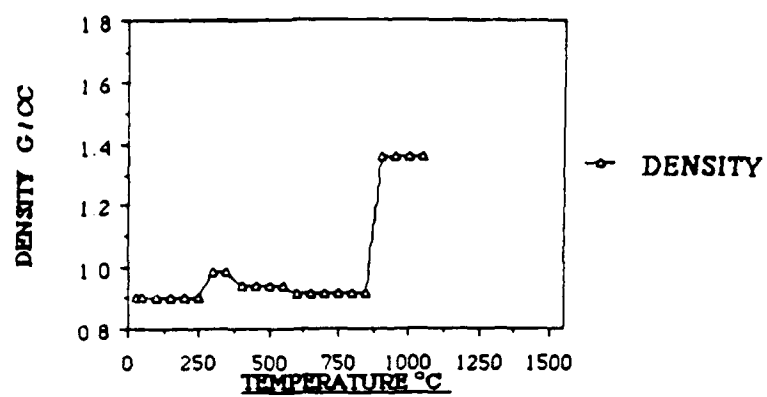Fig. 4. Mass and volume change versus temperature plot for POP polymer.

Fig. 5. Density versus temperature plot for POP polymer.